Polaron Dynamics in the Alpha Helix: Models of Electron Transport in Hydrogen-Bonded Polypeptides

JINGXI LUO

Polaron Dynamics in the Alpha Helix

Models of Electron Transport in Hydrogen-Bonded Polypeptides

Thesis Presented for the Degree of Doctor of Philosophy

to the

Department of Mathematical Sciences

of

Durham University

by

Jingxi Luo

on

17 September 2018

Abstract

Polaron Dynamics in the Alpha Helix

In this thesis, I present two mathematical models which are capable of explaining the phenomenon of directed electron transport in α-helical regions of protein macromolecules. The models are built upon the framework of polaron theory, which originated in condensed matter physics, and which I argue is applicable to biophysical systems such as an extra electron interacting electromagnetically with peptide units in an α-helix. The two models concern the electron's coupling to, respectively, picosecond-scale intrapeptide oscillators and nanosecond-scale hydrogen bond phonons in the α-helix. I show that the models permit the auto-localisation of the electron in stationary polaron states, and that certain electromagnetic fields cause the polaron to propagate along the polypeptide, transporting the electron in a solitonic manner. Taking effects of the cell environment into account, I demonstrate that stochastic forces arising from thermal fluctuations can enhance the electron transport, and that the stability of the polaron dynamics exhibit contrasting degrees of tolerance to temperature in the two models. When interpreting my results, I describe their biological implications, as well as the physical realisability of the models' forcing parameters. In particular, I establish that some electromagnetic fields which can facilitate directed electron transport are intrinsic physical features of the cell.

Declaration

This thesis is based on research conducted in the Department of Mathematical Sciences, Durham University, United Kingdom. No part of this thesis has been submitted elsewhere for any other degree or qualification. The thesis is entirely my own work unless referenced to the contrary in the text.

Chapter 3 is partly adapted from joint work with B. M. A. G. Piette [LP18].

Chapter 4 is partly adapted from joint work with B. M. A. G. Piette [LP17].

Copyright Statement

Acknowledgements

Nobody* crosses the sea alone. Now that I have emerged from this Ph.D. odyssey of mine, weathered but largely unscathed, and with any luck a better person, I am heartily obliged to a great number of people.

I wish first and foremost to thank my supervisor, mentor and colleague, Dr Bernard Piette, who has steered me clear of the reefs and bergs on my perilous route to enlightenment, and whose resolute enthusiasm for science and unfaltering dedication to our work have inspired me continually to strive for excellence. He has shown me by example just what it means to be an exceptional researcher and exemplary teacher, and I am grateful for his abiding belief in me that I have what it takes to be the same.

To the superb staff members in my Department and my fellow Ph.D. students, particularly anyone with whom I have shared an office: thank you for bearing with me.

Folks who are closest to me and who have held my heart in their hands through the darkest of storms - Akemi Herráez, Alex Aldred, Ana-Maria Cîrstea, Charlotte Bentley, Diana Flindt, Hattie Induni, Helen Webster, Irene Pasquinelli, Kyle Wong, Nora Romek, Sam Jackson, Smita Sahu, Steffi John, Stephan Wojtowytsch, Tharindi Udalagama, Young Ah Kim and Zuzanna Świrad: I am grateful for the warmth of your company. For every soul wrestling the waves, there is a lighthouse on the shore; mine has been you, and the hope that your friendship will long outlast the shine on my doctoral certificate.

Saving the most personal till last, I must declare that I am indebted in more ways than one to my long-suffering parents. I am here today only because when I decided to move to England at sixteen, they said *Go*; when I decided to study mathematics, they said *Do it*; when I decided to travel the world instead of flying home to see them every Christmastime, they said *Good for you*; and when I decided to embark upon this bewildering, ridiculous expedition of a Ph.D., they doffed their imaginary hats on Skype and called me *Doctor*. Most importantly of all, whilst I grew up and away from their shelter, they gave me the strength and wisdom to make my own decisions - to take the helm of my own ship.

Now, the end of a voyage is as much an opportunity for reminiscence as it is a time to prepare for yet stranger waters. If truths lay in troves at sea, let the record show that I am ready more than ever for a lifetime of treasure hunting beyond the subsiding tide.

*Except for Ellen MacArthur, obviously.

Contents

List of Figures

Notations, Units and Constants

Notations shall be self-consistent within each individual Chapter, although some symbols may take on one meaning in one Chapter and another in the next. Whenever a notation is defined or redefined, I will explicate its meaning in detail, and in any case its interpretation shall always be clear in the context. For the reader's reference, there now follows a Chapter-by-Chapter breakdown of the definitions of some key symbols.

Chapter 3

$$\widehat{H}_{\mathrm{e}}, \widehat{H}_{\mathrm{p}}, \widehat{H}_{\mathrm{int}}, \widehat{H}_{\mathrm{ext}} :$$

Hamiltonians for, respectively, a tight-binding extra electron, intrapeptide oscillators on the lattice nodes, interaction between the electron and intrapeptide oscillators, and interaction between the electron and an external electromagnetic field.

$$J_0, J_1, M, \Omega, R, \chi :$$

Respectively, the electron site energy, nearest-neighbour electron transfer integral, reduced mass of a C=O oscillator, natural angular frequency of a C=O oscillator in the amide-I mode, equilibrium distance between centres of mass of neighbouring C=O oscillators, and strength of the electron-oscillator coupling.

$$\widehat{Q}_n, \widehat{P}_n, u_n :$$

Respectively, the operator for displacement of the n^{th} C=O oscillator, the operator for momentum conjugate to that displacement, and dimensionless expected value of relative displacement of the n^{th} oscillator.

$$\rho, \kappa :$$

Dimensionless quantities representing, respectively, the characteristic time-scale separation between electron dynamics and C=O oscillator dynamics (*adiabaticity parameter*), and electron-oscillator coupling strength (*coupling constant*).

Chapter 4

$$\widehat{H}_{\mathrm{e}}, \widehat{H}_{\mathrm{p}}, \widehat{H}_{\mathrm{int}}, \widehat{H}_{\mathrm{ext}} :$$

Hamiltonians for, respectively, a tight-binding extra electron, hydrogen bond-stretching oscillations, interaction between the electron and hydrogen bond oscillations, and interaction between the electron and an external electromagnetic field.

$$J_0, J_1, M, K, \Omega, R :$$

Respectively, the electron site energy, nearest-neighbour electron transfer integral, average mass of a peptide unit in a transmembrane α-helix, force constant of a hydrogen bond in the α-helix, characteristic time-scale defined by $\Omega = \sqrt{K/M}$, and equilibrium distance between centres of mass of neighbouring peptide units.

$$\chi_l, \chi_r, \chi, \beta :$$

Respectively, strength of the electron-hydrogen bond coupling towards one end of the α-channel, strength of the coupling towards the other end of the channel, total strength of the coupling defined by $\chi = \chi_r + \chi_l$, and a dimensionless *symmetry parameter* defined by $\beta = (\chi_r - \chi_l)/\chi$ representing the spatial anisotropy of electron-hydrogen bond coupling.

$$U_n, P_n, S_n :$$

Respectively, the displacement of the n^{th} peptide unit, the momentum conjugate to that displacement, and distortion of the hydrogen bond between the n^{th} and $(n+1)^{\mathrm{th}}$ peptide units.

$$\rho, \kappa :$$

Dimensionless quantities representing, respectively, the characteristic time-scale separation between electron dynamics and lattice phonon dynamics (*adiabaticity parameter*), and electron-hydrogen bond coupling strength (*coupling constant*).

Chapter 5

$$\widehat{H}_{\mathrm{e}}, \widehat{H}_{\mathrm{p}}, \widehat{H}_{\mathrm{int}}, \widehat{H}_{\mathrm{ext}}, J_0, J_1, J_2, M, K, \Omega, R, \chi_l, \chi_r, \chi, \beta, \zeta :$$

Same as in Chapter 4 except that J_1 is the nearest-neighbour electron transfer integral between peptide units along an α-channel, J_2 is the nearest-neighbour electron transfer

integral between peptide units across adjacent channels, and ζ is a dimensionless geometry parameter accounting for the twisting of the channels.

$$U_{n,j}, P_{n,j}, S_{n,j} :$$

Respectively, the displacement of the $(n,j)^{\text{th}}$ peptide unit projected onto the helical axial direction, momentum conjugate to that displacement, and distortion of the hydrogen bond between the $(n,j)^{\text{th}}$ and $(n+1,j)^{\text{th}}$ peptide units projected onto the helical axial direction.

$$\rho_1, \rho_2, \kappa :$$

Dimensionless quantities representing, respectively, the characteristic time-scale separation between intra-channel electron dynamics and lattice dynamics, characteristic time-scale separation between inter-channel electron dynamics and lattice dynamics, and electron-hydrogen bond coupling strength.

Chapters 3 to 5

In all instances,

$$\widehat{H} = \widehat{H}_{\text{e}} + \widehat{H}_{\text{p}} + \widehat{H}_{\text{int}} + \widehat{H}_{\text{ext}}$$

is the total Hamiltonian, which encapsulates all aspects of the dynamics of the system except for its thermalisation.

$$E, \epsilon, \Gamma, \gamma, \Theta, \theta$$

are, respectively: amplitude of the electric field component, along the helical axis, of the external electromagnetic field; dimensionless amplitude of that electric field component; viscous damping coefficient describing the effect of friction on the lattice nodes due to its thermal environment; dimensionless viscous damping coefficient; temperature of the environment; and dimensionless thermal energy due to temperature of the environment.

$$E_{\text{b}}, E_{\text{b}}^{0}, E_{\text{b}}^{(\theta)}$$

are, respectively, internal energy of the polaron, binding energy of the stationary polaron, and quasi-stationary internal energy of the polaron at thermal equilibrium. Finally,

$$\widehat{A}^{\dagger}, \widehat{A}$$

are, respectively, electron creation and annihilation operators, and are singly- or doubly-indexed depending on the model.

Other notes on notations

If the limits of a sum or product are unspecified, then it is implied that the sum or product is performed over all possible values of the index or indices. Similarly, if the limits are unspecified for an integral, then it is implied that the integration is performed over the entire domain.

Unit conversions

The ångström: $1\ \text{Å} = 10^{-10}\ \text{m}$.

The electronvolt: $1\ \text{eV} = 1.602 \times 10^{-19}\ \text{J}$.

The debye: $1\ \text{D} = 3.336 \times 10^{-30}\ \text{C} \cdot \text{m}$.

Unit prefixes shall have the following usual meanings.

f (femto-): 10^{-15}, p (pico-): 10^{-12}, n (nano-): 10^{-9}, μ (micro-): 10^{-6},
m (milli-): 10^{-3}, k (kilo-): 10^{3}, M (mega-): 10^{6}, G (giga-): 10^{9},
T (tera-): 10^{12}, P (peta-): 10^{15}.

Universal constants

Speed of light in vacuum: $c = 2.998 \times 10^{8}\ \text{m} \cdot \text{s}^{-1}$.

Reduced Planck constant: $\hbar = 1.054 \times 10^{-34}\ \text{J} \cdot \text{s}$.

The elementary charge: $e = 1.602 \times 10^{-19}\ \text{C}$.

Vacuum permittivity: $\epsilon_0 = 8.854 \times 10^{-12}\ \text{F} \cdot \text{m}^{-1}$.

Boltzmann constant: $k_\text{B} = 1.381 \times 10^{-23}\ \text{J} \cdot \text{K}^{-1}$.

Chapter 1

Introduction

The foundational principle of this thesis is that one may apply theoretical frameworks from physics, particularly condensed matter physics, to studying biological processes on the molecular scale.

There exists a rich catalogue of mathematical models that serve to explain or make predictions about biological phenomena. The key to creating these models is always to simplify the biological system to such an extent that the relationships between its variables may be encapsulated by a set of equations, and any assumptions or insights leading to the requisite simplifications are usually physical. For example, the Lotka-Volterra model of population dynamics depended upon the physical assumption of a closed system, whereby the species concerned occupied an unchanging space under no external influence [Lot20, Vol26]. Turing's theory of morphogenesis approximated any discrete system of cells as a continuum, and the derivation of his famous equations relied on the insight that certain physical laws of motion are invariant under orientation reversal [Tur52]. In neurobiology, Hodgkin and Huxley's Nobel Prize-winning work on the initiation and propagation of action potentials involved representing the cell membrane as an electrical circuit, and therefore the theories of conductance and ion gradients were vital to their model [HH52, Hil01]. Physics, therefore, tends to provide the bridge between an idealised representation of a biological system and a mathematical model consisting of variables, parameters and equations.

Assumptions in a model are not always realisable in nature; nevertheless, they are essential to ensuring that the equations therein are sufficiently simple in the mathematical sense, so that solutions may be found at least by numerical methods. In many cases, even the simplest of models produce results which closely align with empirical data; but equally,

one often finds the need to generalise a model, meaning to discard some of its simplifying assumptions. Generalisations may manifest themselves in many forms: extra terms in the equations, modifications to the parameters, or even the addition of new variables, and so on. In any case, it is crucial that one should be able to recover old models from their generalised versions by imposing appropriate constraints on the system. The Lotka-Volterra model in its simplest form, for instance, could not produce results matching the Hudson Bay Company's records spanning 200 years of lynx-hare population dynamics in the Canadian boreal forest, but a generalised model provided a good match with the data [Gil73]. The new model relaxed two of the original's simplifying assumptions: instead of exponential growth, the lynx population in isolation would grow logistically, with a carrying capacity proportional to the hare population; and instead of a closed system, now there was an external influence in the form of an epidemic that killed lynx as soon as the hare population reached some threshold. These generalisations manifested themselves in extra terms in the equations involving the following new parameters: a coefficient of proportionality between the carrying capacity of the lynx population and the density of the hare population, an epidemic threshold and a lynx mortality rate due to the epidemic. By setting the first and second parameters to infinity, and the third to zero, one recovers the original Lotka-Volterra model. On the other hand, by fitting the parameters to the existing data, meaning to fix parameters at values which lead to results that best fit the data, one is able to use the model to make predictions about the lynx-hare dynamics in future years. Moreover, given another two-species predator-prey system, if one assumes that it behaves in the same characteristic manner as the lynx-hare system does, then one is able to use the same generalised Lotka-Volterra model with refitted parameters to make predictions about the new system. Thus, whether or not a generalisation is motivated by an inadequacy of an existing model, it is always the pursuit of a model with yet stronger explanatory or predictive powers, even if in exchange for the more accurate representation of reality one has to sacrifice some of the model's mathematical simplicity.

Now, let us turn to the problem at hand. When I embarked upon the research project which has culminated in this thesis, I was interested in the following conundrum: *how do proteins conduct electricity?* In terms which are specific enough to formulate a Ph.D. research question, I wanted to answer: *by what mechanism is an electron transported along the hydrogen-bonded polypeptide of a protein macromolecule?*

The directed motion of electrons in proteins is known to be essential to a wide range of biological processes. A prime example is oxygenic photosynthesis, where the transfer of electrons through the protein *photosystem II* (PSII) drives the oxidation of water, a reaction which is responsible for producing almost all atmospheric oxygen and which generates proton gradients that help to create the energy storage molecule *adenosine triphosphate* (ATP) [FAOR89, Jol03, JL08, UKSK11, SAH$^+$15, KMB$^+$16]. A related process in which electron transport is heavily involved is aerobic respiration, the main means by which fungi and animals convert chemical energy into ATP, where the donor-acceptor transfer of electrons releases energy through redox reactions and enables ATP production [Mit61, MM67, DKM00, Ric03]. Despite its importance, the exact mechanism of electron transport in proteins is not yet fully elucidated. A popular hypothesis is known as *superexchange theory*, whereby the transfer of an electron from a donor to an acceptor is modelled as a quantum tunnelling process through a series of potential barriers [McC61, BJMBO89, BBO91, BBO92]. Although the theory has been successful in interpreting some experimental data [MKW$^+$92, FMD93, JBVR02], a recurring critique of it has related to its inadequacy at accounting for the intervening polypeptide structure between donor and acceptor [GK93, GW96]. In recent years, an alternative modelling approach utilising the framework of *polaron theory* has gained traction, and that is the approach I shall be exploring in this thesis.

In condensed matter physics, a polaron is a quasi-particle comprising two parts: an electron and a phonon. The phonon itself is a quasi-particle, first introduced as a theoretical concept in 1929 [Tam29]. It was assumed that in a crystalline material, the *adiabatic condition* held for each of the atoms or molecules that constituted the crystal lattice, meaning that the subatomic or submolecular components of each lattice node moved in sync as a whole. A phonon is a collective excitation of the lattice where all nodes oscillate with the same frequency. The cause of such a collective oscillation is the interatomic or intermolecular forces along the chemical bonds joining one node to the next. Under those forces, every node attracts or repels neighbouring ones, and a possible resulting behaviour is a collective oscillation with one unified frequency. Mathematically, one may model the system of nodes and forces either as a classical mechanics problem of masses and springs [PY58, Joy74], or as a quantum mechanics problem of collective boson excitations [Kit63, Mah13]; either way, the phonon is a normal mode solution to a many-body problem. While the classical picture permits any vibrational frequency, hence any amount

of phonon energy, on a continuous spectrum, the phonon's energy spectrum in the quantum picture is, by definition, quantised. Experimental evidence has long suggested that the energy spectra of phonons in materials such as metal and metal matrix composites are quasi-continuous with almost-indistinguishable levels [Wal56, RAT63], a phenomenon which has been accurately explained by the quantum model of phonons [LP86, BIST89], though a classical model could also produce comparable results [Bre79, SB80, Mis12].

When an extra electron is introduced to the lattice, it interacts electromagnetically with all the charged or polar lattice nodes. In 1933, Landau theorised that the electron could cause localised distortions in the lattice, affecting the phonon oscillations, and in return the distorted lattice could provide a deep potential well for the electron, causing it to localise [Lan33]. This process was called the *auto-localisation* or *self-trapping* of the electron, and the auto-localised electron-phonon composite became known as a polaron. Moreover, it was theorised that under suitable conditions, the electron and localised lattice distortion could move in sync, stabilising each other through their interaction, resulting in a kind of solitonic electron transport, known as polaron propagation, which displayed little or no dispersion. In the years that followed Landau's initial conceptualisation, the mathematical model of the polaron was refined by, among others, Pekar [Pek46, LP48], Fröhlich [Frö50, Frö52, Frö54] and Holstein [Hol59a, Hol59b, FH63, Hol64], who in their numerous works found applications of polaron theory to explaining or predicting a variety of physical phenomena, from superconductivity to the Hall effect. It became standard practice to write polaron models in the *Hamiltonian formalism* of dynamics, whereby a *Fröhlich Hamiltonian* encapsulated the dynamics of the system that it modelled. The Fröhlich Hamiltonian always consisted of three components, respectively describing the electron, phonon and electron-phonon interaction. It also became canonical knowledge that every polaron model contained a parameter of paramount importance: the electron-phonon *coupling constant*, a measure of the electron-phonon interaction strength, whose value fundamentally determined the model's outputs. Empirical observations of polarons quickly followed, in a vast number of systems including indium antimonide (InSb) [JL66], epitaxial thin film of indium arsenide (InAs) [LDS69], crystals of silver bromide (AgBr) [BLCW69], and alkali and silver halides [Hod71]. Using their experimental data, the authors fitted the dimensionless electron-phonon coupling constant in the polaron model, and its value ranged from 0.02 in the InSb system to upwards of 3 in alkali halide systems. It was natural that the value of the coupling constant should depend on the system's

intrinsic properties. Nonetheless, the immensity of its variation was simultaneously a testament to the strength of the polaron model - it was valid in hugely varied settings - and a challenge for theorists modelling any specific system without empirical data, who needed to tune a parameter's value over two orders of magnitude and accordingly to parametrise every aspect of their model's outputs.

The application of polaron theory to studying biological systems began in the 1970s, but it was not applied specifically to the problem of electron transport: in 1973, Davydov proposed a polaron-type model to explain the localisation and transport of quanta of *amide-I* energy along α-helical regions of protein macromolecules [Dav73]. Amide-I is the name of an intrapeptide vibrational mode in proteins, corresponding to the linear stretching of C=O double bonds in amino acid residues [MB61, STS67]. In Davydov's model of a quantum of amide-I interacting vibrationally with a polypeptide, the peptide units were lattice nodes, each of which moved as a whole under the assumption of adiabaticity, and phonons resulted from the stretching and compressing of interpeptide hydrogen bonds. Under suitable conditions, Davydov's model permitted not only the auto-localisation of the amide-I quantum, but crucially also the propagation along the polypeptide of the amide-I in sync with a local lattice distortion. The motivation behind Davydov's work was twofold. Firstly, it was known that the hydrolysis of ATP into ADP is the main means by which organisms generate biological energy; it releases approximately 0.42 eV of free energy, which roughly equals two quanta of amide-I [Bur58, Dav63]. Davydov therefore hypothesised that the propagation of amide-I carried the free energy that was released by ATP hydrolysis from one location in the cell to another, so that it could be used for biomechanical work such as muscle contraction. Secondly, the α-helix was known to be the most common secondary protein structure, and its stable, periodic geometry enabled mathematical simplifications of the system [PCB51, Ken61, OH68, HY70]. Following his initial study, Davydov refined and broadened the scope of his model in a series of publications, and his propagating pseudo-polaron - the composite of an amide-I quantum, or *exciton*, and a local distortion of the polypeptide - became known as a *Davydov soliton* [Dav74, Dav77, Dav79a, Dav79b, Sco81]. Notwithstanding his theory's mathematical elegance, Davydov did not fit the exciton-phonon coupling constant, due entirely to the lack of empirical data at his disposal. He did, however, parametrise his model's outputs by the coupling constant. He varied the parameter by more than the aforementioned two orders of magnitude. In fact, he considered the theoretical extremes

of strong and weak coupling, and his model predicted characteristically different behaviour in the two cases.

Whilst Davydov's work energised the field of bioenergetics, other researchers, both theoretical and experimental, also pushed polaron theory in new directions, finding novel applications such as semiconductivity [Bar74, TK75, SZGR78] and piezoelectricity [Oka74, TW74, Nag77]. Vilfan authored the first study of polaronic electron transport in an organic compound, where he calculated the electron mobility in anthracene ($C_{14}H_{10}$) using a polaron model and matched his results with experimental data [Vil73]. There was a fundamental difference between Vilfan's polaron and Davydov's soliton: while the latter always localised over many lattice sites, or was 'large', the former localised over a few sites only, or was 'small'. This discrepancy necessitated a departure from Davydov's *continuum approximation* approach to solving his model, where he approximated the polypeptide lattice as a continuum; instead, solving a small-polaron model required a *dynamical systems* approach, which in turn demanded numerical methods due to the large number of equations involved. The pioneers of polaronic modelling of electron transport in organic polymers were Su, Schrieffer and Heeger, who modelled polaron dynamics in polyacetylene ($(C_2H_2)_n$) by adapting the Fröhlich Hamiltonian to the polymer's quasi-one-dimensional geometry [SSH79, SSH80, SS80]. Although analytical solutions of the model in the continuum limit still served as approximations, numerical investigations took precedence and provided stronger results. A fundamental difference between the Su-Schrieffer-Heeger (SSH) and Davydov models was that, while the latter assumed that the phonon affected the exciton's site energy via *local coupling*, the former assumed that the phonon affected the electron transfer integrals via *non-local coupling*. Both were justifiable assumptions within their respective contexts, but in comparison the non-local coupling was much less dependent on intrapeptide and interpeptide geometries, which made it ideal for modelling simple structures such as polyacetylene, while being less effective at modelling complex structures with intricate intrapeptide geometries, such as proteins. Heeger *et al.* went on to study electron transport in other organic polymers such as polythiophene ($(C_9H_{12}O_6S_2)_x(C_9H_{11}O_3S)_y$), experimentally using spectroscopic techniques and explaining their findings in relation to the SSH model [VEB$^+$86, BWH87]. With the publication of the influential 1988 review, '*Solitons in Conducting Polymers*', it became widely accepted that polaron effects were inherent features of quasi-one-dimensional organic polymers [HKSS88]; this paved the way for the adaptation of polaron models to

electron transport problems in biomolecules such as proteins.

In 1993, Chuev and Lakhno devised the earliest polaron model of electron transport in proteins [CL93]; but instead of using the Fröhlich Hamiltonian, the authors invoked an older formalism of polaron theory credited to Pekar, representing the protein macromolecule as a linear medium. Then, in 1995, there appeared in *Physics Letters* the first polaron model using the Fröhlich Hamiltonian to study electron transport with a view to applications to proteins: Brizhik and her colleagues adapted the Fröhlich Hamiltonian to molecular chains and, in two successive papers, investigated the interactions between an extra electron and lattice phonons that were either optical (out-of-phase) [BELM95] or acoustic (coherent) [BELMP95]. In both cases, the authors derived from the Hamiltonian a set of coupled, nonlinear dynamical equations, which described the time-evolutions of the electron and phonon, and used numerical variational methods to solve those equations. They deduced phase diagrams for polaron states parametrised by the electron-phonon coupling constant and a dimensionless *adiabaticity parameter*, which was the characteristic time-scale separation between the electron and lattice dynamics. The authors suggested that, due to the hydrogen bond phonons in polypeptides being acoustic, their results might be applicable to electron transport in proteins - if one could fit the parameters in their model. The Brizhik-Eremko-La Magna-Pucci (BELMP) model was in fact a generalisation of Davydov's soliton model [Dav82]: while the latter accounted for one phonon frequency only, the former considered a superposition of all possible phonon frequencies. In a 1998 study, Brizhik *et al.* further generalised the BELMP model by introducing an extra term to the Fröhlich Hamiltonian which represented the interaction between the electron and an external electromagnetic field [BCHE98]. Throughout the 2000s, Brizhik remained the pre-eminent researcher on the subject of polaron dynamics in proteins and, collaborating with Eremko, Piette and Zakrzewski, published on topics such as degenerate polaron states in the α-helix [BEPZ04], radiative lifetimes of α-helical polarons [BEPZ06], and ratchet behaviour of polarons in polypeptides [BEPZ08]. The authors developed a unique numerical approach to solving the dynamical equations of the electron-hydrogen bond phonon system under the influence of external EMFs. Hennig contributed another substantial theoretical advance during this time, when he published a study on the self-sustaining propagation of polarons in helical proteins in 2001 [Hen01]. His model was distinct from Brizhik-Eremko-Piette-Zakrzewski (BEPZ) in two important ways. Firstly, whilst BEPZ launched and sustained polaron motion using an external EMF, Hennig did so by imparting an impulse

on a stationary polaron and then letting the system evolve on its own. Secondly, whilst BEPZ was based on the *Davydov-Scott model* - Scott having made a significant modification to Davydov's original theory [Sco82a, Sco82b] - Hennig's model, by his own account, was more closely related to an older polaron model by Holstein [Hol59a, Hol59b]. This was because he considered the coupling of the electron to *intrapeptide oscillators* that were independent from each other. Thus, polarons within the *Holstein-Hennig model* could be considered *pseudo-polarons*, because the lattice on its own could not produce phonons, and one lattice node affected another only indirectly via coupling to the extra electron. That being said, Hennig did introduce an immediate generalisation whereby the electron was coupled to hydrogen bond phonons as well as intrapeptide oscillators, both in his 2001 study and in [Hen02]. In the meantime, researchers began looking into polarons in other biomolecules, most notably Conwell [CR00, Con05], who reiterated the inadequacy of superexchange theory to explain the long-distance transfer of electrons in DNA and proposed a polaron model instead to account for experimental observations such as those in [GAK$^+$01, OB04]; and Lakhno, who studied bioelectronic properties of DNA-based conductors [LF03, Lak08]. In the current decade, despite direct observations of polarons in other biomolecules [SDSC10] and theoretical advances such as thermal enhancement of the BEPZ model [BEPZ14], any experimental verification of polaron models of electron transport in proteins has remained elusive.

To answer my research question, with its historical context in mind, I set out to devise physically justifiable and mathematically robust generalisations to two polaron models, in order to study electron transport in the α-helix: the Holstein-Hennig model of pseudo-polarons resulting from electron-intrapeptide oscillator coupling, and the Davydov-Scott model of polarons resulting from electron-hydrogen bond phonon coupling. My main objectives in this thesis are to present these two generalised models, to demonstrate their solutions, and to provide biophysical interpretations of my results. For the first model, the generalisation shall comprise two parts: a quantum correction, discarding Hennig's classical approximation for the intrapeptide oscillators; and thermalisation, taking into account the response of the lattice nodes to stochastic forces arising from the cell's thermal environment. I shall also use an external EMF, rather than the initial impulse as per Hennig, to launch and maintain polaron propagation, because the EMF mechanism is more relevant to transport systems such as transmembrane α-helices where a potential difference exists between the helix termini. I will present my generalised Holstein-Hennig

model in Chapter 3. As for the Davydov-Scott model, even though it did not in itself describe electron transport, I will base my model upon it, similarly to Brizhik *et al.* who generalised it in various ways to suit electron transport systems. My generalisation will consist of two parts: the introduction of a symmetry parameter which represents the spatial bias of electron-phonon coupling, and thermalisation of the lattice. In Chapter 4, I will present the model in the context of electron transport along a single channel of hydrogen-bonded polypeptide in the α-helix, and in Chapter 5 I will suit the model to electron transport in the three-channel structure of the entire helix. In either case, I shall use an EMF to drive the polaron propagation. Physical justifications for all the generalisations will accompany mathematical descriptions of the models, and I will delineate all parameters involved, paying due attention to any whose values remain undetermined by empirical data and accordingly parametrising the models' outputs. Each of Chapters 3 to 5 shall be structurally similar, commencing with motivations for the model, followed by mathematical formalisms and stationary polaron solutions of the model, before *numerical experiments* describing how a polaron propagates under external forces, which always form the majority of every Chapter. To conclude the thesis, I will summarise my findings in Chapter 6, and outline ideas for further developments of my theories.

It is assumed that the reader is familiar with the mathematical principles and practices of analytical mechanics, differential equations, dynamical systems, numerical integration and vector calculus. It is also assumed that the reader possesses a proficient grasp of both the wavefunction and the Dirac formalisms of quantum mechanics, and a rudimentary understanding of the biochemical concepts of amino acids and hydrogen bonding. There are more advanced physical concepts, such as the polaron, to which the reader may not be accustomed and which therefore warrant further introductions. I will give a technical overview of these concepts in Chapter 2, alongside descriptions of biological systems such as the α-helix.

Chapter 2

Preliminaries

The purpose of this Chapter is to provide a technical introduction to the physical and biological concepts that are relevant to the electron transport models of Chapters 3 to 5.

We divide the Chapter into two Sections. Firstly, we explain some concepts from condensed matter physics in Section 2.1, building towards a generic polaron model from first principles with the help of some new results. Then, in Section 2.2 we review biological concepts such as the α-helix, and give an overview of the application of polaron models to biological systems.

2.1 Concepts from Condensed Matter Physics

Unless otherwise stated, we follow in this Section standard treatments which appear in graduate-level textbooks [Zim72, FW03, AS06, YC10, Mis12, FV16], adapted for contexts which are appropriate to our pursuits.

The two central objects in any quantum mechanical system are a normalised *quantum state* $|\Psi\rangle$, which provides probability distributions for all the observables in the system, and a *Hamiltonian* $\widehat{H}$, which determines how the quantum state evolves in time. Solving the system means to solve the *Schrödinger equation*,

$$i\hbar\frac{\partial}{\partial t}|\Psi\rangle = \widehat{H}|\Psi\rangle\,, \tag{2.1.1}$$

for $|\Psi\rangle$ at time $t > 0$ given some initial state of the system at time $t = 0$. An eigenstate of $\widehat{H}$, or *energy eigenstate*, is a state $|\Psi^0\rangle$ obeying the *stationary Schrödinger equation*,

$$\widehat{H}|\Psi^0\rangle = \mathcal{E}|\Psi^0\rangle\,, \tag{2.1.2}$$

with some constant *energy eigenvalue* $\mathcal{E}$. If we evolve the system from an initial enegy eigenstate, then $|\Psi(t)\rangle$ takes the simple form,

$$|\Psi(t)\rangle = |\Psi^0\rangle \exp\left(-i\mathcal{E}t/\hbar\right). \tag{2.1.3}$$

In the context of an extra electron interacting electromagnetically with lattice nodes, there are approximations that one can make to simplify the equations involved. In Section 2.1.1, we describe an approximation which allows us to write the quantum state of the electron-lattice system as a direct product of an electron state $|\Psi_\mathrm{e}\rangle$ and a lattice state $|\Psi_\mathrm{p}\rangle$:

$$|\Psi\rangle = |\Psi_\mathrm{e}\rangle\,|\Psi_\mathrm{p}\rangle\,, \tag{2.1.4}$$

each of which is normalised. The same approximation also lets us write the system's Hamiltonian as a sum of two parts,

$$\widehat{H} = \widehat{H}_\mathrm{e} + \widehat{H}_\mathrm{p}, \tag{2.1.5}$$

respectively governing the electron and lattice dynamics. We then describe in Section 2.1.2 an approximation which leads to a simple expression for $\widehat{H}_\mathrm{e}$ along with a simple expression for $|\Psi_\mathrm{e}\rangle$, and in Section 2.1.3 an approximation of $\widehat{H}_\mathrm{p}$ as a classical Hamiltonian with phonon solutions. In Section 2.1.4, we introduce the defining assumption of polaron models, that the electron-lattice interaction manifests itself as a third part of $\widehat{H}$:

$$\widehat{H} = \widehat{H}_\mathrm{e} + \widehat{H}_\mathrm{p} + \widehat{H}_\mathrm{int}, \tag{2.1.6}$$

where $\widehat{H}_\mathrm{int}$ affects the dynamics of both electron and lattice. Finally, in Section 2.1.5, we present results, some of which are new, relating to the localisation of an extra electron in generic polaron models.

2.1.1 The Born-Oppenheimer Approximation

Since atomic nuclei are $\mathcal{O}(10^4)$ times heavier than an electron, and since the electromagnetic forces on both nuclei and electrons are of the same order, the acceleration of a nucleus must be negligible compared to that of an electron. Thus, whenever a nucleus moves away from its equilibrium position, the shell electrons must be able instantly to adjust to the energy eigenstates in the new nuclear configuration; this is the *adiabaticity condition*. In a crystalline lattice with an extra electron, the adiabaticity condition allows us to model each lattice node as a point particle, and the *Born-Oppenheimer* approximation, first devised

by the eponymous physicists in 1927 [BO27], further posits that we may separate the electron motion from the node dynamics. In the Dirac formalism of quantum mechanics, we say that the state of the electron-lattice system is a direct product of normalised electron and lattice states, as per Equation (2.1.4). Equivalently, we say that the wavefunction Ψ of the system is the product of normalised electron and lattice wavefunctions, respectively denoted by Ψ_e and Ψ_p:

$$\Psi(\mathbf{r}, \{\mathbf{X}_n\}) = \Psi_\mathrm{e}(\mathbf{r}; \{\mathbf{X}_n\})\Psi_\mathrm{p}(\{\mathbf{X}_n\}), \tag{2.1.7}$$

where $\mathbf{r}$ is the electron coordinate with respect to some Cartesian inertial frame, and $\{\mathbf{X}_n\}$ is the lattice configuration in the same frame, with n labelling the lattice nodes. Ψ_e is a function of $\mathbf{r}$ *parametrised by* $\{\mathbf{X}_n\}$ - the semicolon before $\{\mathbf{X}_n\}$ indicating parametrisation. We are using the wavefunction formalism of quantum mechanics because it most clearly demonstrates eigenfunction relations under differential operators. The normalisation of the wavefunctions means

$$\int \mathrm{d}\mathbf{r}\ \Psi_\mathrm{e}(\mathbf{r}; \{\mathbf{X}_n\}) = 1, \tag{2.1.8a}$$

$$\int \prod_j \mathrm{d}\mathbf{X}_j\ \Psi_\mathrm{p}(\{\mathbf{X}_n\}) = 1. \tag{2.1.8b}$$

To see the Born-Oppenheimer approximation in action, suppose we want to find the electron-lattice system's energy levels under the Hamiltonian,

$$\begin{aligned}\widehat{H} &= \widehat{H}(\mathbf{r}, \{\mathbf{X}_n\}) \\ &= -\frac{\hbar^2}{2M_\mathrm{e}}\nabla^2_{\mathbf{r}} + \widehat{V}_\mathrm{e}(\mathbf{r}, \{\mathbf{X}_n\}) - \sum_j \frac{\hbar^2}{2M_j}\nabla^2_j + \widehat{U}(\{\mathbf{X}_n\}),\end{aligned} \tag{2.1.9}$$

where M_e is the electron mass, $\nabla^2_{\mathbf{r}}$ is the Laplace operator in $\mathbf{r}$ space, $\widehat{V}_\mathrm{e}$ is the operator for potential energy of the electron due to the lattice configuration, M_j is the mass of the j^{th} lattice node, ∇^2_j is the Laplace operator in $\mathbf{X}_j$ space, and $\widehat{U}$ is the operator for potential energy due to node-node interactions in the lattice. We look firstly for $\Psi_\mathrm{e}(\mathbf{r}; \{\mathbf{X}_n\})$ with the lattice assumed static - this is reasonable under the adiabatic condition. The final two terms in $\widehat{H}$ then do not act on Ψ_e, so the electronic eigen-energies $\mathcal{E}_\mathrm{e}$ are determined by

$$\left(-\frac{\hbar^2}{2M_\mathrm{e}}\nabla^2_{\mathbf{r}} + \widehat{V}_\mathrm{e}(\mathbf{r}, \{\mathbf{X}_n\})\right)\Psi_\mathrm{e}(\mathbf{r}; \{\mathbf{X}_n\}) = \mathcal{E}_\mathrm{e}(\{\mathbf{X}_n\})\Psi_\mathrm{e}(\mathbf{r}; \{\mathbf{X}_n\}), \tag{2.1.10}$$

where we have made explicit the dependence of $\mathcal{E}_\mathrm{e}$ on $\{\mathbf{X}_n\}$. Once we have solved Equation (2.1.10) for $\mathcal{E}_\mathrm{e}$ and Ψ_e, we use them to solve the stationary Schrödinger equation for

the whole system, as follows. Denoting any eigen-energy of $\widehat{H}$ by $\mathcal{E}$, and assuming that $\widehat{U}(\{\mathbf{X}_n\})$ contains no differential operators, we have

$$\begin{aligned}\mathcal{E}(\mathbf{r},\{\mathbf{X}_n\})\Psi(\mathbf{r},\{\mathbf{X}_n\}) &= \Big(\mathcal{E}_{\mathrm{e}}(\{\mathbf{X}_n\})+\widehat{U}(\{\mathbf{X}_n\})\Big)\Big[\Psi_{\mathrm{e}}(\mathbf{r};\{\mathbf{X}_n\})\Psi_{\mathrm{p}}(\{\mathbf{X}_n\})\Big]\\ &\quad-\sum_j\frac{\hbar^2}{2M_j}\nabla_j^2\Big[\Psi_{\mathrm{e}}(\mathbf{r};\{\mathbf{X}_n\})\Psi_{\mathrm{p}}(\{\mathbf{X}_n\})\Big]\\ &=\Psi_{\mathrm{e}}(\mathbf{r};\{\mathbf{X}_n\})\left(\mathcal{E}_{\mathrm{e}}(\{\mathbf{X}_n\})-\sum_j\frac{\hbar^2}{2M_j}\nabla_j^2+\widehat{U}(\{\mathbf{X}_n\})\right)\Psi_{\mathrm{p}}(\{\mathbf{X}_n\})\\ &\quad-\sum_j\frac{\hbar^2}{M_j}\nabla_j\Psi_{\mathrm{e}}(\mathbf{r};\{\mathbf{X}_n\})\cdot\nabla_j\Psi_{\mathrm{p}}(\{\mathbf{X}_n\})\\ &\quad-\sum_j\frac{\hbar^2}{2M_j}\Psi_{\mathrm{p}}(\{\mathbf{X}_n\})\nabla_j^2\Psi_{\mathrm{e}}(\mathbf{r};\{\mathbf{X}_n\}),\end{aligned}\tag{2.1.11}$$

where ∇_j is the gradient operator in the $\mathbf{X}_j$ space. To simplify this equation, we consider the orders of magnitude of the terms on the right-hand side, and discover which ones make negligible contributions to the overall energy. Left-multiplying Equation (2.1.11) by Ψ^*, then integrating over $\mathbf{r}$ space and $\mathbf{X}_k$ space for all k, and invoking the normalisation of Ψ_{e} and Ψ_{p}, we obtain

$$\begin{aligned}\mathcal{E}&=\mathcal{E}_{\mathrm{e}}+\int\prod_k\mathrm{d}\mathbf{X}_k\;\Psi_{\mathrm{p}}^*\left(\widehat{U}-\sum_j\frac{\hbar^2}{2M_j}\nabla_j^2\right)\Psi_{\mathrm{p}}\\ &\quad-\sum_j\frac{\hbar^2}{M_j}\int\prod_k\mathrm{d}\mathbf{X}_k\left(\Psi_{\mathrm{p}}^*\nabla_j\Psi_{\mathrm{p}}\int\mathrm{d}\mathbf{r}\;\Psi_{\mathrm{e}}^*\nabla_j\Psi_{\mathrm{e}}\right)\\ &\quad-\sum_j\frac{\hbar^2}{2M_j}\int\prod_k\mathrm{d}\mathbf{X}_k\left(|\Psi_{\mathrm{p}}|^2\int\mathrm{d}\mathbf{r}\;\Psi_{\mathrm{e}}^*\nabla_j^2\Psi_{\mathrm{e}}\right),\end{aligned}\tag{2.1.12}$$

where we have suppressed the arguments $\mathbf{r}$ and $\{\mathbf{X}_n\}$ for ease of reading. Assuming there are no spin or magnetic dynamics in the system, so that one can always choose the electron wavefunction Ψ_{e} to be real, then the $\mathrm{d}\mathbf{r}$ integral in second line of Equation (2.1.12) becomes

$$\int\mathrm{d}\mathbf{r}\;\Psi_{\mathrm{e}}^*\nabla_j\Psi_{\mathrm{e}}=\frac{1}{2}\nabla_j\int\mathrm{d}\mathbf{r}\;|\Psi_{\mathrm{e}}|^2=0,\tag{2.1.13}$$

so the entire second line contributes nothing to $\mathcal{E}$. As for the third line in Equation (2.1.12), we may assume that $\Psi_{\mathrm{e}}(\mathbf{r};\{\mathbf{X}_n\})=\Psi_{\mathrm{e}}(\{\mathbf{Y}_n\})$ where $\mathbf{Y}_n=\mathbf{r}-\mathbf{X}_n$, thereby decoupling the double integral:

$$\begin{aligned}\frac{\hbar^2}{2M_j}\int\prod_k\mathrm{d}\mathbf{X}_k\left(|\Psi_{\mathrm{p}}|^2\int\mathrm{d}\mathbf{r}\;\Psi_{\mathrm{e}}^*\nabla_j^2\Psi_{\mathrm{e}}\right)&=\frac{\hbar^2}{2M_j}\left(\int\prod_k\mathrm{d}\mathbf{X}_k|\Psi_{\mathrm{p}}|^2\right)\left(\int\prod_l\mathrm{d}\mathbf{Y}_l\;\Psi_{\mathrm{e}}^*\widetilde{\nabla}_j^2\Psi_{\mathrm{e}}\right)\\ &=\frac{M_{\mathrm{e}}}{M_j}\int\prod_l\mathrm{d}\mathbf{Y}_l\;\Psi_{\mathrm{e}}^*\frac{\hbar^2}{2M_{\mathrm{e}}}\widetilde{\nabla}_j^2\Psi_{\mathrm{e}},\end{aligned}\tag{2.1.14}$$

where $\widetilde{\nabla}_j^2$ is the Laplace operator in $\mathbf{Y}_j$ space. The final expression in Equation (2.1.14) is the electronic kinetic energy multiplied by the ratio of electron mass to lattice node mass, which is vanishingly small, therefore the third line in Equation (2.1.12) makes negligible contribution to $\mathcal{E}$. This result implies that in Equation (2.1.11), the final two lines may be neglected, so the Schrödinger equation for the whole system simplifies to the following Schrödinger equation for the lattice wavefunction:

$$\mathcal{E}(\mathbf{r}, \{\mathbf{X}_n\})\Psi_{\mathrm{p}}(\{\mathbf{X}_n\}) = \left(\mathcal{E}_{\mathrm{e}}(\{\mathbf{X}_n\}) - \sum_j \frac{\hbar^2}{2M_j}\nabla_j^2 + \widehat{U}(\{\mathbf{X}_n\})\right)\Psi_{\mathrm{p}}(\{\mathbf{X}_n\}), \tag{2.1.15}$$

where $\mathcal{E}_{\mathrm{e}}$ is already known from Equation (2.1.10). By solving Equation (2.1.15), one obtains not only Ψ_{p} but also the eigen-energy $\mathcal{E}$ of the system. Moreover, we see from Equation (2.1.15) that the *lattice Hamiltonian*,

$$\widehat{H}_{\mathrm{p}}(\{\mathbf{X}_n\}) := -\sum_j \frac{\hbar^2}{2M_j}\nabla_j^2 + \widehat{U}(\{\mathbf{X}_n\}), \tag{2.1.16}$$

admits its own spectrum of eigenvalues, just as the *electron Hamiltonian*,

$$\widehat{H}_{\mathrm{e}}(\mathbf{r}, \{\mathbf{X}_n\}) := -\frac{\hbar^2}{2M_{\mathrm{e}}}\nabla_{\mathbf{r}}^2 + \widehat{V}_{\mathrm{e}}(\mathbf{r}, \{\mathbf{X}_n\}), \tag{2.1.17}$$

did in Equation (2.1.10). Equation (2.1.15) dictates that the sum of the $\widehat{H}_{\mathrm{e}}$ and $\widehat{H}_{\mathrm{p}}$ eigen-energies is $\mathcal{E}$. We may therefore write the system Hamiltonian as a sum,

$$\widehat{H} = \widehat{H}_{\mathrm{e}} + \widehat{H}_{\mathrm{p}}, \tag{2.1.18}$$

where $\widehat{H}_{\mathrm{e}}$ governs the electron dynamics as per Equation (2.1.10), $\widehat{H}_{\mathrm{p}}$ governs the lattice dynamics as per Equation (2.1.15), and the sum of the two energy eigenvalues is the eigen-energy of the whole system.

The substantial simplifications that the Born-Oppenheimer approximation affords, as we have demonstrated in the example above, makes it an indispensible tool in various pursuits in physics and quantum chemistry, and it is fundamental for our polaron models.

2.1.2 The Tight-Binding Electron

To compute the electron wavefunction under the Born-Oppenheimer approximation in large systems, traditional methods such as Hartree-Fock and its derivatives are far too computationally laborious [BER73, ZR77]. The more sophisticated methods of density functional theory are, although more efficient [Bec92,SSF98], unable to account for significant dispersion effects in large systems such as biomolecules [vMG02,VBKH05]. Since both

computational efficiency and accounting for dispersion effects are vital to our investigations of polaron dynamics in proteins, we must opt for an alternative approach. The obvious candidate is the *tight-binding method*, which itself has a long history and has remained widely in use since its conception [SK54, Sin01, Dov03].

The first step of the tight-binding method is to invoke *Bloch's theorem* [Blo28]: the electron wavefunction in a lattice must be invariant, up to a multiplicative constant phase factor, upon translation by a *lattice translation vector*, $\mathbf{R}$, which is a vector pointing from a lattice site to any other lattice site (or a trivial translation vector, $\mathbf{R} = \mathbf{0}$). Using the same notation as in Section 2.1.1, Bloch's theorem is expressed mathematically as

$$\Psi_{\mathrm{e}}(\mathbf{r} + \mathbf{R}; \{\mathbf{X}_n\}) = \exp(i\mathbf{k} \cdot \mathbf{R})\Psi_{\mathrm{e}}(\mathbf{r}; \{\mathbf{X}_n\}), \tag{2.1.19}$$

where $\mathbf{k}$ is some constant *wave-vector*. Now, rather than directly solving the stationary Schrödinger equation for the energy spectrum of $\widehat{H}_{\mathrm{e}}$, we decompose $\widehat{H}_{\mathrm{e}}$ into two parts:

$$\widehat{H}_{\mathrm{e}} = \widehat{H}_{\mathrm{e}}^{(0)} + \widehat{H}_{\mathrm{e}}^{(1)}, \tag{2.1.20}$$

where $\widehat{H}_{\mathrm{e}}^{(0)}$ consists of the kinetic energy operator for the electron, $-\frac{\hbar^2}{2M_{\mathrm{e}}}\nabla_{\mathbf{r}}^2$, and the operator for potential energy *due to a single lattice node*. Then, $\widehat{H}_{\mathrm{e}}^{(1)}$ is a correction to the potential energy operator due to other nodes in the lattice. The choice of 'which node' in $\widehat{H}_{\mathrm{e}}^{(0)}$ is entirely arbitrary. The chief motivation for performing the decomposition of Equation (2.1.20) is that determining the energy spectrum of $\widehat{H}_{\mathrm{e}}^{(0)}$ is usually straightforward; indeed, it is well known that if $\widehat{H}_{\mathrm{e}}^{(0)}$ relates to the potential energy due to a hydrogen nucleus, then its spectrum as well as eigenfunctions have exact analytical expressions. Suppose we have a complete spectrum of eigenvalues, with normalised eigenfunctions, of a generic $\widehat{H}_{\mathrm{e}}^{(0)}$:

$$\widehat{H}_{\mathrm{e}}^{(0)}(\mathbf{r}, \{\mathbf{X}_n\})\phi_j(\mathbf{r}; \{\mathbf{X}_n\}) = J_{0,j}(\{\mathbf{X}_n\})\phi_j(\mathbf{r}; \{\mathbf{X}_n\}), \tag{2.1.21}$$

where j labels the energy levels. The ϕ_js are known as *orbitals*. For the purpose of this demonstration of the tight-binding method, we have assumed that the energy levels in Equation (2.1.21) are non-degenerate; in other words, that for each j there is only one orbital that contributes to $J_{0,j}$. However the results below are readily generalisable to degenerate energy levels, corresponding physically to common systems such as multi-shell atoms and exotic systems such as graphene, which exhibits sp^2 hybridisation [BKL05].

The orbitals may not obey Bloch's theorem in general, but for a fixed j, the following superposition of linearly-translated copies of ϕ_j does obey Bloch's theorem:

$$\Psi_{j,\mathbf{k}}(\mathbf{r};\{\mathbf{X}_n\}) := \frac{1}{\sqrt{\mathcal{N}}}\sum_{\mathbf{R}}\exp(i\mathbf{k}\cdot\mathbf{R})\phi_j(\mathbf{r}-\mathbf{R};\{\mathbf{X}_n\}), \tag{2.1.22}$$

where the summation is over all lattice translation vectors, and $1/\sqrt{\mathcal{N}}$ is a normalisation constant. The wavefunction $\Psi_{j,\mathbf{k}}$ is known as a *Bloch wave*; it obeys Bloch's theorem given any wave-vector $\mathbf{k}$, and we can prove this as follows. Suppressing the $\{\mathbf{X}_n\}$ argument for notational convenience, we consider

$$\Psi_{j,\mathbf{k}}(\mathbf{r}+\mathbf{R}) = \frac{1}{\sqrt{\mathcal{N}}}\sum_{\mathbf{R}'}\exp(i\mathbf{k}\cdot\mathbf{R}')\phi_j(\mathbf{r}-\mathbf{R}''), \tag{2.1.23}$$

where we have defined $\mathbf{R}'' := \mathbf{R}' - \mathbf{R}$. Since the summation is over *all* $\mathbf{R}'$ and since $\mathbf{R}$ is some given, fixed vector, we may equivalently sum over all $\mathbf{R}''$, resulting in

$$\begin{aligned}\Psi_{j,\mathbf{k}}(\mathbf{r}+\mathbf{R}) &= \frac{1}{\sqrt{\mathcal{N}}}\sum_{\mathbf{R}''}\exp\Big(i\mathbf{k}\cdot(\mathbf{R}+\mathbf{R}'')\Big)\,\phi_j(\mathbf{r}-\mathbf{R}'')\\ &= \exp(i\mathbf{k}\cdot\mathbf{R})\frac{1}{\sqrt{\mathcal{N}}}\sum_{\mathbf{R}''}\exp(i\mathbf{k}\cdot\mathbf{R}'')\phi_j(\mathbf{r}-\mathbf{R}'')\\ &= \exp(i\mathbf{k}\cdot\mathbf{R})\Psi_{j,\mathbf{k}}(\mathbf{r}),\end{aligned} \tag{2.1.24}$$

as required, hence proving that $\Psi_{j,\mathbf{k}}$ satisfied Bloch's theorem. What is also true simply by the linearity of the Schrödinger equation is that $\Psi_{j,\mathbf{k}}$ has the same energy eigenvalue as ϕ_j does, under the single-node Hamiltonian $\widehat{H}_{\mathrm{e}}^{(0)}$. If the electron is indeed in a state described by $\Psi_{j,\mathbf{k}}$, in other words if $\Psi_{\mathrm{e}} = \Psi_{j,\mathbf{k}}$, then in order to determine the electron's energy $\mathcal{E}_{\mathrm{e}}^{(j)}$, we calculate the integral,

$$\mathcal{E}_{\mathrm{e}}^{(j)}(\mathbf{k}) = \int \mathrm{d}\mathbf{r}\ \Psi_{j,\mathbf{k}}^*(\mathbf{r})\widehat{H}_{\mathrm{e}}\Psi_{j,\mathbf{k}}(\mathbf{r}). \tag{2.1.25}$$

Suppressing the index j for convenience, we deduce

$$\begin{aligned}\mathcal{E}_{\mathrm{e}}(\mathbf{k}) &= \frac{1}{\mathcal{N}}\sum_{\mathbf{R}'}\sum_{\mathbf{R}''}\exp\Big(i\mathbf{k}\cdot(\mathbf{R}''-\mathbf{R}')\Big)\int \mathrm{d}\mathbf{r}\ \phi^*(\mathbf{r}-\mathbf{R}')\widehat{H}_{\mathrm{e}}\phi(\mathbf{r}-\mathbf{R}''),\\ &= \frac{1}{\mathcal{N}}\sum_{\mathbf{R}'}\sum_{\mathbf{R}''}\exp\Big(i\mathbf{k}\cdot(\mathbf{R}''-\mathbf{R}')\Big)\int \mathrm{d}\mathbf{x}\ \phi^*(\mathbf{x})\widehat{H}_{\mathrm{e}}\phi(\mathbf{x}-(\mathbf{R}''-\mathbf{R}')),\end{aligned} \tag{2.1.26}$$

where $\mathbf{R}'$ and $\mathbf{R}''$ are lattice translation vectors as before, and in deducing the final line we have performed the change of variables, $\mathbf{x} := \mathbf{r} - \mathbf{R}'$, by which the Hamiltonian $\widehat{H}$ is unaffected, because of the spatial translation invariance $\widehat{H}(\mathbf{r}) = \widehat{H}(\mathbf{r}-\mathbf{R}')$ afforded by the

lattice periodicity. For each fixed $\mathbf{R}'$ in Equation (2.1.26), $\mathbf{R} := \mathbf{R}'' - \mathbf{R}'$ is just another fixed lattice translation vector; so instead of summing over all $\mathbf{R}''$, summing over all $\mathbf{R}$ will give the same result. We therefore have

$$\mathcal{E}_{\mathrm{e}}(\mathbf{k}) = \frac{1}{\mathcal{N}} \sum_{\mathbf{R}'} \sum_{\mathbf{R}} \exp\left(i\mathbf{k}\cdot\mathbf{R}\right) \int \mathrm{d}\mathbf{x}\ \phi^*(\mathbf{x}) \widehat{H}_{\mathrm{e}} \phi(\mathbf{x}-\mathbf{R}), \tag{2.1.27}$$

To make progress from here, we need to make one simplifying assumption, that the electron orbitals are orthonormal:

$$\int \mathrm{d}\mathbf{r}\ \phi^*(\mathbf{r}-\mathbf{R}')\phi(\mathbf{r}-\mathbf{R}'') = \delta_{\mathbf{R}',\mathbf{R}''}, \tag{2.1.28}$$

where $\delta_{\cdot,\cdot}$ is the Kronecker delta. Equation (2.1.28) is the first of three *tight-binding approximations* that we will make. What it says physically is that ϕ is highly localised, so that the overlap between $\phi(\mathbf{r})$ and a copy of it which has been spatially translated by any lattice translation vector is vanishingly small. With Equation (2.1.28) in place, we are able to approximate the normalisation factor $\mathcal{N}$ simply by the total number of possible lattice translation vectors. We show this by writing out the normalisation condition,

$$\begin{aligned}
1 &= \int \mathrm{d}\mathbf{r}\ \Psi^*_{j,\mathbf{k}}(\mathbf{r})\Psi_{j,\mathbf{k}}(\mathbf{r}) \\
&= \frac{1}{\mathcal{N}} \sum_{\mathbf{R}'} \sum_{\mathbf{R}''} \exp\Big(i\mathbf{k}\cdot(\mathbf{R}''-\mathbf{R}')\Big) \int \mathrm{d}\mathbf{r}\ \phi^*(\mathbf{r}-\mathbf{R}')\phi(\mathbf{r}-\mathbf{R}'') \\
&= \frac{1}{\mathcal{N}} \sum_{\mathbf{R}'} \sum_{\mathbf{R}''} \exp\Big(i\mathbf{k}\cdot(\mathbf{R}''-\mathbf{R}')\Big) \delta_{\mathbf{R}',\mathbf{R}''} \\
&= \frac{1}{\mathcal{N}} \sum_{\mathbf{R}'} 1,
\end{aligned} \tag{2.1.29}$$

as required. We note that the number of possible lattice translation vectors is equal to the number of lattice nodes: choosing arbitrarily one node as origin, $\mathbf{R}$ can point to any of the nodes in the lattice including the origin itself. Now, putting Equation (2.1.29) into Equation (2.1.27), we have

$$\mathcal{E}_{\mathrm{e}}(\mathbf{k}) = \sum_{\mathbf{R}} \exp\left(i\mathbf{k}\cdot\mathbf{R}\right) \int \mathrm{d}\mathbf{x}\ \phi^*(\mathbf{x}) \widehat{H}_{\mathrm{e}} \phi(\mathbf{x}-\mathbf{R}). \tag{2.1.30}$$

The $\mathbf{R} = \mathbf{0}$ contribution to $\mathcal{E}_{\mathrm{e}}$ is

$$\begin{aligned}
\int \mathrm{d}\mathbf{x}\ \phi^*(\mathbf{x})\widehat{H}_{\mathrm{e}}\phi(\mathbf{x}) &= \int \mathrm{d}\mathbf{x}\ \phi^*(\mathbf{x}) J_0 \phi(\mathbf{x}) + \int \mathrm{d}\mathbf{x}\ \phi^*(\mathbf{x})\widehat{H}^{(1)}_{\mathrm{e}}\phi(\mathbf{x}) \\
&= J_0 + \int \mathrm{d}\mathbf{x}\ \phi^*(\mathbf{x})\widehat{H}^{(1)}_{\mathrm{e}}\phi(\mathbf{x}),
\end{aligned} \tag{2.1.31}$$

where we have made use of $\widehat{H}_{\mathrm{e}}^{(0)}\phi = J_0\phi$ [cf. Equation (2.1.21)] and the normalisation of ϕ. This is when we invoke a second tight-binding approximation, that the lattice-correction Hamiltonian $\widehat{H}_{\mathrm{e}}^{(1)}$ has negligible expected value in the highly-localised, single-node orbital ϕ. The $\mathbf{R} = \mathbf{0}$ contribution to $\mathcal{E}_{\mathrm{e}}$ therefore becomes approximately J_0. The third and final tight-binding approximation is that the only $\mathbf{R} \neq \mathbf{0}$ terms in Equation (2.1.30) that actually make significant contributions to $\mathcal{E}_{\mathrm{e}}$ are nearest-neighbour terms. Thus,

$$\mathcal{E}_{\mathrm{e}}(\mathbf{k}) = J_0 + \sum_{\mathbf{S}} \exp\left(i\mathbf{k}\cdot\mathbf{S}\right) \int \mathrm{d}\mathbf{x}\ \phi^*(\mathbf{x})\widehat{H}_{\mathrm{e}}\phi(\mathbf{x}-\mathbf{S}), \tag{2.1.32}$$

where $\mathbf{S}$ is a vector that points from a lattice node to any of its neighbouring nodes. In practice, the tight-binding method which we have described is semi-empirical, meaning that instead of calculating the integral in Equation (2.1.32) explicity, we replace it with a parameter, I_1, whose value we adjust to match experimental data:

$$I_1(|\mathbf{S}|) := \int \mathrm{d}\mathbf{x}\ \phi^*(\mathbf{x})\widehat{H}_{\mathrm{e}}\phi(\mathbf{x}-\mathbf{S}), \tag{2.1.33}$$

where it has been assumed that the integral depends only on the magnitude of the lattice translation vector.

For the simplest example, we consider a one-dimensional lattice, where every lattice translation vector is a scalar multiple of some constant unit vector $\mathbf{e}$, and so is every wave-vector $\mathbf{k} = k\mathbf{e}$. Suppose that the *lattice constant*, i.e. equilibrium spacing between neighbouring nodes, is a, then only $\mathbf{S} = \pm a\mathbf{e}$ contribute to the sum in Equation (2.1.32). We therefore have

$$\begin{aligned}\mathcal{E}_{\mathrm{e}}(k) &= J_0 + \exp(ika)I_1(a) + \exp(-ika)I_1(a)\\ &= J_0 + 2I_1(a)\cos(ka).\end{aligned} \tag{2.1.34}$$

This is a dispersion relation, relating the energy of a wavefunction to the *wavenumber* k. As k varies in the domain of $0 \leq k \leq 2\pi/a$ - known as the *Brillouin zone* - $\mathcal{E}_{\mathrm{e}}$ describes the *electron band*: all the permissible energies of the electron. The minimum and maximum energies in the electron band in this 1D example are, respectively, $J_0 - 2|I_1(a)|$ and $J_0 + 2|I_1(a)|$, and therefore its *bandwidth* is $4|I_1(a)|$.

In a two-dimensional lattice with lattice constants a and b respectively in the $\mathbf{e}_x$ and $\mathbf{e}_y$ directions, four lattice translation vectors contribute to the sum in Equation (2.1.32):

$\mathbf{S} = \pm a\mathbf{e}_x, \pm b\mathbf{e}_y$. The wave-vector $\mathbf{k}$ takes the general form $k_x\mathbf{e}_x + k_y\mathbf{e}_y$. The dispersion relation that determines the 2D electron band is therefore

$$\begin{aligned}\mathcal{E}_{\mathrm{e}}(k_x, k_y) &= J_0 + \exp(ik_x a)I_1(a) + \exp(-ik_x a)I_1(a) \\ &\quad + \exp(ik_y b)I_1(b) + \exp(-ik_y b)I_1(b) \\ &= J_0 + 2I_1(a)\cos(k_x a) + 2I_1(b)\cos(k_y b). \end{aligned} \tag{2.1.35}$$

$\mathcal{E}_{\mathrm{e}}$ in this case may be visualised as a surface over an k_x-k_y plane, where the Brillouin zone is $0 \leq k_x \leq 2\pi/a, 0 \leq k_y \leq 2\pi/b$. The minimum and maximum energies in the electron band are, respectively, $J_0 - 2|I_1(a)| - 2|I_1(b)|$ and $J_0 + 2|I_1(a)| + 2|I_1(b)|$, hence the bandwidth $4\left(|I_1(a)| + |I_1(b)|\right)$.

Our remaining task in the tight-binding method is to write down the electron Hamiltonian, $\widehat{H}_{\mathrm{e}}$, in the *second quantisation* formalism, meaning in terms of electron creation and annihilation operators, $\widehat{A}^\dagger$ and $\widehat{A}$. A second-quantisation Hamiltonian will enable us to perform calculations in the Dirac formalism of quantum mechanics, which is more notationally convenient than doing calculations in the wavefunction formalism.

Let us focus for now on the one-dimensional example. Suppose the total number of lattice translation vectors, or equivalently the number of lattice nodes, is $N + 1$, labelled by $n = 0, 1, 2, \ldots, N$. Suppose also that the lattice constant is a. The electron creation operator at lattice site n, written $\widehat{A}_n^\dagger$, creates from the vacuum state $|0\rangle$ an orbital with lattice translation vector $na\mathbf{e}$. We write the resulting state $\widehat{A}_n^\dagger|0\rangle$, and call it the *local excitation state* at lattice site n. Meanwhile, the electron annihilation operator at any site n nullifies the vacuum state:

$$\widehat{A}_n|0\rangle = 0. \tag{2.1.36}$$

A fundamental property of the creation and annihilation operators is that they satisfy the fermionic anti-commutation relation,

$$\widehat{A}_m\widehat{A}_n^\dagger + \widehat{A}_n^\dagger\widehat{A}_m = \delta_{m,n}, \tag{2.1.37}$$

which in turn implies that the states $\widehat{A}_n^\dagger|0\rangle$ form an orthonormal set, a conclusion that we earlier came to via wavefunctions. Instead of Equation (2.1.22), we now have the following analogous expression for the electron state as a superposition of local excitation states:

$$|\Psi_{\mathrm{e}}\rangle = \sum_{n=0}^{N} \alpha_n \widehat{A}_n^\dagger|0\rangle\,, \tag{2.1.38}$$

where the normalisation constant, now $1/\sqrt{N+1}$, has been absorbed into the coefficients:

$$\alpha_n := \frac{1}{\sqrt{N+1}} \exp(ikna). \tag{2.1.39}$$

Our goal is to write down a $\widehat{H}_\mathrm{e}$, involving $\widehat{A}_n^\dagger$ and $\widehat{A}_n$, which reproduces the same minimum and maximum electron band energies, and electron bandwidth, as Equation (2.1.34) did. To that end, we define for convenience

$$J_1 := \frac{N+1}{N} |I_1(a)|, \tag{2.1.40}$$

and consider

$$\widehat{H}_\mathrm{e} = \sum_{n=0}^{N} J_0 \widehat{A}_n^\dagger \widehat{A}_n - \sum_{n=0}^{N-1} J_1 \left(\widehat{A}_{n+1}^\dagger \widehat{A}_n + \widehat{A}_n^\dagger \widehat{A}_{n+1} \right). \tag{2.1.41}$$

Then, making use of Equation (2.1.37) and the fact that $\langle 0|0\rangle = 1$, we have

$$\begin{aligned}
\mathcal{E}_\mathrm{e} \equiv \langle \Psi_\mathrm{e}|\widehat{H}_\mathrm{e}|\Psi_\mathrm{e}\rangle &= J_0 \sum_{m=0}^{N}\sum_{n=0}^{N}\sum_{k=0}^{N} \alpha_m^* \alpha_k \langle 0| \widehat{A}_m \widehat{A}_n^\dagger \widehat{A}_n \widehat{A}_k^\dagger |0\rangle \\
&\quad - J_1 \sum_{m=0}^{N}\sum_{n=0}^{N-1}\sum_{k=0}^{N} \alpha_m^* \alpha_k \langle 0| \widehat{A}_m \widehat{A}_{n+1}^\dagger \widehat{A}_n \widehat{A}_k^\dagger + \widehat{A}_m \widehat{A}_n^\dagger \widehat{A}_{n+1} \widehat{A}_k^\dagger |0\rangle \\
&= J_0 \sum_{m=0}^{N}\sum_{n=0}^{N} \alpha_m^* \alpha_n \langle 0| \widehat{A}_m \widehat{A}_n^\dagger |0\rangle \\
&\quad - J_1 \sum_{m=0}^{N}\sum_{n=0}^{N-1} \left(\alpha_m^* \alpha_n \langle 0| \widehat{A}_m \widehat{A}_{n+1}^\dagger |0\rangle + \alpha_m^* \alpha_{n+1} \langle 0| \widehat{A}_m \widehat{A}_n^\dagger |0\rangle \right) \\
&= J_0 \sum_{n=0}^{N} \alpha_n^* \alpha_n - J_1 \sum_{n=0}^{N-1} \left(\alpha_{n+1}^* \alpha_n + \alpha_n^* \alpha_{n+1} \right).
\end{aligned} \tag{2.1.42}$$

Invoking Equation (2.1.39), which implies

$$\alpha_n^* \alpha_n = \frac{1}{N+1}, \tag{2.1.43a}$$

$$\begin{aligned}
\alpha_{n+1}^* \alpha_n + \alpha_n^* \alpha_{n+1} &= \frac{1}{N+1} \left(\exp(-ika) + \exp(ika) \right) \\
&= \frac{2}{N+1} \cos(ka),
\end{aligned} \tag{2.1.43b}$$

we further deduce from Equation (2.1.42) that

$$\begin{aligned}
\mathcal{E}_\mathrm{e} \equiv \langle \Psi_\mathrm{e}|\widehat{H}_\mathrm{e}|\Psi_\mathrm{e}\rangle &= J_0 - J_1 \frac{2N}{N+1} \cos(ka) \\
&= J_0 - 2|I_1(a)| \cos(ka).
\end{aligned} \tag{2.1.44}$$

As required, this dispersion relation produces the same minimum and maximum electron band energies, and electron bandwidth, as Equation (2.1.34) did; the only possible differece

now being the values of k at which the minimum and maximum band energies are attained, but this is physically inconsequential. Henceforth, we call the parameters J_0 and J_1, respectively, the *electron site energy* and *(nearest-neighbour) electron transfer integral*. In a large lattice, the factor $(N+1)/N$ becomes so close to unity that we may simply say that the minimum and maximum electron band energies are, respectively, $J_0 - 2J_1$ and $J_0 + 2J_1$, giving a bandwidth of $4J_1$. After all, the approximation of $(N+1)/N \approx 1$ will not be the most influential simplification that we have made in the tight-binding method.

The second-quantisation $\widehat{H}_{\mathrm{e}}$ for a two-dimensional lattice, with lattice constants a, b and node-counts $N+1, \widetilde{N}+1$ respectively in the two directions, may be readily obtained after a straightforward generalisation of the results above, via a definition of

$$J_2 := \frac{\widetilde{N}+1}{\widetilde{N}} \left| I_1(b) \right| . \tag{2.1.45}$$

The result is

$$\begin{aligned} \widehat{H}_{\mathrm{e}} = &\sum_{\nu=0}^{\widetilde{N}} \sum_{n=0}^{N} J_0 \widehat{A}^{\dagger}_{n,\nu} \widehat{A}_{n,\nu} - \sum_{\nu=0}^{\widetilde{N}} \sum_{n=0}^{N-1} J_1 \Big(\widehat{A}^{\dagger}_{n+1,\nu} \widehat{A}_{n,\nu} + \widehat{A}^{\dagger}_{n,\nu} \widehat{A}_{n+1,\nu} \Big) \\ &- \sum_{\nu=0}^{\widetilde{N}-1} \sum_{n=0}^{N} J_2 \Big(\widehat{A}^{\dagger}_{n,\nu+1} \widehat{A}_{n,\nu} + \widehat{A}^{\dagger}_{n,\nu} \widehat{A}_{n,\nu+1} \Big), \end{aligned} \tag{2.1.46}$$

giving an electron bandwidth of $4(J_1 + J_2)$, with minimum energy $J_0 - 2J_1 - 2J_2$ and maximum energy $J_0 + 2J_1 + 2J_2$.

2.1.3 The Classical Phonon

In our treatment of the electron-lattice system so far, we have already described the adiabatic condition, that the rate of change of momentum of a lattice node is negligible compared to that of an electron. Now, it is well known that the de Broglie wavelength of a particle is inversely proportional to its momentum; it also has long been known that when the de Broglie wavelength is slowly-varying, the quantum dynamics of the particle may be approximated in its classical limit [BM72, Ser03]. Thus, when applying polaron theory to organic or biological systems, where the mass ratio between a lattice node and electron is typically $\mathcal{O}(10^5)$ or more, a standard approach is to model the lattice dynamics classically [HKSS88,BEPZ08]. We show in this Section that a classical lattice Hamiltonian, H_{p}, can give rise to a good mathematical description of acoustic phonons.

For the purpose of this demonstration, we consider a one-dimensional lattice, though the results are readily generalisable to higher dimensions. In a masses-and-springs model of

identical lattice nodes and forces between nearest neighbours, let the mass of each node be M and the *force constant* of each 'spring', representing the electromagnetic force between neighbouring nodes, be K. If we were modelling an organic polymer such polyacetylene, all nodes would be truly identical and so would all force constants; but in polypeptides, we will be neglecting the small variations in node masses, and in force constants, which arise from the varying compositions of amino acid side chains. Let U_n be the displacement of the n^{th} node, where $n = 0, 1, 2, \ldots, N$, from its equilibrium position. The force on each node comes from springs on either side, giving

$$M\frac{\mathrm{d}^2U_0}{\mathrm{d}t^2} = K\left(U_1 - U_0\right), \tag{2.1.47a}$$

$$\begin{aligned} M\frac{\mathrm{d}^2U_n}{\mathrm{d}t^2} &= K\left(U_{n+1} - U_n\right) - K\left(U_n - U_{n-1}\right) \\ &= K\left(U_{n+1} + U_{n-1} - 2U_n\right), \quad \text{for } n = 1, 2, \ldots, N-1, \end{aligned} \tag{2.1.47b}$$

$$M\frac{\mathrm{d}^2U_N}{\mathrm{d}t^2} = -K\left(U_N - U_{N-1}\right), \tag{2.1.47c}$$

which form a set of $N + 1$ coupled equations. In a simple scenario, we impose a periodic boundary condition on the lattice, that

$$U_0 = U_N, \tag{2.1.48}$$

then the equations represent a circular chain of lattice nodes, where even a boundary node has two springs attached. If we then identify U_{-1} with U_{N-1} and identify U_{N+1} with U_1, then one equation encapsulates the dynamics of the entire lattice:

$$M\frac{\mathrm{d}^2U_n}{\mathrm{d}t^2} = K\left(U_{n+1} + U_{n-1} - 2U_n\right), \quad \text{for } n = 0, 1, 2, \ldots, N. \tag{2.1.49}$$

For solutions representing collective oscillations, we utilise the *normal mode* ansatz,

$$U_n = Q\exp\left[i(kna - \omega t)\right], \tag{2.1.50}$$

where Q is some constant amplitude, k is a constant wavenumber, a is the lattice constant, and ω is a constant angular frequency. We require without loss of generality that $k > 0$ and $\omega > 0$. The boundary condition, Equation (2.1.48), translates into

$$kNa = 2m\pi, \tag{2.1.51}$$

where $m > 0$ is an integer which labels the normal modes. Writing the normal mode ansatz in terms of m, we have

$$U_n = Q\exp\left[i\left(\frac{2\pi mn}{N} - \omega t\right)\right], \tag{2.1.52}$$

from which we see that the wavelength of the m^{th} normal mode is

$$\lambda_m = \frac{Na}{m}. \tag{2.1.53}$$

Putting Equation (2.1.50) into Equation (2.1.49), we deduce

$$-M\omega^2 U_n = KU_n \left[\exp(ika) + \exp(-ika) - 2\right], \tag{2.1.54}$$

and therefore

$$\omega = \sqrt{\frac{2K}{M}\left(1 - \cos(ka)\right)} = \sqrt{\frac{2K}{M}\left(1 - \cos\left(\frac{2m\pi}{N}\right)\right)}, \tag{2.1.55}$$

which relates the angular frequency ω of the lattice's collective oscillation to the wavenumber k, or to the normal mode number m. The total number of permitted normal modes is determined by the fact that there exists a minimum permissible wavelength of $2a$, which comes about because any wavelength smaller than $2a$ can always be mapped onto a wavelength larger than $2a$, by the lattice periodicity. Putting $\lambda_m \geq 2a$ in Equation (2.1.53) gives us $m \leq N/2$, so there are in total $N/2$ (or $(N-1)/2$ if N is odd) normal modes, of which the lowest frequency, according to Equation (2.1.55), is $\omega_1 = \sqrt{\frac{2K}{M}\left(1 - \cos(2\pi/N)\right)}$. The general solution to Equation (2.1.49) is a superposition of all the normal modes, but that will not be a collective oscillation with a unified frequency. In other words, while every normal mode is a phonon, the general solution is not.

To write down a Hamiltonian H_{p} that gives rise to the dynamical equations (2.1.47), we consider

$$H_{\text{p}} = \sum_{n=0}^{N} \frac{P_n^2}{2M} + \sum_{n=0}^{N-1} K\left(U_{n+1} - U_n\right)^2, \tag{2.1.56}$$

where P_n is the momentum conjugate to U_n. The first and second sums in Equation (2.1.56) are, respectively, the kinetic and potential energies in the lattice. It is then straightforward to derive Equation (2.1.47) from Equation (2.1.56) via the classical Hamilton's equations,

$$\frac{\mathrm{d}U_n}{\mathrm{d}t} = \frac{\partial H_{\text{p}}}{\partial P_n}, \quad \frac{\mathrm{d}P_n}{\mathrm{d}t} = -\frac{\partial H_{\text{p}}}{\partial U_n}. \tag{2.1.57}$$

We note two caveats concerning our results thus far. Firstly, when modelling a system such as a membrane α-helix, it is unreasonable to assume the periodic boundary condition $U_0 = U_N$. It is still possible to describe the lattice dynamics in one unifying equation similar to Equation (2.1.49), via the use of fictitious points beyond the boundaries, and

we will detail this approach in the models of Chapters 4 to 5 where appropriate. However the normal mode analysis that we have carried out will not apply in the case of non-periodic boundaries. That being said, in a polaron model we do not expect to find normal modes for the lattice anyway, because of effects of the electron-lattice interaction on the lattice dynamics. We will therefore use the Hamiltonian of Equation (2.1.56) and its variants in our polaron models, as the SSH and BEPZ models did [HKSS88, BEPZ08]. The second caveat is that in some situations, where we wish to assign a specific frequency rather than a force constant to the model, we may find that a quantum mechanical treatment of the lattice provides a much more precise fit of the relevant parameter to experimental data than a classical treatment does. We encounter this situation in Chapter 3, where we have independent oscillators on the lattice nodes rather than spring oscillations between nodes, and we wish to assign a natural oscillation frequency. Our approach then will be to quantise the lattice Hamiltonian and to utilise a quantised version of the normal mode ansatz known as a *Glauber state* [Gla63], as we will detail when we present our model.

2.1.4 The Polaron

The principal feature of a polaron model is that the extra electron and the lattice affect each other's dynamics via an *interaction Hamiltonian*, $\widehat{H}_{\text{int}}$. Bardeen was the first to formulate a polaron model explicitly involving some $\widehat{H}_{\text{int}}$ [Bar50], and soon afterwards Wentzel proposed a slightly different version of $\widehat{H}_{\text{int}}$ [Wen51] which motivated further work by Fröhlich. In 1952, Fröhlich devised the first model to contain a $\widehat{H}_{\text{int}}$ that was *bilinear* in the electron wavefunction and in the spatial derivative of the lattice displacement field [Frö52], lending his name to all later polaron models that contained bilinear interactions. The eponymous Fröhlich Hamiltonian is of the form

$$\widehat{H} = \widehat{H}_{\text{e}} + \widehat{H}_{\text{p}} + \widehat{H}_{\text{int}}, \tag{2.1.58}$$

where $\widehat{H}_{\text{e}}$ is a tight-binding electron Hamiltonian which we presented in Section 2.1.2, $\widehat{H}_{\text{p}}$ is a lattice Hamiltonian which is usually treated classically in the way that we demonstrated in Section 2.1.3, and $\widehat{H}_{\text{int}}$ is a bilinear function with a coupling constant. In Fröhlich's original formulation, the lattice was a continuum with spatial coordinate $\mathbf{r}$, and

$$\widehat{H}_{\text{int}} = C' \int \mathrm{d}\mathbf{r}\ \psi^* \psi\ \nabla \cdot \mathbf{P}, \tag{2.1.59}$$

where $\psi = \psi(\mathbf{r}, t)$ was the electron wavefunction, $\mathbf{P} = \mathbf{P}(\mathbf{r}, t)$ was the lattice displacement, $\nabla\cdot$ was the divergence operator, and C' was the coupling constant with the dimension of an energy. In the context of the one-dimensional, *discrete* lattice example which we have been describing, and in second-quantisation notation, the Fröhlich interaction Hamiltonian is

$$\widehat{H}_{\text{int}} = \chi \sum_n G_n \widehat{A}_n^\dagger \widehat{A}_n, \tag{2.1.60}$$

where G_n is a linear function of the relative lattice displacement,

$$S_n := U_{n+1} - U_n, \tag{2.1.61}$$

U_n being the classical, local lattice displacement [cf. Section 2.1.3]; $\widehat{A}_n^\dagger$ and $\widehat{A}_n$ are respectively the electron creation and annihilation operators [cf. Section 2.1.2]; the summation is over all values of n for which G_n is well-defined; and now χ is the coupling constant, with the dimension of a force. Some specific examples of G_n include

$$G_n^{\text{Dav}} = \frac{S_n + S_{n-1}}{2}, \tag{2.1.62}$$

which Davydov used to model the coupling of an amide-I exciton to hydrogen bonds in the α-helix [Dav82], and

$$G_n^{\text{Sco}} = S_n, \tag{2.1.63}$$

which was Scott's modification to Davydov's model, citing the reason that an amide-I should be coupled to the hydrogen bond on one side only, rather than the bonds on both sides [Sco92]. Mathematically, both Equations (2.1.62) and (2.1.63) were legitimate discretisations of the $\nabla \cdot \mathbf{P}$ that appeared in Fröhlich's orginal, continuum Hamiltonian. Brizhik *et al.* proposed a generalisation to the Davydov-Scott model when studying electron transport in molecular chains: they considered a lattice whose nodes alternated between two types, a large mass and a small mass [BEPZ08, BEPZ10, BEPZ14]. The equilibrium lattice spacings, or equivalently the equilibrium bond lengths between nodes, also alternated, and consequently the BEPZ model contained two different coupling constants, respectively for the long and short bonds. In Chapters 4 and 5, we will introduce a new type of generalisation, which uses a new parameter to extrapolate between the Davydov and Scott models, giving rise to a family of models reducible to Davydov's and Scott's when the new parameter takes its extreme values of, respectively, 0 and 1. We will justify this generalisation where appropriate from a biophysical standpoint.

Another type of polaron model, distinct from the Fröhlich kind, first appeared in Holstein's 1959 studies of polarons [Hol59a, Hol59b]. The model was still expressible in a three-part Fröhlich Hamiltonian as per Equation (2.1.58) and the interaction part was still bilinear, but - as we have already described in Chapter 1 and Section 2.1.3 - Holstein's lattice Hamiltonian modelled independent oscillators residing on the lattice nodes, therefore could not produce any phonons on its own. Holstein's interaction Hamiltonian, which he did not actually write down, was not linear in the spatial derivative of the lattice displacement field, but linear in the displacement field itself. In a discrete lattice and in second-quantisation notation, Holstein's interaction Hamiltonian would have read

$$\widehat{H}_{\text{int}}^{\text{Hol}} = \chi \sum_n U_n \widehat{A}_n^\dagger \widehat{A}_n. \tag{2.1.64}$$

Hennig in 2001 generalised the Holstein model by applying it to the α-helix [Hen01]. In Chapter 3, we will further generalise the Holstein-Hennig model by quantising the lattice, so that the U_n appearing in Equation (2.1.64) is replaced by a displacement operator $\widehat{Q}_n$, giving where appropriate a reason for the quantisation.

That which does unify models of the Fröhlich type and those of the Holstein type is that the interaction Hamiltonian involves a sum of the electron number operator, $\widehat{A}_n^\dagger \widehat{A}_n$. Recall from Section 2.1.2 that the tight-binding electron Hamiltonian, $\widehat{H}_{\text{e}}$, also contains a sum of $\widehat{A}_n^\dagger \widehat{A}_n$, multiplied by the electron site energy J_0. Therefore, both the Fröhlich and Holstein interactions represent physically a modification of the electron site energy, from the constant J_0 to the site-dependent $J_0 + \chi G_n$ (Fröhlich) or $J_0 + \chi U_n$ (Holstein). The Su-Schrieffer-Heeger (SSH) polaron model is different from both Fröhlich and Holstein because its interaction modifies the electron transfer integrals instead [SSH80, HKSS88]:

$$\widehat{H}_{\text{int}}^{\text{SSH}} = \chi \sum_n S_n \left(\widehat{A}_{n+1}^\dagger \widehat{A}_n + \widehat{A}_n^\dagger \widehat{A}_{n+1} \right). \tag{2.1.65}$$

Specifically, the electron transfer energy is modified from the constant $-J_1$ to the site-dependent $-J_1 + \chi S_n$. As we have argued in Chapter 1, the SSH model is insensitive to the intricate geometries of complex molecules such as proteins, therefore we do not explore it in this thesis.

2.1.5 Where Is the Electron?

We present here one crucial result which holds for a generic polaron model, of either the Fröhlich kind or the Holstein kind. Though it is inspired by Holstein's work [Hol59a], the result below holds under greater generality, and therefore may be considered new.

We continue to consider the system of one extra electron in a one-dimensional lattice. When the electron's dynamics is affected by the electron-lattice interaction, its wavefunction no longer has to obey Bloch's theorem, meaning it no longer has to be invariant up to a multiplicative phase factor under spatial translations by lattice translation vectors [cf. Section 2.1.2]. What this implies in terms of the electron's *probability distribution* is that it no longer has to be spatially periodic. Indeed, as we have discussed in Chapter 1, the central purpose of a polaron model is to allow the localisation, or more specifically the auto-localisation, of an electron, whereby its probability distribution has a single, well-defined global maximum, away from which the distribution sharply decays. Moreover, while the electron-lattice system evolves according to a Fröhlich Hamiltonian, the polaron model should permit solitonic propagation of the electron, whereby its probability distribution roughly retains its shape. As per the standard approach in polaron theory, we still assume a Bloch-style ansatz for the electron state written in the Dirac formalism as Equation (2.1.38), and only discard the translational invariance restriction. Equivalently, we assume that the electron wavefunction Ψ_{e} is

$$\Psi_{\mathrm{e}}(x,t) = \sum_n \alpha_n(t)\phi_n(x), \tag{2.1.66}$$

where x is the spatial coordinate along the lattice, the α_n are complex-valued coefficients, and ϕ_n are electron orbitals, which we choose to be real by absorbing its phase factor into α_n. We have reverted back to the wavefunction formalism because it allows us to calculate the quantity

$$\mathbb{P}_n(t) := \int_{n_-(t)}^{n_+(t)} \mathrm{d}x \; |\Psi_{\mathrm{e}}(x,t)|^2, \tag{2.1.67}$$

where $n_- \leq x \leq n_+$ describes a small interval around the n^{th} lattice node. To be precise, letting U_n be the node displacement in the positive-x direction from equilibrium, we have

$$n_\pm = na + U_n \pm \delta \left[a \pm (U_{n\pm1} - U_n)\right], \tag{2.1.68}$$

where a is the lattice constant, so that $a+(U_{n+1}-U_n)$ is the distance between the n^{th} and $(n+1)^{\text{th}}$ nodes, and $\delta > 0$ is some small number. $n_\pm(t)$ inherits its time-dependence from $U_n(t)$. Despite the time-dependence, if the node displacements remain small compared to the lattice constant at all times (which is indeed always the case in all our results relating to the models of Chapters 3 to 5), then, even a small δ value can ensure that the interval

$n_- \leq x \leq n_+$ always contains the equilibrium position of the n^{th} node. For example, if the node displacements remain $\mathcal{O}(10^{-3}a)$ for all time, then $\delta = 10^{-2}$ ensures coverage of the n^{th} equilibrium position.

The $\mathbb{P}_n(t)$ in Equation (2.1.67) is the probability of finding the electron localised around the n^{th} lattice node at time t, henceforth referred to as the electron's *on-site localisation probability*. As an aside, we note that a localised electron is *not* captured by the node atom(s) or molecules(s) as a shell electron. In fact, if that were the case then one would need to model the interactions between the captured electron and existing shell electrons on the node, which is beyond the scope of this thesis.

Now, we proceed to show that the quantity $|\alpha_n|^2$ is a zeroth-order approximation for $\mathbb{P}_n$. To this end, firstly we note that the normalisation condition on Ψ_{e} reads

$$1 = \int \mathrm{d}x\ |\Psi_{\text{e}}|^2 = \sum_{m,k} \alpha_m^* \alpha_k \int \mathrm{d}x\ \phi_m \phi_k = \sum_{m,k} \alpha_m^* \alpha_k \int \mathrm{d}x\ \delta_{m,k} = \sum_m |\alpha_m|^2, \tag{2.1.69}$$

where we have invoked the tight-binding approximation that the orbitals are orthonormal. It then follows that the on-site localisation probability of the electron is

$$\mathbb{P}_n = \sum_{m,k} \alpha_m^* \alpha_k \int_{n_-}^{n_+} \mathrm{d}x\ \phi_m \phi_k. \tag{2.1.70}$$

Oweing to the fact that the orbitals are highly localised around the equilibrium lattice node positions, and that those positions are always contained in the interval $n_- \leq x \leq n_+$, it follows that $\int_{n_-}^{n_+} |\phi_n|^2 \approx \int \mathrm{d}x\ |\phi_n|^2 = 1$, and that any term in which either $m \neq n$ or $\kappa \neq n$ makes a negligible contribution to the sum in Equation (2.1.70). Thus, as a zeroth-order approximation, we have

$$\mathbb{P}_n(t) = |\alpha_n(t)|^2. \tag{2.1.71}$$

This result is vital for two reasons. Firstly, the dynamical equations arising from a discrete Fröhlich Hamiltonian will be coupled equations for α_n and for the lattice displacements, and Equation (2.1.71) says that the α_n solutions will suffice to give us the electron's on-site localisation probabilities at all times, without our knowing the electron orbitals. Secondly, combining Equation (2.1.71) with the fact that $\sum_n |\alpha_n|^2 = 1$, we understand that whenever the electron in the polaron model is localised, it will be localised around a lattice node. It has zero probability of localising in the inter-node space, or, zero 'off-site localisation probability'. Exactly how tight the localisation space is around the lattice node

depends upon the number δ in Equation (2.1.68), which in turn depends on the magnitude of node displacements from equilibria. Nevertheless, as we have already argued, localising 'around a lattice node' remains a meaningful expression because the node displacements will always be small compared to the lattice constant. In practice, when we have solved the polaron model for α_n at some time t, a plot of the discrete function $|\alpha_n|^2$ against n will reveal the electron's on-site localisation probability at each node, regardless of exactly where the node is at that time. We shall simply say that $|\alpha_n(t)|^2$ is the electron's *probability distribution* at time t. If the system is in a polaron state, then we expect the $|\alpha_n|^2$ to exhibit a localised, bell curve-shaped profile, whereby a pronounced global maximum exists at some $n = n_0$, away from which $|\alpha_n|^2$ sharply decays.

2.2 Polaron Models in Biology

After a review of the structure of the α-helix in Section 2.2.1, we give a brief and technical synopsis of the polaron models that have inspired this thesis, including the Davydov-Scott model in Section 2.2.2, and the Holstein-Hennig and BEPZ models in Section 2.2.3. We conclude this Chapter with a discussion about parameter-fitting in Section 2.2.4.

2.2.1 The α-Helix and α-Channels

Pauling, Corey and Branson were the first to illucidate the secondary protein structure that we now know as the α-helix [PCB51]. Remarkably, they predicted the structure by theoretical modelling alone, based purely on physico-chemical properties of the components of a protein macromolecule. Though it has undergone minor revisions [Dun01], the original conception by Pauling *et al.* has largely stood the test of time and countless experiments, accurately describing vital properties of the α-helical structure such as hydrogen bonding arrangements and the step size of the helical coil. Today, it is widely accepted that the α-helix is one of the most vital structures underpinning all manner of life [Eis03].

The α-helix is a right-handed helical configuration of amino acid residues, each comprising an N–H group, a C=O group, and a carbon atom known as the α-carbon with an organic side chain attached. The α-carbon is located between the N–H and C=O groups, and together with its side chain it is known as the R group. There exist 21 different proteinogenic amino acids in eukaryotes [AG02], characterised by 21 unique R groups. Of the 21 different residues, 6 are uncharged but polar, 3 are positively charged and 2 are

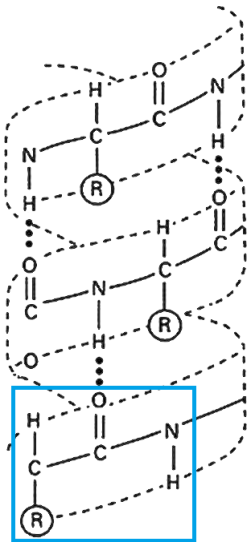

Figure 2.1: The α-helix [Dai08]. Dotted lines represent hydrogen bonds. The blue box indicates a peptide unit.

negatively charged [BTS12]. The residues are linked by *peptide bonds*, which are covalent, along the helical coil, between the C=O group of one residue and the N–H group of the next residue. The N–H end of the α-helix is known as the N-terminus, and the C=O end the C-terminus. We shall label the amino acid residues starting from the N terminus. The *step rise* of the α-helix, meaning the vertical (along helical axis) distance from the m^{th} α-carbon to the $(m+1)^{\text{th}}$ α-carbon, is 1.5 Å. The *step turn* of the α-helix, meaning the azimuthal angle between the m^{th} and $(m+1)^{\text{th}}$ α-carbons, is 100°. Finally, the mean radius of the helical coil, measured from the centre of the coil to the centre of the α-carbons, is 2.3 Å [BT88].

Hydrogen bonds link every C=O group of the m^{th} residue to the N–H group of the $(m+4)^{\text{th}}$ residue, thereby stabilising the helical structure. Figure 2.1 provides a graphical illustration of the α-helix with its hydrogen bonds. In the figure, the orientation of the α-helix is such that its N-terminus is at the bottom, and its C-terminus at the top. A *peptide unit* consists of the R and C=O groups in the m^{th} residue, and the N–H group in the $(m+1)^{\text{th}}$ residue. Thus, the α-helix consists of three distinct channels of equally-spaced peptide units, which we will call *α-channels*. If we use dotted lines to represent hydrogen bonds and solid lines for peptide bonds, and label the C=O and N–H groups in the m^{th} residue by mC and mN respectively, starting from $m = 0$, then we may depict

the three α-channels in a 10-residue α-helix as follows:

$$(1\mathrm{N}-0\mathrm{C})\cdots(4\mathrm{N}-3\mathrm{C})\cdots(7\mathrm{N}-6\mathrm{C})\,, \tag{2.2.1a}$$

$$(2\mathrm{N}-1\mathrm{C})\cdots(5\mathrm{N}-4\mathrm{C})\cdots(8\mathrm{N}-7\mathrm{C})\,, \tag{2.2.1b}$$

$$(3\mathrm{N}-2\mathrm{C})\cdots(6\mathrm{N}-5\mathrm{C})\cdots(9\mathrm{N}-8\mathrm{C})\,. \tag{2.2.1c}$$

where parentheses indicate peptide units. We have omitted all the R groups and some peptide bonds, for ease of reading. In Figure 2.1, if we say that the C=O group in the boxed peptide unit is 0C, then the figure illustrates the bonding $(1\mathrm{N}-0\mathrm{C})\cdots(4\mathrm{N}-3\mathrm{C})\cdots 7\mathrm{N}$. It also illustrates $4\mathrm{C}\cdots 8\mathrm{N}$. Instead of labelling the amino acid residues, it is better to label the peptide units instead, using $\mu = 0, 1, 2, \ldots$. Then, the $(1\mathrm{N}-0\mathrm{C})$ in Equation (2.2.1) is the 0^{th} peptide unit, $(2\mathrm{N}-1\mathrm{C})$ the 1^{st}, and so on. A simpler schematic of the hydrogen bonding structure of the α-helix therefore follows:

$$0\cdots 3\cdots 6, \tag{2.2.2a}$$

$$1\cdots 4\cdots 7, \tag{2.2.2b}$$

$$2\cdots 5\cdots 8, \tag{2.2.2c}$$

where the numbers are labels of peptide units. Though not shown in Equation (2.2.2), there are peptide bonds linking the μ^{th} unit to the $(\mu+1)^{\text{th}}$. Since the step rise of the α-helix is 1.5 Å, the equilibrium spacing between neighbouring peptide units in an α-channel, projected along the helical axis, is $R = 4.5$ Å.

The hydrogen bonds are much weaker, and consequently much less rigid, than the peptide bonds and intrapeptide bonds, all of which are covalent [Ems80]. This fact affords us two routes to simplification, from a modelling perspective. Firstly, it implies that covalent bond oscillations and hydrogen bond oscillations occur on vastly different time-scales, and indeed the latter is two orders of magnitude slower [BESP72, NC76]. Therefore if we wish to model the dynamics of intrapeptide bond oscillations, and their interactions with an extra electron, we may assume the hydrogen bonds to be static; that is the basis of the Holstein-Hennig model and is what we do in Chapter 3. Secondly, if we wish to model the dynamics of hydrogen bonds and their interactions with an extra electron, then the rigidity of covalent bonds allows us to treat every peptide unit as a point particle, or indeed point dipole, which is the basis of the Davydov-Scott model. We may even decouple the three α-channels and simply consider the electron transport along a single

channel, which is what we do in Chapter 4; and in Chapter 5 we take into account the electron transfer between channels.

2.2.2 Davydov's Soliton and Scott's Model

In Davydov's original formulation [Dav82], the Fröhlich Hamiltonian describing the system of an amide-I interacting with hydrogen bond oscillations in a single α-channel, where the peptide units were lattice nodes labelled by $n = 0, 1, 2, \ldots, N$, was

$$\begin{aligned}\widehat{H}^{\mathrm{Dav}} &= \widehat{H}_{\mathrm{e}} + \widehat{H}_{\mathrm{p}} + \widehat{H}_{\mathrm{int}}^{\mathrm{Dav}} \\ &= \sum_{n=0}^{N} J_0 \widehat{A}_n^{\dagger}\widehat{A}_n - \sum_{n=0}^{N-1} J_1 \left(\widehat{A}_{n+1}^{\dagger}\widehat{A}_n + \widehat{A}_n^{\dagger}\widehat{A}_{n+1}\right) \\ &\quad + \sum_{n=0}^{N} \frac{\widehat{P}_n^2}{2M} + \sum_{n=0}^{N-1} \frac{K\left(\widehat{U}_{n+1} - \widehat{U}_n\right)^2}{2} \\ &\quad + \sum_{n=1}^{N-1} \widetilde{\chi}\left(\widehat{U}_{n+1} - \widehat{U}_{n-1}\right) \widehat{A}_n^{\dagger}\widehat{A}_n. \end{aligned} \tag{2.2.3}$$

$\widehat{A}_n^{\dagger}, \widehat{A}_n$ are the electron creation and annihilation operators respectively, $J_0 > 0$ is the electron site energy, $J_1 > 0$ the nearest-neighbour electron transfer integral, M the peptide unit mass, K the hydrogen bond force constant, $\widehat{U}_n$ the operator for peptide unit displacement, $\widehat{P}_n$ the operator for momentum conjugate to $\widehat{U}_n$, and $\widetilde{\chi}$ the electron-hydrogen bond coupling constant. Assuming the Bloch ansatz for the electron,

$$|\Psi_{\mathrm{e}}(t)\rangle = \sum_{n=0}^{N} \alpha_n(t) \widehat{A}_n^{\dagger} |0_{\mathrm{e}}\rangle , \tag{2.2.4}$$

where α_n are complex coefficients and $|0_{\mathrm{e}}\rangle$ is the electron vacuum state, and assuming the Glauber ansatz for the lattice which is a superposition of quantised normal modes,

$$|\Psi_{\mathrm{p}}(t)\rangle = \exp\left(\frac{i}{\hbar}\sum_{n=0}^{N}\left(P_n(t)\widehat{U}_n - U_n(t)\widehat{P}_n\right)\right)|0_{\mathrm{p}}\rangle , \tag{2.2.5}$$

where P_n, U_n are real coefficients and $|0_{\mathrm{p}}\rangle$ is the lattice vacuum state, Davydov derived a set of coupled, nonlinear dynamical equations for α_n, P_n and Q_n. In particular, the first-order U_n equation was

$$M\frac{\mathrm{d}U_n}{\mathrm{d}t} = P_n, \tag{2.2.6}$$

which, when combined with the first-order P_n equation, provided a second-order U_n equation. The α_n and U_n equations together entirely determined the system's dynamics:

$$i\hbar\frac{\mathrm{d}\alpha_n}{\mathrm{d}t} = \left[J_0 + W + \widetilde{\chi}\left(U_{n+1} - U_{n-1}\right)\right]\alpha_n - J_1\left(\alpha_{n+1} + \alpha_{n-1}\right), \tag{2.2.7a}$$

$$M\frac{\mathrm{d}^2U_n}{\mathrm{d}t} = K\left(U_{n+1} + U_{n-1} - 2U_n\right) + \widetilde{\chi}\left(|\alpha_{n+1}|^2 - |\alpha_{n-1}|^2\right), \tag{2.2.7b}$$

where

$$W = W(t) = \sum_{m=0}^{N}\frac{P_n^2}{2M} + \sum_{n=0}^{N-1}K\left(U_{n+1} - U_n\right). \tag{2.2.8}$$

Equation (2.2.7) was valid for all values of n at which all the terms were well-defined. This excluded the boundary terms, but that did not matter, because Davydov then approximated the lattice as a continuum. The continuum ansatz for α_n was

$$\alpha_n(t) = \exp\left[i\left(kx - \frac{\mathcal{E}_0 t}{\hbar}\right)\right]\phi(x,t), \tag{2.2.9}$$

where x is the spatial coordinate in the continuum approximation of the lattice, k some constant wavenumber, $\mathcal{E}_0$ some constant, and ϕ a real, smooth function. By putting Equation (2.2.9), and the representation of $U_{n\pm1}$ as a Taylor series of some smooth function $B(x,t)$, into Equation (2.2.7), Davydov deduced that ϕ and B satisfied the equations,

$$\left(\widetilde{\mathcal{E}}_0(k) + R^2J_1\cos(kR) + 2\widetilde{\chi}B(x,t)\right)\phi(x,t) = 0, \tag{2.2.10a}$$

$$\left(\frac{\partial^2}{\partial t^2} - V_0^2\right)B(x,t) + \frac{2\widetilde{\chi}V_0^2}{K}\frac{\partial^2}{\partial x^2}\phi(x,t) = 0, \tag{2.2.10b}$$

where R is the lattice constant, and

$$\widetilde{\mathcal{E}}_0(k) = \mathcal{E}_0 - W - J_0 + 2J_1\cos(kR), \tag{2.2.11a}$$

$$V_0 = R\sqrt{\frac{K}{M}}. \tag{2.2.11b}$$

Davydov then found that a solution existed where both ϕ and B propagated as solitons. Indeed, by requiring

$$B(x,t) = \frac{2\widetilde{\chi}}{K\left(1 - \frac{V^2}{V_0^2}\right)}\phi(x,t)^2, \tag{2.2.12}$$

for some constant V, Davydov showed that ϕ had a travelling wave solution, $\phi(x,t) = \widetilde{\phi}(z)$ where $z := x - Vt$, with $\widetilde{\phi}$ obeying the *nonlinear Schrödinger equation*,

$$\left(\widetilde{\mathcal{E}}_0(k) + \widetilde{J_1}(k)\frac{\partial^2}{\partial z^2} + \widetilde{\lambda}\widetilde{\phi}(z)^2\right)\widetilde{\phi}(z) = 0, \tag{2.2.13}$$

where

$$\widetilde{J_1}(k) = R^2 J_1 \cos(kR), \quad \widetilde{\lambda} = \frac{4\widetilde{\chi}^2}{K\left(1 - \frac{V^2}{V_0^2}\right)}. \tag{2.2.14}$$

The nonlinear Schrödinger equation was well known to admit soliton solutions, where the travelling wave has a sech profile [ZS72, Hir73]. Davydov therefore concluded that in the continuum limit, his polaron model of amide-I hydrogen bond coupling in the α-helix permitted solitonic transport of the amide-I quantum.

Scott's modification to Davydov's model was motivated by the fact that in the α-helix, the C=O bond in the n^{th} peptide unit is located near the $(n+1)^{\text{th}}$ unit but far from the $(n-1)^{\text{th}}$ unit [Sco92]. Scott therefore claimed that the electron-hydrogen bond interaction should rely solely upon $\widehat{U}_{n+1} - \widehat{U}_n$, and not $\widehat{U}_n - \widehat{U}_{n-1}$. Thus, in the Scott model, the Fröhlich Hamiltonian was

$$\begin{aligned}
\widehat{H}^{\text{Sco}} &= \widehat{H}_{\text{e}} + \widehat{H}_{\text{p}} + \widehat{H}_{\text{int}}^{\text{Sco}} \\
&= \sum_{n=0}^{N} J_0 \widehat{A}_n^\dagger \widehat{A}_n - \sum_{n=0}^{N-1} J_1 \left(\widehat{A}_{n+1}^\dagger \widehat{A}_n + \widehat{A}_n^\dagger \widehat{A}_{n+1} \right) \\
&\quad + \sum_{n=0}^{N} \frac{\widehat{P}_n^2}{2M} + \sum_{n=0}^{N-1} \frac{K\left(\widehat{U}_{n+1} - \widehat{U}_n\right)^2}{2} \\
&\quad + \sum_{n=0}^{N-1} \chi \left(\widehat{U}_{n+1} - \widehat{U}_n \right) \widehat{A}_n^\dagger \widehat{A}_n,
\end{aligned} \tag{2.2.15}$$

where the coupling constant was χ. The resulting dynamical equations,

$$i\hbar \frac{\mathrm{d}\alpha_n}{\mathrm{d}t} = \left[J_0 + W + \chi \left(U_{n+1} - U_n \right) \right] \alpha_n - J_1 \left(\alpha_{n+1} + \alpha_{n-1} \right), \tag{2.2.16a}$$

$$M \frac{\mathrm{d}^2 U_n}{\mathrm{d}t} = K \left(U_{n+1} + U_{n-1} - 2U_n \right) + \chi \left(|\alpha_n|^2 - |\alpha_{n-1}|^2 \right), \tag{2.2.16b}$$

were similar to Davydov's, but the breaking of the symmetry between U_{n+1} and U_{n-1} meant that if one took the continuum limit as Davydov did, the equations would no longer be approximated by the nonlinear Schrödinger equation. Nevertheless, Scott showed that in a stationary system, where $\dot{U}_n = \ddot{U}_n = 0$, the U_n equation had an exact solution:

$$U_{n+1} - U_n = -\frac{\chi}{K} |\alpha_n|^2. \tag{2.2.17}$$

By putting Equation (2.2.17) into Equation (2.2.16a), and then approximating the lattice as a continuum, Scott did deduce the nonlinear Schrödinger equation after all. However in

this situation, any solitonically propagating solution would be invalid, because if $\alpha_n(t)$ were a (discretised) travelling wave, then the requirement that Equation (2.2.17) described a stationary lattice would be violated. Thus, in this case only the stationary (phase-varying) solutions to the nonlinear Schrödinger equation were valid.

We may therefore summarise the mathematical differences between the Davydov and Scott models as follows. In the former case, one can take the entire system of equations to its continuum limit, in which the nonlinear Schrödinger equation approximates the electron equation, and derive soliton solutions for both electron and lattice. However using the same method on Scott's equations does not lead to the same outcome. Indeed, if we tried, we would obtain (this is a new result):

$$\left(\widetilde{\mathcal{E}}_0(k) + \widetilde{J_1}(k)\frac{\partial^2}{\partial z^2} + \lambda\widetilde{\phi}(z)^2 - \eta\frac{\partial^2}{\partial z^2}\phi(z)^2\right)\widetilde{\phi}(z) = 0, \tag{2.2.18}$$

where $k, \widetilde{\mathcal{E}}_0, \widetilde{J_1}, z$ and $\widetilde{\phi}$ are as they were before, and

$$\lambda = \frac{\chi^2}{K\left(1 - \frac{V^2}{V_0^2}\right)}, \quad \eta = \frac{\chi^2 R^2}{4K\left(1 - \frac{V^2}{V_0^2}\right)}. \tag{2.2.19}$$

If we identify $\widetilde{\chi}$ in the Davydov model with $\chi/2$ in the Scott model, then the first three terms of Equation (2.2.19) give exactly the nonlinear Schrödinger equation (2.2.13), but there is still the term involving η in Equation (2.2.19) which makes it fundamentally different from Equation (2.2.13). On the other hand, Scott's equations are reducible to the nonlinear Schrödinger equation by a different method: instead of taking the whole system to the continuum limt, one first finds the exact, discretised lattice solution in the stationary state, and then approximate the electron equation. In this case, only stationary solutions to the nonlinear Schrödinger equation are relevant.

We give the name Davydov-Scott to any model whose interaction Hamiltonian is bilinear in $\widehat{A}_n^\dagger\widehat{A}_n$ and in some discretised spatial gradient of U_n. When we study our generalised Davydov-Scott model in Chapters 4 and 5, we choose (where required) the Scott method of continuum approximation, for two reasons. Firstly, and as we have discussed in Chapter 1, Davydov's continuum method applied when the soliton was 'large', or localised over many lattice sites. We would like to use a method which is applicable to both large and small polarons, which rules out Davydov's method and necessitates a numerical approach, solving our equations on the discrete lattice. Secondly, when approaching the system numerically and looking for a stationary polaron state, we would like to use a discretised ansatz for

the stationary solution to the system, so that we can apply an iterative scheme in order to 'improve' the ansatz towards the true stationary solution. In this regard, Scott's approximation method is ideal, because it works by expressing the true stationary lattice solution in terms of the true stationary electron solution. This halves the number of equations that we need to take into account in our numerical iterative scheme: we use a stationary nonlinear Schrödinger equation solution as electron ansatz, to find the true stationary electron solution, then obtain for free the stationary lattice solution.

Also in Chapters 4 and 5, we will adopt the semi-classical approximation where the lattice dynamics is treated classically, as per our demonstration in Section 2.1.3. Brizhik *et al.* justified this approximation when they generalised the Davydov-Scott model for their own systems [BEPZ08, BEPZ10, BEPZ14].

2.2.3 Electrosolitons in the α-Helix

In the Holstein-Hennig model of electron transport along an α-channel mediated by electron-intrapeptide oscillator coupling, the Fröhlich Hamiltonian reads [Hol59a, Hen01]

$$\begin{aligned}\widehat{H}^{\mathrm{HH}} &= \widehat{H}_{\mathrm{e}} + \widehat{H}_{\mathrm{p}}^{\mathrm{HH}} + \widehat{H}_{\mathrm{int}}^{\mathrm{HH}} \\ &= \sum_{n=0}^{N} J_0 \widehat{A}_n^\dagger \widehat{A}_n - \sum_{n=0}^{N-1} J_1 \left(\widehat{A}_{n+1}^\dagger \widehat{A}_n + \widehat{A}_n^\dagger \widehat{A}_{n+1} \right) \\ &\quad + \sum_{n=0}^{N} \left(\frac{P_n^2}{2M} + \frac{M\Omega^2 Q_n^2}{2} \right) \\ &\quad + \sum_{n=0}^{N} \chi Q_n \widehat{A}_n^\dagger \widehat{A}_n, \end{aligned} \tag{2.2.20}$$

where n labels the lattice nodes, each of which is a C=O oscillator. $\widehat{A}_n^\dagger, \widehat{A}_n$ are the electron creation and annihilation operators respectively, $J_0 > 0$ is the electron site energy, $J_1 > 0$ the nearest-neighbour electron transfer integral, M the reduced mass of a C=O oscillator, Ω a constant angular frequency, Q_n the classical relative C=O displacement measured from equilibrium, P_n the momentum conjugate to Q_n, and χ the electron-oscillator coupling constant. Hennig showed that a self-trapped stationary electron could form under the electron-oscillator interaction, and that a suitable initial impulse could dislodge the stationary electron, causing it and an accompanying local oscillator displacement to propagate as a soliton along the polypeptide. In Chapter 3, we generalise the the Holstein-Hennig model by quantising the lattice, replacing P_n and Q_n respectively with operators $\widehat{P}_n$ and $\widehat{Q}_n$. We also consider, instead of an initial impulse, the system's response to an external

electromagnetic field. To that end, we adapt the work of Brizhik, Cruzeiro-Hansson and Eremko, who derived a simple expression for an *external Hamiltonian* representing the interaction between an extra electron in a lattice and electromagnetic radiation [BCHE98]. In the case of a one-dimensional lattice approximated as a dipole, the original result of Brizhik *et al.* was that the external Hamiltonian was

$$\widehat{H}^0_{\text{ext}} = -E|\mathbf{D}|, \tag{2.2.21}$$

where $E = E(t)$ was the amplitude of the electric field vector in the direction of the lattice, and $\mathbf{D}$ was the dipole moment of the lattice. Adapted for the case of a one-dimensional lattice where every node is a point dipole, labelled by n, the external Hamiltonian becomes the form that Brizhik *et al.* used in [BEPZ08] and later publications:

$$\widehat{H}_{\text{ext}} = -\sum_{n=0}^{N} eER(n - n_0)\widehat{A}^\dagger_n \widehat{A}_n, \tag{2.2.22}$$

where $\widehat{A}^\dagger_n$ and $\widehat{A}_n$ are as before, e is the elementary charge, R is the lattice constant, and n_0 is some arbitrary lattice site at which the potential energy due to E is set to zero. Modelling the interaction between an extra electron and a lattice of diatomic molecules, with an electromagnetic field incorporated into $\widehat{H}_{\text{ext}}$, Brizhik *et al.* found that a biharmonic radiation induced a polaron motion known as a ratchet drift. This was a form of directed electron transport along the lattice, and the authors argued for the applicability of their model to polypeptides. More generally, the four-part *Fröhlich-Brizhik Hamiltonian*,

$$\widehat{H} = \widehat{H}_{\text{e}} + \widehat{H}_{\text{p}} + \widehat{H}_{\text{int}} + \widehat{H}_{\text{ext}}, \tag{2.2.23}$$

is applicable whenver an external electromagnetic field interacts with the extra electron in a Fröhlich system. We use it in Chapter 3, and also to study electron transport in the generalised Davydov-Scott model in Chapters 4 and 5.

Another vital part of our electron transport models is the response of the lattice to its thermal environment. To account for that, we invoke *Langevin dynamics*, named after Paul Langevin who in 1908 published a seminal study on the Newtonian motion of a Brownian particle [Lan08], and whose theory has been widely adapted for various contexts including cellular environments [LG97,Sch10]. The idea is relatively straightforward: once we have dynamical equations for the lattice displacements, in the form of 'rate of change of momentum equals force', we add to the force a viscous damping term and a noise term.

The damping term opposes the momentum of the node, and is proportional to the node velocity, with a proportionality known as the *viscous damping coefficient*; it represents the momentum dissipation of the lattice due to friction against the cell environment. The noise term is stochastic with zero mean, and we will describe its correlation function where appropriate in Chapters 3 to 5. It represents the random forces on the lattice due to thermal fluctuations in the cell environment. It is the addition of Langevin dynamics to the Fröhlich-Brizhik system that enabled the study in 2014 by Brizhik *et al.* of the thermal stability of polarons, and thermal enhancement of polaron propagation, in molecular chains such as polypeptides [BEPZ14]. Building on the results of their ratchet drift studies, the authors discovered that a low temperature in the cell environment promoted the directed transport of the extra electron by effectively lowering its self-trapping potential, but that a high temperature destroyed the self-trapping polaron state altogether. We will find characteristically similar results in all our models, with the systems exhibiting varying levels of stability against thermal fluctuations.

2.2.4 Physical Parameters in the Models

The main difficulty in our modelling is choosing values for our parameters. In the case of fitting parameters, which we allow to take various values, and by which we parametrise our models' outputs, the difficulty is a computational one. We may need to vary a parameter by several orders of magnitude, because all of them lead to reasonable results; this is what we find ourselves doing with some parameters which contribute to the external electromagnetic field. Alternatively, we may need to vary a parameter by small increments, because the model depends sensitively upon them; this is true for the electron-intrapeptide oscillator or electron-hydrogen bond coupling constant. In cases where the value of a parameter can and should be fixed, we may still have the difficulty that different studies, using different experimental setups or theoretical methods, claim different values for that parameter. In Chapters 3 to 5, we will wherever applicable discuss our choices for the model-specific parameters in detail. Here, we offer an overview of one parameter that will be relevant to all our models.

Following the preceding Section, we consider the viscous damping coefficient, Γ, which is the proportionality constant relating the drag force on a lattice node, such as a peptide unit, to the node velocity. The value of Γ depends on the dynamic viscosity of the cell environment at physiological temperature, as well as the size of the node. Whilst the

latter is straightforward to determine, the former is a contentious topic. Many empirical estimates of cytoplasmic viscosity exist, but understandably they vary depending not only on the experiment, but also on the cells being tested. On one end of the spectrum, Fushimi and Verkman estimated the cytoplasmic viscosity of Swiss 3T3 fibroblasts to be the same order of magnitude as the viscosity of water [FV91]. On the other end of the scale, Bausch *et al.* measured the mean cytoplasmic viscosity of J774 macrophages to be $\mathcal{O}(10^5)$ times that of water [BMS99]. A variation of $\mathcal{O}(10^5)$ in the value of one parameter alone is simply too great to handle computationally, and there are more important parameters in our models, for instance the coupling constant, which we expect to have much greater influence on our systems' behaviour than the damping force does, which is in any case a small perturbation. For those reasons, we choose to fix the cytoplasmic viscosity in our models, at a constant value of 0.068 $\text{Pa} \cdot \text{s}$, according to a 2011 study by Margraves *et al.* who tested live human brain cancer cells in order to obtain their results [MKY$^+$11]. Not only is this the most recent experimental study of its kind, the authors cited the aforementioned extremal results and took into account the factors that could have led to such a large discrepancy between them. Using this value of cytoplasmic viscosity, we are able easily to calculate Γ using Stokes' Law, the details of which we will demonstrate in due course because they are model-specific.

Chapter 3

The Electron-Amide-I System in a Linear α-Channel

This Chapter is adapted from [LP18].

We propose a model of electron transport along a single α-channel, where the electron interacts only with a particular mode of intramolecular oscillations residing within peptide units. We consider specifically the amide-I mode, i.e. linear stretching, of C=O double oscillators, of which there is one per peptide unit, and which are aligned along the α-channel. We assume, for simplicity, that the α-channel is linear. We treat the oscillators quantum mechanically, and within our model the amide-I excitation can be induced by electromagnetic interactions between an oscillator and a passing electron, whilst the same interaction can also induce the electron's auto-localisation, analogously to the way in which electron-phonon interactions cause auto-localisation in polaron models. Thus, ours is a *pseudo-polaron* model, where a 'polaron' refers for the remainder of this Chapter to the electron-amide-I composite. Moreover, ours is a generalised Holstein-Hennig model [Hol59a,Hol59b,Hen01], the generalisation manifesting itself as a quantum correction term and a stochastic term in the dynamical equations.

Our aims are to characterise the stationary polarons that our model admits, and to find suitable external electromagnetic fields (EMFs) which facilitate directed polaron motion along the α-channel from a stationary state, taking thermal effects into account. We discover that an electric pulse with appropriate amplitudes and time-spans of hundreds of femtoseconds can displace a polaron by tens of lattice sites. Such electric pulses match in both amplitude and time-span those induced by charge separation observed in biological complexes [GBM$^+$88, ZZ01]. When these pulses are repeated periodically in time, we find that the polaron can remain intact for several periods, even at physiological temperature,

during which it can propagate by hundreds of sites.

In Section 3.1, we outline our mathematical model and describe relevant physical parameters. Then in Sections 3.2 and 3.3, we present solutions which represent stationary and quasi-stationary polaron states, computing the latter by including in our equations a stochastic term that arises from the thermal environment. Section 3.4 concerns propagating solutions, where we find suitable EMFs capable of displacing a polaron from its stationary or quasi-stationary state and sustaining its motion. We investigate the effect of a single electric pulse as well as periodically repeating pulses, and we characterise the resulting polaron motion in terms of velocity and stability. In particular, we examine the polaron's stability with respect to stochastic thermal fluctuations at physiological temperature. Finally, we summarise our results and explain their biophysical implications in Section 3.5.

3.1 A Pseudo-Polaron Model

We model the α-channel as a linear lattice with identical C=O oscillators at the lattice sites, and identical equilibrium spacing between sites. In the absence of extraneous electrons, the oscillators move independently, all with the same natural angular frequency. We model the oscillators by quantum mechanical operators as opposed to classical variables, because we wish to assign a specific frequency corresponding to the amide-I mode, and it has been shown that the absorption band of a classical amide-I oscillator is 40 times wider than that of a quantum mechanical one [CHT97].

We present the Hamiltonian for our electron-amide-I system in Section 3.1.1, before deriving dynamical equations governing the motion of the electron as well as displacements of lattice sites, the latter of which correspond to the magnitudes of linear stretching of C=O bonds. In Section 3.1.2, we give values of physical parameters in our system, justifying our choices where appropriate.

3.1.1 The Hamiltonian and Dynamical Equations

We write the Hamiltonian for the electron-amide-I system in Fröhlich-Brizhik form,

$$\widehat{H} = \widehat{H}_{\mathrm{e}} + \widehat{H}_{\mathrm{p}} + \widehat{H}_{\mathrm{int}} + \widehat{H}_{\mathrm{ext}}, \tag{3.1.1}$$

where

$$\widehat{H}_{\mathrm{e}} = \sum_{n=0}^{N} J_0 \widehat{A}_n^{\dagger} \widehat{A}_n - \sum_{n=0}^{N-1} J_1 \left(\widehat{A}_{n+1}^{\dagger} \widehat{A}_n + \widehat{A}_n^{\dagger} \widehat{A}_{n+1} \right), \tag{3.1.2a}$$

$$\widehat{H}_{\mathrm{p}} = \sum_{n=0}^{N} \left(\frac{\widehat{P}_n^2}{2M} + \frac{M\Omega^2 \widehat{Q}_n^2}{2} \right), \tag{3.1.2b}$$

$$\widehat{H}_{\mathrm{int}} = \sum_{n=0}^{N} \chi \widehat{Q}_n \widehat{A}_n^{\dagger} \widehat{A}_n, \tag{3.1.2c}$$

$$\widehat{H}_{\mathrm{ext}} = -\sum_{n=0}^{N} eER\,(n - n_0)\, \widehat{A}_n^{\dagger} \widehat{A}_n. \tag{3.1.2d}$$

In Equation (3.1.2), $n = 0, 1, 2, \ldots, N$ labels the lattice sites. $\widehat{H}_{\mathrm{e}}$ describes a tight-binding electron, where $\widehat{A}_n^{\dagger}$ and $\widehat{A}_n$ are, respectively, the operators of electron creation and annihilation at the n^{th} lattice site. J_0 is the electron site energy, and J_1 the nearest-neighbour electron transfer integral. $\widehat{H}_{\mathrm{p}}$ corresponds to the energy contribution from the lattice, where M is the reduced mass of a C=O oscillator, and Ω the natural angular frequency of each oscillator. $\widehat{Q}_n$ is the operator for relative displacement between C and O in the n^{th} oscillator, and $\widehat{P}_n$ is the momentum operator conjugate to $\widehat{Q}_n$. The form of the interaction Hamiltonian, $\widehat{H}_{\mathrm{int}}$, is derived from the assumption that the electron site energy is modified by the displacement field, $\widehat{Q}_n$, and we have retained only the linear term, involving coupling constant χ, in the Taylor expansion for this modified energy [Hen01]. Finally, $\widehat{H}_{\mathrm{ext}}$ represents the modification of electron site energy due to the presence of an external EMF [BCHE98, BEPZ08]. $-e$ is the electron charge, $E = E(t)$ the amplitude of the electric field along the α-channel, R the equilibrium lattice spacing, and n_0 an arbitrary lattice site at which the potential energy due to E is set to zero. The operators satisfy the commutation relations,

$$\left[\widehat{Q}_m, \widehat{P}_n\right] = \left[\widehat{Q}_m^{\dagger}, \widehat{P}_n^{\dagger}\right] = -\left[\widehat{Q}_m, \widehat{P}_n^{\dagger}\right] = -\left[\widehat{Q}_m^{\dagger}, \widehat{P}_n\right] = i\hbar\, \delta_{mn}, \tag{3.1.3a}$$

$$\left[\widehat{Q}_m, \widehat{A}_n\right] = \left[\widehat{Q}_m, \widehat{A}_n^{\dagger}\right] = \left[\widehat{P}_m, \widehat{A}_n\right] = \left[\widehat{P}_m, \widehat{A}_n^{\dagger}\right] = 0, \tag{3.1.3b}$$

and the fermionic anti-commutation relation,

$$\widehat{A}_m \widehat{A}_n^{\dagger} + \widehat{A}_n^{\dagger} \widehat{A}_m = \delta_{mn}. \tag{3.1.4}$$

Denoting the vacuum states of $\widehat{H}_{\mathrm{e}}$ and $\widehat{H}_{\mathrm{p}}$, respectively, by $|0_{\mathrm{e}}\rangle$ and $|0_{\mathrm{p}}\rangle$, we have

$$\widehat{A}_n |0_{\mathrm{e}}\rangle = 0, \tag{3.1.5a}$$

$$\langle 0_{\mathrm{p}}| \widehat{Q}_n |0_{\mathrm{p}}\rangle = \langle 0_{\mathrm{p}}| \widehat{P}_n |0_{\mathrm{p}}\rangle = 0. \tag{3.1.5b}$$

At time t, the electronic state is a superposition of single excitations,

$$|\Psi_{\mathrm{e}}(t)\rangle = \sum_{n=0}^{N} \alpha_n(t) \widehat{A}_n^\dagger \, |0_{\mathrm{e}}\rangle \,, \tag{3.1.6}$$

for some complex coefficients α_n. We then assume that the intramolecular oscillators are in a Glauber state [Gla63, ELS84, KL87],

$$|\Psi_{\mathrm{p}}(t)\rangle = \exp\left(\widehat{\sigma}(t)\right) |0_{\mathrm{p}}\rangle \,, \tag{3.1.7}$$

where

$$\widehat{\sigma}(t) = \frac{i}{\hbar} \sum_{n=0}^{N} \Big(p_n(t) \widehat{Q}_n - q_n(t) \widehat{P}_n \Big) \,, \tag{3.1.8}$$

for some real coefficients q_n, p_n, so that

$$\widehat{\sigma}^\dagger = -\widehat{\sigma}. \tag{3.1.9}$$

In the Born-Oppenheimer approximation, the state of the composite electron-amide-I system is

$$|\Psi(t)\rangle = |\Psi_{\mathrm{e}}(t)\rangle \, |\Psi_{\mathrm{p}}(t)\rangle = \sum_{n=0}^{N} \alpha_n(t) \exp\left(\widehat{\sigma}(t)\right) \widehat{A}_n^\dagger \, |0_{\mathrm{e}}\rangle \, |0_{\mathrm{p}}\rangle \,, \tag{3.1.10}$$

with the normalisation condition,

$$\sum_{n=0}^{N} |a_n|^2 = 1. \tag{3.1.11}$$

Dynamical equations for the system are first-order differential equations for the variables α_n, q_n and p_n. We derive these equations by minimising the energy, $\langle \widehat{H} \rangle := \langle \Psi | \widehat{H} | \Psi \rangle$, as follows. From Equations (3.1.8) and (3.1.9), we deduce

$$\begin{aligned} \Big[\widehat{\sigma}^\dagger, \widehat{Q}_n \Big] &= \frac{i}{\hbar} \Big[\sum_{m=0}^{N} q_m \widehat{P}_m, \ \widehat{Q}_n \Big] - \frac{i}{\hbar} \Big[\sum_{m=0}^{N} p_m \widehat{Q}_m, \ \widehat{Q}_n \Big] \\ &= \frac{i}{\hbar} \sum_{m=0}^{N} (-i\hbar) \, q_m \delta_{mn} \\ &= q_n. \end{aligned} \tag{3.1.12}$$

It follows that

$$\begin{aligned} \Big[\widehat{\sigma}^\dagger, \widehat{Q}_n^2 \Big] &= \Big[\widehat{\sigma}^\dagger, \widehat{Q}_n \Big] \widehat{Q}_n + \widehat{Q}_n \Big[\widehat{\sigma}^\dagger, \widehat{Q}_n \Big] \\ &= 2 q_n \widehat{Q}_n. \end{aligned} \tag{3.1.13}$$

Similarly, we have

$$\left[\widehat{\sigma}^\dagger, \widehat{P}_n\right] = p_n, \tag{3.1.14a}$$

$$\left[\widehat{\sigma}^\dagger, \widehat{P}_n^2\right] = 2p_n\widehat{P}_n. \tag{3.1.14b}$$

Using the Baker-Hausdorff identity for generic operators $\widehat{B}$ and $\widehat{O}$,

$$\exp(\widehat{B})\widehat{O}\exp(-\widehat{B}) = \widehat{O} + \sum_{n=1}^{\infty}\frac{1}{n!}\widehat{O}_n, \tag{3.1.15}$$

where $\widehat{O}_1 = [\widehat{B}, \widehat{O}]$ and $\widehat{O}_{n+1} = [\widehat{B}, \widehat{O}_n]$ for $n \geq 1$, we obtain the following:

$$\exp(\widehat{\sigma}^\dagger)\widehat{Q}_n\exp(\widehat{\sigma}) = \widehat{Q}_n + q_n, \quad \exp(\widehat{\sigma}^\dagger)\widehat{Q}_n^2\exp(\widehat{\sigma}) = \widehat{Q}_n^2 + 2q_n\widehat{Q}_n + q_n^2, \tag{3.1.16a}$$

$$\exp(\widehat{\sigma}^\dagger)\widehat{P}_n\exp(\widehat{\sigma}) = \widehat{P}_n + p_n, \quad \exp(\widehat{\sigma}^\dagger)\widehat{P}_n^2\exp(\widehat{\sigma}) = \widehat{P}_n^2 + 2p_n\widehat{P}_n + p_n^2. \tag{3.1.16b}$$

Since the electron operators commute with the lattice operators, we have

$$\begin{aligned}\exp(\widehat{\sigma}^\dagger)\widehat{H}\exp(\widehat{\sigma}) = \widehat{H}_{\mathrm{e}} + \widehat{H}_{\mathrm{ext}} + \sum_{n=0}^{N}\Bigg(&\frac{\widehat{P}_n^2 + 2p_n\widehat{P}_n + p_n^2}{2M} \\ &+ \frac{M\Omega^2\left(\widehat{Q}_n^2 + 2q_n\widehat{Q}_n + q_n^2\right)}{2} + \chi\Big(\widehat{Q}_n + q_n\Big)\widehat{A}_n^\dagger\widehat{A}_n\Bigg).\end{aligned} \tag{3.1.17}$$

We therefore deduce the following expression for $\langle\widehat{H}\rangle$:

$$\langle\widehat{H}\rangle = \sum_{j=0}^{N}\sum_{k=0}^{N}\alpha_j^*\alpha_k\left\langle 0\,\middle|\,\widehat{A}_j\exp(\widehat{\sigma}^\dagger)\widehat{H}\exp(\widehat{\sigma})\widehat{A}_k^\dagger\,\middle|\,0\right\rangle \tag{3.1.18a}$$

$$= \sum_{j=0}^{N}\sum_{k=0}^{N}\alpha_j^*\alpha_k\left\langle 0\,\middle|\,\widehat{A}_j\left(\widehat{H}_{\mathrm{e}} + \widehat{H}_{\mathrm{ext}} + \sum_{m=0}^{N}\left(\frac{p_m^2}{2M} + \frac{M\Omega^2q_m^2}{2} + \chi q_m\widehat{A}_m^\dagger\widehat{A}_m\right)\right)\widehat{A}_k^\dagger\,\middle|\,0\right\rangle, \tag{3.1.18b}$$

where we have defined $|0\rangle = |0_{\mathrm{e}}\rangle\,|0_{\mathrm{p}}\rangle$, so that for all n,

$$\widehat{A}_n\,|0\rangle = \langle 0_{\mathrm{p}}|\,\widehat{Q}_n\,|0\rangle = \langle 0_{\mathrm{p}}|\,\widehat{P}_n\,|0\rangle = 0. \tag{3.1.19}$$

To obtain the dynamical equations for q_n and p_n, we use Hamilton's equations,

$$\frac{\mathrm{d}q_n}{\mathrm{d}t} = \frac{\partial\langle\widehat{H}\rangle}{\partial p_n} = \frac{p_n}{M}, \tag{3.1.20a}$$

$$\frac{\mathrm{d}p_n}{\mathrm{d}t} = -\frac{\partial\langle\widehat{H}\rangle}{\partial q_n} = -\left(M\Omega^2q_n + \chi|\alpha_n|^2\right), \tag{3.1.20b}$$

the combination of which gives us the second-order equation for q_n:

$$M\frac{\mathrm{d}^2q_n}{\mathrm{d}t^2} = -\left(M\Omega^2q_n + \chi|\alpha_n|^2\right). \tag{3.1.21}$$

For the α_n equation, we return to eq. (3.1.18a), from which it follows that

$$\frac{\partial \langle \widehat{H} \rangle}{\partial \alpha_n^*} = \sum_{k=0}^{N} \alpha_k \left\langle 0 \,\middle|\, \widehat{A}_n \exp(\widehat{\sigma}^\dagger) \widehat{H} \exp(\widehat{\sigma}) \widehat{A}_k^\dagger \,\middle|\, 0 \right\rangle = \left\langle 0 \,\middle|\, \widehat{A}_n \exp(\widehat{\sigma}^\dagger) \widehat{H} \,\middle|\, \Psi \right\rangle . \tag{3.1.22}$$

Making use of the Schrödinger equation, $\widehat{H} \left| \Psi \right\rangle = i\hbar \, \partial \left| \Psi \right\rangle / \partial t$, we deduce

$$\frac{\partial \langle \widehat{H} \rangle}{\partial \alpha_n^*} = i\hbar \sum_{k=0}^{N} \left\langle 0 \,\middle|\, \widehat{A}_n \exp(\widehat{\sigma}^\dagger) \left(\frac{\mathrm{d}\alpha_k}{\mathrm{d}t} + \alpha_k \frac{\mathrm{d}\widehat{\sigma}}{\mathrm{d}t} \right) \exp(\widehat{\sigma}) \widehat{A}_k^\dagger \,\middle|\, 0 \right\rangle . \tag{3.1.23}$$

At this point, a standard treatment is to invoke the approximation that $\mathrm{d}\widehat{\sigma}/\mathrm{d}t$ is negligible, as was done in [Sco92]. We do not make such an assumption, and therefore

$$\begin{aligned}
\frac{\partial \langle \widehat{H} \rangle}{\partial \alpha_n^*} &= i\hbar \sum_{k=0}^{N} \frac{\mathrm{d}\alpha_k}{\mathrm{d}t} \left\langle 0 \,\middle|\, \widehat{A}_n \exp(\widehat{\sigma}^\dagger) \exp(\widehat{\sigma}) \widehat{A}_k^\dagger \,\middle|\, 0 \right\rangle \\
&\quad + i\hbar \sum_{k=0}^{N} \alpha_k \left\langle 0 \,\middle|\, \widehat{A}_n \exp(\widehat{\sigma}^\dagger) \frac{i}{\hbar} \sum_{m=0}^{N} \left(\frac{\mathrm{d}p_m}{\mathrm{d}t} \widehat{Q}_m - \frac{\mathrm{d}q_m}{\mathrm{d}t} \widehat{P}_m \right) \exp(\widehat{\sigma}) \widehat{A}_k^\dagger \,\middle|\, 0 \right\rangle \\
&= i\hbar \sum_{k=0}^{N} \frac{\mathrm{d}\alpha_k}{\mathrm{d}t} \, \delta_{nk} \\
&\quad - \sum_{k=0}^{N} \alpha_k \left\langle 0 \,\middle|\, \widehat{A}_n \sum_{m=0}^{N} \left(\frac{\mathrm{d}p_m}{\mathrm{d}t} \left(\widehat{Q}_m + q_m \right) - \frac{\mathrm{d}q_m}{\mathrm{d}t} \left(\widehat{P}_m + p_m \right) \right) \widehat{A}_k^\dagger \,\middle|\, 0 \right\rangle \\
&= i\hbar \frac{\mathrm{d}\alpha_n}{\mathrm{d}t} - \sum_{m=0}^{N} \left(\frac{\mathrm{d}p_m}{\mathrm{d}t} q_m - \frac{\mathrm{d}q_m}{\mathrm{d}t} p_m \right) \sum_{k=0}^{N} \alpha_k \left\langle 0 \,\middle|\, \widehat{A}_n \widehat{A}_k^\dagger \,\middle|\, 0 \right\rangle \\
&= i\hbar \frac{\mathrm{d}\alpha_n}{\mathrm{d}t} - \sum_{m=0}^{N} \left(M \frac{\mathrm{d}^2 q_m}{\mathrm{d}t^2} q_m - M \left(\frac{\mathrm{d}q_m}{\mathrm{d}t} \right)^2 \right) \alpha_n \\
&= i\hbar \frac{\mathrm{d}\alpha_n}{\mathrm{d}t} - \sum_{m=0}^{N} \left(- \left(M\Omega^2 q_m + \chi |\alpha_m|^2 \right) q_m - M \left(\frac{\mathrm{d}q_m}{\mathrm{d}t} \right)^2 \right) \alpha_n \\
&= i\hbar \frac{\mathrm{d}\alpha_n}{\mathrm{d}t} + (2W + I) \, \alpha_n ,
\end{aligned} \tag{3.1.24}$$

where

$$W(t) = \langle \widehat{H}_\mathrm{p} \rangle = \frac{1}{2} \sum_{m=0}^{N} \left(M \left(\frac{\mathrm{d}q_m}{\mathrm{d}t} \right)^2 + M\Omega^2 q_m^2 \right) , \tag{3.1.25a}$$

$$I(t) = \langle \widehat{H}_\mathrm{int} \rangle = \sum_{m=0}^{N} \chi q_m |\alpha_m|^2 . \tag{3.1.25b}$$

In the meantime, instead of deriving Equation (3.1.24) from Equation (3.1.18a), we could also derive, from eq. (3.1.18b),

$$\begin{aligned}
\frac{\partial \langle \widehat{H} \rangle}{\partial \alpha_n^*} &= \sum_{k=0}^{N} \alpha_k \Bigg\langle 0 \Bigg| \widehat{A}_n \Bigg(\sum_{m=0}^{N} J_0 \widehat{A}_m^\dagger \widehat{A}_m - \sum_{m=0}^{N-1} J_1 \left(\widehat{A}_{m+1}^\dagger \widehat{A}_m + \widehat{A}_m^\dagger \widehat{A}_{m+1} \right) \\
&\quad - \sum_{m=0}^{N} eER\,(m - n_0)\, \widehat{A}_m^\dagger \widehat{A}_m + \sum_{m=0}^{N} \left(\frac{p_m^2}{2M} + \frac{M\Omega^2 q_m^2}{2} + \chi q_m \widehat{A}_m^\dagger \widehat{A}_m \right) \Bigg) \widehat{A}_k^\dagger \Bigg| 0 \Bigg\rangle \\
&= \sum_{k=0}^{N} \alpha_k \Bigg\langle 0 \Bigg| \widehat{A}_n \left(J_0 \widehat{A}_k^\dagger - J_1 \left(\widehat{A}_{k+1}^\dagger + \widehat{A}_{k-1}^\dagger \right) - eER\,(k - n_0)\, \widehat{A}_k^\dagger + \chi q_k \widehat{A}_k^\dagger \right) \Bigg| 0 \Bigg\rangle \\
&\quad + \sum_{m=0}^{N} \left(\frac{p_m^2}{2M} + \frac{M\Omega^2 q_m^2}{2} \right) \sum_{k=0}^{N} \alpha_k \left\langle 0 \left| \widehat{A}_n \widehat{A}_k^\dagger \right| 0 \right\rangle \\
&= \alpha_n \left[J_0 + \chi q_n - eER\,(n - n_0) + W \right] - J_1 \left(\alpha_{n-1} + \alpha_{n+1} \right). \qquad (3.1.26)
\end{aligned}$$

We have defined

$$\alpha_{-1} = \alpha_{N+1} = 0, \qquad (3.1.27)$$

so that Equation (3.1.26) holds at the boundaries where $n = 0, N$. Equating the right-hand sides of Equations (3.1.24) and (3.1.26), we obtain the following:

$$i\hbar \frac{\mathrm{d}\alpha_n}{\mathrm{d}t} = \alpha_n \left[J_0 + \chi q_n - eER\,(n - n_0) - (W + I) \right] - J_1 \left(\alpha_{n-1} + \alpha_{n+1} \right). \qquad (3.1.28)$$

Equations (3.1.21) and (3.1.28) are the dynamical equations of our system. We note that, since $\langle \Psi | \widehat{Q}_n | \Psi \rangle = q_n$ and $\langle \Psi | \widehat{P}_n | \Psi \rangle / M = p_n / M = \mathrm{d}q_n / \mathrm{d}t$, the physical interpretation of q_n is the expected value of relative displacement of the n^{th} C=O oscillator, and the physical interpretation of $\mathrm{d}q_n/\mathrm{d}t$ is the expected value of relative velocity of the n^{th} oscillator.

Next, we define a variable $\psi_n(t)$ by the gauge transformation,

$$\alpha_n(t) = \psi_n(t) \exp\left[\frac{it}{\hbar} \left(-J_0 + 2J_1 \right) \right], \qquad (3.1.29)$$

which preserves the probability density $|\alpha_n| = |\psi_n|$. Equation (3.1.28) then becomes an equation for ψ_n, in which every α_n becomes a ψ_n, J_0 no longer appears, and the J_1 term becomes a discrete Laplacian, $-J_1 \left(\psi_{n-1} + \psi_{n+1} - 2\psi_n \right)$. Moreover, to account for the effect on the lattice of its thermal environment, we add the Langevin terms, $-\Gamma\, \mathrm{d}Q_n/\mathrm{d}t + F_n(t)$, to the right-hand side of Equation (3.1.21) [Lan08, LG97, Sch10, BEPZ14]. Here, Γ is a viscous damping coefficient, which depends on the temperature of the environment,

and $F_n(t)$ is a Gaussian stochastic term describing thermal fluctuations, with zero mean and satisfying the correlation relation,

$$\langle F_m(t), F_n(t') \rangle = 2\Gamma k_{\mathrm{B}} \Theta \delta_{m,n} \delta(t - t'), \tag{3.1.30}$$

where k_{B} is the Boltzmann constant and Θ is the temperature in Kelvin. Scaling time by Ω^{-1} and length by

$$L := \sqrt{\hbar M^{-1} \Omega^{-1}}, \tag{3.1.31}$$

we have the following non-dimensionalised dynamical equations, for $n = 0, 1, 2, \ldots N$:

$$i\dot{\psi}_n = (\kappa u_n - w - \eta)\,\psi_n - \rho\,(\psi_{n-1} + \psi_{n+1} - 2\psi_n) - \epsilon(n - n_0)\psi_n, \tag{3.1.32a}$$

$$\ddot{u}_n = -u_n - \kappa|\psi_n|^2 - \gamma \dot{u}_n + f_n, \tag{3.1.32b}$$

where

$$\tau = \Omega t, \quad u_n = \frac{q_n}{L}, \quad w = \frac{W}{\hbar\Omega}, \quad \eta = \frac{I}{\hbar\Omega}, \tag{3.1.33}$$

and

$$\kappa = \frac{\chi}{\sqrt{\hbar M \Omega^3}}, \quad \rho = \frac{J_1}{\hbar\Omega}, \quad \epsilon = \frac{eER}{\hbar\Omega}, \quad \gamma = \frac{\Gamma}{M\Omega}, \quad f_n = \frac{F_n}{\sqrt{\hbar M \Omega^3}}. \tag{3.1.34}$$

ρ is an *adiabaticity parameter* representing the characteristic time-scale separation between the lattice and electron dynamics, and κ is a *coupling constant* providing a measure of interaction strength between the electron and lattice. At the boundaries, we have the fictitious points

$$\psi_{-1} = \psi_{N+1} = 0, \tag{3.1.35}$$

and we also impose the following boundary condition for the lattice:

$$u_0 = \dot{u}_0 = 0, \tag{3.1.36}$$

which is always valid in the inertial frame with the 0^{th} site at the origin. By setting $w = \eta = \gamma = f_n = 0$ in Equation (3.1.32), and by repurposing ϵ as an initial impulse acting on the u_n equation, we reduce ours to the Holstein-Hennig model [Hen01].

3.1.2 Parameters

We take the following parameter values appropriate for an α-channel [PCB51, NC76, CLR77, Zav87, BT88, Dun01, Hen01]:

$$M = 1.147 \times 10^{-26} \text{ kg}, \quad R = 4.5 \text{ Å}, \quad \Omega = 3.1 \times 10^{14} \text{ s}^{-1}, \quad J_1 \lessapprox 1 \text{ eV}. \tag{3.1.37}$$

In particular, M is the reduced mass of a CO nuclear dyad. We obtain an estimate of Γ by approximating the lattice unit as an *equivalent sphere* and using Stokes' Law [PBM90],

$$\Gamma = 6\pi r \mu, \tag{3.1.38}$$

where $r = 3.3$ fm is the equivalent spherical radius of a CO nuclear dyad [JP88,AM13], and $\mu = 0.068$ Pa$\cdot$s is the dynamic viscosity of cytoplasmic fluid at physiological temperature, as we explained in Section 2.2.4. We therefore fix

$$\gamma = 0.001. \tag{3.1.39}$$

For the other dimensionless parameters, we have

$$\rho \lessapprox 5, \tag{3.1.40}$$

and the physiological thermal energy at $\Theta = 310$K is

$$\theta = k_B \Theta / (\hbar \Omega) = 0.13. \tag{3.1.41}$$

θ enters the system via the stochastic forces, $f_n(\tau)$, which satisfy

$$\langle f_n(\tau) \rangle = 0, \quad \langle f_m(\tau), f_n(\tau + \Delta\tau) \rangle = 2\gamma\theta\delta_{m,n}/\Delta\tau. \tag{3.1.42}$$

We use a conservatively small time-step, $\Delta\tau = 0.01$, to ensure numerical stability. Finally, since no empirically-determined values are available for χ, and since we wish to investigate the electron's response to a variety of EMFs, we vary κ and ϵ in order to obtain our results.

Our parameter values imply that the characteristic time-scale and length-scale in our system, the latter having been defined in Equation (3.1.31), are respectively

$$\Omega^{-1} = 3.2 \text{ fs}, \quad L = 0.054 \text{ Å} = 0.012R. \tag{3.1.43}$$

Moreover, the characteristic energy-scale in our system is

$$\hbar\Omega = 0.2 \text{ eV}. \tag{3.1.44}$$

3.2 Analytical Results

Though it is not possible to use purely analytical methods to find complete solutions to Equation (3.1.32), the analysis can help us make a lot of progress towards understanding our model. Firstly, we write down in Section 3.2.1 the equations describing our system in its stationary state. We then derive expressions for the internal energy of the polaron, as well as its *binding energy* in a stationary state, in Section 3.2.2. Finally in Section 3.2.3, we look at the system in the continuum limit, which reduces the stationary-state equations to a single differential equation. We solve the continuum equation analytically.

3.2.1 The Stationary System

A stationary solution to Equation (3.1.32) comprises a stationary electron state, i.e. some $\psi_n = \psi_n^0$ such that $|\psi_n^0|^2$ is time-independent, and a stationary lattice, $u_n = u_n^0$. Neglecting stochastic effects, so that $f_n(\tau) = 0$, the stationary solution to eq. (3.1.32b) is expressible in terms of $|\psi_n^0|^2$ as

$$u_n = u_n^0 := -\kappa|\psi_n^0|^2. \tag{3.2.1}$$

This reflects the fact that lattice excitations and electronic excitations in our model are directly related, one arising from the presence of the other. To find ψ_n^0, we note that in a stationary state, we have constants $w(\tau) = w_0$ and $\eta(\tau) = \eta_0$, which enables us to define the gauge transformation,

$$\psi_n^0(\tau) = \phi_n^0 \exp\left[i\tau\left(-\rho H_0 + w_0 + \eta_0\right)\right], \tag{3.2.2}$$

where H_0 is a dimensionless eigenvalue to be determined, and ϕ_n^0 is time-independent. The transformation ensures that the time-evolution of ψ_n^0 manifests only as a variation in its phase. Putting Equations (3.2.1) and (3.2.2) into Equation (3.1.32a), we obtain the following algebraic equation for ϕ_n^0:

$$H_0\phi_n^0 + \left(\phi_{n-1}^0 + \phi_{n+1}^0 - 2\phi_n^0\right) + \lambda{\phi_n^0}^3 = 0, \tag{3.2.3}$$

where we have defined the *effective coupling parameter*,

$$\lambda := \frac{\kappa^2}{\rho} = \frac{\chi^2}{M\Omega^2 J_1}. \tag{3.2.4}$$

A stationary electron state is characterised by a ϕ_n^0 solution together with an eigenvalue H_0, and it is clear from Equation (3.2.3) that such a state is parametrised by λ.

3.2.2 Energetics

Apart from the $|\psi_n^0|^2$ and u_n^0 solutions, another crucial aspect of the stationary polaron is its binding energy. In general, the polaron's internal energy E_b is the expected value of $\widehat{H}_\mathrm{e} + \widehat{H}_\mathrm{p} + \widehat{H}_\mathrm{int}$ in a polaron state, $|\Psi\rangle$, measured from the lowest energy in the electron band, $J_0 - 2J_1$. In units of eV, we have

$$\begin{aligned} E_\mathrm{b} &= 0.2 \times \frac{\langle\Psi|\widehat{H}_\mathrm{e} + \widehat{H}_\mathrm{p} + \widehat{H}_\mathrm{int}|\Psi\rangle - J_0 + 2J_1}{\hbar\Omega} \\ &= 0.2\rho\left[2 - \sum_{n=0}^{N-1}\left(\psi_{n+1}^*\psi_n + \psi_n^*\psi_{n+1}\right)\right] + 0.2\sum_{n=0}^{N}\left(\frac{u_n^2}{2} + \frac{\dot{u}_n^2}{2}\right) + 0.2\sum_{n=0}^{N}\kappa u_n|\psi_n|^2\,. \end{aligned} \tag{3.2.5}$$

In the stationary state $|\Psi\rangle = |\Psi^0\rangle$, we use Equation (3.2.1) and the fact that $\dot{u}_n = 0$ to simplify the above expression, obtaining the stationary polaron binding energy in eV,

$$E_\mathrm{b}^0 = 0.2\rho\left[2 - \sum_{n=0}^{N-1}\left(\psi_{n+1}^{0*}\psi_n^0 + \psi_n^{0*}\psi_{n+1}^0\right)\right] - \sum_{n=0}^{N}\frac{0.2\kappa^2}{2}\left|\psi_n^0\right|^4. \tag{3.2.6}$$

3.2.3 Approximate Stationary Solutions in the Continuum Limit

We now proceed to show that in the continuum limit of $N \gg 1$, Equation (3.2.3) is equivalent to the stationary *nonlinear Schrödinger equation* (NLSE). To do so, we begin with the NLSE in an attractive cubic potential, in appropriate units,

$$i\frac{\partial\psi}{\partial t} + \frac{\partial^2\psi}{\partial x^2} + \lambda|\psi|^2\psi = 0, \tag{3.2.7}$$

for some function ψ of real variables x and t in the domain $t \geq 0, -N/2 \leq x \leq N/2$. A stationary solution to the NLSE may be written in the form

$$\psi(x,t) = \phi(x)\exp(-iH_0t), \tag{3.2.8}$$

for some function $\phi(x)$ satisfying the ODE,

$$H_0\phi + \frac{\mathrm{d}^2\phi}{\mathrm{d}x^2} + \lambda\phi^3 = 0. \tag{3.2.9}$$

This is the stationary NLSE. Now, in the limit $N \gg 1$, we can write $x = \tilde{x}N$ for some $\tilde{x}$ and write $\phi(x) = \widetilde{\phi}(\tilde{x})$ for some $\widetilde{\phi}$, so that

$$\phi(x \pm 1) = \widetilde{\phi}(\tilde{x} \pm N^{-1}) = \widetilde{\phi}(\tilde{x}) \pm N^{-1}\frac{\mathrm{d}\widetilde{\phi}}{\mathrm{d}\tilde{x}}(\tilde{x}) + \frac{N^{-2}}{2}\frac{\mathrm{d}^2\widetilde{\phi}}{\mathrm{d}\tilde{x}^2}(\tilde{x}) + \mathcal{O}(N^{-3}), \tag{3.2.10}$$

for $-1/2 + N^{-1} \leq \tilde{x} \leq 1/2 - N^{-1}$. It follows that, for $-N/2 + 1 \leq x \leq N/2 - 1$,

$$\phi(x-1) + \phi(x+1) - 2\phi(x) = N^{-2}\frac{\mathrm{d}^2\widetilde{\phi}}{\mathrm{d}\tilde{x}^2}(\tilde{x}) + \mathcal{O}(N^{-3}). \tag{3.2.11}$$

Using

$$\frac{\mathrm{d}^2\widetilde{\phi}}{\mathrm{d}\tilde{x}^2}(\tilde{x}) = N^2\frac{\mathrm{d}\phi}{\mathrm{d}x}(x), \tag{3.2.12}$$

we further deduce

$$\phi(x-1) + \phi(x+1) - 2\phi(x) = \left(1 + \mathcal{O}(N^{-1})\right)\frac{\mathrm{d}^2\phi}{\mathrm{d}x^2}(x). \tag{3.2.13}$$

If we make the indentification

$$\phi\left(n - \frac{N}{2}\right) \equiv \phi_n^0 \quad \text{for } 0 \leq n \leq N, \tag{3.2.14}$$

then we have, for $1 \leq n \leq N-1$,

$$\begin{aligned}\frac{\mathrm{d}^2\phi}{\mathrm{d}x^2}\left(n - \frac{N}{2}\right) &\approx \phi\left(n - \frac{N}{2} - 1\right) + \phi\left(n - \frac{N}{2} + 1\right) - 2\phi\left(n - \frac{N}{2}\right) \\ &\equiv \phi_{n-1}^0 + \phi_{n+1}^0 - 2\phi_n^0.\end{aligned} \tag{3.2.15}$$

Putting Equations (3.2.14) and (3.2.15) into Equation (3.2.9), we see that the latter becomes equivalent to Equation (3.2.3) whenever $x = n - N/2$. We have therefore established that in the $N \gg 1$ limit, if we find a global solution to Equation (3.2.9), then discretising that solution gives us an approximation for ϕ_n^0. The accuracy of this approximation will decrease as we make N smaller, but it would still give us a good ansatz to feed into a numerical scheme which computes an exact stationary solution. If we let $N \to \infty$, then there is indeed a well-known, normalised solution to Equation (3.2.9),

$$\phi(x) = \sqrt{\lambda/8}\,\operatorname{sech}\left[\lambda\left(x - x_0\right)/4\right], \tag{3.2.16}$$

with eigenvalue $H_0 = -\lambda^2/16$, and where x_0 is arbitrary oweing to the translational invariance of Equation (3.2.9) [ZS72, Hir73, LLH$^+$07]. Therefore an approximate solution to Equation (3.2.3) is as follows.

$$\phi_n^0 \approx \sqrt{\lambda/8}\,\operatorname{sech}\left[\lambda(n - n_0)/4\right], \tag{3.2.17a}$$

$$H_0 \approx -\lambda^2/16, \tag{3.2.17b}$$

where n_0 is arbitrary. Now we can invoke Equation (3.2.2) and say that the stationary state for the electron,

$$\psi_n^0(\tau) = \phi_n^0 \exp\left[i\rho\tau\left(-H_0 + \frac{w_0+\eta_0}{\rho}\right)\right], \tag{3.2.18}$$

may be approximated by Equation (3.2.17), and consequently the stationary lattice solution $u_n^0 = -\kappa|\psi_n^0|^2$ may also be approximated by

$$u_n^0 \approx -\frac{\kappa\lambda}{8}\text{sech}^2\left[\lambda(n-n_0)/4\right]. \tag{3.2.19}$$

The value of $w_0+\eta_0$, which is the dimensionless and stationary version of $W(\tau)+I(\tau)$ as defined in Equation (3.1.25), is

$$\begin{aligned} w_0+\eta_0 &= \frac{\langle\Psi^0|\widehat{H}_{\text{p}}+\widehat{H}_{\text{int}}|\Psi^0\rangle}{\hbar\Omega} \\ &= \sum_{n=0}^{N}\left(\frac{(u_n^0)^2}{2}+\kappa u_n^0|\psi_n^0|^2\right) \\ &= -\sum_{n=0}^{N}\frac{\kappa^2}{2}\left|\phi_n^0\right|^4, \end{aligned} \tag{3.2.20}$$

and using Equation (3.2.17a) yields the approximation,

$$\frac{w_0+\eta_0}{\rho} \approx -\sum_{n=0}^{N}\frac{\lambda^3}{128}\,\text{sech}^4\left[\lambda(n-n_0)/4\right]. \tag{3.2.21}$$

Moreover, the electron probability distribution in this approximate stationary state is

$$|\psi_n^0|^2 = |\phi_n^0|^2 \approx (\lambda/8)\,\text{sech}^2\,[\lambda(n-n_0)/4], \tag{3.2.22}$$

so the half-width of the distribution is proportional to λ^{-1}, whilst the maximum height is proportional to λ.

We make one final remark about the continuum limit. Due to the spatial translational invariance of Equation (3.2.7), it admits travelling wave solutions. But those solutions cannot be used to approximate solutions to Equation (3.1.32a), because Equation (3.2.7) approximates Equation (3.1.32a) only when the lattice displacement, u_n, is stationary; and when u_n is stationary, it is not physical to have an electron propagating without dispersion along the lattice.

3.3 Numerical Results on Electron Auto-Localisation

In this Section, we find stationary polaron states by solving Equation (3.1.32) numerically, with $\dot{u}_n = \epsilon = f_n = 0$. With the value of γ being fixed, we look for solutions corresponding to various points in the parameter space (ρ, κ). We wish to determine key quantities associated with the stationary polaron state, such as the electron's *maximum localisation probability*, defined as the maximum value of $|\psi_n^0|^2$ and denoted by $\max|\psi_n^0|^2$, as functions of (ρ, κ). We expect to find that the numerical and approximate solutions match up closely in cases where $\max|\psi_n^0|^2$ is small and the polaron half-width is large, and that the two kinds of solutions are less similar in cases where the polaron is highly localised. This is because obtaining the approximate solutions relied upon the continuum limit which captures broad polarons much better than it does highly localised ones.

We describe in Section 3.3.1 the numerical algorithm that we employ to compute stationary polaron solutions, before presenting the solutions in Section 3.3.2. Then in Section 3.3.3, we investigate the effect of stochastic forces on the stationary polaron state.

3.3.1 The Convergence Algorithm

As Section 3.2 detailed, the dynamical system whose stationary solutions we seek to compute is Equation (3.2.3). A standard approach to computing the stationary solutions is as follows [KAT98]. Observe that any solution ϕ_n^0 is an attractor of the following map:

$$\phi_n^0 \mapsto \frac{\mathcal{H}(\phi_n^0)}{\|\mathcal{H}(\phi_n^0)\|}, \tag{3.3.1}$$

where

$$\mathcal{H}(\phi_n^0) = \left(\phi_{n-1}^0 + \phi_{n+1}^0 - 2\phi_n^0\right) + \lambda {\phi_n^0}^3, \tag{3.3.2a}$$

$$\|\mathcal{H}(\phi_n^0)\| = \sqrt{\sum_{n=0}^{N} \mathcal{H}(\phi_n^0)^2}. \tag{3.3.2b}$$

For each set of (ρ, κ), one could take the approximate solution from Section 3.2.3 as initial guess, and repeatedly apply Equation (3.3.1) until convergence. In practice, however, this method is computationally labour-intensive, particularly when N is large; so we have devised an alternative convergence algorithm which significantly speeds up proceedings.

We do not attempt to solve Equation (3.2.3) directly. Instead, we integrate an appropriate variant of Equation (3.1.32a) forward in time. The equation is written in terms

of some complex-valued $\widetilde{\psi}_n(\tau)$ and a parameter $\mathcal{H}_0$ which we redefine at regular time-intervals according to some algorithm, and we integrate the equation until such time that $\widetilde{\psi}_n$ becomes stationary and $\mathcal{H}_0$ has converged to a fixed value. We then use the stationary $\widetilde{\psi}_n$ and $\mathcal{H}_0$ to deduce the stationary solution ϕ_n^0 to Equation (3.2.3) together with eigenvalue H_0. The appropriate variant of Equation (3.1.32a) is

$$-\frac{\mathrm{d}}{\mathrm{d}\tau}\widetilde{\psi}_n = \left(-\kappa^2\left|\widetilde{\psi}_n\right|^2 + \mathcal{H}_0\right)\widetilde{\psi}_n - \rho\left(\widetilde{\psi}_{n-1} + \widetilde{\psi}_{n+1} - 2\widetilde{\psi}_n\right). \tag{3.3.3}$$

Equations (3.3.3) and (3.1.32a) are similar but notably different. In particular, whereas on the left-hand side of Equation (3.1.32a) we had $i \cdot \mathrm{d}/\mathrm{d}\tau$, on the left-hand side of Equation (3.3.3) we have $-\mathrm{d}/\mathrm{d}\tau$. Thus, when we write out the real and imaginary parts of Equation (3.3.3), for $\widetilde{\psi}_n = y_n + iz_n$, we end up with two equations which are symmetric with respect to re-labelling:

$$\dot{y}_n = \left(\kappa^2(y_n^2 + z_n^2) - \mathcal{H}_0\right)y_n + \rho\left(y_{n-1} + y_{n+1} - 2y_n\right), \tag{3.3.4a}$$

$$\dot{z}_n = \left(\kappa^2(y_n^2 + z_n^2) - \mathcal{H}_0\right)z_n + \rho\left(z_{n-1} + z_{n+1} - 2z_n\right). \tag{3.3.4b}$$

This in turn enables us to set $y_n = z_n$, thereby decoupling the real and imaginary parts of $\widetilde{\psi}_n$, and without loss of generality simply solve for y_n:

$$\dot{y}_n = \left(2\kappa^2 y_n^2 - \mathcal{H}_0\right)y_n + \rho\left(y_{n-1} + y_{n+1} - 2y_n\right), \tag{3.3.5}$$

on a grid defined by $n = 0, 1, \ldots, N$ with fictitious boundary terms $y_{-1} = y_{N+1} = 0$. From an initial configuration $y_n(0)$, and an initial value for $\mathcal{H}_0$, we integrate Equation (3.3.5) forward in time using the standard RK4 method; except, after a certain number of integration time-steps, each of length $\Delta\tau = 0.01$, we redefine $\mathcal{H}_0$ according to some algorithm. The algorithm is valid if the initial $y_n(0)$ is such that it drops off sharply away from some global maximum, as in a sech function for example, and if the stationary y_n also exhibits the same qualitative characteristic.

The algorithm is as follows. We first observe that when y_n has become some stationary y_n^0 and $\mathcal{H}_0$ has converged, their values must be such that

$$\mathcal{H}_0 y_n^0 = 2\kappa^2 {y_n^0}^3 + \rho\left(y_{n-1}^0 + y_{n+1}^0 - 2y_n^0\right), \tag{3.3.6}$$

for all n. Equation (3.2.3) would have led to a similar result for the eigenvalue H_0. Now, we take some initial guess for $\mathcal{H}_0$ and some initial $y_n(0)$ with a global maximum at

$n = n_0$, which is such a configuration that the value of $y_n(0)$ drops off significantly beyond $n = n_0 \pm 2$, and we integrate Equation (3.3.5) forward in time. If the initial guess for $\mathcal{H}_0$ is good enough, i.e. sufficiently close to the $\mathcal{H}_0$ that eventually satisfies Equation (3.3.6), then $y_n(\tau)$ will continue to exhibit the characteristic drop-off away from $n = n_0$. When we reach $\tau = 10^4\Delta\tau$ (an arbitrarily chosen time-interval which is moderate in length) we make use of $y_n(10^4\Delta\tau)$ to redefine $\mathcal{H}_0$ before performing further integration steps. Specifically, we use only three points in $y_n(10^4\Delta\tau)$, namely y_{n_0} and $y_{n_0\pm1}$, and let

$$\widetilde{\mathcal{H}}_{n_0} := 2\kappa^2 y_{n_0}^2 + \rho\left(\frac{y_{n_0-1} + y_{n_0+1}}{y_{n_0}} - 2\right), \tag{3.3.7}$$

and similarly $\widetilde{\mathcal{H}}_{n_0\pm1}$. The numerical stability of this scheme relies upon the values of y_{n_0} and $y_{n_0\pm1}$ being sufficiently far from zero. Assuming that is always the case, which is automatically verified if the scheme successfully produces stationary solutions, then for each n, $\widetilde{\mathcal{H}}_n$ is the value that $\mathcal{H}_0$ should take if y_n and $y_{n\pm1}$ were all taken from the stationary solution y_n^0. We then take the average of $\widetilde{\mathcal{H}}_{n_0}$ and $\widetilde{\mathcal{H}}_{n_0\pm1}$, defining

$$\widetilde{\mathcal{H}}_0' := \frac{1}{3}\left(\widetilde{\mathcal{H}}_{n_0-1} + \widetilde{\mathcal{H}}_{n_0} + \widetilde{\mathcal{H}}_{n_0+1}\right), \tag{3.3.8}$$

and redefine $\mathcal{H}_0$ according to

$$\mathcal{H}_0 \mapsto \frac{\mathcal{H}_0 + \widetilde{\mathcal{H}}_0'}{2}. \tag{3.3.9}$$

This process 'nudges' $\mathcal{H}_0$ closer to the value it needs to be; and we only make use of the values of y_n at its maximum and immediate neighbours because, assuming the sharp drop-off of y_n away from its maximum, those three points have the most significant impact on the dynamics of Equation (3.3.5). The new $\mathcal{H}_0$ obtained by Equation (3.3.9) is then fed back into Equation (3.3.5) before we continue to integrate the equation from $\tau = 10^4\Delta\tau$ to $\tau = 2\cdot10^4\Delta\tau$. When we reach $\tau = 2\cdot10^4\Delta\tau$, we re-run the process from Equation (3.3.7) to Equation (3.3.9), this time making use of $y_n(2\cdot10^4\Delta\tau)$, to obtain a new $\mathcal{H}_0$. We repeat this process once every 10^4 integration time-steps, obtaining a new $\mathcal{H}_0$ each time which is fed back into the system before the integration continues. If our initial guess for $\mathcal{H}_0$ is good enough, and if both the initial $y_n(0)$ and the eventual stationary y_n^0 are sufficiently localised, then in practice this algorithm converges concurrently in the y_n configuration and in the $\mathcal{H}_0$ value, within $\mathcal{O}(10^6)$ integration steps. Once convergence has occurred, one could make use of the fact that $\widetilde{\psi}_n = y_n + iz_n$ and $y_n = z_n$ to recover the stationary $\widetilde{\psi}_n$

solution to Equation (3.3.3), namely $\widetilde{\psi}_n^0 = \sqrt{2} y_n^0 \exp(i\pi/4)$. However, Equation (3.3.3) is not our real aim; we wish instead to express the stationary ϕ_n^0 solution to Equation (3.2.3) in terms of y_n^0. This is when the similarities between Equations (3.2.3) and (3.3.6) come to the fore. Indeed, by making the identification

$$\mathcal{H}_0 \equiv -\rho H_0, \tag{3.3.10}$$

we are able to observe that, if y_n^0 solves Equation (3.3.6), then

$$\phi_n^0 \equiv \sqrt{2} y_n^0 \tag{3.3.11}$$

solves Equation (3.2.3), and vice versa.

The question remains as to what we should take as our initial guess for $\mathcal{H}_0$ and initial configuration $y_n(0)$. The answer, naturally, is to make use of the continuum approximation from Section 3.2.3, specifically from Equation (3.2.17), and to invoke Equations (3.3.10) and (3.3.11). Thus, given a pair of parameter values (ρ, κ) and hence a value of λ, we take the initial value $\mathcal{H}_0 = \kappa^4/(16\rho)$ and initial configuration $y_n(0) = \sqrt{\lambda/16}\,\mathrm{sech}\,[\lambda(n - n_0)/4]$; and on a grid defined by $n = 0, 1, \ldots, 200$, we choose $n_0 = 100$.

To summarise: given parameters (ρ, κ), we wish to find the stationary solution to the eigenvalule problem of Equation (3.2.3). In order to do so, the conventional approach is to use an iterative scheme as per Equations (3.3.1) and (3.3.2); but we use a *relaxation method*, which we have described in detail in this Section, to find the stationary solution $\widetilde{\psi}_n^0$ to an alternative eigenvalue problem, as in Equation (3.3.3). $\widetilde{\psi}_n^0$ is expressed in terms of some y_n^0, and the eigenvalue is $\mathcal{H}_0$. From y_n^0 and $\mathcal{H}_0$ we are able to deduce the stationary solution ϕ_n^0 to Equation (3.2.3), together with eigenvalue H_0, using the identities (3.3.11) and (3.3.10). Crucially, if all we really wish to find is $|\psi_n^0|^2$, i.e. the electron probability distribution in the stationary polaron state, then combining $|\psi_n^0|^2 = |\phi_n^0|^2$, $|\widetilde{\psi}_n^0|^2 = 2|y_n^0|^2$ and Equation (3.3.11) leads us to conclude

$$\left|\psi_n^0\right|^2 = \left|\widetilde{\psi}_n^0\right|^2. \tag{3.3.12}$$

That is to say, the original problem of Equation (3.2.3) and the alternative problem of Equation (3.3.3) give us the same stationary electron distribution, even though the stationary wavefunctions differ by a constant phase and the eigenvalues differ by a constant multiple. In practice, given all the (ρ, κ) that we have studied, we find that the relaxation

method always converges, in CPU times that are 3 to 4 orders of magnitude less than the CPU times of using the conventional method to find a stationary polaron state. This significant improvement in speed is largely due to the fact that, whereas the conventional method performs a summation over the entire lattice after every iteration, our relaxation method performs a summation over 3 lattice points only, once every 10^4 iterations.

3.3.2 Stationary Electrons in the Deterministic System

For a range of (ρ, κ) values, we use the convergence algorithm described in Section 3.3.1 to find stationary polaron states under zero electric field, i.e. $\epsilon = 0$, and neglecting stochastic forces, i.e. $f_n = 0$, on a grid of size $N = 200$. From the $|\psi_n^0|^2$ and u_n^0 solutions we can infer all the important information about the stationary polaron state.

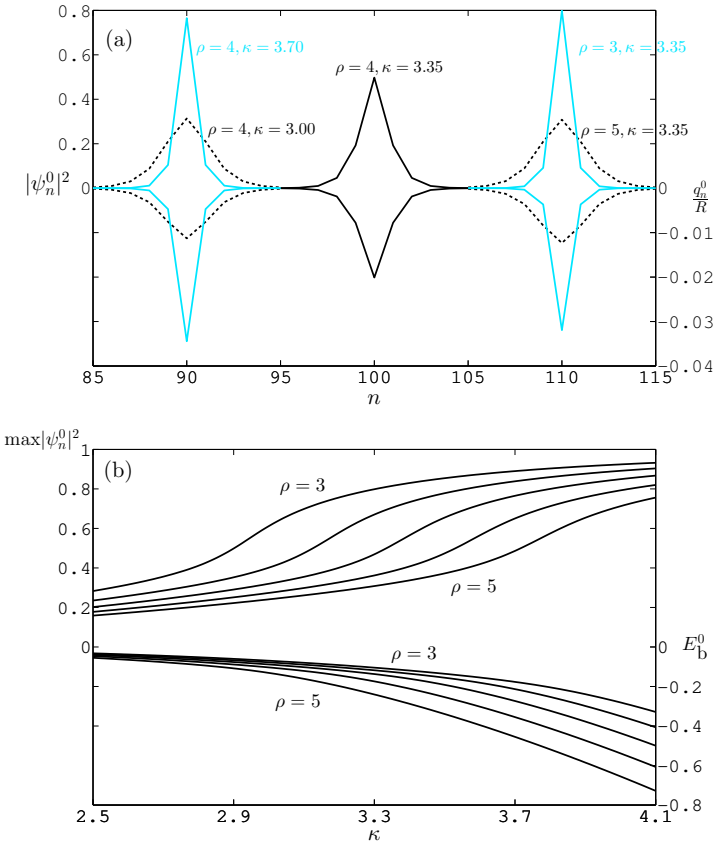

Figure 3.1: Stationary polaron solutions. (a) Some electron probability distributions (left axis), and corresponding lattice displacements in units of equilibrium spacing (right axis), computed using various combinations of parameters ρ and κ. (b) Dependence on ρ and κ of two key characteristics of stationary polaron states: the maximum localisation probability (left axis), and the binding energy (eV) (right axis). Both are expressed as families of functions of κ, parametrised by $\rho = 3.0, 3.5, 4.0, 4.5, 5.0$.

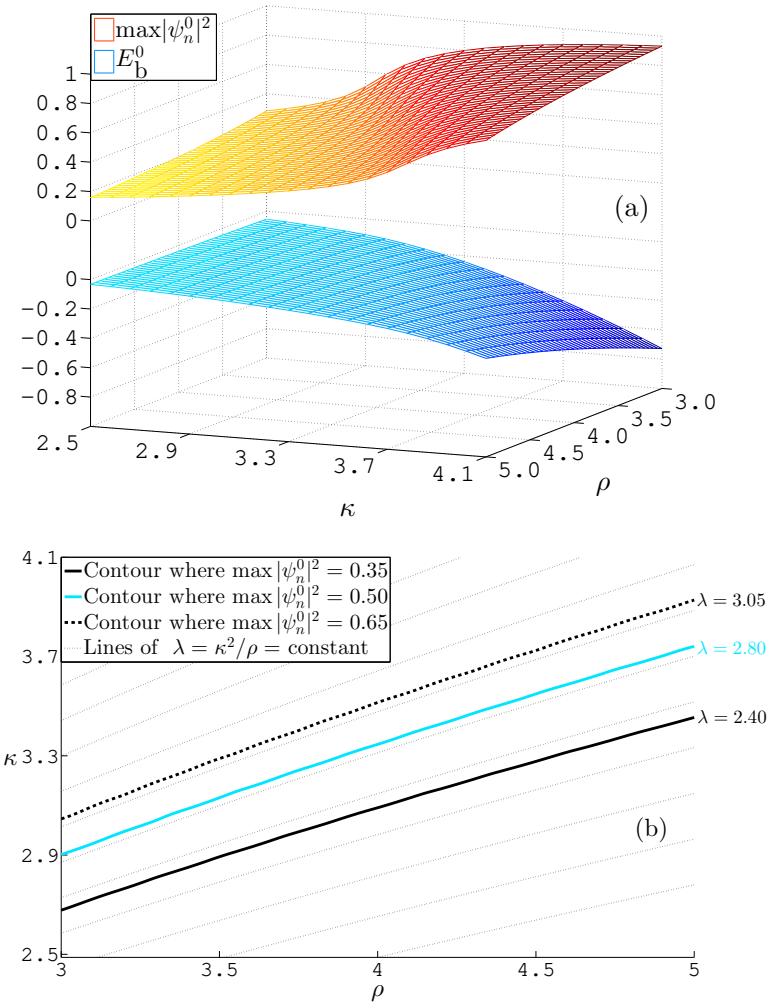

Figure 3.2: Dependence of electron's maximum localisation probability and the polaron binding energy on parameter space (ρ, κ). (a) Maximum localisation probability (positive vertical axis) and binding energy (eV) (negative vertical axis) as surfaces over the (ρ, κ) plane. (b) Some contour lines in the surface of maximum localisation probability, projected onto the (ρ, κ) plane. Lines of $\kappa^2/\rho =$ constant are included for comparison.

In Figure 3.1(a) we see some $|\psi_n^0|^2$ solution profiles, the height of which increases with κ and decreases with ρ. This is as we expected, since the stationary solutions are fully characterised by $\lambda = \kappa^2/\rho$. It also shows the lattice displacement at the n^{th} site being proportional to $|\psi_n^0|^2$, as it should be.

Figure 3.1(b) serves to illustrate how the stationary polaron state varies with κ if ρ is fixed, or varies with ρ if κ is fixed. For fixed ρ, the electron's maximum localisation probability, $\max|\psi_n^0|^2$, increases with κ, whilst the polaron binding energy E_b^0 decreases with κ. The negative sign of E_b^0 indicates that energy needs to be put into the system in

order to break up the polaron; thus, a decrease in E_{b}^0 is an indication that the electron is more strongly bound to the lattice. Since a larger κ indicates a stronger electron-lattice interaction, we do expect it to result in a more strongly bound polaron. Meanwhile, for fixed κ, $\max|\psi_n^0|^2$ and E_{b}^0 both decrease with ρ. An extension of Figure 3.1(b) is Figure 3.2(a), where we see $\max|\psi_n^0|^2$ and E_{b}^0 as surfaces over the parameter space (ρ, κ). By drawing contour lines of the $\max|\psi_n^0|^2$ surface, we obtain Figure 3.2(b). Indeed, these contour lines are the parabolae $\kappa^2/\rho =$ constant, i.e. lines of constant λ. This means that the shape of a $|\psi_n^0|^2$ profile depends solely on λ, as we predicted.

3.3.3 Quasi-Stationary Electrons in the Stochastic System

We thermalise the stationary polaron by time-evolving the system in the presence of stochastic forces $f_n(\tau)$, which take values according to Equation (3.1.42) with $\theta = 0.13$ (physiological temperature of 310 K). Regardless of the values of (ρ, κ), the polaron always settles in a *quasi-stationary state*, where its internal energy, after a very small initial increase, oscillates about a steady value, and the electron probability distribution fluctuates around a steady configuration. This is a state of thermal equilibrium. The quasi-stationary mean value of internal energy at thermal equilibrium is always higher than the stationary polaron binding energy, but the relative difference is typically only $\mathcal{O}(10^{-4})$, as Figure 3.3 illustrates. The change in $|\psi_n|^2$ caused by the thermalisation process is also small, with $\max|\psi_n|^2$ never deviating by more than 0.01 times $\max|\psi_n^0|^2$. These results show that our polarons are stable against thermal fluctuations acting on the lattice at physiological temperature.

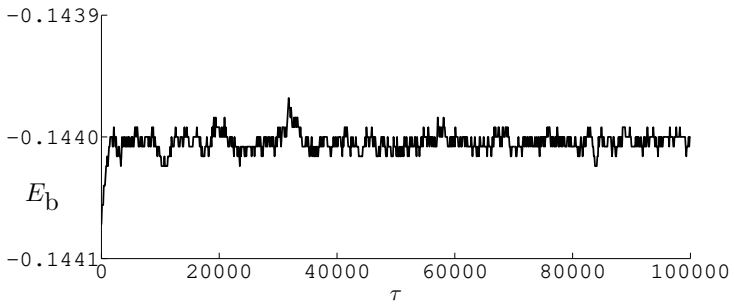

Figure 3.3: Under stochastic forces at thermal energy $\theta = 0.13$, the polaron's internal energy (eV) fluctuates around a quasi-stationary mean, after a rapid initial increase. 10000 units of τ equals 32 ps. Parameter: $\lambda = 2.80$.

3.4 Numerical Results on Electron Propagation

With either stationary or quasi-stationary polarons as initial condition, we impose external EMFs represented by the $\epsilon(\tau)$ term in Equation (3.1.32a), and integrate our system forward in time using the standard RK4 method. The time-step remains $\Delta\tau = 0.01$. In the ϵ term we set n_0 to be the lattice site where the stationary $|\psi_n^0|^2$ or quasi-stationary $|\psi_n|^2$ attains its maximum. At any time τ, suppose $|\psi_n(\tau)|^2$ attains its maximum at lattice site n_0, then we define the polaron's position to be the vertex location of the parabola extrapolated from three points: $(n_0, |\psi_{n_0}|^2), (n_0 - 1, |\psi_{n_0-1}|^2), (n_0 + 1, |\psi_{n_0+1}|^2)$.

We begin our investigation by neglecting $f_n(\tau)$, and looking for suitable $\epsilon(\tau)$ which can facilitate polaron propagation. We present our results in Sections 3.4.1 to 3.4.3. In particular, we outline in Section 3.4.1 negative results that we obtain using certain types of EMFs. Then we describe in Sections 3.4.2 and 3.4.3 positive results from using pulse-like EMFs, which can cause stable polaron propagation with large polaron displacements. Finally in Section 3.4.4, we investigate the effects of stochastic forces by turning on $f_n(\tau)$.

When we alter ρ and κ, we keep $\lambda = \kappa^2/\rho = 2.80$ fixed. This is because as we saw in Section 3.3, the electron probability distributions of (quasi-)stationary polarons are parametrised only by λ. We would like to study the motion of polarons with a moderate maximum localisation probability, and indeed for $\lambda = 2.80$ we have $\max|\psi_n^0|^2 = 0.5$ in the stationary state, as well as $\max|\psi_n|^2 \approx 0.5 \pm 0.005$ in the quasi-stationary state. We discover that, in addition to λ, the parameter κ (or equivalently ρ) is also important to the dynamics of a non-stationary polaron, in that $(\lambda = 2.80, \kappa = 3.35)$ and $(\lambda = 2.80, \kappa = 3.00)$ produce very different results.

3.4.1 Effects of Constant or Temporally Sinusoidal EMFs

Several natural choices of $\epsilon(\tau)$ produce negative results in terms of polaron propagation. A temporally sinusoidal EMF, for instance, causes the polaron simply to oscillate, regardless of the EMF's amplitude and period. Alternatively, using constant ϵ, we find that for every initial condition there exists a threshold amplitude ϵ_c such that no polaron displacement occurs if $\epsilon < \epsilon_c$, and if $\epsilon \geq \epsilon_c$ then the electron delocalises within several hundred units of τ, or roughly 1 ps in physical units. *Delocalisation* is the phenomenon where the electron 'escapes' the local potential well, thus destroying the polaron as its two constituent parts become decoupled. This can occur when excessive energy is imparted to the electron.

Although a theoretical delocalised state is represented by a probability density with $|\psi_n|^2 \sim \mathcal{O}(1/N)$, for practical purposes we consider delocalisation to have occurred whenever the weaker condition of $\max|\psi_n|^2 < 0.1$ is satisfied, at which point secondary peaks in $|\psi_n|^2$ have the same order of magnitude as $\max|\psi_n|^2$, and this is always accompanied by a significant decay in the polaron's internal energy. Our understanding is that the constant EMF is prone to destroying the polaron because it raises the electron energy in a sudden and continual manner. Attempting to counter these issues, we have used a period of linear increase in $\epsilon(\tau)$ which brings it slowly to a constant value over $\mathcal{O}(10^6)$ units of τ, and we have also tried adding a sinusoidal component to a small constant ϵ to bring the amplitude above its threshold periodically. However, the results remain that soon after ϵ reaches the threshold value, the electron delocalises. This calls for a pulse-like EMF, which peaks at a certain amplitude before resetting to zero, in theory allowing the polaron to regain stability once the peak has passed.

3.4.2 Displacement Under a Pulse-Like EMF

We consider a pulse-like EMF of the form

$$\epsilon(\tau) = \begin{cases} A\sin^2(\pi\tau/\Delta T), & \text{if} \quad 0 < \tau < \Delta T, \\ 0, & \qquad\quad \tau \geq \Delta T, \end{cases} \tag{3.4.1}$$

where ΔT is the time-span of the pulse and A is the amplitude. For every ΔT we find that there is some critical pulse amplitude A_c with the following property.

If $A < A_\mathrm{c}$, the pulse causes the polaron to move away and then back to the vicinity of its initial position, before settling in a quasi-stationary state of small oscillations about the initial position. The energy of the polaron is raised slightly by the pulse. If $A \geq A_\mathrm{c}$, the polaron moves away during the pulse but does not return, and instead settles in an oscillatory quasi-stationary state some lattice sites away from its starting position. Some examples of trajectories caused by $A \geq A_\mathrm{c}$ are shown in Figure 3.4(a). We see that A_c is negatively correlated with ΔT, which is to be expected as a longer pulse need not have as high an amplitude as a shorter one in order to impart the same amount of energy to the electron. When the polaron is displaced, its mean internal energy in the new quasi-stationary state is significantly higher than its stationary binding energy in the initial state, as Figure 3.4(b) illustrates. This means that the electron has gained a large amount of energy from the pulse.

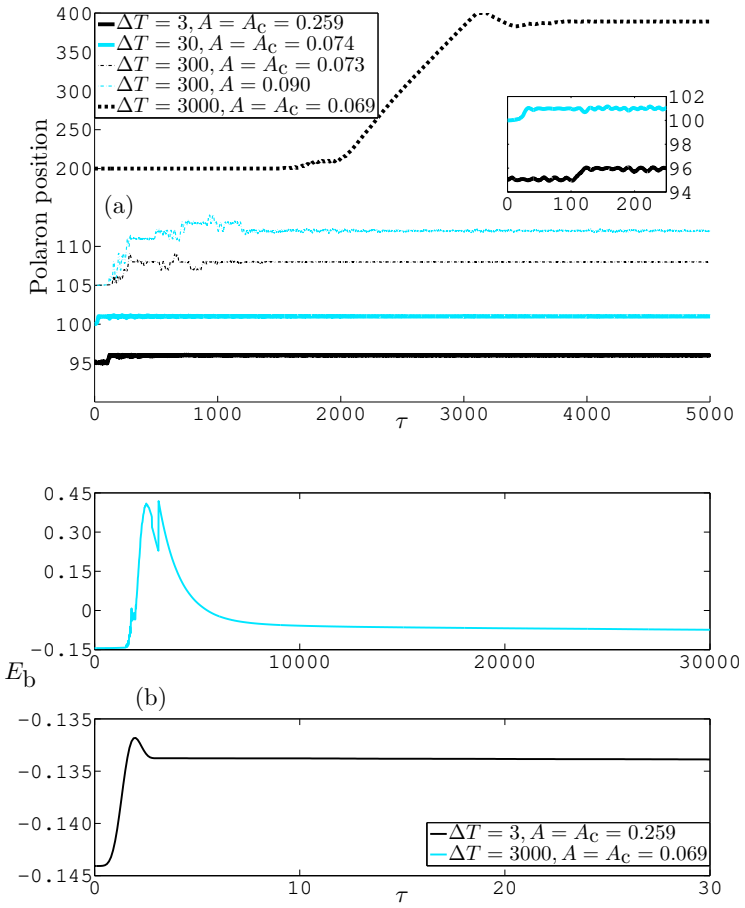

Figure 3.4: Polaron motion under the pulse-like EMF with time-span ΔT and amplitude A. 1000 units of τ equals 3.2 ps. Parameters: $\lambda = 2.80$, $\kappa = 3.35$. (a) Some polaron trajectories. (b) Evolution of polaron internal energy (eV).

Figure 3.5 captures the way in which polaron displacement, D, varies as we increase A beyond the critical value. We see that the relationship between D and $A > A_c$ is fairly erratic, with no clear indication of positive correlation. However we can discern that the longer ΔT is, the larger D becomes. This is because the system is subject to the extra energy from the pulse for longer. We note two more features of the polaron dynamics. Firstly, some combinations of ΔT and A cause displacement of the polaron in the direction of higher electric potential, i.e. smaller n. This occurs when, for instance, $\Delta T = 30$ and $A = 0.080$ or 0.087, even though for $0.080 < A < 0.087$ (at our resolution of $\Delta A = 0.001$) the polaron displacement is non-negative. This anomaly could be a type of resonance effect which warrants further investigation. Secondly, some values of A cause the electron to delocalise before the end of the pulse, due to excessive energy input. For example, when

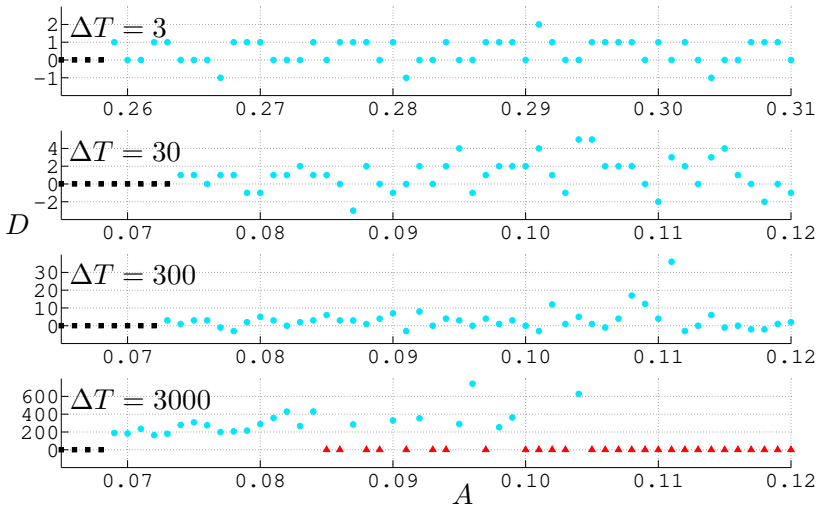

Figure 3.5: Polaron displacement, D, as function of time-span ΔT and amplitude A, under the single pulse. Squares (black) indicate zero displacement due to A being too small. Triangles (red) indicate zero displacement due to delocalisation before end of pulse. Parameters: $\lambda = 2.80$, $\kappa = 3.35$.

$\Delta T = 3000$, if $A \geq 0.105$ then delocalisation always occurs before $\tau = 3000$, and some smaller values of A such as 0.085 produce the same effect.

3.4.3 Propagation Under Time-Periodic Pulse-Like EMFs

If we simply repeat the propagation-inducing single pulse over time, so that $\epsilon(\tau)$ is periodic and takes the form $\epsilon(\tau) = A \sin^2(\pi\tau/\Delta T)$ for $\tau > 0$, we obtain polaron motion which is unsustainable, in the sense that delocalisation occurs within two or three periods. Whereas for the single pulse the polaron is permanent, i.e. it remains quasi-stationary once the EMF is reset to zero (as long as delocalisation has not occurred during the pulse), under the repeated pulses the polaron is transient, as it has a finite lifetime τ_0 at which the electron delocalises. We understand the cause of the polaron's short lifetime to be as follows. We saw in Section 3.4.2 that as a pulse hits the polaron, it raises the polaron's internal energy, making the electron less bound to the lattice. Repeated applications of the same pulse therefore eventually decouples the electron from the lattice. Crucially, the time it takes the polaron's internal energy to re-settle at a quasi-stationary value can be significantly longer than the time-span of the pulse [cf. Figure 3.4(b)]. This means that right at the end of the first pulse the internal energy is much higher than it would be in a quasi-stationary state, and hitting the system with a second pulse straight away would raise the energy

even higher. Thus, to prolong the polaron lifetime, we set $\epsilon(\tau)$ to zero after each pulse for an amount of time equal to some $S\Delta T$, which we call the *relaxation period*, allowing the system the necessary time to settle in a new quasi-stationary state before another pulse hits. We write this periodic forcing as

$$\epsilon(\tau) = \begin{cases} A\sin^2(\pi\tau/\Delta T), & \text{if} \quad 0 < \tau - c\left[(1+S)\,\Delta T\right] < \Delta T, \\ 0, & \qquad\quad \tau - c\left[(1+S)\,\Delta T\right] \geq \Delta T, \end{cases} \tag{3.4.2}$$

where c is the largest integer such that $\tau - c\left[(1+S)\,\Delta T\right] \geq 0$. For example, suppose $S = 10$. Then, for $0 < \tau < 11\Delta T$, we have $c = 0$, and therefore $\epsilon(\tau)$ is non-zero if and only if $0 < \tau < \Delta T$; for $11\Delta T \leq \tau < 22\Delta T$, we have $c = 1$, and therefore $\epsilon(\tau)$ is non-zero if and only if $11\Delta T < \tau < 12\Delta T$; and so on. We find that, for $\Delta T = 3000$, regardless of S, delocalisation always occurs before the end of the second pulse. For this reason, we restrict ourselves to $\Delta T = 3, 30$ and 300, for which $S = 10$ gives a long enough relaxation period for our purposes.

Figure 3.6(a) contains examples of polaron trajectories under the periodic pulses with relaxation, and Figure 3.6(b) shows the corresponding evolutions of the polaron's internal energy. We see that by adding a relaxation period after each pulse we allow time for the polaron to settle into a quasi-stationary state, hence the periodic lowering of internal energy. As the polaron stabilises, its movement stalls, hence the ladder-like trajectories featuring jumps of tens of lattice sites followed by plateaus. Compared to the single pulse of Section 3.4.2, periodic pulses with relaxation cause much larger polaron displacements. Moreover, we saw in Section 3.4.2 that a pulse always raises the polaron energy (even if it does not cause a displacement), making the polaron more susceptible to moving under further pulses, which is why the critical pulse amplitude A_c for periodic pulses is lower than the A_c we saw for the single pulse. It is also why, as we see in Figure 3.6(a), at $A = A_\mathrm{c}$ the polaron does not begin to move until several pulses have hit.

Figure 3.7 is a visualisation of the way in which a polaron moves during a pulse and settles afterwards. The polaron's size, represented by the breadth of the electron probability distribution, oscillates during the pulse, and after each pulse the probability distribution always becomes broader than it was before.

Examining Figure 3.8, we recognise a clear negative correlation between the polaron's displacement D and the pulse amplitude $A > A_\mathrm{c}$, as opposed to the erratic relationship between D and $A > A_\mathrm{c}$ in the case of a single pulse [cf. Figure 3.5]. The negative correlation can be explained as follows.

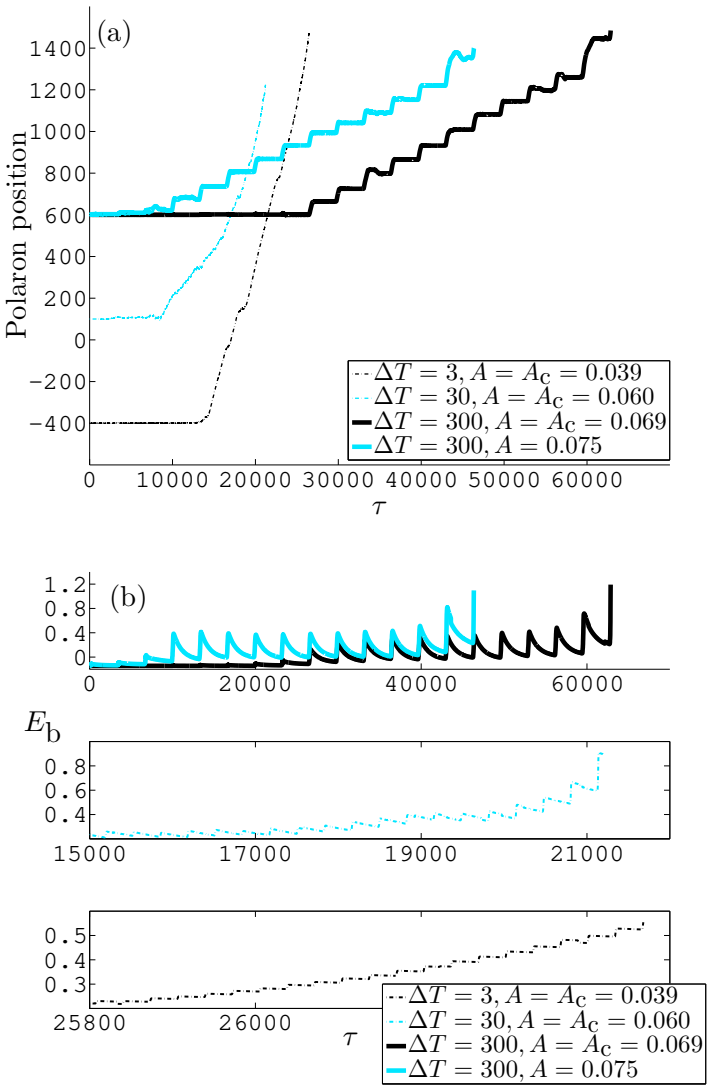

Figure 3.6: Polaron motion under periodic pulses with time-span ΔT and amplitude A, and relaxation period $10\Delta T$. 10000 units of τ equals 32 ps. Parameters: $\lambda = 2.80$, $\kappa = 3.35$. (a) Some polaron trajectories. (b) Evolution of polaron internal energy (eV).

The polaron's lifetime is negatively correlated with A, as a stronger pulse raises the polaron energy by a larger amount and its repeated application causes delocalisation more quickly. Meanwhile, the polaron's displacement per pulse, V, tends to increase with A, as we see in the rightmost column of subfigures in Figure 3.8, but this increase is small compared to the decay in polaron lifetime. As a result, total displacement over the polaron's lifetime is a decreasing function of A, for $A > A_c$. This has the implication that A_c is not only the critical amplitude, but also the *optimal amplitude*, and it induces the largest amount of polaron displacement. We note in addition that under the periodic

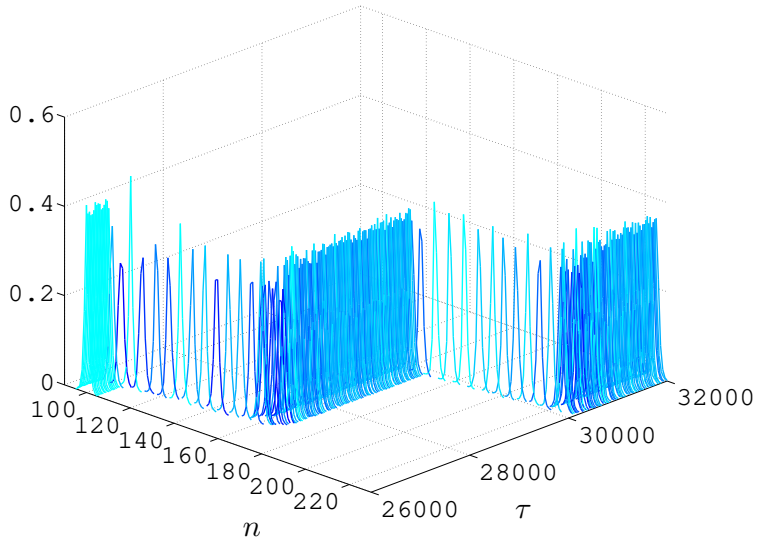

Figure 3.7: Evolution of the electron probability distribution, $|\psi_n|^2$, under periodic pulses with time-span $\Delta T = 300$, amplitude $A = A_c = 0.069$. 1000 units of τ equals 3.2 ps. Parameters: $\lambda = 2.80, \kappa = 3.35$. Each curve is a $|\psi_n|^2$ profile at some time τ. The broader the distribution, the darker the colour of the curve.

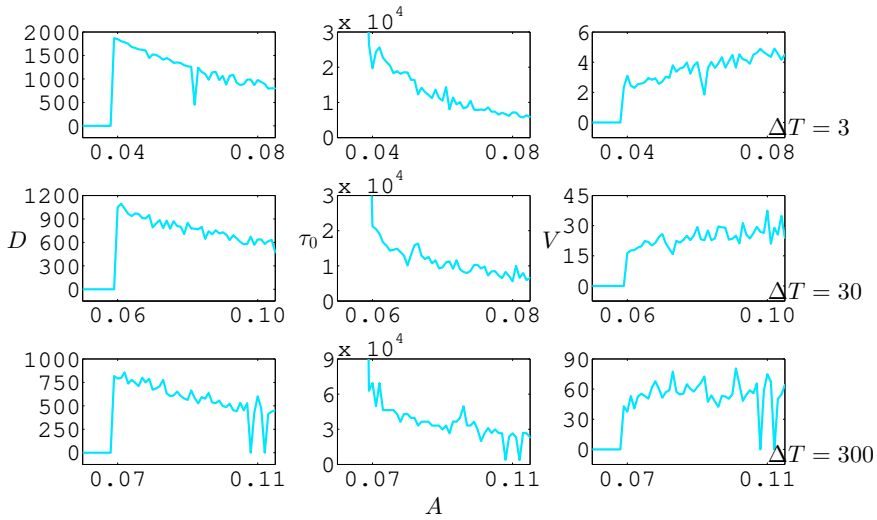

Figure 3.8: Polaron displacement, D, lifetime, τ_0, and displacement per pulse, V, as functions of time-span ΔT and amplitude A of time-periodic pulses. 1000 units of τ equals 3.2 ps.

forcing the polaron propagation is *directed*, meaning all combinations of ΔT and A cause displacements in the same direction, which was not the case under single-pulse forcing.

Our results show that using different combinations of ρ and κ, keeping $\lambda = \kappa^2/\rho$ fixed, produces figures which are characteristically similar to Figure 3.8, showing polaron

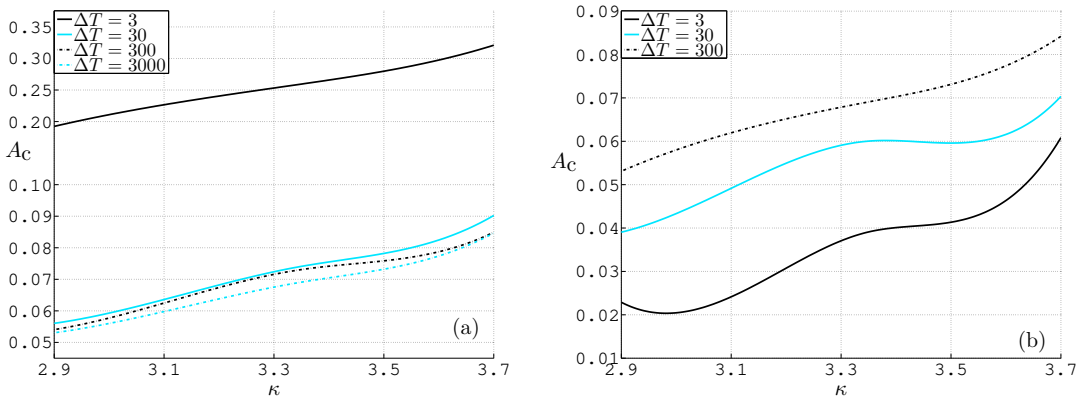

Figure 3.9: Critial amplitude A_c as a function of κ, parametrised by the time-span ΔT of single or periodic pulses. Parameter: $\lambda = 2.80$. (a) Single-pulse forcing by eq. (3.4.1). (b) Periodic forcing by eq. (3.4.2).

displacement and lifetime as decreasing functions of A for $A > A_c$. However the value of A_c is dependent on more than just λ. Figure 3.9 exhibits the dependence of A_c on the electron-lattice coupling constant κ, with $\lambda = 2.80$ fixed. It shows that the more strongly coupled our system is, the more difficult it becomes to displace a polaron using pulse-like EMFs, in the sense that a larger amplitude is required to cause the onset of polaron propagation. Comparing Figure 3.9(a) and Figure 3.9(b), we see that periodic pulses (with relaxation) require a much lower pulse amplitude to achieve polaron displacement than single-pulse forcing, particularly when ΔT is small. Indeed, when $\Delta T = 3$, A_c for the periodic forcing is an order of magnitude smaller than that for the single pulse.

3.4.4 Effects of Stochastic Forces

We study the effect of stochastic forces by first evolving the system of eq. (3.1.32) under a non-zero $f_n(\tau)$ and $\epsilon(\tau) = 0$ until it reaches thermal equilibrium, and then turning on $\epsilon(\tau)$ as per Section 3.4. The stochastic term exists due to thermal energy $\theta = 0.13$ which corresponds to physiological temperature (310K). For each set of parameter values $(\lambda, \kappa, \Delta T, A)$, we have run 100 numerical simulations and taken the mean values of key scalar quantities associated with the polaron motion, namely its displacement and, in the case of periodic pulse-like EMFs, lifetime and displacement per pulse. Figure 3.10 illustrates the way in which the polaron displacement D depends on the amplitude A of the single-pulse EMF, under stochastic thermal fluctuations, and it may be compared directly to Figure 3.5, for which $f_n = 0$.

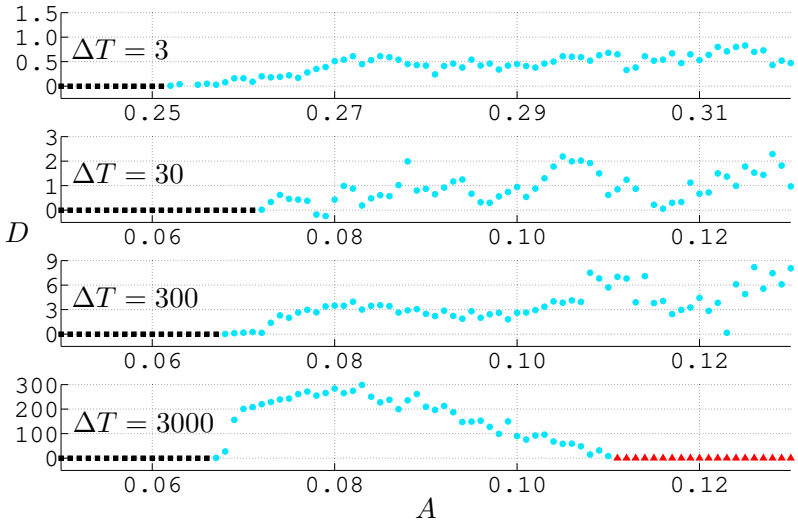

Figure 3.10: Mean displacement D as function of time-span ΔT and amplitude A of a single pulse, under stochastic forces. Squares (black) indicate zero displacement due to A being too small. Triangles (red) indicate zero displacement due to delocalisation before end of pulse. Parameters: $\lambda = 2.80$, $\kappa = 3.35$, $\theta = 0.13$.

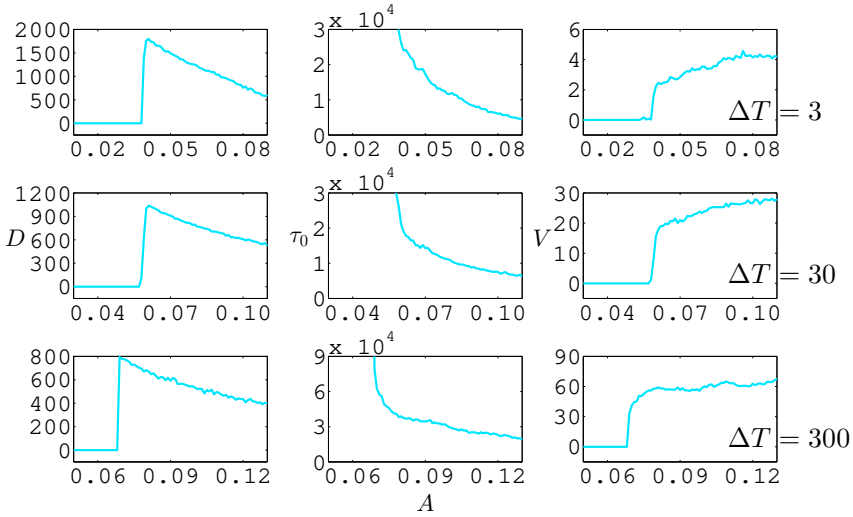

Figure 3.11: Mean values of displacement, D, lifetime, τ_0, and displacement per pulse, V, as functions of ΔT and A, under periodic pulses. 1000 units of τ equals 3.2 ps. Parameters: $\lambda = 2.80$, $\kappa = 3.35$, $S = 10$, $\theta = 0.13$.

One of the notable effects of the stochastic forces is making the polaron motion more directed, as Figure 3.10 shows: few combinations of ΔT and A cause negative displacements. Figure 3.11 shows results of adding stochastic forces to periodic pulse-like EMFs with relaxation, and we can compare it with Figure 3.8 for which $f_n = 0$. The phenomenon that polaron displacement per pulse is an increasing function of A is more clearly seen when

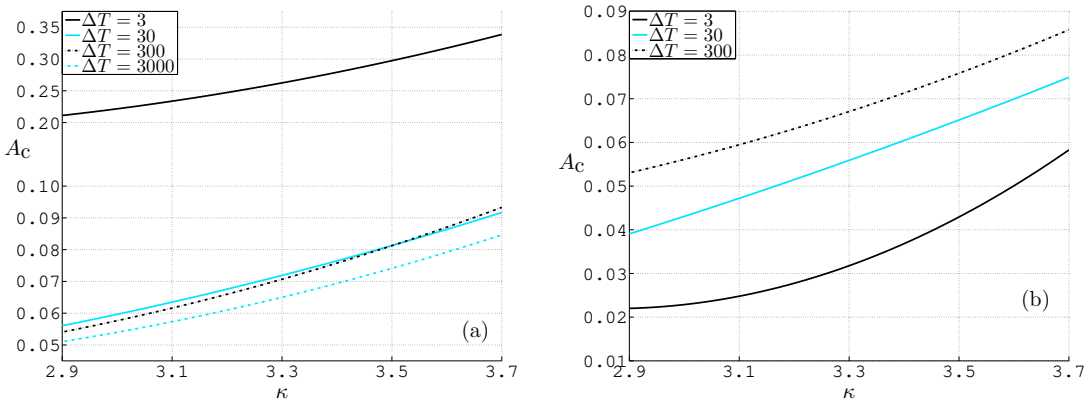

Figure 3.12: Critical amplitude A_c as a function of κ, parametrised by the timespan ΔT of single or periodic pulses. Parameters: $\lambda = 2.80, \theta = 0.13$. (a) Single-pulse forcing by eq. (3.4.1). (b) Periodic forcing by eq. (3.4.2).

stochastic forces are in play. The correlation between total displacement and $A > A_c$, and between polaron lifetime and $A > A_c$, both of which are negative correlations, are also clearer under stochastic forces. Due to these negative correlations, the critical pulse amplitude A_c serves also as optimal amplitude, being the pulse strength that induces the largest amount of polaron displacement. Polaron propagation is strongly directed, in that the mean value over 100 numerical simulations of total displacement is several hundred lattice sites in the positive direction. We also note the stabilising effect of the stochastic forces, which is evidenced by the smoothness of the displacement function D of A, as opposed to the jagged D-versus-A curves under $f_n = 0$ [cf. Figure 3.8], which exhibited significant dips at some values of A. Crucially, the polaron's lifetime is not at all reduced in the thermal environment compared to its lifetime under zero f_n. Figure 3.12 also reveals that the stochastic forces have little bearing on the way in which A_c increases with the electron-lattice coupling constant, κ. Finally, we note that A_c increases with ΔT under periodic pulse-like EMFs, whilst the correlation is negative under single-pulse EMFs.

3.5 Summary and Biophysical Interpretations

We have put forward a model for the interaction between an electron and intrapeptide amide-I oscillators in an α-channel. We have shown that the interaction can result in stationary polarons whose electronic probability distribution and binding energy depend on an effective coupling parameter $\lambda = \kappa^2/\rho$, where ρ and κ represent respectively the adiabaticity and coupling strength in the system. In particular, the maximum value of the

electron probability distribution in the stationary state is proportional to λ, and a more localised distribution represents a state with lower energy. To induce the propagation of a polaron with a moderate size from its stationary state, we have used an external excitation in the form of a squared-sinusoidal electric pulse, after constant and permanently sinusoidal electric fields produced negative results. The time-span of a pulse ranged between 3 and 3000 units, which correspond respectively to 0.01 ps and 10 ps, ensuring that the dynamical evolution of our polaron under a single pulse takes place within the picosecond timescale reported in [EH02] as the lifetime of amide-I excitations. We have discovered that for every pulse time-span ΔT there exists a pulse amplitude $A = A_{\mathrm{c}}$ which is critical, in the sense that an excitation displaces the polaron if and only if $A \geq A_{\mathrm{c}}$. When displacement occurs, the polaron typically moves along the polypeptide by a distance which is positively correlated with ΔT, before settling in a quasi-stationary state, with its energy raised compared to its pre-excitation level. By repeating the electric pulse periodically in time, with a sufficiently long relaxation period between pulses to allow the polaron to settle, we have found that the polaron can remain intact for up to tens of pulses, as each pulse causes a displacement in the same direction along the α-channel. For sufficiently small ΔT, there can be many pulses within the characteristic amide-I lifetime, causing a total displacement by hundreds of peptide units. For $A > A_{\mathrm{c}}$, the total displacement and polaron lifetime are both decreasing functions of A, even though the displacement per pulse increases with A. Moreover, while fixing λ we have varied the coupling constant κ in order to investigate its effect on the polaron dynamics, and we have found that A_{c} is positively correlated with κ. Our results also show that polaron propagation induced by pulse-like EMFs can occur at physiological temperatures. Indeed, thermally-induced stochastic forces on the peptide units have a stabilising effect on the system, and it promotes directed transport towards one end of the α-channel over the other.

We have thermalised the system classically using Langevin terms for the lattice field. Förner [För93] showed that when using a quantum thermalisation of the Davydov system, the thermal stability of a Davydov soliton is smaller than what is predicted by a classical thermalisation. While it would be interesting to do a full quantum thermalisation for our model, we believe it would make very little difference as in our case the transfer integral J_1 is three orders of magnitude larger than in the Davydov model, and approximately 30 times larger than the physiological thermal energy at 310 Kelvin.

The electric field amplitudes involved in our model range from 0.5 to 20 mv $\cdot$ Å^{-1}. In the biological cell, if a pair of opposite charges spontaneously localised on opposite sides of the plasma membrane, the resulting dipole would create an electric field in the centre of the membrane with strength $\sim 1/(\epsilon_{\mathrm{r}} d^2)$, where ϵ_{r} and d are respectively the relative permittivity and width of the membrane [LLZA13]. Indeed, if $\epsilon_{\mathrm{r}} = 5$ [WS03] and $d = 80$Å [MK80, HEWM83], then this electric field has strength 3.6 mv $\cdot$ Å^{-1}, which is within the range of values we have used in our model. Moreover, there have been reported observations in biological complexes of hundred-femtosecond charge separation [GBM$^+$88, ZZ01], the timescale of which matches the characteristic time-span of the pulse-like EMFs that we have considered. It is therefore conceivable that the pulse-like EMFs in our model could naturally occur and induce directed electron transport along α-channels across the cell membrane.

Chapter 4

The Electron-Phonon System in a Linear α-Channel

This Chapter is adapted from [LP17].

We present a generalisation of the Davydov-Scott model [cf. Section 2.2.2] for polarons in a linear α-channel, resulting from the interaction between an extraneous electron and collective phonon oscillations of hydrogen bonds in the channel. The generalisation manifests itself as a *symmetry parameter*, which reduces the model to Davydov's or Scott's when taking specific values. We explain in Section 4.1 that the introduction of the symmetry parameter is necessary in order to account for a physical property of polarons in polypeptides which has not previously been considered.

In Section 4.2, we write down the Hamiltonian for our model, and derive a set of dynamical equations which govern the dynamics of the electron and phonon parts of the polaron, justifying our choices of parameter values which are appropriate for an α-channel. Then in Section 4.3, we look at stationary polaron solutions to our equations, neglecting stochastic forces, and deduce properties of stationary polarons such as the binding energy. We obtain the stationary solutions using both analytical and numerical methods. By the former approach, a closed-form expression for the solution is found via the continuum limit. Indeed, in the continuum limit we show that the equations become a generalised nonlinear Schrödinger equation, and we describe the solution method in detail. Numerically, we employ an iterative method to solve the equations on a discrete grid, using the continuum solutions as ansatzes. We make comparisons between the numerical solutions and the analytical continuum solutions.

Section 4.4 concerns propagating polarons. We discover that it is possible to use an external electromagnetic field (EMF) to displace the stationary polaron, and to sustain

its motion in such a way that its trajectory is directed and its energy remains highly stable. We find that a constant EMF is sufficient for displacing the polaron but is incapable of sustaining energetically stable motion, whereas an EMF consisting of a constant component and a temporally sinusoidal one can facilitate propagation which is more stable. We investigate how the polaron motion depends upon our forcing parameters. We also take thermal fluctuations of the system into account, examining the effect of stochastic forces which arise from non-zero temperatures. We find that thermal fluctuations at low temperatures enhance polaron propagation in the sense that we can lower the amplitude of our EMF and still achieve stable, directed polaron trajectories. We use only numerical methods to obtain our results in Section 4.4. We conclude this Chapter in Section 4.5 by discussing the physical realisabililty of our external forcing and biological implications of our results.

4.1 Motivation for Generalising the Davydov-Scott Model

As we have discussed in Section 2.2.2, the original Davydov soliton on a polypeptide lattice comprised three components: an intrapeptide vibrational exciton, the lattice phonon, and their interaction. In his model, Davydov assumed that the exciton site energy depended upon lattice deformations in the immediate vicinity. For a one-dimensional, hydrogen-bonded polypeptide, modelled as a lattice, let us denote the displacement of the n^{th} site by U_n, and define

$$S_n := U_{n+1} - U_n. \tag{4.1.1}$$

This is the amount by which the length of the hydrogen bond between sites n and $n+1$ deviates from equilibrium. By Davydov's assumption, the exciton site energy is modified by the coupling to the lattice:

$$J_0 \mapsto J_0 + \chi G_n(S_n, S_{n-1}), \tag{4.1.2}$$

where J_0 and χ are constants, G_n is a bilinear function, and

$$|\chi G_n / J_0| \ll 1. \tag{4.1.3}$$

Specifically, Davydov assumed that

$$G_n = (S_n + S_{n-1})/2. \tag{4.1.4}$$

That is to say that the exciton is equally coupled to lattice sites on either side. Scott's modification, which we have also detailed in Section 2.2.2, was instead to take

$$G_n = S_n, \tag{4.1.5}$$

signifying a coupling exclusively to one side. Scott's reasoning was that the intrapeptide oscillator is always located adjacent to one hydrogen bond and far from the other. Thus, Davydov's and Scott's models were, respectively, spatially symmetric and anti-symmetric.

We are interested in modelling the electron, whose position relative to the centre of mass of a peptide unit is not fixed, and for this reason we cannot assume its coupling to the lattice is either symmetric or anti-symmetric. Ideally, the partition of interaction energy between S_n and S_{n-1} should be determined dynamically, dependent upon the electron wavefunction. For simplicity, we consider a parameter whose value is fixed, which represents the extent to which the electron-phonon interaction is spatially symmetric. This parameter allows us to extrapolate between the two extreme symmetries of Davydov and Scott, casting their models as special cases of a more general picture.

4.2 A Generalised Davydov-Scott Model

In the context of electron-phonon coupling, it is justified to make the semi-classical approximation in which the peptide units are modelled as classical particles [BEPZ08, Hen01]. This approach is reflected in the Hamiltonian that we present in Section 4.2.1. We derive our dynamical equations in Section 4.2.2, and assign parameter values appropriate for a linear α-channel in Section 4.2.3. In Section 4.2.4, we find an expression for the energy of a polaron that forms within our system.

4.2.1 The Hamiltonian

To model the system of an extra electron interacting with hydrogen bond phonons in an α-channel, we use a Hamiltonian in the following Fröhlich-Brizhik form:

$$\widehat{H} = \widehat{H}_{\mathrm{e}} + \widehat{H}_{\mathrm{p}} + \widehat{H}_{\mathrm{int}} + \widehat{H}_{\mathrm{ext}}, \tag{4.2.1}$$

where $\widehat{H}_{\mathrm{e}}$ describes a tight-binding electron, $\widehat{H}_{\mathrm{p}}$ describes phonon oscillations, $\widehat{H}_{\mathrm{int}}$ accounts for the electron-phonon interaction, and $\widehat{H}_{\mathrm{ext}}$ represents the effect of an external

EMF [BCHE98]. We assume that the α-channel is linear, and consists of $N+1$ identical units linked by N identical hydrogen bonds. In the tight-binding approximation [cf. Section 2.1.2], we have

$$\widehat{H}_{\mathrm{e}} = \sum_{n=0}^{N} J_0 \widehat{A}_n^{\dagger} \widehat{A}_n - \sum_{n=0}^{N-1} J_1 \left(\widehat{A}_{n+1}^{\dagger} \widehat{A}_n + \widehat{A}_n^{\dagger} \widehat{A}_{n+1} \right). \tag{4.2.2}$$

The subscript n in Equation (4.2.2) labels peptide units, which are our lattice sites. $\widehat{A}_n^{\dagger}$ and $\widehat{A}_n$ are local electron creation and annihilation operators, respectively. J_0 and J_1 are, respectively, the electron site energy and nearest-neighbour electron transfer integral. In the classical harmonic approximation [cf. Section 2.1.3], the hydrogen bonds are modelled as Hookean springs with force constant K, and therefore $\widehat{H}_{\mathrm{p}}$ takes the form

$$\widehat{H}_{\mathrm{p}} = \sum_{n=0}^{N} \frac{P_n^2}{2M} + \sum_{n=0}^{N-1} \frac{M\Omega^2 \left(U_{n+1} - U_n\right)^2}{2}, \tag{4.2.3}$$

where M is the mass of a peptide unit and we have defined the angular frequency,

$$\Omega := \sqrt{K/M}. \tag{4.2.4}$$

We note that, as we showed in Section 2.1.3, Ω is the angular frequency of one possible phonon mode, and it provides a characteristic time-scale of our lattice dynamics. U_n and P_n in Equation (4.2.3) are, respectively, the displacement and conjugate momentum of the n^{th} peptide unit. Thus, the first and second terms in the expression for $\widehat{H}_{\mathrm{p}}$ represent, respectively, the kinetic and potential energies of the lattice. As we argued in Section 4.1, the interaction Hamiltonian, $\widehat{H}_{\mathrm{int}}$, should take the form

$$\widehat{H}_{\mathrm{int}} = \sum_{n=0}^{N} \chi G_n \widehat{A}_n^{\dagger} \widehat{A}_n, \tag{4.2.5}$$

where χ is the electron-phonon coupling constant and G_n is a bilinear function of S_n and S_{n-1}, where $S_n = U_{n+1} - U_n$. Davydov's symmetric G_n [cf. eq. (4.1.4)] led to

$$\widehat{H}_{\mathrm{int}}^{\mathrm{Dav}} = \frac{\chi}{2} \left[S_0 \widehat{A}_0^{\dagger} \widehat{A}_0 + S_{N-1} \widehat{A}_N^{\dagger} \widehat{A}_N + \sum_{n=1}^{N-1} \left(S_n + S_{n-1}\right) \widehat{A}_n^{\dagger} \widehat{A}_n \right]. \tag{4.2.6}$$

Meanwhile, Scott's anti-symmetric G_n [cf. eq. (4.1.5)] gave

$$\widehat{H}_{\mathrm{int}}^{\mathrm{Sco}} = \sum_{n=0}^{N-1} \chi S_n \widehat{A}_n^{\dagger} \widehat{A}_n. \tag{4.2.7}$$

We propose

$$G_n = \chi_r S_n + \chi_l S_{n-1}, \tag{4.2.8}$$

taking without loss of generality $\chi_r > 0$ and $0 \leq \chi_l \leq \chi_r$, representing a partition of interaction energy between S_n and S_{n-1}. Then, our interaction Hamiltonian is

$$\widehat{H}_{\text{int}} = \chi_r S_0 \widehat{A}_0^\dagger \widehat{A}_0 + \chi_l S_{N-1} \widehat{A}_N^\dagger \widehat{A}_N + \sum_{n=1}^{N-1} \Big[\chi_r S_n + \chi_l S_{n-1} \Big] \widehat{A}_n^\dagger \widehat{A}_n. \tag{4.2.9}$$

By defining

$$\chi := \chi_r + \chi_l, \tag{4.2.10}$$

and introducing the *symmetry parameter*,

$$\beta := \frac{\chi_r - \chi_l}{\chi}, \tag{4.2.11}$$

so that

$$0 \leq \beta \leq 1, \tag{4.2.12}$$

we may write

$$\begin{aligned} \widehat{H}_{\text{int}} = \frac{\chi}{2} \Bigg[& (1+\beta)\,(U_1 - U_0)\,\widehat{A}_0^\dagger \widehat{A}_0 + (1-\beta)\,(U_N - U_{N-1})\,\widehat{A}_N^\dagger \widehat{A}_N \\ & + \sum_{n=1}^{N-1} \Big[(U_{n+1} - U_{n-1}) + \beta\,(U_{n+1} + U_{n-1} - 2U_n) \Big] \widehat{A}_n^\dagger \widehat{A}_n \Bigg]. \end{aligned} \tag{4.2.13}$$

$\widehat{H}_{\text{int}}$ is entirely characterised by β and χ, and $\beta = 0$ reduces our Hamiltonian to the symmetric model represented by Equation (4.2.6), whilst $\beta = 1$ reduces our Hamiltonian to the anti-symmetric model represented by Equation (4.2.7). The larger β is, the less spatial symmetry our model possesses. Indeed, for $0 \leq \beta < 1$, the ratio of n-to-$(n+1)$ coupling strength to n-to-$(n-1)$ coupling strength is given by

$$\chi_r / \chi_l = (1+\beta)/(1-\beta), \tag{4.2.14}$$

and this ratio is strictly increasing with β. Finally, The external Hamiltonian,

$$\widehat{H}_{\text{ext}} = -\sum_{n=0}^{N} eER\,(n - n_0)\,\widehat{A}_n^\dagger \widehat{A}_n, \tag{4.2.15}$$

models the effect of an EMF with longitudinal (along α-channel) electric field amplitude $E = E(t)$ on the potential energy of a electron with charge $-e$. The potential energy due to E is set to zero at some arbitrary n_0, and R is the equilibrium lattice spacing.

4.2.2 Dynamical Equations

The state of the system is a linear superposition of localised excitations,

$$|\Psi(t)\rangle = \sum_{n=0}^{N} \alpha_n(t)\widehat{A}_n^\dagger |0\rangle\,, \tag{4.2.16}$$

where $|0\rangle$ is the vacuum state, so that $\widehat{A}_n |0\rangle = 0$, and α_n are complex coefficients, subject to the normalisation condition,

$$\sum_{n=0}^{N} |\alpha_n|^2 = 1. \tag{4.2.17}$$

We proceed to derive dynamical equations for α_n and U_n. The equation for α_n follows from the time-evolution of $|\Psi(t)\rangle$ according to the Schrödinger equation,

$$i\hbar\, \frac{\partial\, |\Psi\rangle}{\partial t} = (\widehat{H}_\mathrm{e} + \widehat{H}_\mathrm{int} + \widehat{H}_\mathrm{ext})\, |\Psi\rangle\,. \tag{4.2.18}$$

We expand $|\Psi\rangle$ using Equation (4.2.16), and invoke Equations (4.2.2), (4.2.13) and (4.2.15) for the definitions of the various Hamiltonian components, to obtain

$$\begin{aligned}
i\hbar \sum_{m=0}^{N} \frac{\mathrm{d}\alpha_m}{\mathrm{d}t} \widehat{A}_m^\dagger |0\rangle &= \sum_{m=0}^{N} \alpha_m \left[\sum_{k=0}^{N} J_0 \widehat{A}_k^\dagger \widehat{A}_k - \sum_{k=0}^{N-1} J_1 \left(\widehat{A}_{k+1}^\dagger \widehat{A}_k + \widehat{A}_k^\dagger \widehat{A}_{k+1} \right) \right] \widehat{A}_m^\dagger |0\rangle \\
&\quad + \frac{\chi}{2} \sum_{m=0}^{N} \alpha_m \Bigg[(1+\beta)(U_1 - U_0) \widehat{A}_0^\dagger \widehat{A}_0 + (1-\beta)(U_N - U_{N-1}) \widehat{A}_N^\dagger \widehat{A}_N \\
&\quad + \sum_{k=1}^{N-1} \Big[(U_{k+1} - U_{k-1}) + \beta(U_{k+1} + U_{k-1} - 2U_k) \Big] \widehat{A}_k^\dagger \widehat{A}_k \Bigg] \widehat{A}_m^\dagger |0\rangle \\
&\quad - \sum_{m=0}^{N} \alpha_m \sum_{k=0}^{N} eER\,(k - n_0)\, \widehat{A}_k^\dagger \widehat{A}_k \widehat{A}_m^\dagger |0\rangle \\
&= J_0 \sum_{m=0}^{N} \alpha_m \widehat{A}_m^\dagger |0\rangle \\
&\quad - J_1 \left[\alpha_0 \widehat{A}_1^\dagger + \alpha_N \widehat{A}_{N-1}^\dagger + \sum_{m=1}^{N-1} \alpha_m \left(\widehat{A}_{m+1}^\dagger + \widehat{A}_{m-1}^\dagger \right) \right] |0\rangle \\
&\quad + \frac{\chi}{2} \left[\alpha_0 (1+\beta)(U_1 - U_0) \widehat{A}_0^\dagger + \alpha_N (1-\beta)(U_N - U_{N-1}) \widehat{A}_N^\dagger \right] |0\rangle \\
&\quad + \frac{\chi}{2} \sum_{m=1}^{N-1} \alpha_m \Big[(U_{m+1} - U_{m-1}) + \beta(U_{m+1} + U_{m-1} - 2U_m) \Big] \widehat{A}_m^\dagger |0\rangle \\
&\quad - eER \sum_{m=0}^{N} \alpha_m\, (m - n_0)\, \widehat{A}_m^\dagger |0\rangle\,,
\end{aligned} \tag{4.2.19}$$

where we have used the anti-commutation relation for fermionic ladder operators,

$$\widehat{A}_m \widehat{A}_k^\dagger + \widehat{A}_k^\dagger \widehat{A}_m = \delta_{mk}. \tag{4.2.20}$$

Equating the coefficients of $\widehat{A}_n^\dagger |0\rangle$ on both sides of Equation (4.2.19) yields

$$i\hbar \frac{\mathrm{d}\alpha_0}{\mathrm{d}t} = J_0\alpha_0 - J_1\alpha_1 + \frac{\chi}{2}\alpha_0 (1+\beta)(U_1 - U_0) - eER(-n_0)\alpha_0, \tag{4.2.21a}$$

$$\begin{aligned} i\hbar \frac{\mathrm{d}\alpha_n}{\mathrm{d}t} &= J_0\alpha_n - J_1(\alpha_{n-1} + \alpha_{n+1}) + \frac{\chi}{2}\alpha_n \Big[(U_{n+1} - U_{n-1}) + \beta (U_{n+1} + U_{n-1} - 2U_n) \Big] \\ &\quad - eER(n - n_0)\alpha_n, \qquad \text{for } 1 \le n \le N-1, \end{aligned} \tag{4.2.21b}$$

$$\begin{aligned} i\hbar \frac{\mathrm{d}\alpha_N}{\mathrm{d}t} &= J_0\alpha_N - J_1\alpha_{N-1} + \frac{\chi}{2}\alpha_N (1-\beta)(U_N - U_{N-1}) \\ &\quad - eER(N - n_0)\alpha_N. \end{aligned} \tag{4.2.21c}$$

Invoking $S_n = U_{n+1} - U_n$, we define fictitious points at $n = -1, N+1$ by

$$S_{-1} = S_N = 0, \quad \alpha_{-1} = \alpha_{N+1} = 0, \tag{4.2.22}$$

so that the three parts of Equation (4.2.21) are condensed into a single equation for all $0 \le n \le N$:

$$\begin{aligned} i\hbar \frac{\mathrm{d}\alpha_n}{\mathrm{d}t} &= \left[J_0 + \frac{\chi}{2}(S_n + S_{n-1}) + \frac{\chi}{2}\beta (S_n - S_{n-1}) \right] \alpha_n - J_1(\alpha_{n+1} + \alpha_{n-1}) \\ &\quad - eER(n - n_0)\alpha_n. \end{aligned} \tag{4.2.23}$$

Now we introduce the gauge transformation,

$$\alpha_n(t) = \psi_n(t) \exp\left[-\frac{it}{\hbar}(J_0 - 2J_1) \right], \tag{4.2.24}$$

which preserves the probability density $|\psi_n|^2 = |\alpha_n|^2$, and which implies

$$i\hbar \frac{\mathrm{d}\alpha_n}{\mathrm{d}t} = \left[i\hbar \frac{\mathrm{d}\psi_n}{\mathrm{d}t} + (J_0 - 2J_1)\psi_n \right] \exp\left[-\frac{it}{\hbar}(J_0 - 2J_1) \right]. \tag{4.2.25}$$

Putting Equation (4.2.25) into Equation (4.2.23), then cancelling the exponential factors on both sides, we obtain the dynamical equation for ψ_n:

$$\begin{aligned} i\hbar \frac{\mathrm{d}\psi_n}{\mathrm{d}t} &= \left[\frac{\chi}{2}(S_n + S_{n-1}) + \frac{\chi}{2}\beta (S_n - S_{n-1}) \right] \psi_n - J_1(\psi_{n+1} + \psi_{n-1} - 2\psi_n) \\ &\quad - eER(n - n_0)\psi_n. \end{aligned} \tag{4.2.26}$$

Next, we derive dynamical equations for U_n from classical Hamilton equations,

$$\frac{\mathrm{d}U_n}{\mathrm{d}t} = \frac{\partial H_{\mathrm{cla}}}{\partial P_n}, \tag{4.2.27a}$$

$$\frac{\mathrm{d}P_n}{\mathrm{d}t} = -\frac{\partial H_{\mathrm{cla}}}{\partial U_n}, \tag{4.2.27b}$$

where we have defined

$$\begin{aligned}
H_{\text{cla}} &:= \langle\Psi|(\widehat{H}_{\text{p}} + \widehat{H}_{\text{int}})|\Psi\rangle \\
&= H_{\text{p}} + \frac{\chi}{2}\langle 0|\sum_{j=0}^{N}\sum_{m=0}^{N}\widehat{A}_j\alpha_j^*\alpha_m\Bigg[(1+\beta)\,S_0\widehat{A}_0^\dagger\widehat{A}_0 + (1-\beta)\,S_{N-1}\widehat{A}_N^\dagger\widehat{A}_N \\
&\quad + \sum_{k=1}^{N-1}\Big[(S_k + S_{k-1}) + \beta\,(S_k - S_{k-1})\Big]\widehat{A}_k^\dagger\widehat{A}_k\Bigg]\widehat{A}_m^\dagger|0\rangle \\
&= H_{\text{p}} + \frac{\chi}{2}\langle 0|\sum_{j=0}^{N}\widehat{A}_j\alpha_j^*\Bigg[\alpha_0\,(1+\beta)\,S_0\widehat{A}_0^\dagger + \alpha_N\,(1-\beta)\,S_{N-1}\widehat{A}_N^\dagger \\
&\quad + \sum_{m=1}^{N-1}\alpha_m\Big[(S_m + S_{m-1}) + \beta\,(S_m - S_{m-1})\Big]\widehat{A}_m^\dagger\Bigg]|0\rangle \\
&= H_{\text{p}} + \frac{\chi}{2}\Bigg[|\alpha_0|^2\,(1+\beta)\,S_0 + |\alpha_N|^2\,(1-\beta)\,S_{N-1} \\
&\quad + \sum_{j=1}^{N-1}|\alpha_j|^2\Big[(S_j + S_{j-1}) + \beta\,(S_j - S_{j-1})\Big]\Bigg],
\end{aligned} \tag{4.2.28}$$

with

$$H_{\text{p}} := \sum_{j=0}^{N}\frac{P_j^2}{2M} + \sum_{j=0}^{N-1}\frac{M\Omega^2 S_j^2}{2}. \tag{4.2.29}$$

From Equation (4.2.27a) we have, for $0 \le n \le N$,

$$M\frac{\mathrm{d}U_n}{\mathrm{d}t} = P_n, \tag{4.2.30}$$

which, when combined with Equation (4.2.27b), implies

$$M\frac{\mathrm{d}^2U_n}{\mathrm{d}t^2} = -\frac{\partial H_{\text{cla}}}{\partial U_n}. \tag{4.2.31}$$

Putting Equations (4.2.28) and (4.2.29) into Equation (4.2.31) gives

$$M\frac{\mathrm{d}^2U_0}{\mathrm{d}t^2} = M\Omega^2 S_0 + \frac{\chi}{2}\Big[|\alpha_1|^2\,(1-\beta) + |\alpha_0|^2\,(1+\beta)\Big], \tag{4.2.32a}$$

$$\begin{aligned}
M\frac{\mathrm{d}^2U_n}{\mathrm{d}t^2} &= M\Omega^2\,(S_n - S_{n-1}) + \frac{\chi}{2}\Big[|\alpha_{n+1}|^2\,(1-\beta) \\
&\quad + 2\beta|\alpha_n|^2 - |\alpha_{n-1}|^2\,(1+\beta)\Big] \qquad \text{for } 1 \le n \le N-1,
\end{aligned} \tag{4.2.32b}$$

$$M\frac{\mathrm{d}^2U_N}{\mathrm{d}t^2} = -M\Omega^2 S_{N-1} - \frac{\chi}{2}\Big[|\alpha_N|^2\,(1-\beta) + |\alpha_{N-1}|^2\,(1+\beta)\Big]. \tag{4.2.32c}$$

Since we only consider large lattices with $N \gg 1$, we take the liberty of requiring that

$$\alpha_0 = \alpha_N = 0. \tag{4.2.33}$$

This condition is physically justified as we expect the probability distribution $|\alpha_n|^2$ to be highly localised. Indeed, our numerical results later will confirm that on a lattice with $N = 200$, $|\alpha_n|^2$ is $\mathcal{O}(10^{-1})$ at only several sites, and towards the boundaries we have $|\alpha_n|^2 \sim \mathcal{O}(10^{-30})$. With Equation (4.2.33) as well as Equation (4.2.22) in place, we can combine Equations (4.2.32a) to (4.2.32c) into the following single equation for all $0 \leq n \leq N$:

$$\begin{aligned} M\frac{\mathrm{d}^2U_n}{\mathrm{d}t^2} = M\Omega^2\left(S_n - S_{n-1}\right) + \frac{\chi}{2}\left(|\alpha_{n+1}|^2 - |\alpha_{n-1}|^2\right) \\ - \frac{\chi}{2}\beta\left(|\alpha_{n+1}|^2 + |\alpha_{n-1}|^2 - 2|\alpha_n|^2\right). \end{aligned} \tag{4.2.34}$$

We impose the following boundary condition on U_n:

$$U_0 = \frac{\mathrm{d}U_0}{\mathrm{d}t} = 0, \tag{4.2.35}$$

which is also satisfied in an inertial frame with the 0^{th} peptide unit at the origin. To account for the interaction between the polypeptide and its environment, we add *Langevin terms* to the right-hand side of Equation (4.2.34) [Lan08, LG97, Sch10, BEPZ14]. The Langevin terms are a damping term representing dissipation due to friction, $-\Gamma \mathrm{d}U_n/\mathrm{d}t$, where Γ is the viscous damping coefficient, and a stochastic term $F_n(t)$, representing forces that arise from thermal fluctuations. Specifically, $F_n(t)$ is normally-distributed with zero mean and correlation function

$$\langle F_m(t)F_n(t')\rangle = 2\Gamma k_{\mathrm{B}}\Theta\delta_{m,n}\delta(t-t'), \tag{4.2.36}$$

where k_{B} is the Boltzmann constant, Θ is the temperature of the environment, $\delta_{\cdot,\cdot}$ is the Kronecker delta and $\delta(\cdot)$ is the delta function. Using the fact that $|\psi_n|^2 = |\alpha_n|^2$ for all n, we write the complete dynamical equation for U_n as

$$\begin{aligned} M\frac{\mathrm{d}^2U_n}{\mathrm{d}t^2} = M\Omega^2\left(S_n - S_{n-1}\right) + \frac{\chi}{2}\left(|\psi_{n+1}|^2 - |\psi_{n-1}|^2\right) \\ - \frac{\chi}{2}\beta\left(|\psi_{n+1}|^2 + |\psi_{n-1}|^2 - 2|\psi_n|^2\right) - \Gamma\frac{\mathrm{d}U_n}{\mathrm{d}t} + F_n. \end{aligned} \tag{4.2.37}$$

If we re-scale time and length by

$$t = \Omega^{-1}\tau, \quad U_n = Lu_n, \tag{4.2.38}$$

where

$$L := \sqrt{\hbar M^{-1}\Omega^{-1}}, \tag{4.2.39}$$

then we can rewrite Equations (4.2.26) and (4.2.37) to obtain the following dimensionless dynamical equations for ψ_n and u_n, for $n = 0, 1, \ldots, N$:

$$\begin{aligned} i\dot{\psi}_n &= \kappa\psi_n \left[(s_n + s_{n-1}) + \beta\,(s_n - s_{n-1})\right] - \rho\,(\psi_{n+1} + \psi_{n-1} - 2\psi_n) \\ &\quad - \epsilon(n - n_0)\psi_n, \qquad (4.2.40a) \\ \ddot{u}_n &= (s_n - s_{n-1}) + \kappa\left[\left(|\psi_{n+1}|^2 - |\psi_{n-1}|^2\right) - \beta\left(|\psi_{n+1}|^2 + |\psi_{n-1}|^2 - 2|\psi_n|^2\right)\right] \\ &\quad - \gamma\dot{u}_n + f_n, \qquad (4.2.40b) \end{aligned}$$

where the overdot denotes differentiation with respect to τ, and

$$s_n = u_{n+1} - u_n. \qquad (4.2.41)$$

The dimensionless parameters that appear in Equation (4.2.40) are

$$\kappa = \frac{\chi}{2\sqrt{\hbar M\Omega^3}}, \quad \rho = \frac{J_1}{\hbar\Omega}, \quad \epsilon = \frac{eER}{\hbar\Omega}, \quad \gamma = \frac{\Gamma}{M\Omega}, \quad f_n = \frac{F_n}{\sqrt{\hbar M\Omega^3}}, \qquad (4.2.42)$$

where the stochastic forces f_n have zero mean and are correlated by

$$\langle f_m(\tau) f_n(\tau')\rangle = 2\gamma\theta\delta_{m,n}\delta(\tau - \tau'), \qquad (4.2.43)$$

with

$$\theta = \frac{k_{\mathrm{B}}\Theta}{\hbar\Omega} \qquad (4.2.44)$$

being thermal energy in units of $\hbar\Omega$. In practice, we replace the delta function in Equation (4.2.43) by

$$\delta(\tau - \tau') = \frac{1}{\Delta\tau}, \qquad (4.2.45)$$

where $\Delta\tau$ is some small integration time-step. Equations (4.2.40a) and (4.2.40b) hold subject to the fictitious-point and boundary conditions [cf. Equations (4.2.22), (4.2.33) and (4.2.35)]:

$$s_{-1} = s_N = 0, \quad \psi_{-1} = \psi_{N+1} = 0, \quad \psi_0 = \psi_N = 0, \quad u_0 = \dot{u}_0 = 0, \qquad (4.2.46)$$

as well as the normalisation condition,

$$\sum_{n=0}^{N} |\psi_n|^2 = 1. \qquad (4.2.47)$$

It is easily verifiable that by setting $\epsilon = \gamma = f_n = 0$ in Equation (4.2.40), and then setting $\beta = 0$ or $\beta = 1$, one recovers respectively the Davydov or Scott dynamical equations [cf. Section 2.2.2].

4.2.3 Parameters

In the phonon Hamiltonian given by Equation (4.2.3), we take

$$M = 1.774 \times 10^{-25} \text{ kg}, \tag{4.2.48}$$

which is the average mass of a peptide unit in a membrane α-helix [Lid04, LWBR10]. For the value of Ω, we take the hydrogen bond force constant [BESP72, Cho83]

$$K = 11.7 \text{ N} \cdot \text{m}^{-1}, \tag{4.2.49}$$

which implies [cf. Equation (4.2.4)]

$$\Omega = 8.1 \times 10^{12} \text{ s}^{-1}. \tag{4.2.50}$$

We let the equilibrium lattice spacing be

$$R = 4.5 \text{ Å}, \tag{4.2.51}$$

which is the distance between centres of mass of neighbouring peptide units along an α-channel [PCB51, BT88]. As for the viscous damping coefficient, Γ, we make an approximation as follows. We use Stokes' Law to calculate the coefficient for each atom in the peptide unit [JP88, PBM90, AM13], with $\mu = 0.068$ Pa·s as the dynamic viscosity [cf. Section 2.2.4], and then deduce an overall Γ value for the average peptide unit in a membrane α-helix, under the assumption that the drag force on the peptide unit is the sum of drag forces on individual atoms. For example, the viscous damping coefficients for atoms of hydrogen, carbon, nitrogen and oxygen in the membrane environment are, by our method, 1.1, 3.2, 3.3 and 3.5 pg $\cdot$ s^{-1}, respectively. A peptide unit with, say, an alanine side-chain, has chemical formula C_3H_5NO, and we therefore estimate its viscous damping coefficient to be 22 pg $\cdot$ s^{-1}. Data in [LWBR10], concerning the relative occurrence frequencies of all possible peptide units in a membrane α-helix, then allow us to estimate Γ for an average peptide unit to be

$$\Gamma = 34 \text{ pg} \cdot \text{s}^{-1}. \tag{4.2.52}$$

We therefore fix the value of the dimensionless viscous damping coefficient at

$$\gamma = 0.024. \tag{4.2.53}$$

We also fix the value of ρ, which is an *adiabaticity parameter* in our system, as it represents the characteristic time-scale separation between the lattice and electron dynamics. Following [BEPZ08, BEPZ10, BEPZ14], which fixed a parameter $C \equiv 1/\rho^2 = 0.22$, for the rest of this Chapter we set

$$\rho = 2.1. \tag{4.2.54}$$

This implies $J_1 = 11$ meV, which is nearly 2 orders of magnitude smaller than the transfer integral applicable to the electron-amide-I model of Chapter 3. The discrepancy may be due to the fact that we now consider the transfer of electrons between entire peptide units, rather than just between neighbouring C=O groups which have a much stronger electric dipole. That being said, both values of J_1 are theoretical estimates, and the fact that a 2-order discrepancy exists is indicative of the difficulty of building these models without empirical data on electron transfer integrals.

The dimensionless parameters whose influence on the system are to be studied, and therefore whose values will be varied, are β, κ, ϵ and the thermal energy θ which affects the stochastic forces f_n via Equation (4.2.43). Finally, we note that the characteristic time-scale and length-scale [cf. Equation (4.2.39)] in our system are, respectively,

$$\Omega^{-1} = 0.12 \text{ ps}, \quad L = 0.086 \text{ Å} = 0.019R, \tag{4.2.55}$$

and the characteristic energy-scale in our system is

$$\hbar\Omega = 5.3 \text{ meV}. \tag{4.2.56}$$

4.2.4 Energetics

The polaron's total internal energy, measured with respect to the lowest energy in the electron band, $J_0 - 2J_1$, and in units of meV, is

$$E_\mathrm{b} := 5.3 \times \frac{\langle\Psi|\widehat{H}_\mathrm{e} + \widehat{H}_\mathrm{p} + \widehat{H}_\mathrm{int}|\Psi\rangle - J_0 + 2J_1}{\hbar\Omega}. \tag{4.2.57}$$

We can find an expression for $\langle\widehat{H}_\mathrm{e}\rangle := \langle\Psi|\widehat{H}_\mathrm{e}|\Psi\rangle$ by invoking Equation (4.2.2) for the definition of $\widehat{H}_\mathrm{e}$, and utilising the electron state,

$$|\Psi\rangle = \sum_{n=0}^{N} \psi_n \exp\left(-\frac{it}{\hbar}(J_0 - 2J_1)\right) \widehat{A}_n^\dagger |0\rangle . \tag{4.2.58}$$

The result is that

$$\begin{aligned}\frac{\langle \widehat{H}_{\rm e}\rangle}{\hbar\Omega} &= \frac{J_0}{\hbar\Omega}\sum_{m=0}^{N}\sum_{n=0}^{N}\sum_{k=0}^{N}\psi_m^*\psi_k\,\langle 0|\,\widehat{A}_m\widehat{A}_n^\dagger\widehat{A}_n\widehat{A}_k^\dagger\,|0\rangle \\ &\quad - \frac{J_1}{\hbar\Omega}\sum_{m=0}^{N}\sum_{n=0}^{N-1}\sum_{k=0}^{N}\psi_m^*\psi_k\,\langle 0|\,\widehat{A}_m\widehat{A}_{n+1}^\dagger\widehat{A}_n\widehat{A}_k^\dagger + \widehat{A}_m\widehat{A}_n^\dagger\widehat{A}_{n+1}\widehat{A}_k^\dagger\,|0\rangle \\ &= \frac{J_0}{\hbar\Omega}\sum_{n=0}^{N}|\psi_n|^2 - \frac{J_1}{\hbar\Omega}\sum_{n=0}^{N-1}\left(\psi_{n+1}^*\psi_n + \psi_n^*\psi_{n+1}\right), \\ &= \frac{J_0}{\hbar\Omega} - \rho\sum_{n=1}^{N-2}\left(\psi_{n+1}^*\psi_n + \psi_n^*\psi_{n+1}\right), \end{aligned} \tag{4.2.59}$$

where we have used the normalisation condition for ψ_n, Equation (4.2.42) for the definition of ρ, and the boundary condition (4.2.46). For $\langle\widehat{H}_{\rm p}\rangle := \langle\Psi|\widehat{H}_{\rm p}|\Psi\rangle$, we use Equation (4.2.3) for the definition of $\widehat{H}_{\rm p}$ and Equation (4.2.39) for the definition of the scaling factor L:

$$\begin{aligned}\frac{\langle \widehat{H}_{\rm p}\rangle}{\hbar\Omega} &= \frac{1}{2M\hbar\Omega}\sum_{n=1}^{N}M^2L^2\Omega^2\,(\dot{u}_n)^2 + \frac{M\Omega^2}{2\hbar\Omega}\sum_{n=0}^{N-1}L^2\,(u_{n+1}-u_n)^2 \\ &= \frac{1}{2}\left[\sum_{n=1}^{N}(\dot{u}_n)^2 + \sum_{n=0}^{N-1}(u_{n+1}-u_n)^2\right], \end{aligned} \tag{4.2.60}$$

where $\dot{u}_0 = 0$ is excluded from the sum. For $\langle\widehat{H}_{\rm int}\rangle := \langle\Psi|\widehat{H}_{\rm int}|\Psi\rangle$, we have

$$\frac{\langle \widehat{H}_{\rm int}\rangle}{\hbar\Omega} = \frac{\chi L}{2\hbar\Omega}\sum_{n=1}^{N-1}|\psi_n|^2\left[(u_{n+1}-u_{n-1}) + \beta\,(u_{n+1}+u_{n-1}-2u_n)\right], \tag{4.2.61}$$

where terms involving $|\psi_0|^2$ and $|\psi_N|^2$ have again been set to zero again due to condition (4.2.46). Putting Equations (4.2.59) to (4.2.61) together, and noting that $\chi L/(2\hbar\Omega) = \kappa$, we have, in units of meV,

$$\begin{aligned}E_{\rm b} &= 5.3\rho\left[2 - \sum_{n=1}^{N-2}\left(\psi_{n+1}^*\psi_n + \psi_n^*\psi_{n+1}\right)\right] + \frac{5.3}{2}\left[\sum_{n=1}^{N}(\dot{u}_n)^2 + \sum_{n=0}^{N-1}(u_{n+1}-u_n)^2\right] \\ &\quad + 5.3\kappa\sum_{n=1}^{N-1}|\psi_n|^2\left[(u_{n+1}-u_{n-1}) + \beta\,(u_{n+1}+u_{n-1}-2u_n)\right]. \end{aligned} \tag{4.2.62}$$

4.3 Stationary Polarons in the Deterministic System

In this Section, we find stationary solutions to our system, neglecting the stochastic forces $f_n(\tau)$. We begin by looking for approximate solutions using analytical methods, and the approximations are useful in our efforts to compute solutions numerically. We present key characteristics of stationary polarons, such as the maximum localisation probability and binding energy, as functions of parameters in the system.

We begin by writing down in Section 4.3.1 a set of equations describing our system in the stationary state, and in Section 4.3.2 we look at the stationary-state equations in the continuum limit ($N \gg 1$). We show that the continuum limit leads to a generalised nonlinear Schrödinger equation on the real line, and we proceed to solve the equation analytically in Section 4.3.3. Finally, we compute stationary solutions on a finite lattice in Section 4.3.4, using an iterative numerical scheme. Wherever the scheme requires an initial ansatz, we use a spatially discretised version of one of our continuum solutions.

4.3.1 The Stationary-State Equations

We set $f_n = 0$ and $\dot{u}_n = \ddot{u}_n = 0$ in Equation (4.2.40b), obtaining

$$\begin{aligned} s_n - s_{n-1} &= \kappa \left[(\beta - 1)|\psi_{n+1}|^2 + (\beta + 1)|\psi_{n-1}|^2 - 2\beta|\psi_n|^2 \right] \\ &= \kappa \left[\beta \left(g_n - g_{n-1} \right) - \left(c_n - c_{n-1} \right) \right], \end{aligned} \tag{4.3.1}$$

where we have defined

$$g_n := |\psi_{n+1}|^2 - |\psi_n|^2, \quad c_n := |\psi_{n+1}|^2 + |\psi_n|^2. \tag{4.3.2}$$

Equation (4.3.1) holds if

$$s_n = \kappa \left(\beta g_n - c_n \right) = \kappa \left[(\beta - 1)|\psi_{n+1}|^2 - (\beta + 1)|\psi_n|^2 \right]. \tag{4.3.3}$$

Putting this s_n solution into eq. (4.2.40a) and requiring $\epsilon = 0$, we deduce

$$\begin{aligned} i\dot{\psi}_n &= \kappa\psi_n \left[(1 + \beta)\, s_n + (1 - \beta)\, s_{n-1} \right] - \rho \left(\psi_{n+1} + \psi_{n-1} - 2\psi_n \right) \\ &= -\kappa^2 \psi_n \left[\left(1 - \beta^2 \right) |\psi_{n+1}|^2 + \left(1 - \beta^2 \right) |\psi_{n-1}|^2 + 2 \left(1 + \beta^2 \right) |\psi_n|^2 \right] \\ &\quad - \rho \left(\psi_{n+1} + \psi_{n-1} - 2\psi_n \right). \end{aligned} \tag{4.3.4}$$

Upon rearrangement, we have

$$\begin{aligned} &i\dot{\psi}_n + \rho \left(\psi_{n+1} + \psi_{n-1} - 2\psi_n \right) + 4\kappa^2 |\psi_n|^2 \psi_n \\ &+ \kappa^2 \left(1 - \beta^2 \right) \left[|\psi_{n+1}|^2 + |\psi_{n-1}|^2 - 2|\psi_n|^2 \right] = 0. \end{aligned} \tag{4.3.5}$$

Defining

$$\Delta\psi_n := \psi_{n+1} + \psi_{n-1} - 2\psi_n, \tag{4.3.6a}$$

$$\Delta|\psi_n|^2 := |\psi_{n+1}|^2 + |\psi_{n-1}|^2 - 2|\psi_n|^2, \tag{4.3.6b}$$

as well as the composite paramters

$$\lambda := \frac{4\kappa^2}{\rho} \equiv \frac{\chi^2}{M\Omega^2 J_1}, \tag{4.3.7a}$$

$$\eta := \frac{\kappa^2}{\rho}\left(1-\beta^2\right) \equiv \frac{\lambda}{4}\left(1-\beta^2\right), \tag{4.3.7b}$$

allows us to rewrite Equation (4.3.5) as

$$i\rho^{-1}\dot{\psi}_n + \Delta\psi_n + \lambda|\psi_n|^2\psi_n + \eta\Delta|\psi_n|^2\psi_n = 0. \tag{4.3.8}$$

Since ρ is fixed, investigating the dependence of our system on κ is equivalent to exploring the effect of λ. Moreover, there is a physical interpretation of λ: it is the product of two ratios of characteristic force or energy scales, both involving the electron-phonon coupling constant χ. Firstly, the ratio $\chi/(MR\Omega^2)$ is the force-scale separation between the electron-phonon interaction and hydrogen bond strength. Secondly, the ratio $\chi R/J_1$ is the energy-scale separation between the electron-phonon interaction and nearest-neighbour electron transfer. Thus, in literature concerning electron-phonon models, either λ is or $\sqrt{\lambda}$ is commonly known as the *effective coupling parameter* [KAT98].

In a stationary state, the time dependence of ψ_n can be at most a variation of its phase factor. We may therefore consider the stationary-state ansatz,

$$\psi_n(\tau) = \exp\left(i\rho H_0\tau + ikx\right)\phi(x)\big|_{x=n-N/2,} \tag{4.3.9}$$

where x is a real, continuous variable taking values in $-N/2 \le x \le N/2$, ϕ is a real, smooth function, k is a constant real wavenumber, and H_0 is a constant real eigenvalue in the sense that

$$i\rho^{-1}\dot{\psi}_n = -H_0\psi_n. \tag{4.3.10}$$

We will numerically look for such stationary-state solutions to our system in Section 4.3.4. Before that, we present an analytical interlude in the form of the next two Sections.

4.3.2 The Continuum Limit

In the limit $N \gg 1$, we write $x = \xi N$ for some ξ and $\phi(x) = \widetilde{\phi}(\xi)$ for some $\widetilde{\phi}$, so that

$$\begin{aligned}\psi_{n\pm1} &= \exp\left(i\rho H_0\tau + ik\xi N\right)\widetilde{\phi}(\xi)\Big|_{\xi=(n\pm1)/N-1/2} \\ &= \exp\Big(i\rho H_0\tau + ik\left(n\pm1-N/2\right)\Big) \\ &\quad\times\left(\widetilde{\phi}(\xi) \pm N^{-1}\widetilde{\phi}'(\xi) + \frac{N^{-2}}{2}\widetilde{\phi}''(\xi) + \mathcal{O}\Big(N^{-3}\Big)\right)\Bigg|_{\xi=n/N-1/2.}\end{aligned} \tag{4.3.11}$$

Multiplying Equation (4.3.11) by its complex conjugate, we obtain

$$|\psi_{n\pm1}|^2 = \widetilde{\phi}(\xi)^2 \pm 2N^{-1}\widetilde{\phi}(\xi)\widetilde{\phi}'(\xi) + N^{-2}\widetilde{\phi}(\xi)\widetilde{\phi}''(\xi) + N^{-2}\Big(\widetilde{\phi}'(\xi)\Big)^2 + \mathcal{O}\Big(N^{-3}\Big)\Big|_{\xi=n/N-1/2.} \tag{4.3.12}$$

Equation (4.3.11) also implies

$$\begin{aligned}\Delta\psi_n = \exp\Big(i\rho H_0\tau + ik\,(n-N/2)\Big) \\ \times\Bigg[\exp(ik)\Big(\widetilde{\phi}(\xi) + N^{-1}\widetilde{\phi}'(\xi) + \frac{N^{-2}}{2}\widetilde{\phi}''(\xi)\Big) \\ + \exp(-ik)\Big(\widetilde{\phi}(\xi) - N^{-1}\widetilde{\phi}'(\xi) + \frac{N^{-2}}{2}\widetilde{\phi}''(\xi)\Big) \\ - 2\widetilde{\phi}(\xi) + \mathcal{O}\Big(N^{-3}\Big)\Bigg]\Bigg|_{\xi=n/N-1/2,}\end{aligned} \tag{4.3.13}$$

and Equation (4.3.12) implies

$$\Delta|\psi_n|^2 = 2N^{-2}\widetilde{\phi}(\xi)\widetilde{\phi}''(\xi) + 2N^{-2}\Big(\widetilde{\phi}'(\xi)\Big)^2 + \mathcal{O}\Big(N^{-3}\Big)\Big|_{\xi=n/N-1/2.} \tag{4.3.14}$$

Putting Equations (4.3.9), (4.3.10), (4.3.13) and (4.3.14) into Equation (4.3.8), we obtain

$$\begin{aligned}0 = \exp\Big(i\rho H_0\tau + ik\,(n-N/2)\Big) \\ \times\Bigg[-H_0\widetilde{\phi}(\xi) + \Big(\cos(k) + i\sin(k)\Big)\Big(\widetilde{\phi}(\xi) + N^{-1}\widetilde{\phi}'(\xi) + \frac{N^{-2}}{2}\widetilde{\phi}''(\xi)\Big) \\ + \Big(\cos(k) - i\sin(k)\Big)\Big(\widetilde{\phi}(\xi) - N^{-1}\widetilde{\phi}'(\xi) + \frac{N^{-2}}{2}\widetilde{\phi}''(\xi)\Big) - 2\widetilde{\phi}(\xi) + \lambda\widetilde{\phi}(\xi)^3 \\ + \eta\Big[2N^{-2}\widetilde{\phi}(\xi)\widetilde{\phi}''(\xi) + 2N^{-2}\Big(\widetilde{\phi}'(\xi)\Big)^2\Big]\widetilde{\phi}(\xi) + \mathcal{O}(N^{-3})\Bigg]\Bigg|_{\xi=n/N-1/2.}\end{aligned} \tag{4.3.15}$$

Retaining terms up to $\mathcal{O}(N^{-2})$ and rearranging gives

$$\begin{aligned}0 = -H_0\widetilde{\phi}(\xi) + \cos(k)\Big[2\widetilde{\phi}(\xi) + N^{-2}\widetilde{\phi}''(\xi)\Big] + 2i\sin(k)N^{-1}\widetilde{\phi}'(\xi) \\ - 2\widetilde{\phi}(\xi) + \lambda\widetilde{\phi}(\xi)^3 + \eta N^{-2}\Big[2\widetilde{\phi}(\xi)\widetilde{\phi}''(\xi) + 2\Big(\widetilde{\phi}'(\xi)\Big)^2\Big]\widetilde{\phi}(\xi)\Big|_{\xi=n/N-1/2.}\end{aligned} \tag{4.3.16}$$

Equating imaginary parts of Equation (4.3.16) gives $k = l\pi$ where l is any integer, so $\cos(k) = \pm1$. We focus on the case of $\cos(k) = 1$, and at the end of Section 4.3.3 we will argue that $\cos(k) = -1$ cannot lead to a square-normalisable ϕ solution and therefore need not be considered. Now, since $\widetilde{\phi}'(\xi) = N\phi'(x)\Big|_{x=\xi N}$ and $\widetilde{\phi}''(\xi) = N^2\phi''(x)\Big|_{x=\xi N}$, where $'$

always denotes differentiation with respect to the argument in parentheses, the real part of Equation (4.3.16) becomes

$$\begin{aligned} &- H_0\phi(x) + \phi''(x) + \lambda\phi(x)^3 \\ &+ \eta\left[2\phi(x)\phi''(x) + 2\Big(\phi'(x)\Big)^2\right]\phi(x)\Big|_{x=n-N/2} = 0. \end{aligned} \tag{4.3.17}$$

We seek $\phi(x)$ which satisfies eq. (4.3.17) *for all* real x, not just when $x = n - N/2$, and let $N \to \infty$. Noting the identity

$$2\phi(x)\phi''(x) + 2\Big(\phi'(x)\Big)^2 \equiv \Big(\phi(x)^2\Big)'', \tag{4.3.18}$$

we can write the globally-defined version of Equation (4.3.17), for all real x, as

$$-H_0\phi(x) + \phi''(x) + \lambda\phi(x)^3 + \eta\Big(\phi(x)^2\Big)''\phi(x) = 0. \tag{4.3.19}$$

We require that $\phi(x)$ has vanishing derivatives at infinity, and is normalised:

$$\int_{-\infty}^{\infty} \phi(x)^2 \, \mathrm{d}x = 1. \tag{4.3.20}$$

If $\eta = 0$ (i.e. $\beta = 1$), then Equation (4.3.19) reduces to the stationary form of the nonlinear Schrödinger equation with a focusing cubic nonlinearity, which has a well-known normalised solution [Hir73, Sco92],

$$H_0 = \lambda^2/16, \quad \phi(x) = \pm\sqrt{\frac{\lambda}{8}}\,\mathrm{sech}\frac{\lambda x}{4} \quad \text{for all } x. \tag{4.3.21}$$

For a general value of $\eta \geq 0$, we call Equation (4.3.19) a stationary *generalised nonlinear Schrödinger equation* (GNLSE).

We have therefore established that in the continuum limit, Equation (4.3.8) with the stationary ansatz (4.3.9) may be approximated by Equation (4.3.19). If we have a global solution to Equation (4.3.19), then putting it into Equation (4.3.9) gives us an approximate stationary solution to Equation (4.3.8).

4.3.3 Solving the Generalised Nonlinear Schrödinger Equation

In this Section, we use analytical methods to find a global $\phi(x)$ solution to Equation (4.3.19), together with eigenvalue H_0, given parameters $\lambda > 0$ and $\eta > 0$ (i.e. $\beta < 1$). Not only has this particular generalisation of the nonlinear Schrödinger equation never before been

studied, our analytical solution will be useful when we look for stationary polaron states numerically, as it can be an ansatz for our numerical scheme.

We look for a smooth solution $\phi(x)$ satisfying the constraint (4.3.20). Moreover, we observe that Equation (4.3.19) is invariant under spatial translation and reflection, meaning that if $\phi(x)$ is a solution then so is $\varphi(x) = \phi(c - x)$ for any constant c. This fact enables us to look exclusively for solutions which are reflectively symmetric about an arbitrary value of x, which we set without loss of generality to $x = 0$; that is to say, we look for *even* solutions, and for now we restrict the domain for Equation (4.3.19) to $x \geq 0$.

To make progress, firstly we rewrite Equation (4.3.19) as

$$-H_0\phi + \left(1 + 2\eta\phi^2\right)\phi'' + \lambda\phi^3 + 2\eta(\phi')^2\phi = 0, \tag{4.3.22}$$

where we have suppressed the argument x of the function ϕ. Equation (4.3.22) is an autonomous equation for ϕ, which allows us to look for solutions in the *phase space*, where ϕ' is a function of ϕ. In order for ϕ' to be a *well-defined* function of ϕ for all $x \geq 0$, it must be the case that every value of $\phi(x \geq 0)$ gives one and only one value of ϕ'. For now we assume this to be the case, and we will verify it once we have found $\phi(x)$. We define

$$h(\phi) := \phi', \tag{4.3.23}$$

and write

$$\phi'' \equiv \frac{\mathrm{d}\phi'}{\mathrm{d}\phi}\phi' = hh_\phi, \tag{4.3.24}$$

where the subscript ϕ denotes differentiation with respect to ϕ. We then define

$$y(\phi) := h(\phi)^2 = (\phi')^2, \tag{4.3.25}$$

so that

$$y_\phi = 2hh_\phi = 2\phi'', \tag{4.3.26}$$

and we multiply Equation (4.3.22) by 2 to obtain

$$\left(1 + 2\eta\phi^2\right)y_\phi + 4\eta\phi y = 2H_0\phi - 2\lambda\phi^3. \tag{4.3.27}$$

The left-hand side of Equation (4.3.27) is the total derivative of $(1 + 2\eta\phi^2)y$ with respect to ϕ. We therefore have

$$\begin{aligned} y &= \frac{\int \left(2H_0\phi - 2\lambda\phi^3\right)\mathrm{d}\phi}{1 + 2\eta\phi^2} \\ &= \frac{H_0\phi^2 - \lambda\phi^4/2 + C}{1 + 2\eta\phi^2}. \end{aligned} \tag{4.3.28}$$

The integration constant C is determined by considering the limit $x \to \infty$, in which $\phi^2 \to 0$ and $y = (\phi')^2 \to 0$. We therefore have $C = 0$. Now we note that if $H_0 \leq 0$, then the right-hand side of Equation (4.3.28) is negative whenever $\phi \neq 0$, so it cannot equal the left-hand side which is $(\phi')^2$. Thus, if $H_0 \leq 0$ then the only $\phi(x)$ satisfying Equation (4.3.28) is identically zero. We therefore require

$$H_0 > 0, \tag{4.3.29}$$

so that non-trivial solutions are at least possible. Multiplying Equation (4.3.28) by $4\phi^2$, we obtain

$$\left(2\phi\phi'\right)^2 = \frac{4H_0\phi^4 - 2\lambda\phi^6}{1 + 2\eta\phi^2}. \tag{4.3.30}$$

We then define

$$\Phi := \phi^2, \tag{4.3.31}$$

so that Equation (4.3.30) becomes

$$\left(\Phi'\right)^2 = \frac{4H_0\Phi^2 - 2\lambda\Phi^3}{1 + 2\eta\Phi}. \tag{4.3.32}$$

Now, if we had restricted the domain of Equation (4.3.19) to $x < 0$ instead of $x \geq 0$, we would have still derived exactly Equation (4.3.32). Thus, we may say $\Phi(x) = \phi(x)^2$ *for all* real x, and that globally, whenever ϕ satisfies Equation (4.3.19), Equation (4.3.32) holds. The converse, that globally whenever Φ solves Equation (4.3.32), $\phi = \pm\sqrt{\Phi}$ solves Equation (4.3.19), holds under one condition: since the derivation from Equation (4.3.19) to Equation (4.3.32) involved a multiplication by $\phi^2 \equiv \Phi$, the backwards derivation is valid if and only if $\Phi \neq 0$. In other words: say we have a global Φ solution to Equation (4.3.32); wherever $\Phi \neq 0$, we can use $\Phi = \phi^2$ to recover the ϕ solution to Equation (4.3.19), but at any x where $\Phi = 0$, we cannot. We therefore aim to find a solution to Equation (4.3.32) which is globally positive, and satisfies

$$\int_{-\infty}^{\infty} \Phi(x)\ \mathrm{d}x = 1. \tag{4.3.33}$$

In fact, Φ is by definition non-negative; and if Φ globally satisfies Equations (4.3.32) and (4.3.33), is at least twice-differentiable and has vanishing derivatives at infinities, then we can *prove* that Φ never equals zero, as we do over the next 12 steps ((i) to (xii)).

Firstly we claim that:

(i) $\Phi(x)$ *must attain its global upper bound of* $2H_0/\lambda$ *at some finite* x*, and every local maximum of* $\Phi(x)$ *must also be a global maximum.*

The proof of this claim is as follows. Since $\Phi(x)$ is not identically constant (otherwise Equation (4.3.33) would be violated), and since

$$\lim_{x\to\pm\infty} \Phi(x) = 0, \tag{4.3.34}$$

$\Phi(x)$ must have at least one turning point at some finite x and positive Φ. But we observe from Equation (4.3.32) that Φ' vanishes if and only if $\Phi = 0$ or $2H_0/\lambda > 0$. Therefore, $\Phi(x)$ must attain its global upper bound of $2H_0/\lambda$ at least once, and no other local maximum value is possible. This concludes the proof.

We further propose that:

(ii) *Wherever* $\Phi(x)$ *attains its maximum value, say at* $x = x_{\max}$*, the second derivative* Φ'' *does not vanish there.*

The proof is as follows. On the one hand, we have

$$\Phi'' \equiv 2\phi\phi'' + 2(\phi')^2, \tag{4.3.35}$$

as well as

$$\begin{aligned} \phi' &\equiv \Phi'/(2\phi) \\ &= 0 \quad \text{when } x = x_{\max}, \end{aligned} \tag{4.3.36}$$

which together imply

$$\Phi'' = 2\phi\phi'' \quad \text{when } x = x_{\max}. \tag{4.3.37}$$

(Dividing by ϕ in Equation (4.3.36) is permissible because when $x = x_{\max}$, we know that $\phi \neq 0$.) On the other hand, instead of rewriting Equation (4.3.19) as Equation (4.3.22), we could have rewritten it as

$$\eta\phi\Phi'' = H_0\phi - \phi'' - \lambda\phi^3. \tag{4.3.38}$$

Combining Equations (4.3.37) and (4.3.38), we have

$$\left(\frac{1}{2\phi} + \eta\phi\right)\Phi'' = H_0\phi - \lambda\phi^3 \quad \text{when } x = x_{\max}, \tag{4.3.39}$$

which we multiply by 2ϕ to obtain

$$\Phi'' = \frac{2H_0\Phi - 2\lambda\Phi^2}{1 + 2\eta\Phi} \quad \text{when } x = x_{\max}. \tag{4.3.40}$$

Since

$$\Phi(x_{\max}) = \frac{2H_0}{\lambda}, \tag{4.3.41}$$

it follows from Equation (4.3.40) that

$$\Phi''(x_{\max}) = \frac{-4H_0^2}{\lambda + 4\eta H_0} < 0, \tag{4.3.42}$$

as required.

A corollary of the above proposition is that:

(iii) *There must exist some neighbourhood of $x = x_{\max}$ containing no maxima of $\Phi(x)$ other than at $x_{\max}$ itself. We say that $\Phi(x)$ has an* isolated maximum *at $x = x_{\max}$.*

To prove this corollary, we suppose it is false, so that every neighbourhood of $x = x_{\max}$ contains some $x \neq x_{\max}$ at which $\Phi(x)$ is maximal. Then, by choosing x-values from smaller and smaller neighbourhoods of $x_{\max}$, we would be able to construct a sequence x_n approaching $x_{\max}$ such that $\Phi(x)$ is maximal at every x_n, with

$$\Phi(x_n) = \Phi(x_{\max}) \quad \text{for all } n. \tag{4.3.43}$$

But this leads to a contradiction. Indeed, for every x_n we have the Taylor expansion

$$\Phi(x_n) = \Phi(x_{\max}) + \frac{\Phi''(x_{\max})}{2}(x_n - x_{\max})^2 + \mathcal{O}\Big((x_n - x_{\max})^3\Big), \tag{4.3.44}$$

where the first derivative of Φ is absent because $\Phi(x_{\max})$ is maximal; so it follows that

$$\Phi''(x_{\max}) = \lim_{n\to\infty} 2 \cdot \frac{\Phi(x_n) - \Phi(x_{\max})}{(x_n - x_{\max})^2} = \lim_{n\to\infty} 2 \cdot \frac{0}{(x_n - x_{\max})^2} = 0, \tag{4.3.45}$$

which contradicts the previous proposition, in particular Equation (4.3.42). Therefore the corollary is proven.

Due to the translational invariance of Equation (4.3.32), meaning if $\Phi(x)$ is a solution then so is $\Phi(x + c)$ for any constant c, we can require without loss of generality that:

(iv) *$\Phi(x)$ has an isolated maximum at $x = 0$, and we define*

$$\Phi_0 := \Phi(0) = \frac{2H_0}{\lambda}. \tag{4.3.46}$$

Now we claim that:

(v) *There exists $b > 0$, which may be infinite, such that*

$$\lim_{x \to b^-} \Phi(x) = 0, \quad \Phi(x) \neq 0 \text{ for } 0 < x < b. \tag{4.3.47}$$

The proof of this claim is as follows. If $\Phi(x) \neq 0$ for $0 < x < \infty$, then b is infinite, and we are done. Therefore we suppose $\Phi(x) = 0$ for some $0 < x < \infty$, and then the set

$$\mathcal{M}_1 = \{x : 0 < x < \infty \text{ and } \Phi(x) = 0\} \tag{4.3.48}$$

must have a minimum. Indeed, if it does not, then there would be a sequence $x_n > 0$ such that, as $n \to \infty$, $x_n \to 0$ and $\Phi(x_n) \to 0$; but this would contradict the fact that $\Phi(x)$ is continuous at $x = 0$ and takes value $\Phi_0 > 0$ there. Now, letting

$$b = \min \mathcal{M}_1, \tag{4.3.49}$$

then we are done.

Our next proposition, once Φ_0 and b are established, is that:

(vi) *The $\Phi(x)$ solution is unique for $0 \leq x < b$.*

We prove this as follows. If $\Phi(x)$ is maximal at any $0 < x < \infty$, then the set

$$\mathcal{M}_2 = \{x : 0 < x < \infty \text{ and } \Phi(x) \text{ is maximal at } x\} \tag{4.3.50}$$

must have a minimum, because otherwise we would have a contradiction to the fact that $\Phi(x)$ has an *isolated* maximum at $x = 0$. Let

$$x_2 = \min \mathcal{M}_2, \tag{4.3.51}$$

and suppose $x_2 < b$. Since $\Phi(0)$ and $\Phi(x_2)$ are maximal, and since $\Phi(x)$ is not maximal for $0 < x < x_2$, and since $\Phi(x)$ is continuous, $\Phi(x)$ must attain its minimum value at some point x_1 with $0 < x_1 < x_2$. But that minimum value can only be 0 (recall that only $\Phi = 0$ and $\Phi = \Phi(0)$ cause Φ' to vanish), and so we have $\Phi(x_1) = 0$ where $x_1 < x_2 < b$, contradicting the fact that $\Phi(x) \neq 0$ for $0 < x < b$. Therefore, we cannot have $x_2 < b$; and since by definition we cannot have $x_2 = b$ either, we must have $x_2 > b$. Since Φ' vanishes only at maxima (where $\Phi = \Phi_0$) and minima (where $\Phi = 0$), and since we have just established that Φ has no maxima or minima for $0 < x < b$, it follows that Φ' is

non-vanishing for $0 < x < b$, and therefore $\Phi(x)$ is *strictly* decreasing for $0 \leq x < b$. Thus, from Equation (4.3.32) we have

$$\Phi' = -\sqrt{\frac{4H_0\Phi^2 - 2\lambda\Phi^3}{1+2\eta\Phi}} \quad \text{for } 0 \leq x < b, \tag{4.3.52}$$

and using Equation (4.3.46) we further deduce

$$\Phi' = -g(\Phi) := -2\sqrt{H_0}\Phi\sqrt{\frac{1-\Phi/\Phi_0}{1+2\eta\Phi}} \quad \text{for } 0 \leq x < b,\ \Phi_0 \geq \Phi > 0. \tag{4.3.53}$$

Now consider some Φ_1, Φ_2 with $0 < \Phi_2 < \Phi_1 < \Phi_0$. For $\Phi_2 \leq \Phi \leq \Phi_1$, the function $g(\Phi)$ is continuous and non-zero, so the reciprocal function $1/g(\Phi)$ is continuous and bounded, and therefore Riemann integrable from $\Phi = \Phi_2$ to $\Phi = \Phi_1$. But the integrability of $1/g(\Phi)$ from $\Phi = \Phi_2$ to $\Phi = \Phi_0$ is less straightforward, since $\lim_{\Phi\to\Phi_0} g(\Phi) = 0$, which means $1/g(\Phi)$ becomes unbounded as $\Phi \to \Phi_0$. Fortunately, $\Phi = \Phi_0$ is an *integrable singularity* of the function $1/g(\Phi)$, because the Puiseux series of $1/g(\Phi)$ about $\Phi = \Phi_0$ is $\mathcal{O}(|\Phi - \Phi_0|^{-1/2})$. Indeed the Puiseux series is $(-2\sqrt{H_0})^{-1}\sqrt{(1+2\eta\Phi_0)/\Phi_0}\ |\Phi - \Phi_0|^{-1/2} + \mathcal{O}(|\Phi - \Phi_0|^{1/2})$. Therefore $1/g(\Phi)$ is Riemann integrable from $\Phi = \Phi_2$ to $\Phi = \Phi_0$. This means that for any $\widetilde{\Phi}$ satisfying $0 < \widetilde{\Phi} \leq \Phi_0$, we may make use of Equation (4.3.53) to write

$$\int_{\widetilde{\Phi}}^{\Phi_0} \frac{1}{g(\Phi)}\ \mathrm{d}\Phi = \int_{\widetilde{\Phi}}^{\Phi_0} -\frac{\mathrm{d}x}{\mathrm{d}\Phi}\ \mathrm{d}\Phi = x(\widetilde{\Phi}) - x(\Phi_0) = x(\widetilde{\Phi}), \tag{4.3.54}$$

which is an equation that, given $\widetilde{\Phi}$, uniquely determines a corresponding x with $0 \leq x < b$. The left-hand side of Equation (4.3.54) is a strictly decreasing function of $\widetilde{\Phi}$, meaning $x(\widetilde{\Phi})$ has a unique inverse function which is also strictly decreasing, $\widetilde{\Phi}(x)$, on the domain $0 \leq x < b$. Thus, Equation (4.3.54) provides a bijective correspondence between the set of $\widetilde{\Phi}$ with $0 < \widetilde{\Phi} \leq \Phi_0$ and the set of x with $0 \leq x < b$, and this correspondence provides the unique solution to Equation (4.3.32) that we sought. Our proposition is therefore constructively proven. We note also that Equation (4.3.53) implies the corollary:

(vii) $\Phi(x)$ *is strictly decreasing for* $0 \leq x < b$.

Now, using exactly the same arguments as above, we could have found that:

(viii) *There exists some* $a < 0$*, which may be infinite, such that* $\Phi(x)$ *is strictly increasing for* $a < x \leq 0$*, and* $\lim_{x\to a^+} \Phi(x) = 0$*, and* $\Phi(x)$ *is the unique solution for* $a < x \leq 0$*. We can therefore consider Equation* (4.3.32) *on its* domain of uniqueness*,* $a < x < b$*, where Equation* (4.3.32) *is identical to*

$$\Phi' = G(x, \Phi) := -\mathrm{sgn}(x)g(\Phi), \tag{4.3.55}$$

where g is defined by Equation (4.3.53)*, and* sgn *is the sign function.*

So far, we have established the following. If Equation (4.3.32) has a solution $\Phi(x)$ which is globally non-negative and at least twice-differentiable, has vanishing derivatives at infinities and unit integral over the real line, then Φ also has the following properties: it satisfies the condition (4.3.46), is positive and strictly decreasing on $0 \leq x < b$ for some $b > 0$ which may be infinite, is positive and strictly increasing on $a < x \leq 0$ for some $a < 0$ which may be infinite, and $\lim_{x\to b^-} \Phi(x) = \lim_{x\to a^+} \Phi(x) = 0$, and $\Phi(x)$ is the unique solution to Equation (4.3.32) for $a < x < b$. We have also argued that we can use this Φ solution and the relation $\Phi = \phi^2$ to deduce a ϕ solution to the stationary GNLSE, Equation (4.3.19), *on the condition that* $\Phi \neq 0$. That is to say, the equivalence between Equations (4.3.19) and (4.3.32) breaks down outside the interval (a, b). We would therefore like to show that both a and b are infinite, because that would mean $\Phi(x)$ is positive on $-\infty < x < \infty$.

We proceed to describe a method which, given λ and η, determines the unique $\Phi(x)$ for $a < x < b$, and also determines a, b and H_0 in the process. Indeed we will show that:

(ix) *For any λ and any η, both a and b are infinite.*

Our method is as follows. For $0 \leq x < b$, consider the change of variable,

$$Z(\Phi) := \operatorname{arsech}\left(Y(\Phi)\right), \quad \text{where } Y(\Phi) := \sqrt{\frac{\Phi}{\Phi_0}} = \sqrt{\frac{\lambda\Phi}{2H_0}}. \tag{4.3.56}$$

$\Phi(x)$ is a bijection from the interval $[0, b)$ to the interval $(0, \Phi_0]$, $Y(\Phi)$ is a bijection from $(0, \Phi_0]$ to $(0, 1]$, and the inverse sech function, arsech, is a bijection from $(0, 1]$ to $[0, \infty)$. Therefore, all the coordinate transformations are invertible. For $a < x \leq 0$, we consider exactly the same transformations as Equation (4.3.56), except that the map $x \mapsto Z$ now is a bijection from the interval $(a, 0]$ to the interval $[0, \infty)$. Differentiating Z with respect to x we find, for $a < x < b$,

$$\begin{aligned} Z' &= Z_Y \cdot Y_\Phi \cdot \Phi' \\ &= \frac{-1}{Y\sqrt{1-Y^2}} \cdot \frac{1}{2\sqrt{\Phi_0\Phi}} \cdot \Big[-\operatorname{sgn}(x) g(\Phi) \Big] \\ &= \frac{\operatorname{sgn}(x)}{2\Phi\sqrt{1-\Phi/\Phi_0}} \cdot g(\Phi) \\ &= \frac{\operatorname{sgn}(x)\sqrt{H_0}}{\sqrt{1+2\eta\Phi}}, \end{aligned} \tag{4.3.57}$$

where we have used definition (4.3.53) of $g(\Phi)$. Moreover, from Equation (4.3.56) it also follows that

$$2\eta\Phi = 2\eta\Phi_0 Y^2 = 2\eta\frac{2H_0}{\lambda}\mathrm{sech}^2 Z. \tag{4.3.58}$$

Defining

$$\nu := \frac{4\eta H_0}{\lambda}, \tag{4.3.59}$$

and utilising Equation (4.3.58), we rewrite Equation (4.3.57) as

$$Z' = \frac{\mathrm{sgn}(x)\sqrt{H_0}}{\sqrt{1+\nu\ \mathrm{sech}^2 Z}}. \tag{4.3.60}$$

Now, we have $Z(x=0)=0$. We can therefore integrate Equation (4.3.60), obtaining

$$\mathrm{sgn}(x)\sqrt{H_0}\int_0^x \mathrm{d}\widetilde{x} = \int_0^Z \sqrt{1+\nu\ \mathrm{sech}^2\widetilde{Z}}\ \mathrm{d}\widetilde{Z}, \tag{4.3.61}$$

which yields

$$\mathrm{sgn}(x)\sqrt{H_0}\ x = \mathrm{arsinh}\left(\frac{\sinh Z}{\sqrt{1+\nu}}\right) + \sqrt{\nu}\ \arctan\left(\frac{\sqrt{\nu}\ \sinh Z}{\sqrt{\nu+\cosh^2 Z}}\right). \tag{4.3.62}$$

Now we can determine the values of a and b. In the limit $Z\to+\infty$, the definition of the coordinate transformation (4.3.56) dictates that we must have either $x\to a$ or $x\to b$; at the same time, Equation (4.3.62) dictates that we must have $x\to\pm\infty$, because the arctan function on the right-hand side of Equation (4.3.62) is bounded whilst the arsinh function diverges to $+\infty$. It therefore follows that the interval (a,b) is the real line. This implies, as we have already argued, that:

(x) *Equations* (4.3.19) *and* (4.3.32) *are globally equivalent.*

The next step in completely solving Equation (4.3.32) is to rewrite Equation (4.3.62) as an expression for x in terms of Φ, so that we can invert the expression to find $\Phi(x)$. By definition (4.3.56), we have

$$\cosh^2 Z = \frac{1}{Y^2} = \frac{\Phi_0}{\Phi}, \tag{4.3.63}$$

and it follows that

$$\sinh^2 Z = \cosh^2 Z - 1 = \frac{\Phi_0}{\Phi} - 1. \tag{4.3.64}$$

Since Z is by definition non-negative, we must take the positive square root,

$$\sinh Z = \sqrt{\frac{\Phi_0}{\Phi} - 1}. \tag{4.3.65}$$

Then Equation (4.3.62) becomes

$$\operatorname{sgn}(x)\sqrt{H_0}\ x = \operatorname{arsinh}\sqrt{\frac{1-(\Phi/\Phi_0)}{(1+\nu)\,(\Phi/\Phi_0)}} + \sqrt{\nu}\ \arctan\sqrt{\frac{\nu\,(1-(\Phi/\Phi_0))}{1+(\nu\Phi/\Phi_0)}}, \tag{4.3.66}$$

and we claim that:

(xi) *Given* $\Phi_0 > 0$ *and* $-\infty < x < \infty$*, Equation* (4.3.66) *uniquely determines a value of* $\Phi > 0$.

The proof is as follows. If $x = 0$, then immediately from Equation (4.3.66) we have $\Phi = \Phi_0$, and we are done. If $x \neq 0$, consider the function

$$\mathcal{G}(\Phi;\{\Phi_0, x\}) := \operatorname{arsinh}\sqrt{\frac{1-(\Phi/\Phi_0)}{(1+\nu)\,(\Phi/\Phi_0)}} + \sqrt{\nu}\ \arctan\sqrt{\frac{\nu\,(1-(\Phi/\Phi_0))}{1+(\nu\Phi/\Phi_0)}} - \operatorname{sgn}(x)\sqrt{H_0}\ x, \tag{4.3.67}$$

where Φ_0 and x are parameters. Differentiating Equation (4.3.67) with respect to Φ gives

$$\frac{\mathrm{d}\mathcal{G}}{\mathrm{d}\Phi} = -\frac{1}{2\Phi}\sqrt{\frac{1+(\nu\Phi/\Phi_0)}{1-(\Phi/\Phi_0)}} < 0 \quad \text{for } \Phi > 0. \tag{4.3.68}$$

This means $\mathcal{G}$ is strictly decreasing for $\Phi > 0$. Since $\mathcal{G}(\Phi) \to \infty$ in the limit $\Phi \to 0$, and

$$\mathcal{G}(\Phi_0;\{\Phi_0, x\}) = -\operatorname{sgn}(x)\sqrt{H_0}\ x < 0, \tag{4.3.69}$$

and $\mathcal{G}$ is continuous, we must have $\mathcal{G}(\Phi)$ vanishing exactly once in $0 < \Phi < \Phi_0$. This concludes the proof.

We observe that in Equation (4.3.66) the left-hand side is invariant under $x \mapsto -x$. Therefore, we have $\Phi(-x) = \Phi(x)$ for all real x. In practice, given any $\Phi_0 > 0$ and $-\infty < x < \infty$, we can compute $\Phi(x)$ by locating the zero of $\mathcal{G}(\Phi;\{\Phi_0, x\})$. However, the value of Φ_0 cannot be freely chosen. Instead, it is determined by the normalisation condition (4.3.33) which, since $\Phi(x)$ is an even function, now reads

$$1 = 2\int_0^\infty \Phi(x)\ \mathrm{d}x = 2\int_{Z=0}^{Z=\infty} \frac{\Phi}{Z'_+}\ \mathrm{d}Z, \tag{4.3.70}$$

where the Z'_+ is the positive-x branch of Z' [cf. Equation (4.3.60)]. It then follows that

$$1 = 2\int_0^\infty \frac{\Phi\sqrt{1+\nu\ \operatorname{sech}^2 Z}}{\sqrt{H_0}}\ \mathrm{d}Z. \tag{4.3.71}$$

Using $\Phi = \Phi_0\ \operatorname{sech}^2 Z$, we deduce

$$\frac{\sqrt{H_0}}{2\Phi_0} = \int_0^\infty \operatorname{sech}^2 Z\sqrt{1+\nu\ \operatorname{sech}^2 Z}\ \mathrm{d}Z \tag{4.3.72a}$$

$$= \frac{1}{2} + \frac{(1+\nu)\arctan\sqrt{\nu}}{2\sqrt{\nu}}. \tag{4.3.72b}$$

Multiplying Equation (4.3.72b) by $2\sqrt{\nu}$, replacing H_0 by $\lambda\Phi_0/2$, and replacing ν by

$$\nu = \frac{4\eta H_0}{\lambda} = 2\eta\Phi_0, \tag{4.3.73}$$

we obtain the following transcendental equation for Φ_0:

$$\sqrt{\lambda\eta} = \sqrt{2\eta\Phi_0} + (1 + 2\eta\Phi_0)\arctan\sqrt{2\eta\Phi_0}. \tag{4.3.74}$$

We claim that:

(xii) *Given* (λ, η)*, Equation* (4.3.74) *uniquely determines* Φ_0*.*

To prove this claim, we consider the function

$$\mathcal{F}(\Phi_0) := \sqrt{2\eta\Phi_0} + (1 + 2\eta\Phi_0)\arctan\sqrt{2\eta\Phi_0} - \sqrt{\lambda\eta}. \tag{4.3.75}$$

Differentiating $\mathcal{F}(\Phi_0)$ with respect to Φ_0, we find

$$\frac{\mathrm{d}\mathcal{F}}{\mathrm{d}\Phi_0} = 2\eta\left(\frac{1}{\sqrt{2\eta\Phi_0}} + \arctan\sqrt{2\eta\Phi_0}\right) > 0 \quad \text{for } \Phi_0 > 0. \tag{4.3.76}$$

This means $\mathcal{F}(\Phi_0)$ is strictly increasing for $\Phi_0 > 0$. Since

$$\lim_{\Phi_0\to 0}\mathcal{F}(\Phi_0) = -\sqrt{\lambda\eta} < 0, \tag{4.3.77}$$

and $\mathcal{F}(\Phi_0) \to \infty$ in the limit $\Phi_0 \to \infty$, and $\mathcal{F}$ is continuous, we must have $\mathcal{F}$ vanishing at exactly one value of $\Phi_0 > 0$. Given parameters λ and η, we can compute Φ_0 by locating the zero of $\mathcal{F}(\Phi_0)$, and Φ_0 uniquely determines the energy eigenvalue,

$$H_0 = \frac{\lambda\Phi_0}{2}. \tag{4.3.78}$$

We can then feed the values Φ_0 and H_0 into Equation (4.3.66), and then for every real x we can find $\Phi(x)$ by means we have described.

In summary, given λ and η, Equations (4.3.46), (4.3.66) and (4.3.74) together constitute an analytical solution to Equation (4.3.32), which is globally equivalent to Equation (4.3.19); we therefore have the unique global solution to Equation (4.3.19) satisfying all the constraints we have imposed.

We note that if the parameter $\eta \to 0$, we should recover the solution to the nonlinear Schrödinger equation with focusing cubic nonlinearity, given by Equation (4.3.21); and indeed we do. Firstly, in the limit $\eta \to 0$, we have $\nu \to 0$, which means we cannot use Equation (4.3.74) to determine Φ_0, because the derivation of Equation (4.3.74) involved a

multiplication by $\sqrt{\nu}$. Instead, we must extract Φ_0 from Equation (4.3.72a). In the limit $\nu \to 0$, Equation (4.3.72a) is simply

$$\sqrt{\frac{\lambda}{8\Phi_0}} = \int_0^\infty \operatorname{sech}^2 Z \, \mathrm{d}Z = 1. \tag{4.3.79}$$

It follows that $\Phi_0 = \lambda/8$, agreeing with Equation (4.3.21). Then Equation (4.3.46) determines the eigenvalue $H_0 = \lambda\Phi_0/2 = \lambda^2/16$, again agreeing with Equation (4.3.21). Finally, when $\nu \to 0$, Equation (4.3.66) is simply

$$\operatorname{sgn}(x)\sqrt{H_0}\, x = \operatorname{arsinh}\sqrt{\frac{\Phi_0}{\Phi} - 1}, \tag{4.3.80}$$

which is equivalent to

$$\frac{\Phi_0}{\Phi} = 1 + \sinh^2\left(\sqrt{H_0}\, x\right) = \cosh^2\left(\frac{\lambda x}{4}\right), \tag{4.3.81}$$

and therefore

$$\Phi = \Phi_0 \operatorname{sech}^2\left(\frac{\lambda x}{4}\right), \tag{4.3.82}$$

agreeing with Equation (4.3.21) once more.

In Section 4.3.2, we alluded to the fact that had we chosen the wavenumber k in the stationary ansatz (4.3.9) to satisfy $\cos(k) = -1$, instead of the $\cos(k) = 1$ that we did choose, then we would have obtained an equation for ϕ which had no square-normalisable solution. Here, we verify that claim.

If $\cos(k) = -1$ in Equation (4.3.16), then instead of Equation (4.3.22), we obtain

$$-\widetilde{H_0}\phi + \left(-1 + 2\eta\phi^2\right)\phi'' + \lambda\phi^3 + 2\eta(\phi')^2\phi = 0, \tag{4.3.83}$$

where we have suppressed the argument x of the function ϕ, and

$$\widetilde{H_0} := H_0 + 4 \tag{4.3.84}$$

is an eigenvalue. Rewriting Equation (4.3.83) in phase space and defining $y(\phi) := (\phi')^2$, as we did for the $\cos(k) = 1$ case, we have the following relation between y and ϕ, which is analogous to Equation (4.3.28):

$$y = \frac{\widetilde{H_0}\phi^2 - \lambda\phi^4/2}{-1 + 2\eta\phi^2}. \tag{4.3.85}$$

Since ϕ is required to be bounded and smooth, y must be well-defined for every ϕ. Therefore we must have $-1+2\eta\phi^2 \neq 0$ for all values of x. But $-1+2\eta\phi^2$ itself is a continous function of ϕ, which means that we must have either $-1+2\eta\phi^2 > 0$ or $-1+2\eta\phi^2 < 0$ for all x. For ϕ to be square-normalisable, ϕ must be vanishing at $x \to \pm\infty$, which implies that we must have $-1+2\eta\phi^2 < 0$ for all x. Now that we have established that the denominator of the right-hand side of Equation (4.3.85) is always negative, the numerator must be non-positive, because the left-hand side is the square of a real function. We therefore have that either ϕ is identically zero, which trivially satisfies Equation (4.3.83) but is not square-normalisable, or that ϕ^2 takes values in the following range:

$$\frac{2\widetilde{H_0}}{\lambda} \leq \phi^2 < \frac{1}{2\eta}. \tag{4.3.86}$$

If the eigenvalue $\widetilde{H_0}$ is non-negative, then any ϕ which satisfies Equation (4.3.86) cannot possibly be square-normalisable over the real line. Thus, we must require

$$\widetilde{H_0} < 0. \tag{4.3.87}$$

This is problematic, because examining Equation (4.3.85) we see that $y \equiv (\phi')^2$ vanishes if and only if $\phi^2 = 2\widetilde{H_0}/\lambda$, and requiring $\widetilde{H_0} < 0$ implies that ϕ' never vanishes, in other words ϕ is either strictly increasing or strictly decreasing over the real line. Such a function cannot possibly be square-normalisable. Thus, we have established that $\cos(k) = -1$ cannot lead to a physically meaningful ϕ solution, thereby justifying our choice of $\cos(k) = 1$.

4.3.4 Numerical Solutions to the Stationary-State Equations

With the help of analytical results we have already obtained, we use an iterative numerical scheme in this Section to compute stationary solutions to our system, in particular to Equation (4.3.8) for the stationary electron probability density, $|\psi_n|^2$. We will compare our numerical solutions with the approximate solutions we obtained via the continuum limit in Section 4.3.3.

We briefly outline the numerical scheme here, which is a variation on the convergence algorithm that we described in detail in Section 3.3.1, where we also described the motivation for adopting this non-standard approach.

We consider the following equation, written in terms of some complex-valued $\widetilde{\psi}_n(\tau)$

and a parameter $\mathcal{H}_0$, which is a variant of Equation (4.3.8):

$$\begin{aligned}\rho^{-1}\frac{\mathrm{d}}{\mathrm{d}\tau}\widetilde{\psi}_n = &-\mathcal{H}_0\widetilde{\psi}_n + \left(\widetilde{\psi}_{n+1} + \widetilde{\psi}_{n-1} - 2\widetilde{\psi}_n\right) + \lambda\left|\widetilde{\psi}_n\right|^2\widetilde{\psi}_n \\ &+ \eta\left(\left|\widetilde{\psi}_{n+1}\right|^2 + \left|\widetilde{\psi}_{n-1}\right|^2 - 2\left|\widetilde{\psi}_n\right|^2\right)\widetilde{\psi}_n. \end{aligned} \tag{4.3.88}$$

If we write out the real and imaginary parts of Equation (4.3.88), for $\widetilde{\psi}_n = y_n + iz_n$, we obtain two equations which are symmetric with respect to re-labelling:

$$\begin{aligned}\rho^{-1}\dot{y}_n = &-\mathcal{H}_0 y_n + (y_{n+1} + y_{n-1} - 2y_n) + \lambda\left|\widetilde{\psi}_n\right|^2 y_n \\ &+ \eta\left(\left|\widetilde{\psi}_{n+1}\right|^2 + \left|\widetilde{\psi}_{n-1}\right|^2 - 2\left|\widetilde{\psi}_n\right|^2\right) y_n, \end{aligned} \tag{4.3.89a}$$

$$\begin{aligned}\rho^{-1}\dot{z}_n = &-\mathcal{H}_0 z_n + (z_{n+1} + z_{n-1} - 2z_n) + \lambda\left|\widetilde{\psi}_n\right|^2 z_n \\ &+ \eta\left(\left|\widetilde{\psi}_{n+1}\right|^2 + \left|\widetilde{\psi}_{n-1}\right|^2 - 2\left|\widetilde{\psi}_n\right|^2\right) z_n, \end{aligned} \tag{4.3.89b}$$

where

$$\left|\widetilde{\psi}_n\right|^2 = y_n^2 + z_n^2. \tag{4.3.90}$$

This symmetry enables us to set $y_n = z_n$, thereby decoupling the real and imaginary parts of $\widetilde{\psi}_n$, and without loss of generality simply consider the equation for y_n:

$$\begin{aligned}\rho^{-1}\dot{y}_n = &-\mathcal{H}_0 y_n + (y_{n+1} + y_{n-1} - 2y_n) \\ &+ 2\lambda {y_n}^3 + 2\eta\left({y_{n+1}}^2 + {y_{n-1}}^2 - 2{y_n}^2\right) y_n, \end{aligned} \tag{4.3.91}$$

on a grid defined by $n = 0, 1, \ldots, N$ with fictitious points and boundary terms $y_{-1} = y_0 = y_N = y_{N+1} = 0$. If y_n is some stationary y_n^0, then we must have

$$\mathcal{H}_0 y_n^0 = \left(y_{n+1}^0 + y_{n-1}^0 - 2y_n^0\right) + 2\lambda {y_n^0}^3 + 2\eta\left({y_{n+1}^0}^2 + {y_{n-1}^0}^2 - 2{y_n^0}^2\right) y_n^0, \tag{4.3.92}$$

for all n. We take some initial guess for $\mathcal{H}_0$ and some initial $y_n(0)$ with a global maximum at $n = n_0$, which is such a configuration that the value of $y_n(0)$ drops off significantly beyond $n = n_0 \pm 2$, and integrate Equation (4.3.91) forward in time. If the initial guess for $\mathcal{H}_0$ is sufficiently close to the $\mathcal{H}_0$ that eventually satisfies Equation (4.3.92), then $y_n(\tau > 0)$ will continue to exhibit the characteristic drop-off away from $n = n_0$. When we reach $\tau = 10^4\Delta\tau$ - an arbitrarily chosen time-interval which is moderate in length - we make use of $y_n(10^4\Delta\tau)$ to redefine $\mathcal{H}_0$ before performing further integration steps. Specifically, we use only three points in $y_n(10^4\Delta\tau)$, namely y_{n_0} and $y_{n_0\pm1}$, and let

$$\widetilde{\mathcal{H}}_{n_0} := \left(\frac{y_{n_0+1} + y_{n_0-1}}{y_{n_0}} - 2\right) + 2\lambda {y_{n_0}^0}^2 + 2\eta\left({y_{n_0+1}^0}^2 + {y_{n_0-1}^0}^2 - 2{y_{n_0}^0}^2\right), \tag{4.3.93}$$

and similarly $\widetilde{\mathcal{H}}_{n_0\pm1}$. The numerical stability of this scheme relies upon the values of y_{n_0} and $y_{n_0\pm1}$ being sufficiently far from zero. Assuming that is always the case, which is automatically verified if the scheme successfully produces stationary solutions, then for each n, $\widetilde{\mathcal{H}}_n$ is the value that $\mathcal{H}_0$ should take if y_n and $y_{n\pm1}$ were all taken from the stationary solution y_n^0. We then take the average of $\widetilde{\mathcal{H}}_{n_0}$ and $\widetilde{\mathcal{H}}_{n_0\pm1}$, defining

$$\widetilde{\mathcal{H}}_0' := \frac{1}{3}\left(\widetilde{\mathcal{H}}_{n_0-1} + \widetilde{\mathcal{H}}_{n_0} + \widetilde{\mathcal{H}}_{n_0+1}\right), \tag{4.3.94}$$

and redefine $\mathcal{H}_0$ according to

$$\mathcal{H}_0 \mapsto \frac{\mathcal{H}_0 + \widetilde{\mathcal{H}}_0'}{2}. \tag{4.3.95}$$

This process 'nudges' $\mathcal{H}_0$ closer to the value it needs to be. The new $\mathcal{H}_0$ obtained by Equation (4.3.95) is then fed back into Equation (4.3.91) before we continue to integrate the equation from $\tau = 10^4\Delta\tau$ to $\tau = 2\cdot 10^4\Delta\tau$, at which time we redefine $\mathcal{H}_0$ again, and so on. In practice, this algorithm converges concurrently in the y_n configuration and in the $\mathcal{H}_0$ value, within $\mathcal{O}(10^6)$ integration steps. Once convergence has occurred, one could make use of the fact that $\widetilde{\psi}_n = y_n + iz_n$ and $y_n = z_n$ to recover the stationary $\widetilde{\psi}_n$ solution to Equation (4.3.88). However our real aim is to express the stationary ψ_n solution to Equation (4.3.8) in terms of y_n^0. Indeed, if we seek stationary solutions to Equation (4.3.8) of the form

$$\psi_n^0(\tau) := \exp\left(i\rho H_0\tau\right)\phi_n^0, \tag{4.3.96}$$

for some time-independent ϕ_n^0 (we found an approximate ϕ_n^0 solution in the $N \gg 1$ limit in Section 4.3.3), then Equation (4.3.8) transforms into

$$\begin{aligned} &-H_0\phi_n^0 + \left(\phi_{n+1}^0 + \phi_{n-1}^0 - 2\phi_n^0\right) + \lambda\left|\phi_n^0\right|^2\phi_n^0 \\ &+\eta\left(\left|\phi_{n+1}^0\right|^2 + \left|\phi_{n-1}^0\right|^2 - 2\left|\phi_n^0\right|^2\right)\phi_n^0 = 0. \end{aligned} \tag{4.3.97}$$

Now, by making the identification

$$\mathcal{H}_0 \equiv H_0, \tag{4.3.98}$$

we observe that, if y_n^0 solves Equation (4.3.92), then

$$\phi_n^0 \equiv \sqrt{2}y_n^0 \tag{4.3.99}$$

solves Equation (4.3.97), and vice versa. We therefore have a way of translating the $\mathcal{H}_0$ and y_n^0 results from our numerical scheme to the eigenvalue H_0 and stationary solution ψ_n^0 to our system.

To use our numerical scheme, the initial $y_n(0)$ and initial guess for $\mathcal{H}_0$ should both come from the continuum approximation described in Section 4.3.3. In summary, then, given parameters (β, λ) (and η which is a combination of β, λ), we wish to find the stationary solution ψ_n^0 to the eigenvalule problem of Equation (4.3.8). In order to do so, we make use of approximations to ψ_n^0 and to the eigenvalue H_0 which we obtained in Section 4.3.3, feeding them as initial ansatz into the iterative numerical scheme that we have described in this Section. In practice, given all the (β, λ) that we have studied, we find that the our scheme always converges, in CPU times that are 3 to 4 orders of magnitude less than the CPU times of using a conventional method which involves summing over the entire lattice after each iteration.

In the stationary state, we can use the solution for $s_n = u_{n+1} - u_n$ given by Equation (4.3.3) to simplify the expression for the internal energy, E_b [cf. Equation (4.2.62)]. Using the superscript 0 to indicate the stationary state, we compute the *binding energy* of the stationary polaron as follows. Firstly, the expression (4.2.59) for $\langle \widehat{H}_\mathrm{e} \rangle / (\hbar\Omega)$ is unaffected by the fact that the electron is in a stationary state, but for the lattice energy [cf. Equation (4.2.60)], we now have

$$\frac{\langle \widehat{H}_\mathrm{p}^0 \rangle}{\hbar\Omega} = \frac{\kappa^2}{2} \sum_{n=0}^{N-1} \left[(\beta - 1)|\psi_{n+1}|^2 - (\beta + 1)|\psi_n|^2 \right]^2 . \tag{4.3.100}$$

Moreover, for interaction energy [cf. Equation (4.2.61)] we now have

$$\begin{aligned} \frac{\langle \widehat{H}_\mathrm{int}^0 \rangle}{\hbar\Omega} &= \kappa^2 \sum_{n=1}^{N-1} |\psi_n|^2 \Bigg[\Big((\beta - 1)|\psi_{n+1}|^2 - 2|\psi_n|^2 - (\beta + 1)|\psi_{n-1}|^2 \Big) \\ &\qquad + \beta \Big((\beta - 1)|\psi_{n+1}|^2 - 2\beta|\psi_n|^2 + (\beta + 1)|\psi_{n-1}|^2 \Big) \Bigg]. \\ &= -\kappa^2 \sum_{n=1}^{N-1} \Big[\Big(1 - \beta^2 \Big) |\psi_n|^2 \Big(|\psi_{n+1}|^2 + |\psi_{n-1}|^2 \Big) + 2 \Big(1 + \beta^2 \Big) |\psi_n|^4 \Big] \end{aligned} \tag{4.3.101}$$

Since $0 \leq \beta \leq 1$, every term in Equation (4.3.101) is non-positive, and no value of β can make $\langle \widehat{H}_\mathrm{int}^0 \rangle / (\hbar\Omega)$ zero. Thus, the interaction part of the polaron binding energy is always negative, meaning that the interaction between the electron and phonon makes the polaron more strongly bound; this is as we would expect.

Now, using Equation (4.3.7) for the definitions of λ and η, we deduce

$$\frac{\langle \widehat{H}^0_{\rm p} \rangle}{\hbar\Omega} = \frac{\rho\lambda}{8} \sum_{n=0}^{N-1} \left[(\beta-1)|\psi_{n+1}|^2 - (\beta+1)|\psi_n|^2 \right]^2 , \tag{4.3.102}$$

$$\begin{aligned} \frac{\langle \widehat{H}^0_{\rm int} \rangle}{\hbar\Omega} &= -\kappa^2 \sum_{n=1}^{N-1} \left[\left(1-\beta^2\right)|\psi_n|^2 \left(|\psi_{n+1}|^2 + |\psi_{n-1}|^2 - 2|\psi_n|^2 \right) + 4|\psi_n|^4 \right] \\ &= -\rho\eta \sum_{n=1}^{N-1} |\psi_n|^2 \left(|\psi_{n+1}|^2 + |\psi_{n-1}|^2 - 2|\psi_n|^2 \right) - \rho\lambda \sum_{n=1}^{N-1} |\psi_n|^4 . \end{aligned} \tag{4.3.103}$$

We therefore have the following expression for the binding energy of the stationary polaron, in units of meV:

$$\begin{aligned} E^0_{\rm b} = 5.3\rho \Bigg[2 &- \sum_{n=1}^{N-2} \left(\psi^*_{n+1}\psi_n + \psi^*_n \psi_{n+1} \right) + \frac{\lambda}{8} \sum_{n=0}^{N-1} \left[(\beta-1)|\psi_{n+1}|^2 - (\beta+1)|\psi_n|^2 \right]^2 \\ &- \eta \sum_{n=1}^{N-1} |\psi_n|^2 \left(|\psi_{n+1}|^2 + |\psi_{n-1}|^2 - 2|\psi_n|^2 \right) - \lambda \sum_{n=1}^{N-1} |\psi_n|^4 \Bigg] . \end{aligned} \tag{4.3.104}$$

In practice, some terms in Equation (4.3.104) are zero due to the boundary condition (4.2.46); nevertheless we have retained those terms in the sums for notational convenience.

We can make further progress by invoking the ansatz given by Equation (4.3.9) (we have argued that $k = 0$):

$$\psi_n = \phi(n - N/2) \exp\left(\frac{i H_0 J_1 t}{\hbar} \right) , \quad \Phi(x) = \phi(x)^2 . \tag{4.3.105}$$

where ϕ is a real, smooth function of a continuous variable x. The stationary state, $|\Psi^0\rangle = \sum_{n=0}^{N} \psi_n \exp\left(-\frac{it}{\hbar} \left(J_0 - 2J_1 \right) \right) \widehat{A}^\dagger_n |0\rangle$, not only solves the Schrödinger equation,

$$i\hbar \, \partial |\Psi^0\rangle / \partial t = \left(\widehat{H}_{\rm e} + \widehat{H}_{\rm int} \right) |\Psi^0\rangle , \tag{4.3.106}$$

but also solves

$$i\hbar \, \partial |\Psi^0\rangle / \partial t = \left(J_0 - 2J_1 - H_0 J_1 \right) |\Psi^0\rangle . \tag{4.3.107}$$

Comparing Equations (4.3.106) and (4.3.107) gives us

$$\frac{\langle H^0_{\rm e} \rangle + \langle H^0_{\rm int} \rangle - (J_0 - 2J_1)}{\hbar\Omega} = -H_0 \rho . \tag{4.3.108}$$

It then follows that

$$E^0_{\rm b} = 5.3\rho \left[-H_0 + \frac{\lambda}{8} \sum_{n=0}^{N-1} \left[(\beta-1)\,\Phi(n+1-N/2) - (\beta+1)\,\Phi(n-N/2) \right]^2 \right] . \tag{4.3.109}$$

Equation (4.3.109) holds *if* stationary solutions in the form of Equation (4.3.105) exist, and we proceed now to find such solutions numerically. But in Section 4.3.3 we already found approximations to such solutions in the continuum limit, and we could simply put those results into Equation (4.3.109) in order to approximate E_{b}^{0}.

Figure 4.1 shows how various aspects of the *approximate* stationary solutions depend upon the symmetry parameter β, and the effective coupling parameter λ (recall that the former is a measure of the spatial symmetry of the electron-phonon interaction, and the latter measures the strength of this interaction, while the value of the parameter ρ is fixed). These are the only two parameters that affect the stationary polaron's physical properties (as the parameter η is merely a convenient combination of β and λ).

Figure 4.1(a) shows how the maximum height and *half-width* of the approximate electron probability distribution $\Phi(x)$, in the stationary state, vary with β and λ. The maximum height of the distribution is also known as the electron's *maximum localisation probability*. As one would expect, the half-width is negatively correlated with Φ_0. The figure shows Φ_0 increasing with λ, and half-width decreasing with λ, and the rate of change of each quantity is greater given larger values of β. That is to say, the more spatially asymmetric the electron-phonon interaction is, the more influential λ is. The figure also has the following implication on the accuracy of $\Phi(x)$ as an approximation to the discrete stationary solution to our system. In a discrete solution, the physical interpretation of $|\psi_n|^2$ is the probability of the electron being localised around the n^{th} lattice node [cf. Section 2.1.5]. The normalisation condition is defined in terms of a sum, $\sum_{n=0}^{N}|\psi_n|^2 = 1$, and consequently we must have $|\psi_n|^2 \leq 1$ for all n. When a continuum solution $\Phi(x)$ is used to approximate the discrete $|\psi_n|^2$, Φ_0 is supposed to approximate $\max|\psi_n|^2$. Therefore, any continuum solution with $\Phi_0 > 1$ cannot be reliable as an approximant. When $\beta = 1$, Φ_0 exceeds 1 if λ is greater than 8, since $\Phi_0 = \lambda/8$.

In Figure 4.1(b), we see that H_0 increases with λ whilst the polaron's binding energy gains magnitude, meaning the larger λ is, the more strongly bound the polaron is. Once again, the larger β is, the more rapidly these quantities vary with λ. We note that the thick black curve for H_0, corresponding to $\beta = 1$, is exactly the graph of $H_0 = \lambda^2/16$, as Equation (4.3.21) dictated. Comparing Figure 4.1(a) and (b), we see that a polaron which is more strongly bound has a larger Φ_0 and a smaller half-width; in other words, it is more localised.

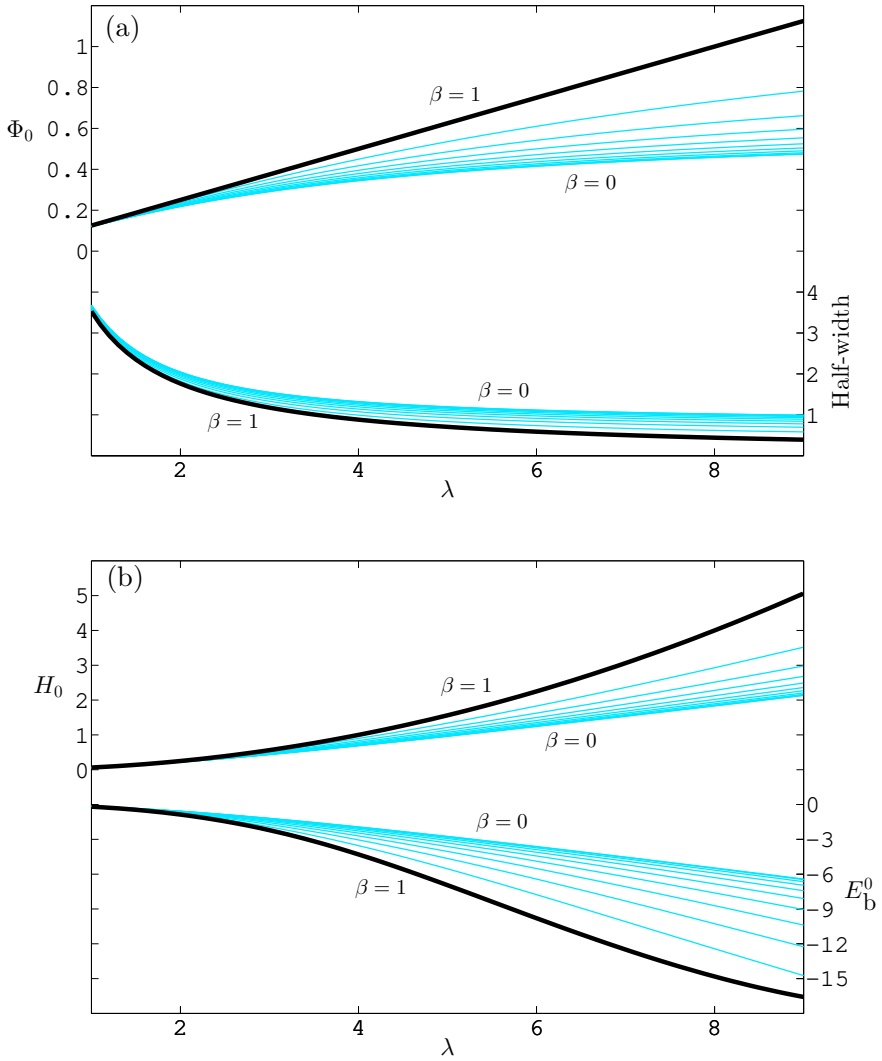

Figure 4.1: (a) The height of the approximate electron probability distribution (left axis), and the half-width of that distribution (right axis), as functions of λ parameterised by $\beta = 0, 0.1, 0.2, \ldots, 1$. (b) The approximate eigenvalue (left axis), and approximate binding energy (meV) of the stationary polaron (right axis), as functions of λ parameterised by $\beta = 0, 0.1, 0.2, \ldots, 1$.

Figure 4.2(a) contains information about two key aspects of the stationary polaron state, obtained numerically: the electron probability distribution, and the polaron binding energy. Qualitatively speaking, it is in agreement with predictions of the continuum approximation, as per Figure 4.1(a): as λ increases, the polaron becomes more localised, and more strongly bound. Moreover, the effect of increasing λ is more profound given larger values of β. However further comparison between Figure 4.1(a) and Figure 4.2(a) reveals a noteworthy difference. When $\beta = 1$, Φ_0 is a linear function of λ, whereas Figure 4.2(a)

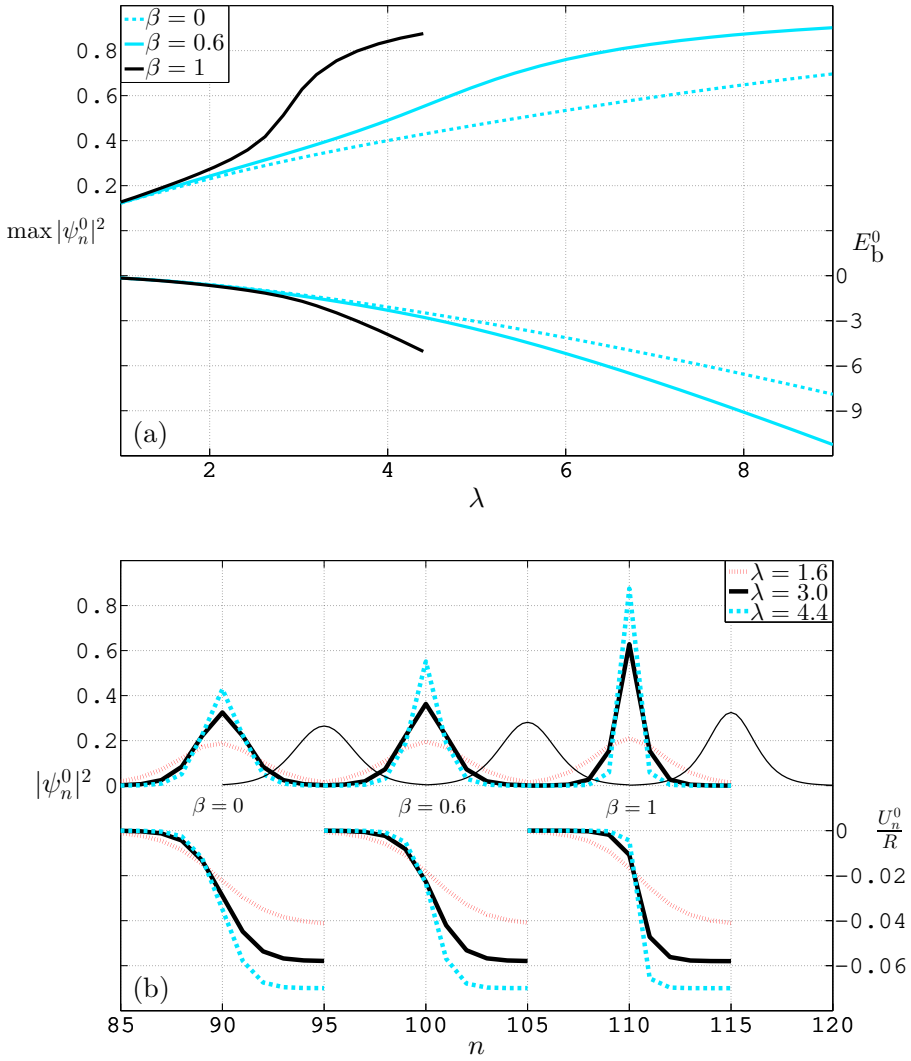

Figure 4.2: (a) In the stationary state, the electron's maximum localisation probability, $\max|\psi_n^0|^2$ (left axis), and polaron binding energy, E_b^0 (meV) (right axis), as functions of λ parametrised by $\beta = 0, 0.6, 1$. (b) Thick lines: stationary solutions parametrised by β and λ: the electron probability distribution $|\psi_n^0|^2$ (left axis) and associated lattice distortion U_n^0 in units of the equilibrium lattice spacing R (right axis). Solutions are shifted along the n-axis to avoid overlap. Thin lines: approximate stationary solutions obtained in the continuum limit; from left to right: $\beta = 0, 0.6, 1$, all with $\lambda = 3.0$.

suggests that $\max|\psi_n^0|^2$ (which is approximated by Φ_0 in the continuum limit) is not linearly dependent on λ. In fact, given any β, $\max|\psi_n^0|^2$ grows significantly faster with λ than Figure 4.1(a) predicts. Despite this, the growth of $\max|\psi_n^0|^2$ in Figure 4.2(a) eventually stalls when λ becomes sufficiently large. This is a manifestation of a fundamental difference between the continuum and discrete equations: the continuum equations place no limit on how large Φ_0 can be, whereas the discrete system limits $\max|\psi_n^0|^2$ to 1.

Figure 4.2(b) shows a selection of $|\psi_n^0|^2$ solutions. Comparing all the dotted (red) lines, which correspond to $\lambda = 1.0$ at various values of β, we see that they are essentially identical. This confirms the belief that when λ is small (close to 1), systems with different β-values unify, because $\lambda \approx 1$ represents the weak-coupling limit in which varying the intrinsic spatial asymmetry of the system makes little difference to the polaron binding energy. The figure also shows some stationary solutions to the other half of our system, namely the displacement U_n^0 of lattice units from their equilibrium positions, or lattice distortions. In order for the point-dipole model of lattice units to be valid, the lattice distortion must satisfy the condition $|U_{n+1}^0 - U_n^0| \ll R$ where R is the equilibrium lattice spacing [Bar07]. This condition is indeed fulfilled in the stationary polaron state, as we can infer from Figure 4.2(b) that $\max\left(|U_{n+1}^0 - U_n^0|/R\right) \sim \mathcal{O}(10^{-2})$.

Comparing all the dashed (blue) lines in Figure 4.2(b), which correspond to $\lambda = 4.4$ at various values of β, enables us to make the following observation. When $\beta = 0$, the U_n^0 solution is centred at the location of $\max|\psi_n^0|^2$, in the sense that its graph is rotationally symmetric about $n = 90$. This agrees with our understanding that when $\beta = 0$, i.e. when the electron-phonon interaction is spatially symmetric, the electron in the stationary state causes equal lattice distortion to its left and right. As β increases, the maximum magnitude of the lattice distortions remains the same, but the centre of U_n^0 shifts away from the location of $\max|\psi_n^0|^2$, in response to the decrease in spatial symmetry. When $\beta = 1$, the molecule at the location of $\max|\psi_n^0|^2$ ($n = 110$ in this case) is barely displaced, whereas molecules to the right of this point are displaced considerably. Now, the potential energy in the lattice is a sum over terms of the form $(U_{n+1}^0 - U_n^0)^2$, which is the square of the gradient of the U_n^0/R graph at site n, in appropriate units. In the stationary state, this gradient is zero except at a few sites around the location of $\max|\psi_n^0|^2$, and it is clear that solutions corresponding to larger values of β have steeper gradients there. We therefore conclude that, in the stationary state, systems with greater spatial asymmetry store more potential energy in the lattice.

In Figure 4.2(b) we also see a comparison between some $|\psi_n^0|^2$ solutions and their counterpart continuum approximations, $\Phi(x)$. In particular, we look at the thick solid (black) lines and, to their right, their accompanying thin solid (black) lines. The comparison reveals that, fixing λ, in this case $\lambda = 3.0$, $\Phi(x)$ is a more accurate approximant for $|\psi_n^0|^2$ when β is smaller. As β increases towards 1, it becomes clear that $\Phi(x)$ under-estimates the height of the $|\psi_n^0|^2$ profile. As β approaches 1, if we fixed $\lambda \lessapprox 7.5$ then $\Phi(x)$ becomes

an under-estimate, but if we fixed λ at a sufficiently large value then $\Phi(x)$ becomes an over-estimate. This is oweing to the fact that the continuum equations do not limit the height of the $\Phi(x)$ solution, allowing it to grow linearly with λ.

4.4 Propagating Polarons

We study polarons which propagate along the α-channel, under an external EMF $\epsilon(\tau)$. Using the stationary solutions which we computed in Section 4.3.4 as initial configurations of the system, parametrised by β and λ, we solve Equation (4.2.40) as an initial value problem. For each $\epsilon(\tau)$ that we prescribe, we set n_0 in the equations to be the location where the stationary $|\psi_n^0|^2$ attains its maximum, then we integrate the system forward in time using the standard RK4 method. To ensure numerical stability, we set the integration time-step at $\Delta\tau = 0.01$. As we integrate the system, we keep track of several scalar quantities associated with the polaron, such as the half-width of the electron probability distribution, and the polaron internal energy E_b, as defined in Equation (4.2.62). Most importantly, we keep track of the polaron's position, defined as follows. If $|\psi_n|^2$ attains its maximum at lattice site n_0, then the polaron's position is the vertex location of the parabola extrapolated from three points: $(n_0, |\psi_{n_0}|^2), (n_0 - 1, |\psi_{n_0-1}|^2), (n_0 + 1, |\psi_{n_0+1}|^2)$.

Each of Sections 4.4.1 to 4.4.3 is dedicated to investigating the effects of a specific type of EMF, respectively a constant field, time-periodic field with zero mean, and time-periodic field with non-zero mean. Then in Section 4.4.4, we look at the dependence of the polaron's dynamics on the system's symmetry parameter, β. Finally in Section 4.4.5, we examine the effects of non-zero stochastic forces $f_n(\tau)$.

4.4.1 Constant EMFs

The most natural choice of EMF has a constant electric field amplitude,

$$\epsilon(\tau) = \bar{\epsilon} > 0 \quad \text{for } \tau \geq 0. \tag{4.4.1}$$

Using moderately-localised stationary states (with $\max |\psi_n^0|^2 = 0.64$) as initial conditions, we compute polaron trajectories under various values of $\bar{\epsilon}$. Our results show that given $\beta = 1$ and $\lambda = 3.0$, a constant forcing of any $\bar{\epsilon} \sim \mathcal{O}(10^{-2})$ induces nothing but small oscillations of the polaron around its initial position.

As $\bar{\epsilon}$ is increased beyond 0.1, we find that the forcing can become strong enough to dislodge the electron from its potential well, and propel the polaron along the polypeptide.

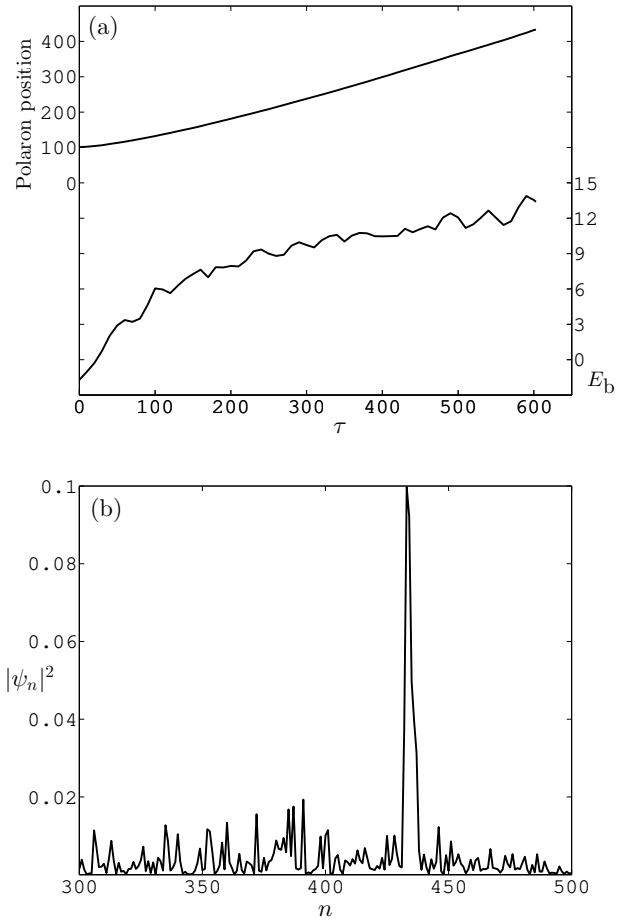

Figure 4.3: Polaron propagation under a constant EMF $\epsilon = 0.15$. Parameters: $\beta = 1, \lambda = 3.0$. (a) The polaron's position (left axis) and internal energy (meV) (right axis) as functions of time. 100 units of τ equals 12 ps. (b) The electron probability distribution $|\psi_n|^2$ upon delocalisation.

However as the polaron propagates, its internal energy increases rapidly, and the electron delocalises within several hundred time-units. A direct manifestation of the polaron's energy gain and electron delocalisation is that the $|\psi_n|^2$ profile loses height and gains local peaks at lattice sites far away from the global maximum. For the sake of consistency, throughout the remainder of this Chapter we say that the electron has delocalised if $\max|\psi_n|^2$ drops below 0.1, as it must then be the case that other local peaks have magnitudes comparable to the global maximum. In Figure 4.3(a) we present an example of a constant EMF large enough to cause polaron displacement, and it illustrates the resulting rapid delocalisation of the electron. We see the trajectory of the polaron which, within roughly 600 time-units (0.07 ns), is displaced by over 300 lattice sites. Its internal

energy steadily increases until the electron delocalises. Meanwhile, Figure 4.3(b) shows the electron probability distribution, $|\psi_n|^2$, at the time of delocalisation. This $|\psi_n|^2$ has evolved from an initial configuration possessing a maximum height of 0.64 and no local peaks apart from the global maximum.

Beyond the example shown in Figure 4.3, all our results are consistent with the hypothesis that, regardless of β and λ, a constant ϵ causes the polaron to undergo either small oscillations, or rapid energy gain leading to delocalisation. We would like to find ways to induce polaron propagation which is energetically stable. Therefore we must look for forms of ϵ other than constants.

4.4.2 Time-Periodic EMFs with Zero Mean

Now we consider EMFs whose electric field amplitudes are periodic in time,

$$\epsilon(\tau) = A \sin \frac{2\pi\tau}{T} \quad \text{for } \tau \geq 0, \tag{4.4.2}$$

where A is the amplitude and $T > 0$ is the period. Physically this may represent an electromagnetic plane wave which is monochromatic, i.e. coherent. With A up to 0.2, regardless of β and λ we find that the polaron simply oscillates about its initial position. The polaron's oscillatory motion has a period which coincides with T, and an amplitude which is positively correlated with A. An example of such trajectories is shown in Figure 4.4. While the polaron remains highly stable over time, its mean position over a period

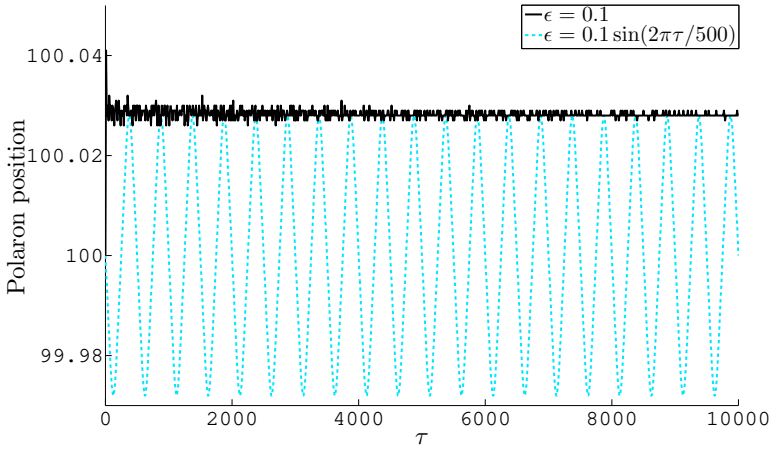

Figure 4.4: Some polaron trajectories under either a constant or a temporally periodic EMF, ϵ. 1000 units of τ equals 0.12 ns. Parameters: $\beta = 1, \lambda = 3.0$.

remains constant for all time. Thus, if we want polarons which transport energy from one lattice site to another, we must again modify ϵ.

4.4.3 Time-Periodic EMFs with Non-Zero Mean

In this Section, we consider EMFs whose electric field amplitudes are of the form

$$\epsilon(\tau) = \bar{\epsilon} - A \sin \frac{2\pi\tau}{T} \quad \text{for } \tau \geq 0, \tag{4.4.3}$$

where $\bar{\epsilon}, A \geq 0$ and $T > 0$. Equation (4.4.3) represents the combination of the two types of EMF considered previously, with a constant component and a temporally sinusoidal one. Strictly speaking, the electric field's phase φ should be another parameter, manifesting itself in $\epsilon(\tau) = \bar{\epsilon} + A \sin\left(\frac{2\pi\tau}{T} - \varphi\right)$. We have fixed $\varphi = \pi$, resulting in the minus sign before A in Equation (4.4.3), for the following reason. With $\bar{\epsilon}$ non-negative, the addition of a non-negative A raises the electric field amplitude immediately after $\tau > 0$, and the increased energy input is likely to cause electron delocalisation, the likes of which we have seen in Section 4.4.1. To stabilise the electron over the initial period of the EMF, we choose to decrease the electric field amplitude first, before raising it above the level of $\bar{\epsilon}$.

One may think of $\epsilon(\tau)$ as a *mean-shifted periodic field* (MSPF). In particular, the mean $\bar{\epsilon}$ is chosen to be lower than the constant field ϵ which is required to displace the polaron in the manner of Figure 4.3. Therefore $\bar{\epsilon}$ on its own would not give the electron enough energy to escape its potential well. But we hope that the component A can periodically push the electron energy over the threshold, resulting in polaron motion. Another possible advantage of this setup is that A may also periodically lower the electron energy, slowing it down and giving the lattice time to 'catch up', thus making the polaron motion more sustainable than it would be under a constant EMF.

Mathematically, $\epsilon(\tau)$ depends on three independent parameters, $\bar{\epsilon}, A$ and T. Before investigating the effect of each of these parameters, we present Figure 4.5, which is a direct comparison with Figure 4.3. We have replaced the constant forcing $\epsilon = 0.15$, which resulted in Figure 4.3, with an MSPF which has the same maximum amplitude as before. The difference is that now this maximum amplitude is reached once every period T. Figure 4.5(a) shows that, within roughly 10 periods, the polaron is displaced by nearly 400 lattice sites. Contrary to the uniform manner in which the polaron moves in Figure 4.3(a), now the polaron moves towards one end of the polypeptide and then the other, within each period of $\epsilon(\tau)$. The overall displacement of the polaron is due to the fact

that each movement to one end of the polypeptide is larger than the subsequent swing back the other way. We note that while the polaron moves slightly further under the MSPF compared to the constant field, the polaron's *lifetime*, i.e. the amount of time elapsed before delocalisation, is much longer under the MSPF. In the example of Figure 4.5, the polaron's lifetime is $\tau_{\mathrm{d}} \approx 4900$, or roughly 0.6 ns. Overall, the polaron in Figure 4.5 propagates with a lower *velocity*, V, defined by

$$V = \frac{\text{average position over final complete period of motion} - \text{initial position}}{\text{number of complete periods} \times T}, \quad (4.4.4)$$

where the numerator is the *displacement* of the polaron, which we denote by D. Our results show that, of the parameters $\bar{\epsilon}, A$ and T, the dominant factor which determines

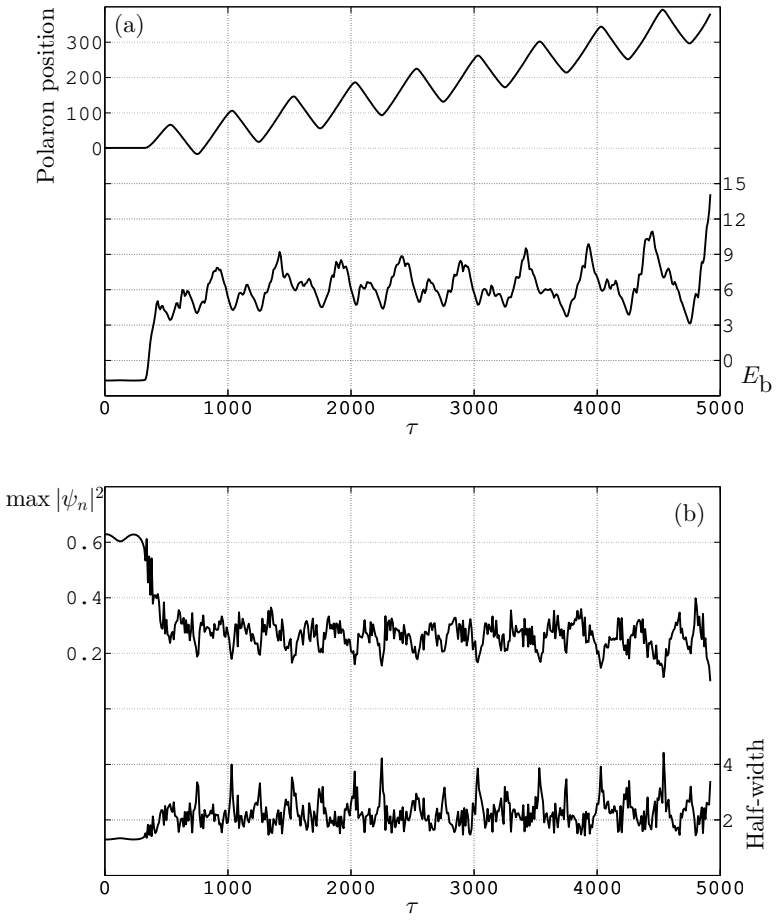

Figure 4.5: Polaron propagation under a MSPF, $\epsilon(\tau) = 0.025 - 0.125\sin(2\pi\tau/500)$. Parameters: $\beta = 1, \lambda = 3.0$. (a) The polaron's position (left axis) and internal energy (meV) (right axis) as functions of time. (b) The electron's maximum localisation probability (left axis) and half-width of the electron probablity distribution (right axis) as functions of time. 1000 units of τ equals 0.12 ns.

the polaron's velocity is the constant component $\bar{\epsilon}$. We will discuss this in more depth in relation to Figure 4.6.

Figure 4.5(a) also shows how the polaron's internal energy, E_b, evolves in time. Following an initial sharp increase, E_b mostly oscillates between 4.5 meV and 9 meV, until another sharp increase leading to delocalisation. Even though the constant EMF propels the polaron with greater speed, we consider the MSPF a better mechanism for electron transport, because the polaron internal energy is more stable. All our results suggest that by splitting a constant EMF into constant and temporally sinusoidal components, we lower the polaron's velocity but increase its stability and lifetime.

In Figure 4.5(b) we see another aspect of the polaron's motion, namely how the height and half-width of the $|\psi_n|^2$ profile evolve in time. Following an initial decrease, the electron's maximum localisation probablity, $\max|\psi_n|^2$, mostly oscillates between 0.2 and 0.4, until a sudden drop to 0.1, leading to delocalisation. Meanwhile, the half-width of the electron probability distribution mostly oscillates between 1.5 and 4, following an initial growth. The peaks in the half-width, as well as the troughs in $\max|\psi_n|^2$, occur precisely when the polaron turns from moving in one direction to moving in the other. This suggests that when the polaron accelerates, it 'spreads out', and so the half-width widens and $\max|\psi_n|^2$ drops.

Based on our observations, we theorise that a polaron's directed motion under the MSPF may be explained physically as follows. Since the forcing $\epsilon(\tau)$ is the effect of an EMF, it provides the electron with extra energy. This effect is manifest in the dramatic energy variation during the first period of $\epsilon(\tau)$, as seen in Figure 4.5. Whenever $|\epsilon(\tau)|$ becomes sufficiently large, the electron is dislodged from its potential well and propelled along the lattice. If the electron-phonon coupling is strong enough, then the localised lattice distortion can keep up with the electron, and so the polaron can remain intact. Whenever $|\epsilon(\tau)|$ drops below the threshold, the electron-phonon interaction slows down the electron and causes its probability distribution to spread out. This is why the half-width of $|\psi_n|^2$ always peaks at times when the polaron's instantaneous velocity is zero. If $|\epsilon(\tau)|$ remains below the threshold for long enough, then the polaron's position can plateau, as we see in Figure 4.6. If $\epsilon(\tau)$ has a large enough periodic component A, then it is possible for $|\epsilon(\tau)|$ to overcome the threshold twice per period: once with $\epsilon > 0$, once with $\epsilon < 0$. If the electron moves towards large n in the $\epsilon > 0$ case, then it will move towards small n in the $\epsilon < 0$ case. This explains the backwards swing exhibited by some polaron trajectories

during each period of motion. The fact that $\bar{\epsilon} \neq 0$ ensures that the electron always spends more time moving one way than the other, hence the overall directedness of the polaron trajectories. This point is most clearly demonstrated by the trajectories in Figure 4.6 for which the period $T = 2000$. When T is small it may seem as though the trajectories are simply linear, for example the solid (black) trajectory labelled 'C1' in Figure 4.6(a), but zooming in, as we can see in the box on the top-right corner of Figure 4.6(a), reveals that the curve does exhibit the characteristic sawtooth shape.

Within each subfigure of Figure 4.6, we can compare the trajectories in certain ways in order to reveal the effect on the polaron dynamics of varying one of the three parameters of the EMF, namely $\bar{\epsilon}, A$ and T. As an example, we consider Figure 4.6(b), for which $\beta = 0.6$ and $\lambda = 5.0$ are fixed. To identify the effect of varying the amplitude A of the sinusoidal component of the electric field, we can pick any of the nine bundles of trajectories labelled 'A1' to 'C3', because each bundle corresponds to a fixed combination of $(\bar{\epsilon}, T)$, and compare the three trajectories within that bundle, each with a different A. We infer from this comparison that the larger A is, the more the polaron oscillates back and forth during each period of motion. It may be tempting to assume that the polaron's velocity is positively correlated with A, but examining Figure 4.6(a) reveals that not to be the case. Indeed, in most cases we see that $A = 0.15$ results in faster polaron motion than $A = 0.20$ does, when all other parameters are fixed. Moreover, examining Figure 4.6(c), we see that in most cases increasing A causes the polaron to delocalise more quickly.

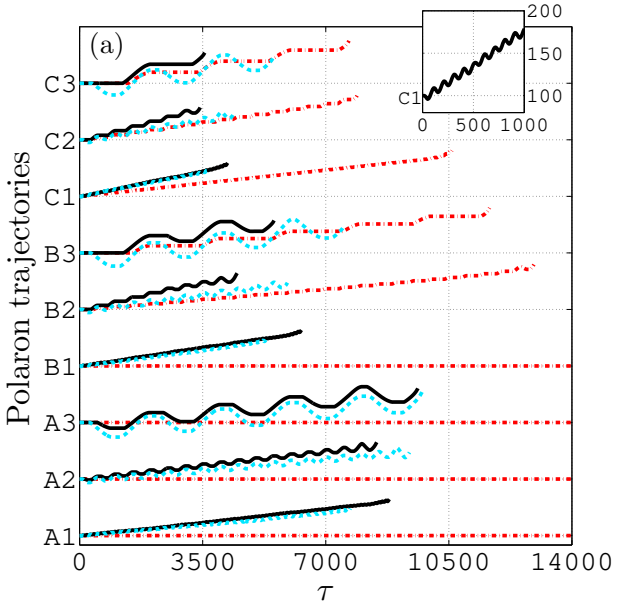

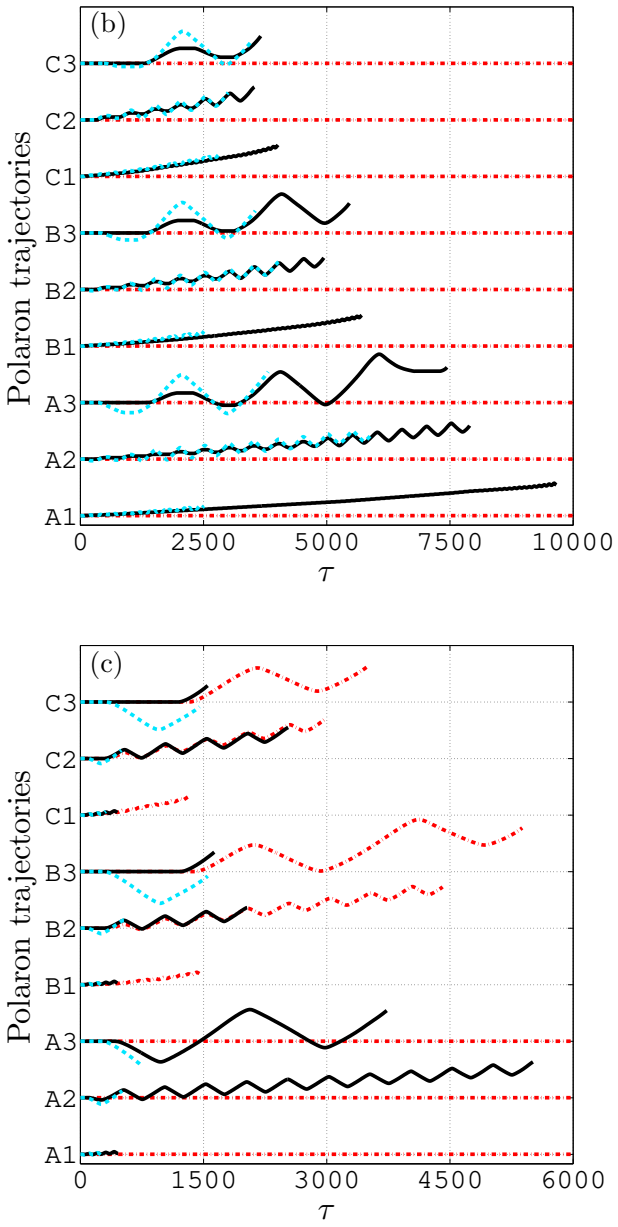

Figure 4.6: Some polaron trajectories under the MSPF, $\epsilon(\tau) = \bar{\epsilon} - A\sin(2\pi\tau/T)$. Parameters: (a) $\beta = 0, \lambda = 7.6$. (b) $\beta = 0.6, \lambda = 5.0$. (c) $\beta = 1, \lambda = 3.0$. λ has to be varied with β, in order to keep the initial $|\psi_n^0|^2$ profiles unchanged, all with $\max|\psi_n^0|^2 = 0.64$. In each subfigure, the labelling of trajectories is in the form of Xn, where X is A, B or C, each corresponding to a value of $\bar{\epsilon}$, and n is 1, 2 or 3, each corresponding to a value of T. X = A: $\bar{\epsilon} = 0.02$, X = B: $\bar{\epsilon} = 0.03$, X = C: $\bar{\epsilon} = 0.04$, $n = 1 : T = 100$, $n = 2 : T = 500$, $n = 3 : T = 2000$. Every Xn corresponds to 3 distinct trajectories, each for a different value of A. Dash-dotted (red) lines: $A = 0.10$; solid (black) lines: $A = 0.15$; dashed (blue) lines: $A = 0.20$. Every grid spacing in the vertical direction represents 600 lattice sites. 1000 units of τ equals 0.12 ns. Every trajectory is drawn up to the time of electron delocalisation.

To identify the effect of varying the constant component $\bar{\epsilon}$ of the MSPF, we can look at any of the subfigures and compare any three trajectories with the same line type and same number in their labels; for instance, the three solid (black) lines respectively labelled 'A2' ($\bar{\epsilon} = 0.02$), 'B2' ($\bar{\epsilon} = 0.03$) and 'C2' ($\bar{\epsilon} = 0.04$) in Figure 4.6(b), all with $\beta = 0.6, \lambda = 5.0, A = 0.15$ and $T = 500$ fixed. All three trajectories show roughly the same amount of polaron displacement, but achieve the displacement in vastly different amounts of time. Indeed, the larger $\bar{\epsilon}$ is, the less time it takes the polaron to travel any certain distance, meaning the polaron moves with greater speed. Examining any appropriate group of three trajectories in any of the subfigures leads to the same conclusion, that the overall velocity of the polaron is predominantly determined by $\bar{\epsilon}$.

If we pick any trajectory in any subfigure, and compare it with its two counterparts in the other two subfigures, we can infer some information about the significance of the symmetry parameter, β. Indeed, it is clear that the extent to which the polaron is susceptible to displacement depends heavily upon β, for we can see that in Figure 4.6(b), where $\beta = 0.6$, significantly fewer trajectories display any polaron displacement compared to how many do in Figures 4.6(a) and (c). This suggests that a moderate value of β such as 0.6 makes the polaron significantly less susceptible to displacement under the MSPF, compared to extreme values of $\beta = 0$ or 1. Of course, the fact that as we varied β to obtain the three subfigures, we also varied λ so that the initial electron probability distribution remained unchanged, means we should also consider the possibility that the variation in λ has a bearing on the polaron's dynamics. We take the approach of considering the pair (β, λ) as a whole, rather than separately, so that whenever we theorise about the effect of β, it is implied that the accompanying λ takes an appropriate value to ensure that the stationary polaron has $\max |\psi_n^0|^2 = 0.64$. It is paramount to ensure the consistency in $\max |\psi_n^0|^2$, for it is possible to make meaningful comparisons between polaron trajectories only if all polaron stationary states have the same electronic probability distribution. From Figure 4.6 only, we have insufficient data to deduce precisely how β affects the polaron's susceptibility to displacement; but in Section 4.4.4, we will investigate the effect of β in more detail.

Finally, if we look at any of the subfigures of Figure 4.6 and compare any three trajectories that have the same line type and share the letter part of their labels, for instance the three solid (black) lines respectively labelled 'C1', 'C2' and 'C3' in Figure 4.6(a), we may hope to see the effect of varying T. However, this comparison is not particularly

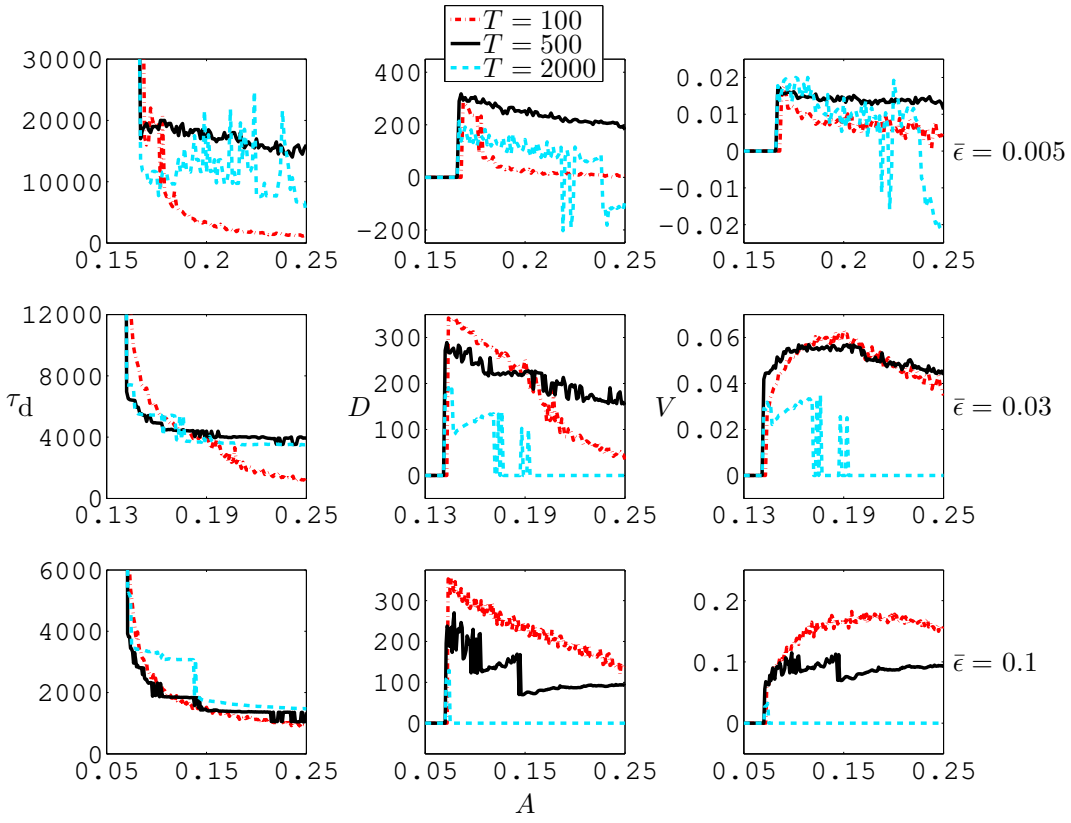

Figure 4.7: Polaron lifetime τ_d, displacement D and velocity V, as functions of A parametrised by $(\bar{\epsilon}, T)$. 1000 units of τ equals 0.12 ns. Parameters: $\beta = 0.6, \lambda = 5.0$.

enlightening. We therefore present Figure 4.7, which not only provides more insight into the effect of T, but also helps to reinforce our theories about the effects of $\bar{\epsilon}$ and A .

For several combinations of $\bar{\epsilon}$ and T, we examine how the polaron's lifetime, displacement and velocity vary with A. The results are displayed together, in Figure 4.7. Firstly we consider the lifetime, τ_d. We computed all our numerical solutions up to $\tau = 30000$, which is several times larger than the typical lifetime of a polaron that moves under the MSPF. If the polaron is not displaced by the MSPF, then it is effectively permanent, in the sense that its energy oscillates instead of dissipating over time, and it would have a lifetime far exceeding 30000. For each combination of $\bar{\epsilon}$ and T, there exists some *critical amplitude*, $A = A_c$, below which the polaron is undisplaced by the MSPF. At $A = A_c$, the combined amplitude of the MSPF, $A^{\text{comb}} := \bar{\epsilon} + A$, becomes large enough to displace the polaron, and τ_d drops sharply. This drop can sometimes result in a lifetime of only several thousand time-units - see for instance the bottom-left subfigure in Figure 4.7, corresponding to $\bar{\epsilon} = 0.1$. When $\bar{\epsilon}$ is smaller, say $\bar{\epsilon} = 0.005$ (top-left subfigure), the drop in

lifetime is less sharp. As A increases beyond A_{c}, the polaron's lifetime drops further, if only slightly.

Next, we look at the polaron's displacement, D. When A is small, the polaron does not move barring small oscillations, the types of which we saw in Figure 4.4. As A reaches critical value A_{c}, the polaron turns from being quasi-stationary to moving by several hundred lattice sites during its lifetime. Evidently, the value of A_{c} is independent of T. We only consider the displacement of polarons whose lifetimes are at least $2T$, and we set the displacement of polarons with shorter lifetimes to zero - see for instance the dashed (blue) lines in the centre and bottom-middle subfigures. Whilst the value of A_{c} does not depend on T, the amount of displacement caused by A_{c} does. However, it is unclear from our results what their correlation is. As A increases beyond A_{c}, the qualitative behaviour of D is that it decreases. This is due to the fact that increasing A causes the electron to delocalise more quickly, and therefore the polaron has less time to move.

To understand how A affects the amount of polaron displacement *per unit time*, we examine the polaron's velocity, V. When A is small, V is zero. As A reaches critical value A_{c}, the velocity becomes typically $\mathcal{O}(10^{-2})$. Exactly what value this *critical velocity* V_{c} takes depends on $\bar{\epsilon}$ - the larger $\bar{\epsilon}$ is, the larger V_{c} becomes. As A increases beyond A_{c}, sometimes V simply decays away - see for instance the top-right subfigure, where $\bar{\epsilon} = 0.005$. Sometimes, however, V grows before its decay - see for instance the middle-right and bottom-right subfigures, where $\bar{\epsilon} = 0.03$ and 0.1 respectively. Such behaviour is possible when the polaron lifetime decays with A more sharply than the displacement does as A is increased beyond A_{c}. When this happens, there may exist some *optimal amplitude*, $A = A_{\mathrm{m}}$, at which the polaron attains maximum velocity, V_{m}. A_{m} may coincide with A_{c} - see for instance the top-right subfigure.

Whilst the value of A_{c} does not depend on T, it does depend on $\bar{\epsilon}$, and we see this by comparing any row of subfigures in Figure 4.7 to any other row. Our results show that as $\bar{\epsilon}$ grows, A_{c} drops, but crucially the combined amplitude $A^{\mathrm{comb}} = \bar{\epsilon} + A_{\mathrm{c}}$ remains roughly constant. Specifically, in the top row we see $\bar{\epsilon} = 0.005$ and $A_{\mathrm{c}} = 0.167$, in the middle row we have $\bar{\epsilon} = 0.03$ and $A_{\mathrm{c}} = 0.142$, and the bottom row shows $\bar{\epsilon} = 0.1$ and $A_{\mathrm{c}} = 0.072$, each case giving $A^{\mathrm{comb}} = 0.172$ when A reaches critical. Recall that, when using a straightforward constant forcing $\epsilon = \bar{\epsilon}$, there was also a threshold value for $\bar{\epsilon}$, below which the polaron simply exhibits small oscillations, and above which the polaron moves at high speed but the electron delocalises rapidly. It is noteworthy that this threshold

was $\epsilon = 0.154$ (given $\beta = 0.6$), which is significantly lower than the critical combined amplitude of 0.172. In other words, $\epsilon = 0.154$ causes polaron displacement, $\epsilon = 0.153$ does not; and if one wishes to add to $\epsilon = 0.153$ a periodic component $A\sin(2\pi\tau/T)$ in order to move the polaron, one needs $A \geq 0.019$, making $\bar{\epsilon} + A$ far exceed what $\bar{\epsilon}$ is required on its own to move the polaron. This phenomenon is observed across all values of β.

In practice, then, what would make a good combination of forcing parameters, which propel the polaron with decent speed but does not cause rapid delocalisation? First of all, a large $\bar{\epsilon}$ results in a large velocity but an energetically unstable polaron, for which the electron delocalises so rapidly that it may move less far in its lifetime than it does under a small $\bar{\epsilon}$. The middle column of Figure 4.7 precisely illustrates this point. Meanwhile, a small $\bar{\epsilon}$ results in long-living polarons which can move very far, because of how stable they are, but they would take more time to reach the same destination, compared to polarons under a large $\bar{\epsilon}$. On balance, a moderate value of $\bar{\epsilon}$ such as 0.03 is preferable. Once a $\bar{\epsilon}$ is chosen, it remains to choose A and T, and the ideal choice of A is the optimal amplitude, $A = A_{\mathrm{m}}$. If T is small, such as $T = 100$, then A_{m} is large. On the other hand, if T is large, such as $T = 2000$, then the maximum velocity resulting from A_{m} is small. We observe both of these extremes clearly in the middle-right subfigure of Figure 4.7. Once again, these observations are not specific to $\beta = 0.6$, but universal for all values of β. Overall, we believe that the best MSPF parameters are such combinations where $\bar{\epsilon} \approx 0.03$, $T \approx 500$, and $A \approx A_{\mathrm{m}}$ which, given $\beta = 0.6$, is $A_{\mathrm{m}} = 0.158$. We will further discuss the relationship between A_{m} and β in Section 4.4.4.

We note an anomaly which we observe in Figure 4.7. When $\bar{\epsilon} = 0.005$ (top row), if $T = 2000$ and A is sufficiently large, then the displacement (and therefore velocity) can take large negative values, meaning the polaron moves in the small-n direction, opposite to what we expected, and with large speeds. This is because A predominantly determines the amount by which the polaron moves back and forth during a period of motion, and it is entirely possible for delocalisation to occur just as the polaron position takes some small n-value during some period of motion. If delocalisation occurs within the first few periods of motion, then it is also possible that the polaron's average position per period has not moved sufficiently far in the large-n direction to cancel out the 'swing' in the small-n direction. Calculations based on this type of trajectory would lead to the conclusion that the polaron's overall displacement, hence velocity, is in the small-n direction.

4.4.4 Significance of the Symmetry Parameter

We have remarked that as we vary β, the ways in which the polaron velocity varies with our forcing parameters remain qualitatively similar, as it is always characterised by a critical amplitude A_{c} and optimal amplitude A_{m}. Quantitatively, the values of A_{c} and A_{m} would change with β. In this Section, we investigate how A_{c} and A_{m} vary with β. Firstly we establish the following preliminary result.

Recall that the stationary polaron is characterised by two quantities: the electron probability distribution $|\psi_n^0|^2$, specifically the maximum localisation probability $\max|\psi_n^0|^2$, and the binding energy E_{b}^0. These are in turn determined by the symmetry parameter β and effective coupling parameter λ. As β varies, so does the value of λ required to keep $\max|\psi_n^0|^2$ constant. The required λ as a function of β is shown in Figure 4.8. It is clear that $\lambda(\beta)$ is a decreasing function. We have made sure that whenever we altered β we also took $\lambda = \lambda(\beta)$, so that all of our moving polarons begin as stationary states which share the same electronic probability distribution. An alternative would have been to take whatever λ is required to keep the binding energy constant. Our results show that if we had decided to keep the binding energy constant at, say, -3.5 meV, then $\max|\psi_n^0|^2$ would have been 0.53 at $\beta = 0$, or 0.81 at $\beta = 1$. It is a central feature of our model that two

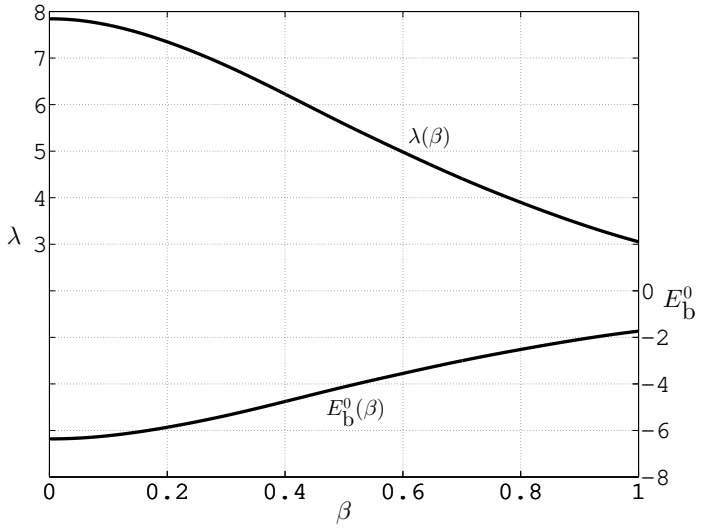

Figure 4.8: $\lambda(\beta)$: the value of λ required, as β varies, in order to maintain $\max|\psi_n^0|^2 = 0.64$ (left axis). $E_{\mathrm{b}}^0(\beta, \lambda(\beta))$: binding energy of stationary polaron resulting from β and $\lambda(\beta)$ (right axis). For example, when $\beta = 0.6$ and $\lambda = \lambda(0.6) = 5.0$, the binding energy is $E_{\mathrm{b}}^0(0.6, 5.0) = -3.5$ meV.

stationary polarons with the same maximum localisation probability need not have the same binding energy, and vice versa.

In Figure 4.9, we present A_c, A_m, V_c and V_m as functions of β, parametrised by $\bar{\epsilon}$ and T. We have already seen in Figure 4.7 that if $\beta = 0.6, \bar{\epsilon} = 0.03$ and $T = 500$, then $A_c = 0.142$ and $A_m = 0.158$. This is shown more clearly in Figure 4.9(e), for which $\bar{\epsilon} = 0.03$ and $T = 500$ are fixed, and from which we can also read the corresponding V_c and V_m. Reading all nine subfigures of Figure 4.9, we make the following observations. Regardless of the values at which we fix $(\bar{\epsilon}, T)$, A_c increases as β increases from 0, and A_c is maximal when $\beta \approx 0.6$. Despite the fact that we expect a system with symmetric interaction ($\beta = 0$) to be least conducive to directed polaron motion, it turns out that a moderately asymmetric system admits polarons which are least susceptible to displacement. Moreover, as β is increased beyond roughly 0.6, A_c decays, and we always have A_c attaining its global minimum when $\beta = 1$, which suggests that a system with antisymmetric electron-phonon interaction is most conducive to directed polaron motion. This is as we would expect, because the system's intrinsic antisymmetry favours electron displacement in one direction over the other. The optimal amplitude, A_m, tends to follow the same trend as A_c does while β varies, although A_m is usually significantly larger than A_c, with some exceptions, for instance in Figure 4.9(b) where A_c and A_m are identical for most values of β.

The critical and optimal velocities, V_c and V_m, are always of the same order of magnitude, and occasionally coincide, just as A_c and A_m sometimes do. By comparing any group of three subfigures where $\bar{\epsilon}$ is fixed, for instance Figures 4.9(a) to (c) where $\bar{\epsilon} = 0.005$, we can verify our earlier assertion that T has little effect on the value of A_c; indeed, the

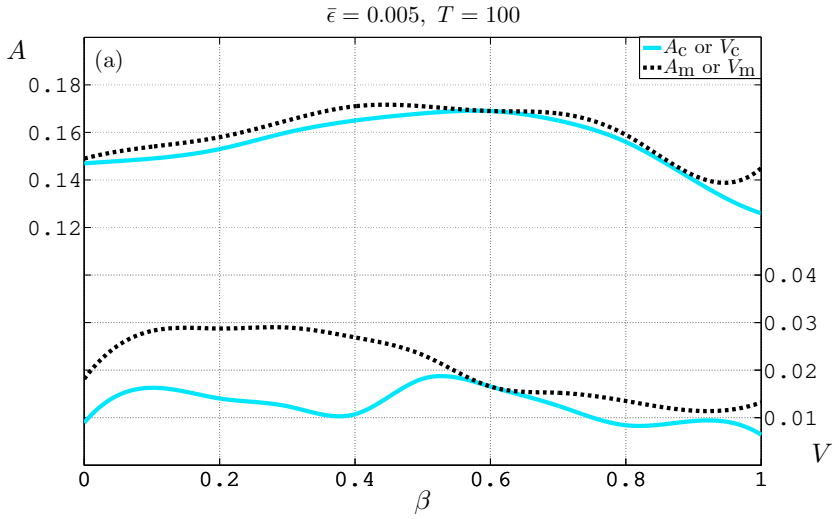

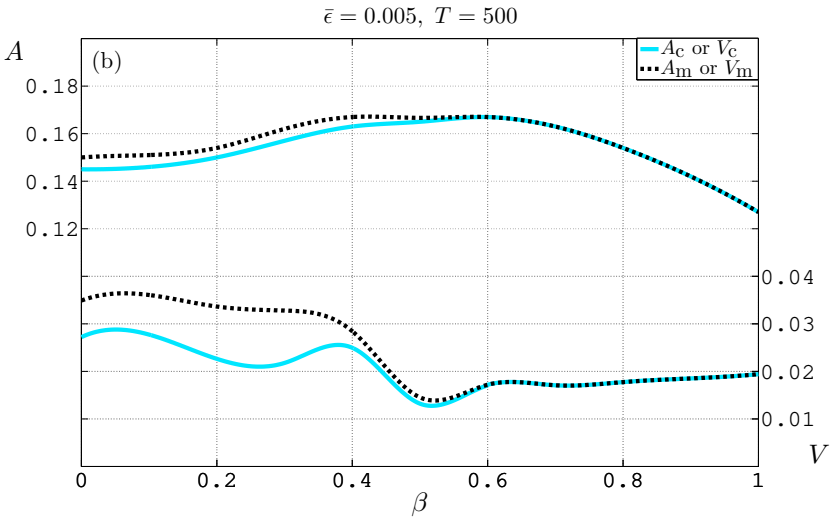
$\bar{\epsilon} = 0.005,\ T = 500$
(b)
A_c or V_c
A_m or V_m
A
V
β
0.18
0.16
0.14
0.12
0.04
0.03
0.02
0.01
0
0.2
0.4
0.6
0.8
1

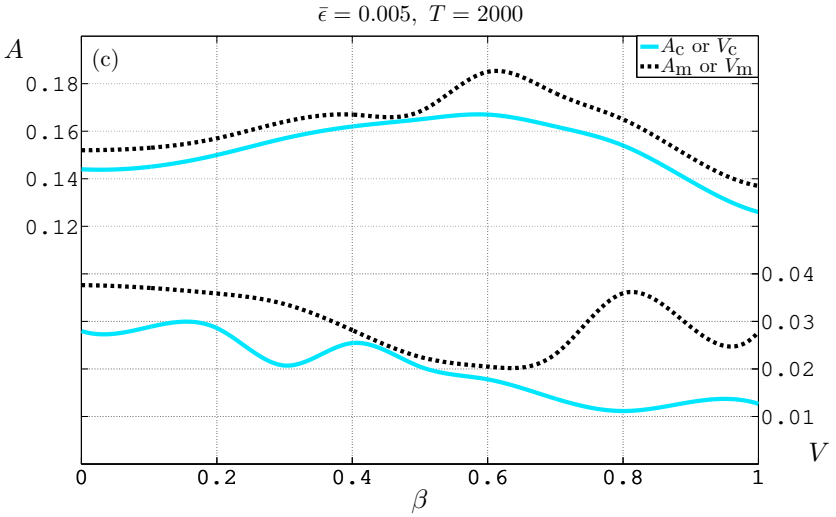
$\bar{\epsilon} = 0.005,\ T = 2000$
(c)
A_c or V_c
A_m or V_m
A
V
β
0.18
0.16
0.14
0.12
0.04
0.03
0.02
0.01
0
0.2
0.4
0.6
0.8
1

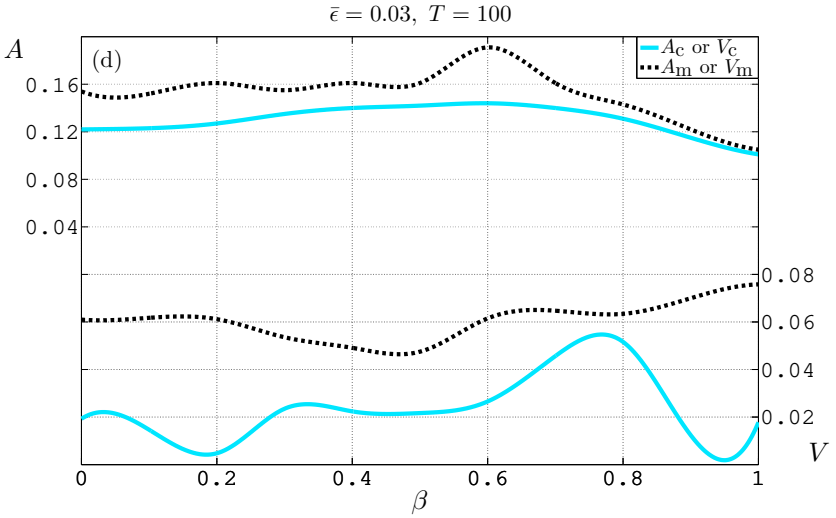
$\bar{\epsilon} = 0.03,\ T = 100$
(d)
A_c or V_c
A_m or V_m
A
V
β
0.16
0.12
0.08
0.04
0.08
0.06
0.04
0.02
0
0.2
0.4
0.6
0.8
1

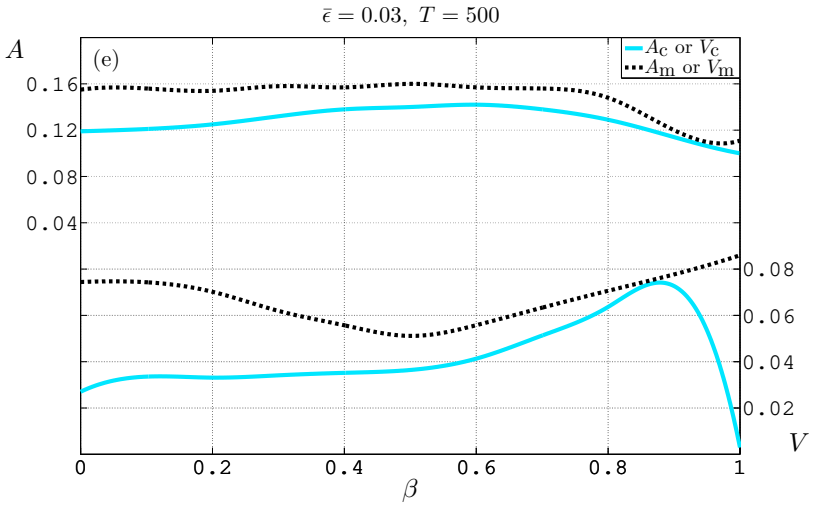
$\bar{\epsilon} = 0.03,\ T = 500$
(e)
A_c or V_c
A_m or V_m
A
V
β
0.16
0.12
0.08
0.04
0.08
0.06
0.04
0.02
0
0.2
0.4
0.6
0.8
1

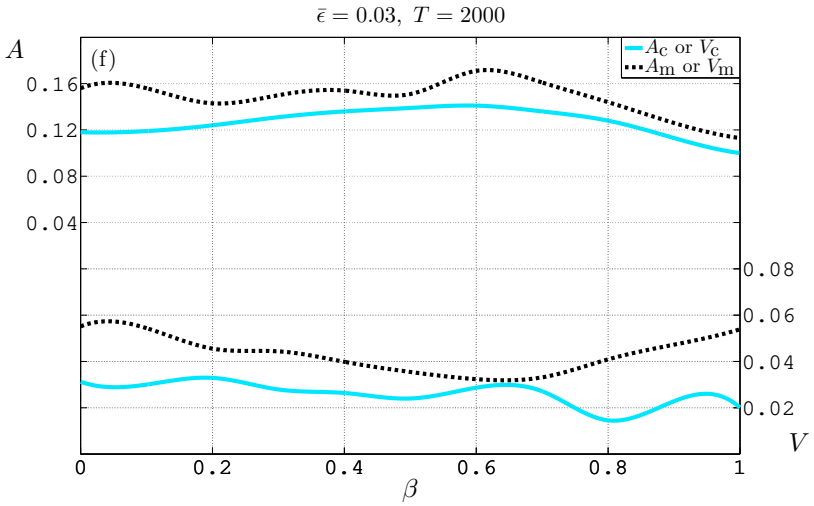
$\bar{\epsilon} = 0.03,\ T = 2000$
(f)
A_c or V_c
A_m or V_m
A
V
β
0.16
0.12
0.08
0.04
0.08
0.06
0.04
0.02
0
0.2
0.4
0.6
0.8
1

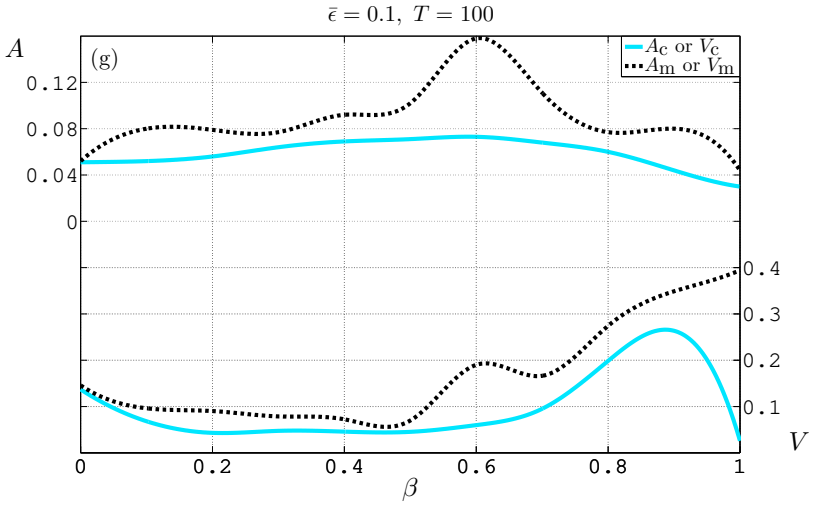
$\bar{\epsilon} = 0.1,\ T = 100$
(g)
A_c or V_c
A_m or V_m
A
V
β
0.12
0.08
0.04
0
0.4
0.3
0.2
0.1
0
0.2
0.4
0.6
0.8
1

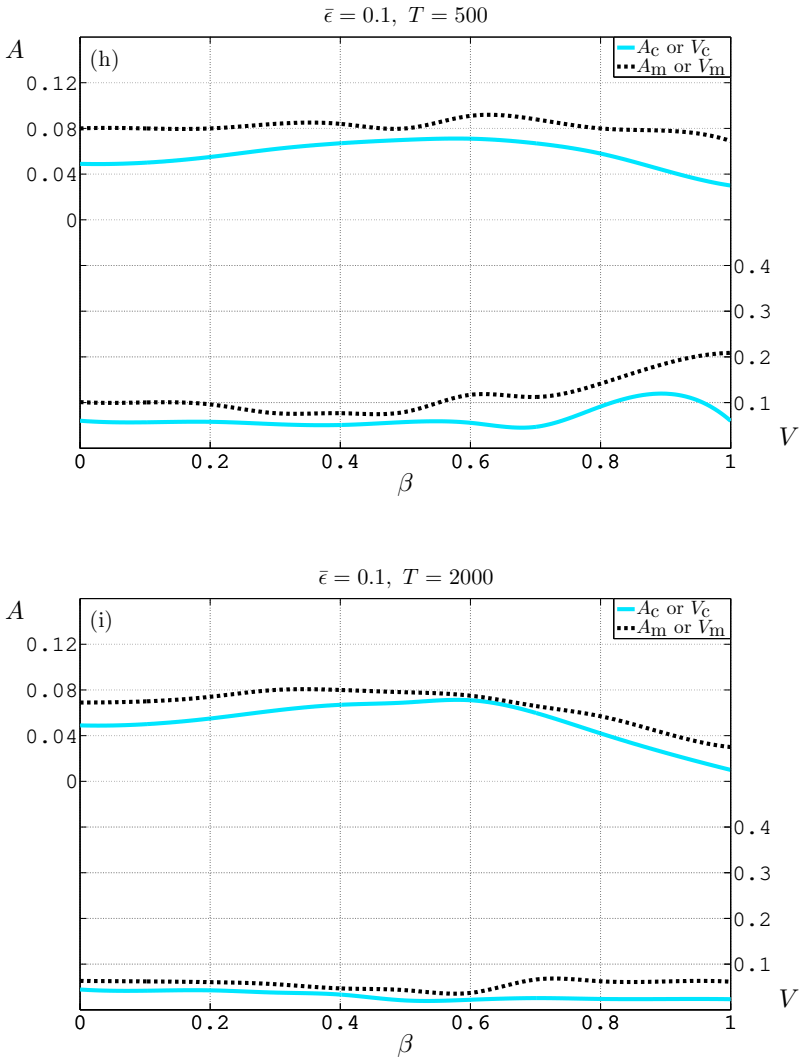

Figure 4.9: Critical amplitude A_c and optimal amplitude A_m (left axis), critical velocity V_c and optimal velocity V_m (right axis), as functions of β, parametrised by $(\bar{\epsilon}, T)$. For each β, the value of λ is that which results in $\max |\psi_n^0|^2 = 0.64$.

$A_c(\beta)$ curves given the three different values of T are virtually identical. The dependence of A_m on T is more pronounced, but there appears to be no clear positive or negative correlation between A_m and T. We also conjectured earlier that A_c is negatively and linearly correlated with $\bar{\epsilon}$, so that the combined amplitude $A^{\text{comb}} = \bar{\epsilon} + A_c$ remains constant as $\bar{\epsilon}$ varies. This is supported by our results. Indeed, looking at any group of three subfigures where T is fixed, for instance Figures 4.9(b), (e) and (h), we see that the A_c curve simply shifts along the vertical axis, by an amount that equals the difference between one $\bar{\epsilon}$ and the next.

4.4.5 Effects of Stochastic Forces

We study the effect of thermal fluctuations which result from non-zero temperatures in the environment surrounding the lattice. The randomised forces on the lattice are represented by the normally-distributed $f_n(\tau)$, which by definition (4.2.43) must have, for $\tau \geq 0$, the following first and second moments:

$$\langle f_n(\tau) \rangle = 0, \quad \langle f_m(\tau) f_n(\tau + \Delta\tau) \rangle = \frac{2\gamma\theta\delta_{mn}}{\Delta\tau}, \tag{4.4.5}$$

where θ is the dimensionless thermal energy:

$$\theta = \frac{k_{\mathrm{B}}\Theta}{\hbar\Omega}, \tag{4.4.6}$$

and Θ is the temperature. As we have done throughout this Chapter, we fix $\Delta\tau = 0.01$. Beginning with a stationary polaron, which we computed numerically in Section 4.3.4, we integrate the system of Equation (4.2.40) forward in time from $\tau = 0$, first with $\epsilon(\tau)$ set to zero. Using a random number generation algorithm, we generate a new vector f_n before each integration step. If θ is large, we find that it can cause large distortions in the lattice, which in turn causes rapid delocalisation of the electron via to the electron-phonon coupling. For appropriate values of θ, we see that the polaron's internal energy undergoes a small initial increase before settling in a quasi-stationary state of small fluctuations around some mean value. For example, given $\beta = 0.6$ and $\lambda = 5.0$, the stationary polaron has binding energy $E_{\mathrm{b}}^0 = -3.5$ meV. Integrating from $\tau = 0$ with $\theta = 0.32$, we find that after $\tau \sim \mathcal{O}(10^4)$ the internal energy settles, on average, around -1.2 meV, which is significantly higher than the stationary binding energy. The period of time required for a polaron to reach such a state of thermal equilibrium is the *thermalisation phase* of the polaron dynamics. During this phase, the electron undergoes small fluctuations around its initial position, due to its coupling to the thermalised lattice, which itself exhibits small distortions. Our results show that irrespective of β, we are unable to raise $\theta > 0.9$, because such a large θ induces excessive lattice distortions which cause delocalisation before the system reaches thermal equilibrium.

In each numerical simulation of the polaron dynamics, we integrate the system with $\epsilon(\tau) = 0$, until the polaron reaches thermal equilibrium. Then we reset $\tau = 0$, and 'turn on' the EMF $\epsilon(\tau)$ for $\tau \geq 0$. We examine how the polaron subsequently moves, under combinations of $\epsilon(\tau)$ and $f_n(\tau)$. To obtain the results in this Section, we run every

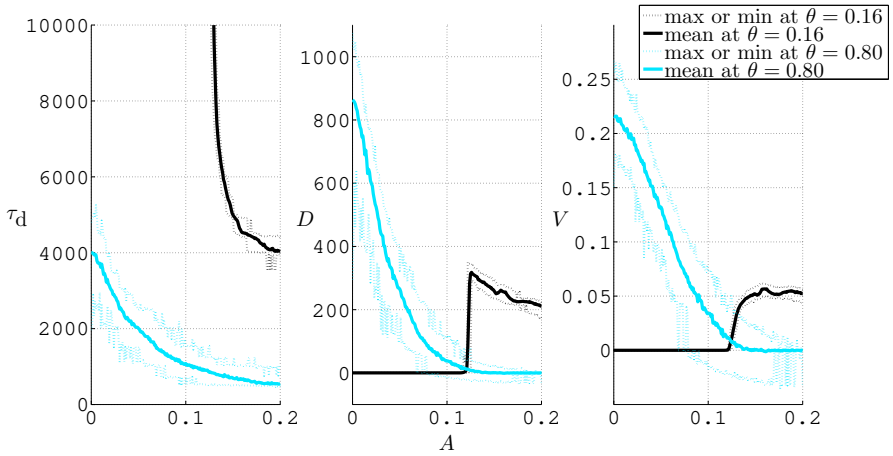

Figure 4.10: Polaron lifetime τ_d, displacement D, and velocity V, under the MSPF, $\epsilon = \bar{\epsilon} - A\sin(2\pi\tau/T)$, and the stochastic forces, $f_n(\tau)$ with thermal energy θ. Each simulation of polaron dynamics is run 100 times, and the mean, maximum and minimum for each of τ_d, D and V are all shown. Parameters: $\beta = 0.6, \lambda = 5.0, \bar{\epsilon} = 0.03, T = 500$.

dynamical simulation, with a set of parameters $(\beta, \lambda(\beta), \bar{\epsilon}, A, T, \theta)$, 100 times, and take mean values of quantities such as polaron lifetime, displacement and velocity, as well as maximum and minimum values of those quantities over the 100 simulations. Since the thermalisation phase raises the polaron energy, we expect that a thermalised polaron would be easier to displace, in the sense that it would require a smaller $\epsilon(\tau)$ to displace it, compared to the $f_n = 0$ system. Indeed our results confirm this.

Figure 4.10 is to be compared directly with Figure 4.7, which contained results for $\beta = 0.6$ and $\theta = 0$. Specifically, we draw comparisons with the solid (black) lines in the middle row of subfigures in Figure 4.7, for which two of the parameters in $\epsilon = \bar{\epsilon} - A\sin(2\pi\tau/T)$ were fixed, at $\bar{\epsilon} = 0.03$ and $T = 500$. We saw that given said parameter values, the critical amplitude of the sinusoidal component of MSPF was $A_c = 0.142$. When we have a non-zero θ in the system, we define A_c to be the smallest A for which the average polaron displacement (over 100 simulations) exceeds 10 lattice sites. According to this definition, when $\beta = 0.6, \bar{\epsilon} = 0.03, T = 500$ and $\theta = 0.16$, we see in Figure 4.10 that $A_c = 0.121$, which is significantly lower than when $\theta = 0$.

Fixing $\bar{\epsilon} = 0.03, T = 500$ and $\theta = 0.16$, we find that the value of A_c depends on β in a manner shown in Figure 4.11, which one may compare directly with Figure 4.9(e), where we had $\bar{\epsilon} = 0.03, T = 500$ and $\theta = 0$. We see that, as before, we still have A_c attaining its minimum value when $\beta = 1$, suggesting that an antisymmetric electron-phonon interaction makes it easiest to displace the polaron. We also still observe the

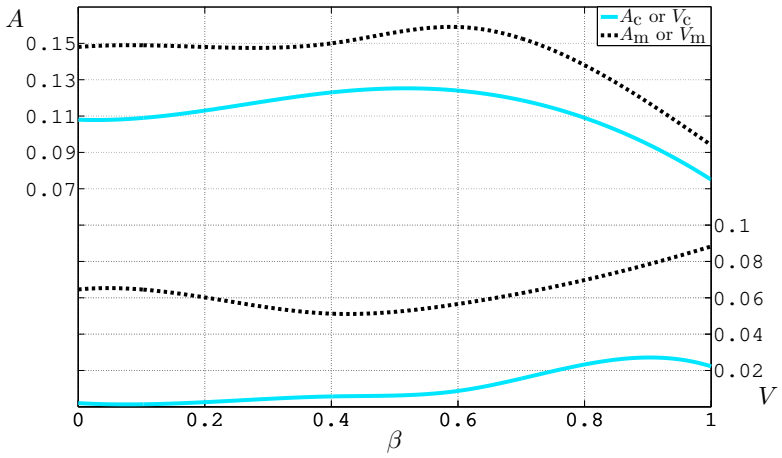

Figure 4.11: Critical amplitude A_c and optimal amplitude A_m (left axis), critical velocity V_c and optimal velocity V_m (right axis), as functions of β. Parameters: $\bar{\epsilon} = 0.03, T = 500, \theta = 0.16$.

phenomenon that displacing the polaron is most difficult not in a symmetric system, but in a moderately asymmetric one where $\beta \approx 0.5$. Indeed, the $A_c(\beta)$ function in Figure 4.11 is characteristically similar to the one in Figure 4.9(e), except that the curve when $\theta = 0.16$ is significantly lower than that when $\theta = 0$. This means that regardless of β, a non-zero θ makes it easier to displace the polaron using the MSPF, in the sense that a smaller combined amplitude $A^{\text{comb}} = \bar{\epsilon} + A$ is required. It is also noteworthy that under a non-zero θ, the onset of polaron motion is more gradual, in the sense that a critical amplitude results in a small velocity, V_c. Indeed, comparing V_c in Figure 4.11 with V_c in Figure 4.9(e), we see that the former is several times smaller.

When we raise the thermal energy to $\theta = 0.8$, we see in Figure 4.10 that the polaron is displaced (on average) by hundreds of sites even if $A = 0$. This suggests that given $\beta = 0.6$ and $\bar{\epsilon} = 0.03$, there exists some *critical thermal energy* $\theta = \theta_c$, with $0 < \theta_c \leq 0.8$, for which the combination of $\epsilon(\tau) = \bar{\epsilon}$ and $f_n(\tau)$ is sufficient to displace the polaron, and no sinusoidal component in $\epsilon(\tau)$ is needed. θ_c is critical in the sense that if θ is any lower than θ_c, then the combination of $\epsilon(\tau) = \bar{\epsilon}$ and $f_n(\tau)$ does not energise the polaron enough to move it, and a non-zero A is required. We have investigated how θ_c changes as we vary β and $\bar{\epsilon}$, and the results are shown in Figure 4.12. We observe the qualitative trend that the larger $\bar{\epsilon}$ is, the less thermal energy is required to make up for the extra energy that the polaron needs in order to move. We also observe that in general, the larger β is, the less thermal energy is required to displace the polaron. This agrees with our understanding

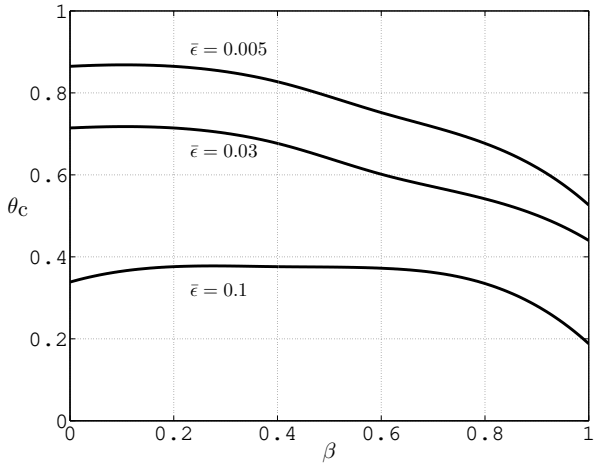

Figure 4.12: Critical thermal energy θ_c as a function of β, parametrised by $\bar{\epsilon}$.

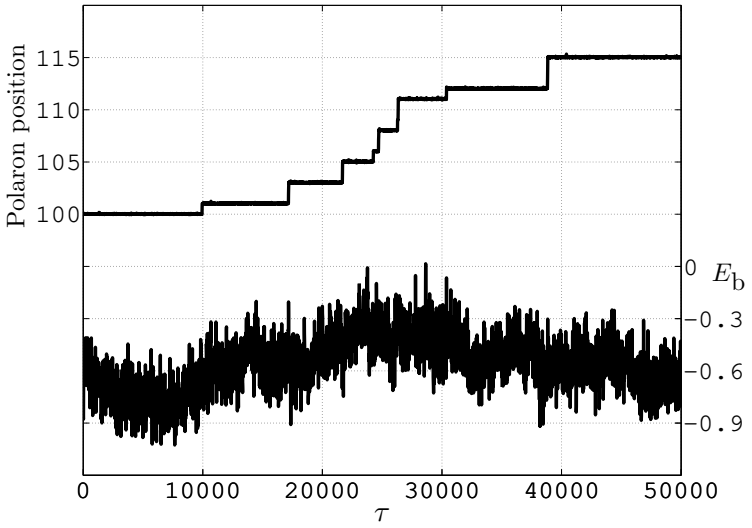

Figure 4.13: A polaron trajectory (left axis), and the corresponding time-evolution of the polaron's internal energy (right axis), given $\beta = 0.6, \lambda = 5.0, \bar{\epsilon} = 0.03, A = 0$, and $\theta = \theta_c = 0.60$.

that when β is large, we have an electron-phonon interaction which is biased towards one end of the lattice, making the polaron more susceptible to displacement.

In Figure 4.13 we present a typical polaron trajectory when $\theta = \theta_c$. Under this critical thermal energy, some simulations would produce no polaron displacement at all, but most trajectories would be similar to that in Figure 4.13, clearly showing a directed movement of the polaron. We propose to explain the shape of such a trajectory as follows. First of all, the combined amplitude of the MSPF, in this case $\bar{\epsilon}$ on its own, is much lower than

what is required to move the polaron under zero f_n. In Figure 4.13 for example, we have $A^{\text{comb}} = \bar{\epsilon} = 0.03$, whereas the critical value for A^{comb} under $\theta = 0$, as we discovered in Section 4.4.3, was 0.172. We see in Figure 4.13 that the polaron spends the majority of its lifetime oscillating by small amounts around its localisation site, but occasionally the random forces on the lattice sites in the vicinity of the electron causes a large distortion, such that the effective potential barrier for the electron is significantly lowered, and the electron can escape the well. Once it does that, the electron is propelled towards one end of the lattice by the EMF $\epsilon = \bar{\epsilon}$, but before the electron has time to move far, the stochastic forces may have further distorted the local lattice sites in such a way that a high potential barrier is restored. The electron therefore becomes trapped again, which gives the polaron time to recover its integrity, before the next random time at which the electron jumps out of its potential well. This explains why a trajectory under the critical thermal energy appears jagged, showing the polaron 'hopping' one or two sites at a time, in stark contrast with the smooth and regular polaron motion that we saw in Figure 4.6.

The way in which our polarons move under $\theta > \theta_c$ remains characteristically similar to that which Figure 4.13 shows, as long as θ is not so large that the excessive thermal energy rapidly destroys the polaron binding and causes delocalisation. We find that regardless of other parameters in the system, stable polaron propagation is possible only if the thermal energy is less than roughly 0.9, which corresponds to a temperature of 55 K. Such a temperature is by no means physiological, but its thermal energy is only several times too small. We will propose in the following Section a means by which we believe our model could be improved to allow higher temperatures.

4.5 Summary and Biophysical Interpretations

In this Chapter, we have presented a new mathematical model describing polaron dynamics in an α-channel, the type of which are found in a transmembrane α-helix. The model is dependent on a symmetry parameter, β, which measures the extent to which the interaction between the polaron's electron and phonon components is spatially symmetric. We have shown that when β takes its extreme values, 0 and 1, the model reduces to existing ones for which it was assumed that the electron-phonon interaction was, respectively, symmetric and antisymmetric. We have justified the physical neccessity of including β in the model, in that one should not simply assume the electron to be coupled equally strongly to hydrogen bonds on either side, or to be coupled only to the bond on one side.

Apart from β, we have also identified two composite parameters which are vital to the intrinsic properties of the polaron. Firstly there is the adiabaticity parameter, ρ, measuring the characteristic time-scale separation between the lattice and electron dynamics, which we have justifiably fixed throughout the Chapter. Then there is the effective coupling parameter, λ, measuring the strength of the electron-phonon interaction. The combination of β and λ determines two key aspects of the stationary state of our system: the electron's maximum localisation probability, and the polaron's binding energy. We have computed both of these quantities as functions of β and λ, using analytical and numerical methods. Specifically, in the continuum (large-lattice) limit, we have obtained approximate stationary solutions, in the process of which we have solved a new generalised nonlinear Schrödinger equation using analytical methods. We have used the analytical results in our numerical scheme, which finds stationary solutions on a finite lattice via an unconventional iterative method.

Our main results relate to using an external EMF to displace the polaron, in a manner which is solitonic and, crucially, directed. Such polaron dynamics could be achieved only if the electron is dislodged from its self-trapping potential well, and the local lattice distortions propagate coherently with the electron, and some mechanism exists which ensures that the electron always moves towards one end of the lattice. If the second condition is not met, then over time the electron probability distribution would become broader, leading to delocalisation. We have found that a constant EMF, with electric field amplitude $\bar{\epsilon}$, is insufficient for displacing the polaron, unless $\bar{\epsilon}$ is larger than some threshold value, but then the forcing causes rapid delocalisation. We have also found that a temporally sinusoidal electric field component, $A\sin(2\pi\tau/T)$, is never sufficient for displacing the polaron. We then combined the constant and sinusoidal electric fields, resulting in the mean-shifted periodic field (MSPF), $\epsilon = \bar{\epsilon} - A\sin(2\pi\tau/T)$. We have discovered that, for each $\bar{\epsilon}$ which is insufficient on its own to displace the polaron, there is some critical value A_{c}, such that the polaron is displaced if and only if $A \geq A_{\mathrm{c}}$. There is also an optimal value A_{m}, such that the polaron attains maximum velocity at $A = A_{\mathrm{m}}$. As $\bar{\epsilon}$ is decreased, A_{c} increases, in such a way that the combined amplitude $A^{\mathrm{comb}} = \bar{\epsilon} + A_{\mathrm{c}}$ remains constant. This suggests that there is a certain amount of extra energy that the electron needs in order to overcome its potential barrier, and how much of it comes from the constant or sinusoidal part of the MSPF is inconsequential, as long as the two parts combine to a large enough overall amplitude. Nevertheless, the split between $\bar{\epsilon}$ and A does determine the manner

in which the polaron propagates, specifically its velocity and stability. The velocity is predominantly determined by $\bar{\epsilon}$, and positively correlated with it; but the stability of the polaron is negatively correlated with $\bar{\epsilon}$. By comparing three sets of $(\bar{\epsilon}, A)$ with the same combined $\bar{\epsilon} + A$, namely $(0.005, 0.167), (0.03, 0.142), (0.1, 0.072)$, while keeping all other parameters fixed, we found that the combination $(0.03, 0.142)$ produces optimal balance between polaron velocity and stability.

We have examined how the system depends upon β. To do so, we needed a way of isolating the effect of varying β. This posed a difficulty, because if we were to fix λ and vary β then both the maximum localisation probability and binding energy of the stationary polaron would change. We would then be comparing dynamical behaviours of entirely dissimilar polarons. We therefore decided to vary λ with β, in a way that allowed us to generate a set of stationary polarons, one for each combination of $(\beta, \lambda(\beta))$, such that they all had the same maximum localisation probability. Then we launched these polarons using the same external forcing and compared the results. We have found that $\beta = 1$, representing a system with spatially antisymmetric electron-phonon interaction, produces a polaron which is easiest to move, in the sense that the least amount of electric field is required. We have also found that the symmetric model, $\beta = 0$, does not make the polaron most difficult to move, whereas $\beta \approx 0.6$ does. This hints at the existence of some intrinsic mechanism in the $\beta = 0$ model which pushes the electron towards one end of the lattice, despite it being coupled to the other end equally strongly.

We have also studied the MSPF under non-zero stochastic forcing, characterised by a thermal energy $\theta > 0$, on the peptide units. We have found that a non-zero θ facilitates polaron propagation, in the sense that it lowers the critical amplitude A_{c}, for any given $\bar{\epsilon}$. Moreover, a non-zero θ results in a gradual onset of polaron motion, meaning the rate of change of polaron velocity with respect to A near $A = A_{\mathrm{c}}$ is small, compared to the onset under $\theta = 0$. Our results have also shown that, whenever there is polaron propagation, whether $\theta = 0$ or $\theta > 0$, the relative displacements between neighbouring peptide units remain under $\mathcal{O}(10^{-2})$. This is a necessary condition which allows us to model the peptide units as point dipoles.

Some of the choices of parameters in the MSPF may be justified physically as follows. It is well known that across the plasma membrane of a living cell, a *resting membrane potential* is maintained by intercellular chemical processes [Luc08]. It is also well known that within the plasma membrane there exist highly stable transmembrane regions of proteins,

for instance the human prolactin receptor 2N7I [BPH$^+$16], and the rat monoamine oxidase A 1O5W [MYY$^+$04], both of which are α-helical structures spanning the entire membrane. Given a constant potential difference of ΔV across a linear, homogeneous, isotropic dielectric medium with constant width d, the effective electric field inside the medium is given by $E_0 = \Delta V/(\epsilon_{\rm r} d)$, where $\epsilon_{\rm r}$ is the dielectric constant (a.k.a. relative permittivity) of the medium [Jac99]. Assuming the plasma membrane is such a medium, we can then attribute the physical origin of $\bar{\epsilon}$ to the resting membrane potential, and calculate $\bar{\epsilon}$ using Equation (4.2.42), namely $\bar{\epsilon} = eE_0R/(\hbar\Omega)$. For many cells, the values of the E_0 and d are well established. As an example, one may look at human red blood cells (erythrocytes), one of the most widely studied cells in nature, and point to [CHV$^+$80] for the value $E_0 = -8.4$ mV, as well as [MK80, HEWM83] for $d = 78$ Å. However the value of $\epsilon_{\rm r}$ for a membrane is highly contentious, due to the fact that it depends sensitively upon a large variety of biophysical attributes of the membrane, such as hydration [MDC08], pH value [SY08], and structural stability [VRW09]. In a recent review, it was reported that the value of $\epsilon_{\rm r}$ in literature ranges from 1 to 40 [LLZA13]. Feeding these values of E_0, d and $\epsilon_{\rm r}$ into the equation for $\bar{\epsilon}$, we find that $\bar{\epsilon}$ ranges from 0.002 to 0.1. We have taken care to ensure that in this Chapter the values of $\bar{\epsilon}$ fall strictly within this range. For a physical origin of the sinusoidal component $A\sin(2\pi\tau/T)$ of the MSPF, one could look to common electromagnetic radiations which fill the environment around us in the modern age, such as the radiation from telecommunication transmitters. In particular, the values of T which we have considered, 100, 500 and 2000, respectively match the frequencies of the IEEE 802.11ad protocal Wi-Fi band, the K_u-band frequencies for satellite communications and broadcasting, and the S-band frequencies for radio communications [IEE12,IEE03]. However the amplitudes of the aforementioned radiations are much smaller than the values of A for which we have observed noteworthy results. For instance, treating the mobile telephone transmitter as an omni-directional dipole with peak power P, we can estimate the amplitude $\widetilde{A}$ of its output waves at operational distance d_0, by using the well-known formula $P/(4\pi d_0^2) = \epsilon_0 c\widetilde{A}^2/\epsilon_{\rm r}$, where $\epsilon_0, c, \epsilon_{\rm r}$ are the vacuum permittivity, speed of light, and relative permittivity of the medium, respectively. Feeding $P = 1$ W [LFV$^+$04] and $1 \leq \epsilon_{\rm r} \leq 40$ [LLZA13] into the formula, we obtain 0.8 V $\leq \widetilde{A}d_0 \leq 35$ V. If we want this quantity to translate into our dimensionless amplitude, via $A = e\widetilde{A}R/(\hbar\Omega)$, as $0.002 \leq A \leq 0.1$ (the range for which we have positive results), then the operational distance needs to be $d_0 = 3\times 10^{-5}$ m, which is unrealistic. If d_0 is much larger, then A becomes too small to cause polaron displacement

in our model. It is therefore clear that, in a real cell, the effect on a polaron due to a combination of resting membrane potential and stochastic thermal forces are dominant over any external electromagnetic radiation that may commonly be present. This highlights the importance of our observation that, given a constant electric field $\bar{\epsilon}$, there exists some critical thermal energy θ_{c}, such that the polaron undergoes directed motion if and only if $\theta \geq \theta_{\mathrm{c}}$. In other words, a combination of $\bar{\epsilon}$ and θ can be sufficient for displacing the polaron, in a manner which is solitonic and directed, just as a combination of $\bar{\epsilon}$ and $A\sin(2\pi\tau/T)$ can. In the former case, the thermal energy θ provides the required extra energy beyond $\bar{\epsilon}$, which would otherwise be provided by the sinusoidal electric field.

We have thus far assumed that the α-channel is linear, in the sense that all hydrogen bonds point in the same direction. We know this is not the case in the α-helix, where every hydrogen bond is at an angle to the helical axis. By expanding the spatial geometry of our system from one-dimensional space to three-dimensional space, we can take these bond angles into account. In the resulting α-helical model, we believe it is possible that we can raise the system's temperature beyond the current limit of roughly 55 K and still obtain stable polaron propagation. We study such a model in the following Chapter.

Chapter 5

The Generalised Davydov-Scott Model for the α-Helix

This Chapter is adapted from [Luo18].

Scott showed in his model of amide-I-hydrogen bond coupling that the α-helix system with unit mass M and bond strength K was equivalent to an α-channel system with unit mass $3M$ and bond strength $3K$, if one assumed an appropriate form of latitudinal symmetry called the *A-mode symmetry*. Essentially this was the assumption that twisting and bending in the helix were negligible, and that the electron is equally spread amongst the three channels of the α-helix at all times. For this Chapter, in the context of our generalised Davydov-Scott (GDS) model for electron-hydrogen bond coupling in the α-helix, we explore a variant of the A-mode symmetry in which the twisting of the helix is not neglected.

In Section 5.1, we present a Hamiltonian for the system which takes into account not only interactions along hydrogen bonds in an α-helix, but also latitudinal electron transfer between adjacent α-channels. We then show in Section 5.2 that under a suitable A-mode symmetry assumption, latitudinal transfer is nullified, and the dynamics of a polaron in our multi-channel system are encapsulated by equations that are highly similar, though not identical, to those in Chapter 4, which were applicable to a single-channel system. The difference between the two sets of equations stems from the twisting of the α-channels around the helical axis. We proceed in Section 5.3 to compute stationary polaron solutions of our system, neglecting stochastic forces, and quasi-stationary polaron solutions with stochastic forces in place. In Section 5.4, we investigate the dynamics of polarons under electromagnetic fields the likes of which we first considered in Chapter 4, with or without stochastic forces. Where appropriate, we draw comparisons between our

results in this Chapter and in the previous, illustrating the differences between a polaron moving along a single α-channel without being influenced by any other channels, and a polaron propagating along all three α-channels under the A-mode symmetry.

In Section 5.5, we propose a GDS model for the α-helix *without* A-mode symmetry. We write down the dynamical equations, and make predictions about polaron solutions based on analytical results. However, our ability to conduct a numerical study is hampered by the lack of existing data relating to the electron band structure of the α-helix, and we will explain this point in detail. Finally, we summarise our results in Section 5.6, giving biophysical interpretations.

5.1 The Hamiltonian and Dynamical Equations

We consider an α-helix where the number of peptide units in α-channels labelled 1, 2 and 3 are, respectively, N_1+1, N_2+1 and N_3+1. Assuming all peptide units to be identical, all equilibrium spacings between units to be identical, and all covalent bonds to be rigid, we treat the α-helix as a lattice, with peptide units as point-particle nodes. We therefore propose the following Hamiltonian to describe electron-hydrogen bond coupling in the α-helix, under the influence of an external electromagnetic field (EMF):

$$\widehat{H} = \widehat{H}_{\mathrm{e}} + \widehat{H}_{\mathrm{p}} + \widehat{H}_{\mathrm{int}} + \widehat{H}_{\mathrm{ext}}, \tag{5.1.1}$$

where

$$\begin{aligned}
\widehat{H}_{\mathrm{e}} = \sum_{j=1}^{3}\Bigg[& \sum_{n=0}^{N_j} J_0 \widehat{A}_{n,j}^{\dagger}\widehat{A}_{n,j} - \sum_{n=0}^{N_j-1} J_1\Big(\widehat{A}_{n+1,j}^{\dagger}\widehat{A}_{n,j} + \widehat{A}_{n,j}^{\dagger}\widehat{A}_{n+1,j}\Big) \\
& - \sum_{n=0}^{N_j} J_2\Big(\widehat{A}_{n,j+1}^{\dagger}\widehat{A}_{n,j} + \widehat{A}_{n,j}^{\dagger}\widehat{A}_{n,j+1}\Big)\Bigg], \qquad (5.1.2a) \\
\widehat{H}_{\mathrm{p}} = \sum_{j=1}^{3}\Bigg[& \sum_{n=0}^{N_j} \frac{\zeta^2 P_{n,j}^2}{2M} + \sum_{n=0}^{N_j-1} \frac{M\zeta^{-2}\Omega^2\left(U_{n+1,j}-U_{n,j}\right)^2}{2}\Bigg], \qquad (5.1.2b) \\
\widehat{H}_{\mathrm{int}} = & \sum_{j=1}^{3} \chi_r\left(U_{1,j}-U_{0,j}\right)\widehat{A}_{0,j}^{\dagger}\widehat{A}_{0,j} + \sum_{j=1}^{3}\chi_l\left(U_{N,j}-U_{N-1,j}\right)\widehat{A}_{N,j}^{\dagger}\widehat{A}_{N,j} \\
& + \sum_{j=1}^{3}\sum_{n=1}^{N_j-1}\Big[\chi_r\left(U_{n+1,j}-U_{n,j}\right) + \chi_l\left(U_{n,j}-U_{n-1,j}\right)\Big]\widehat{A}_{n,j}^{\dagger}\widehat{A}_{n,j}, \qquad (5.1.2c) \\
\widehat{H}_{\mathrm{ext}} = & -\sum_{j=1}^{3}\sum_{n=0}^{N_j} eER\left(n-n_0\right)\widehat{A}_{n,j}^{\dagger}\widehat{A}_{n,j}. \qquad (5.1.2d)
\end{aligned}$$

$\widehat{H}_{\rm e}, \widehat{H}_{\rm p}, \widehat{H}_{\rm int}$ and $\widehat{H}_{\rm int}$ are Hamiltonians associated with, respectively, the electron, lattice, electron-hydrogen bond phonon interaction and electron-EMF interaction. The indices $j = 1, 2, 3$ and $n = 0, 1, \ldots, N_j$ label, respectively, the three α-channels and the units within each channel. Addition in j, for instance $\widehat{A}_{n,j+1}$, is modulo 3, so that $j = 4$ is equivalent to $j = 1$. $\widehat{A}^{\dagger}_{n,j}$ and $\widehat{A}_{n,j}$ are, respectively, the electron creation and annihilation operators at the (n, j) peptide unit; they satisfy the fermionic anti-commutation relation,

$$\widehat{A}_{m,k}\widehat{A}^{\dagger}_{n,j} + \widehat{A}^{\dagger}_{n,j}\widehat{A}_{m,k} = \delta_{mn}\delta_{jk}. \tag{5.1.3}$$

J_0 is the electron site energy, J_1 the nearest-neighbour electron transfer integral across a hydrogen bond along an α-channel, and J_2 the nearest-neighbour electron transfer integral across a peptide bond between adjacent α-channels.

There is a major difference between $\widehat{H}_{\rm e}$ in the current model and $\widehat{H}_{\rm e}$ in Scott's model for amide-I-hydrogen bond coupling. We have a negative inter-channel transfer energy, $-J_2$, whereas Scott had a positive one. The reason for this discrepancy is that in the context of vibrational energy propagation, whilst the amide-I tends to disperse along the longitudinal direction, it tends to do the opposite in the lateral direction and localise on a single α-channel. This is because transfers of vibrational energy along the essentially rigid peptide bonds between channels are highly unlikely. In fact, amide-I oscillations are by definition in the longitudinal direction. In the context of electron transport, however, the electron tends to disperse in all directions, because all neighbouring peptide units are the same point-dipoles, and are therefore equivalent [Hen01].

In $\widehat{H}_{\rm p}$, the origin of the parameter ζ is as follows. In the single-channel model of Chapter 4, the hydrogen bonds were linear in the sense that each peptide unit had one degree of freedom, and the displacements of the units along their common axis were represented as U_n. In the α-helix, every peptide unit has three degrees of freedom, and the distortion in the (n, j)-to-$(n+1, j)$ hydrogen bond, hereafter referred to as the (n^+, j) hydrogen bond, depends upon displacements in all three spatial dimensions of the (n, j) and $(n+1, j)$ peptide units. Every hydrogen bond at equilibrium is at an angle to, rather than collinear with, the next; we call this the twisting of the α-channel. If we want only one degree of freedom, $U_{n,j}$, and its conjugate momentum, $P_{n,j}$, to appear in the Hamiltonian, then we must be careful about what they represent. In reality, a distorted hydrogen bond may not point in the same direction as it does at equilibrium. However we can assume that the bond distortions are *mostly* in the equilibrium bond directions, in

the sense that the distortions *projected along equilibrium bond directions* are the dominant factors in the lattice's potential energy, compared to effects of any deviations from the equilibrium directions. One might therefore let $U_{n,j}$ represent the displacement of the (n,j) unit along the equilibrium direction of the (n^+,j) hydrogen bond. That would, however, make $U_{n+1,j}$ the displacement of the $(n+1,j)$ unit along the equilibrium direction of the $((n+1)^+,j)$ hydrogen bond, which, due to the twisting of the α-channel, is not the same as the equilibrium direction of the (n^+,j) bond. As a result, $U_{n+1,j}-U_{n,j}$ does not represent the distortion of the (n^+,j) hydrogen bond along its equilibrium direction. In fact, it is impossible to define $U_{n,j}$ in such a way that $U_{n+1,j}-U_{n,j}$ consistently represents bond distortions in equilibrium bond directions for all n. The resolution that we propose is to let $U_{n,j}$ be the longitudinal, i.e. along helical axis, displacement of the (n,j) peptide unit. $U_{n+1,j}-U_{n,j}$ is then the (n^+,j) bond distortion projected along the helical axis. Now, Ω in $\widehat{H}_{\mathrm{p}}$ is defined as the square root of the ratio between the bond's force constant K and the node mass M:

$$\Omega := \sqrt{K/M}. \tag{5.1.4}$$

The summand in the second term of Equation (5.1.2b), which represents the lattice's potential energy due to bond distortions, should be $(M\Omega^2/2)(U_{n+1,j}-U_{n,j})^2/|\mathbf{e}^0_{n,j}\cdot\mathbf{e}^0_z|^2$, where $\mathbf{e}^0_{n,j}$ and $\mathbf{e}^0_z$ are basis vectors in the directions of, respectively, the (n^+,j) hydrogen bond at equilibrium and the helical axis at equilibrium. Strictly speaking, we should be dividing $(U_{n+1,j}-U_{n,j})^2$ by $|\mathbf{e}_{n,j}(t)\cdot\mathbf{e}_z(t)|^2$, where $\mathbf{e}_{n,j}(t)$ is the basis vector along the (n^+,j) hydrogen bond at time t, and $\mathbf{e}_z(t)$ is the basis vector along the helical axis at time t. However we neglect bending in the α-helix, meaning that we assume $\mathbf{e}_z(t)=\mathbf{e}^0_z$ for all t. Moreover, assuming that all bond distortions are always small relative to the equilibrium bond length (indeed we will see in subsequent Sections that this relative magnitude never exceeds $\mathcal{O}(10^{-2})$), and assuming that $|\mathbf{e}^0_{n,j}\cdot\mathbf{e}^0_z|$ is sufficiently large (we will verify this in Section 5.2.1), then the difference between $|\mathbf{e}_{n,j}(t)\cdot\mathbf{e}^0_z|$ and $|\mathbf{e}^0_{n,j}\cdot\mathbf{e}^0_z|$ will always be negligible compared to $|\mathbf{e}^0_{n,j}\cdot\mathbf{e}^0_z|$. In other words, any error resulting from using $\mathbf{e}^0_{n,j}$ instead of $\mathbf{e}_{n,j}(t)$ in our expression for the lattice potential energy will always be negligible. We define

$$\zeta := \left|\mathbf{e}^0_{n,j}\cdot\mathbf{e}^0_z\right|, \tag{5.1.5}$$

and the expression in Equation (5.1.2b) for the potential part of $\widehat{H}_{\mathrm{p}}$ immediately follows.

An equivalent way to interpret the ζ^{-2} factor is the following. If we incorporate all three degrees of freedom of the (n, j) peptide unit, namely the longitudinal displacement $U_{n,j}$ and, say, $V_{n,j}$ and $W_{n,j}$, then the square of the distortion of the (n^+, j) hydrogen bond is exactly $(U_{n+1,j}-U_{n,j})^2+(V_{n+1,j}-V_{n,j})^2+(W_{n+1,j}-W_{n,j})^2$. Our assumption is that out of those three components, $(U_{n+1,j}-U_{n,j})^2$ is the dominant one, so that one can treat the ratio between the sum of the other two components and $(U_{n+1,j}-U_{n,j})^2$ as a perturbation about 1; and for simplicity we assume that ratio to be a constant, rather than carry out a perturbation analysis rigorously. Consequently, we simply scale $(U_{n+1,j}-U_{n,j})^2$ by a constant factor of $\zeta^{-2} = 1/|\mathbf{e}^0_{n,j} \cdot \mathbf{e}^0_z|^2$.

The reason that the kinetic part of $\widehat{H}_{\rm p}$ in Equation (5.1.2b) contains a factor of ζ^2, rather than ζ^{-2}, is as follows. The momentum conjugate to $U_{n,j}$ is defined by $P_{n,j} := \partial\mathcal{L}/\partial(\mathrm{d}U_{n,j}/\mathrm{d}t)$, where $\mathcal{L} = \zeta^{-2}\sum_{n,j}\left[(M/2)(\mathrm{d}U_{n,j}/\mathrm{d}t)^2 - (M\Omega^2/2)(U_{n+1,j}-U_{n,j})^2\right]$ is the Lagrangian of the isolated lattice system. The ζ^{-2} factor multiplies the kinetic part in $\mathcal{L}$ because $\mathrm{d}U_{n,j}/\mathrm{d}t$ needs to be scaled by the same factor by which $U_{n,j}$ is scaled. Thus,

$$P_{n,j} = M\zeta^{-2}\frac{\mathrm{d}U_{n,j}}{\mathrm{d}t}. \tag{5.1.6}$$

Then the Hamiltonian $\widehat{H}_{\rm p}$ is derived using the Legendre transform from $\mathcal{L}$, by $\widehat{H}_{\rm p} = \sum_{n,j} P_{n,j}\cdot\mathrm{d}U_{n,j}/\mathrm{d}t - \mathcal{L} = \sum_{n,j} P_{n,j}\cdot\zeta^2 P_{n,j}/M - \mathcal{L}$. Once we use Equation (5.1.6) to write $\mathcal{L}$ in terms of $P_{n,j}$, the expression in Equation (5.1.2b) for $\widehat{H}_{\rm p}$ immediately follows, where ζ^2 appears in the kinetic term while ζ^{-2} appears in the potential.

For the interaction Hamiltonian $\widehat{H}_{\rm int}$ in Equation (5.1.2), we have taken the GDS bilinear form with a coupling constant χ partitioned into χ_r and χ_l [cf. Chapter 4], respectively representing the strength of interaction between a site electron and hydrogen bonds to either side of it. Any scaling factor necessitated by the three-dimensional α-helical geometry may simply be absorbed into χ_r and χ_l, since their values are in any case variable. Without loss of generality, we let $\chi_r > 0$ and $0 \le \chi_l \le \chi_r$. We then define the *symmetry parameter*,

$$\beta := \frac{\chi_r - \chi_l}{\chi}, \tag{5.1.7}$$

where $\chi = \chi_r + \chi_l$, so that

$$0 \le \beta \le 1. \tag{5.1.8}$$

We can therefore write

$$\widehat{H}_{\text{int}} = \sum_{j=1}^{3} \frac{\chi}{2} (1+\beta) (U_{1,j} - U_{0,j}) \widehat{A}^{\dagger}_{0,j} \widehat{A}_{0,j} + \sum_{j=1}^{3} \frac{\chi}{2} (1-\beta) (U_{N,j} - U_{N-1,j}) \widehat{A}^{\dagger}_{N,j} \widehat{A}_{N,j} + \sum_{j=1}^{3} \sum_{n=1}^{N_j-1} \frac{\chi}{2} \Big[(U_{n+1,j} - U_{n-1,j}) + \beta (U_{n+1,j} + U_{n-1,j} - 2U_{n,j}) \Big] \widehat{A}^{\dagger}_{n,j} \widehat{A}_{n,j}. \quad (5.1.9)$$

Finally, $\widehat{H}_{\text{ext}}$ in Equation (5.1.2) models the effect of an EMF with longitudinal electric field strength $E = E(t)$ on the potential energy of an electron with charge $-e$. The potential energy due to E is set to zero at some arbitrary n_0, which we assume to be the same for all three α-channels in the α-helix, and R is the equilibrium distance between peptide units along an α-channel. We have assumed that the EMF has equal influence on electrons at the $(n, j), (n, j+1)$ and $(n, j+2)$ sites. This is of course a gross simplification, and one that we will abandon in Section 5.5; for now, we make this simplification because it is an essential ingredient of the A-mode symmetry which we describe in the next Section.

We write the state of the system as a linear superposition of local excitations,

$$|\Psi(t)\rangle = \sum_{j=1}^{3} \sum_{n=0}^{N_j} \alpha_{n,j}(t) \widehat{A}^{\dagger}_{n,j} |0\rangle , \quad (5.1.10)$$

where $\alpha_{n,j}$ are complex coefficients and $|0_{\text{e}}\rangle$ is the normalised vacuum state. To derive dynamical equations for $\alpha_{n,j}$ and $U_{n,j}$ in this setting, we adopt the same Hamiltonian approach which we described in detail in Section 4.2.2. To avoid repetition, here we omit the intermediate steps in the derivation and simply state that the equations for α_n arise from the Schrödinger equation,

$$i\hbar \frac{\partial |\Psi\rangle}{\partial t} = (\widehat{H}_{\text{e}} + \widehat{H}_{\text{int}} + \widehat{H}_{\text{ext}}) |\Psi\rangle , \quad (5.1.11)$$

and they are as follows:

$$i\hbar \frac{\mathrm{d}\alpha_{0,j}}{\mathrm{d}t} = J_0 \alpha_{0,j} - J_1 \alpha_{1,j} - J_2 (\alpha_{0,j+1} + \alpha_{0,j-1}) + \frac{\chi}{2} \alpha_{0,j} (1+\beta) (U_{1,j} - U_{0,j}) - eER(-n_0)\alpha_{0,j}, \quad (5.1.12a)$$

$$i\hbar \frac{\mathrm{d}\alpha_{n,j}}{\mathrm{d}t} = J_0 \alpha_{n,j} - J_1 (\alpha_{n+1,j} + \alpha_{n-1,j}) - J_2 (\alpha_{n,j+1} + \alpha_{n,j-1}) + \frac{\chi}{2} \alpha_{n,j} \Big[(U_{n+1,j} - U_{n-1,j}) + \beta (U_{n+1,j} + U_{n-1,j} - 2U_{n,j}) \Big] - eER(n-n_0)\alpha_{n,j}, \qquad \text{for } 1 \leq n \leq N_j - 1, \quad (5.1.12b)$$

$$i\hbar \frac{\mathrm{d}\alpha_{N,j}}{\mathrm{d}t} = J_0 \alpha_{N,j} - J_1 \alpha_{N-1,j} - J_2 (\alpha_{N,j+1} + \alpha_{N,j-1}) + \frac{\chi}{2} \alpha_{N,j} (1-\beta) (U_{N,j} - U_{N-1,j}) - eER(N-n_0)\alpha_{N,j}. \quad (5.1.12c)$$

Equations for $U_{n,j}$ are derived from classical Hamilton's equations,

$$\frac{\mathrm{d}U_{n,j}}{\mathrm{d}t} = \frac{\partial H_{\mathrm{cla}}}{\partial P_{n,j}}, \tag{5.1.13a}$$

$$\frac{\mathrm{d}P_{n,j}}{\mathrm{d}t} = -\frac{\partial H_{\mathrm{cla}}}{\partial U_{n,j}}, \tag{5.1.13b}$$

where we have defined

$$\begin{aligned} H_{\mathrm{cla}} &:= \langle\Psi|(\widehat{H}_{\mathrm{p}} + \widehat{H}_{\mathrm{int}})|\Psi\rangle \\ &= \sum_{j=1}^{3}\sum_{n=0}^{N_j}\frac{\zeta^2 P_{n,j}^2}{2M} + \sum_{j=0}^{3}\sum_{n=0}^{N_j-1}\frac{M\zeta^{-2}\Omega^2\left(U_{n+1,j}-U_{n,j}\right)^2}{2} \\ &\quad + \sum_{j=1}^{3}\frac{\chi}{2}\Bigg[(1+\beta)|\alpha_{0,j}|^2\left(U_{1,j}-U_{0,j}\right) + (1-\beta)|\alpha_{N,j}|^2\left(U_{N,j}-U_{N-1,j}\right) \\ &\quad + \sum_{n=1}^{N_j-1}|\alpha_{n,j}|^2\Big[\left(U_{n+1,j}-U_{n-1,j}\right) + \beta\left(U_{n+1,j}+U_{n-1,j}-2U_{n,j}\right)\Big]\Bigg]. \end{aligned} \tag{5.1.14}$$

Combining the two Hamilton's equations gives us, for $j = 1, 2, 3$ and $n = 0, 1, \ldots N$,

$$M\zeta^{-2}\frac{\mathrm{d}^2U_{n,j}}{\mathrm{d}t^2} = -\frac{\partial H_{\mathrm{cla}}}{\partial U_{n,j}}. \tag{5.1.15}$$

We therefore deduce the following dynamical equations for $U_{n,j}$:

$$M\zeta^{-2}\frac{\mathrm{d}^2U_{0,j}}{\mathrm{d}t^2} = M\zeta^{-2}\Omega^2\left(U_{1,j}-U_{0,j}\right) + \frac{\chi}{2}\Big[(1-\beta)|\alpha_{1,j}|^2 + (1+\beta)|\alpha_{0,j}|^2\Big], \tag{5.1.16a}$$

$$\begin{aligned} M\zeta^{-2}\frac{\mathrm{d}^2U_{n,j}}{\mathrm{d}t^2} &= M\zeta^{-2}\Omega^2\left(U_{n-1,j}+U_{n+1,j}-2U_{n,j}\right) + \frac{\chi}{2}\Big[(1-\beta)|\alpha_{n+1,j}|^2 \\ &\qquad + 2\beta|\alpha_{n,j}|^2 - (1+\beta)|\alpha_{n-1,j}|^2\Big] \qquad \text{for } 1 \le n \le N_j - 1, \end{aligned} \tag{5.1.16b}$$

$$M\zeta^{-2}\frac{\mathrm{d}^2U_{N,j}}{\mathrm{d}t^2} = -M\zeta^{-2}\Omega^2\left(U_{N,j}-U_{N-1,j}\right) - \frac{\chi}{2}\Big[(1-\beta)|\alpha_{N,j}|^2 + (1+\beta)|\alpha_{N-1,j}|^2\Big]. \tag{5.1.16c}$$

To account for interactions between the peptide units and the environment, we add Langevin terms to the right-hand side of Equation (5.1.16), which are: $-\Gamma\mathrm{d}U_{n,j}/\mathrm{d}t$, a drag force representing dissipation due to friction, where Γ is a viscous damping coefficient; and $F_{n,j}(t)$, stochastic forces arising from thermal fluctuations [Lan08, LG97, Sch10, BEPZ14]. $F_{n,j}(t)$ is normally-distributed with zero mean and correlation function

$$\langle F_m(t)F_n(t')\rangle = 2\Gamma k_{\mathrm{B}}\Theta\delta_{m,n}\delta(t-t'), \tag{5.1.17}$$

where $k_{\mathrm{B}}, \Theta, \delta_{\cdot,\cdot}$ and $\delta(\cdot)$ are, respectively, the Boltzmann constant, temperature of the environment, the Kronecker delta and the delta function.

By introducing the gauge transformation,

$$\alpha_{n,j}(t) = \psi_{n,j}(t) \exp\left[-\frac{it}{\hbar}\left(J_0 - 2J_1 - 2J_2\right)\right], \tag{5.1.18}$$

we can recast Equation (5.1.12) as equations for $\psi_{n,j}$ whilst preserving the probability distribution, $|\alpha_{n,j}|^2 = |\psi_{n,j}|^2$. By defining

$$S_{n,j} := U_{n+1,j} - U_{n,j} \tag{5.1.19}$$

for $n = -1, 0, 1, \ldots, N$, with quantities that involve fictitious points at $n = -1$ and $n = N + 1$ given by

$$S_{-1} = S_N = 0, \tag{5.1.20}$$

and by requiring

$$\psi_{-1,j} = \psi_{0,j} = \psi_{N,j} = \psi_{N+1,j} = 0, \tag{5.1.21}$$

we can write down one unifying equation for $\psi_{n,j}$ and one unifying equation for $U_{n,j}$ valid for all $j = 1, 2, 3$ and $n = 0, 1, \ldots N_j$, as follows:

$$\begin{aligned} i\hbar\frac{\mathrm{d}\psi_{n,j}}{\mathrm{d}t} &= \frac{\chi}{2}\psi_{n,j}\left[\left(S_{n,j} + S_{n-1,j}\right) + \beta\left(S_{n,j} - S_{n-1,j}\right)\right] \\ &\quad - J_1\left(\psi_{n+1,j} + \psi_{n-1,j} - 2\psi_{n,j}\right) - J_2\left(\psi_{n,j+1} + \psi_{n,j-1} - 2\psi_{n,j}\right) \\ &\quad - eER(n - n_0)\psi_{n,j}, \end{aligned} \tag{5.1.22a}$$

$$\begin{aligned} M\zeta^{-2}\frac{\mathrm{d}^2U_{n,j}}{\mathrm{d}t^2} &= M\zeta^{-2}\Omega^2\left(S_{n,j} - S_{n-1,j}\right) + \frac{\chi}{2}\left(|\psi_{n+1,j}|^2 - |\psi_{n-1,j}|^2\right) \\ &\quad - \frac{\chi}{2}\beta\left(|\psi_{n+1,j}|^2 + |\psi_{n-1,j}|^2 - 2|\psi_{n,j}|^2\right) - \Gamma\frac{\mathrm{d}U_{n,j}}{\mathrm{d}t} + F_{n,j}. \end{aligned} \tag{5.1.22b}$$

Equations (5.1.22a) and (5.1.22b) are the dynamical equations for our system of electron-hydrogen bond coupling in the α-helix. Comparing them to the dynamical equations for the α-channel system in Chapter 4, we see strong similarities between Equation (5.1.22a) and Equation (4.2.26), as well as between Equation (5.1.22b) and Equation (4.2.37).

5.2 The System Under A-Mode Symmetry

The A-mode symmetry refers in essence to the equipartition of the electron among the α-channels. Several other assumptions are also pertinent to the symmetry, and in Section 5.2.1 we describe them mathematically. We also present the dynamical equations which result from simplifications afforded by the A-mode symmetry, and assign parameter values where appropriate. We then derive energy properties of our system in Section 5.2.2.

5.2.1 The Equations and Parameters

The A-mode symmetry manifests itself mathematically as an equipartition of $\psi_{n,j}$ among the α-channels:

$$\psi_{n,1} = \psi_{n,2} = \psi_{n,3}, \tag{5.2.1}$$

as well as the equivalence of lattice displacements between the α-channels:

$$U_{n,1} = U_{n,2} = U_{n,3}. \tag{5.2.2}$$

We further assume that

$$F_{n,1} = F_{n,2} = F_{n,3}, \quad N_1 = N_2 = N_3 = N, \tag{5.2.3}$$

and define

$$\psi_n := \sqrt{3}\psi_{n,j}, \quad U_n := U_{n,j}, \quad S_n := U_{n+1} - U_n, \quad F_n := F_{n,j}. \tag{5.2.4}$$

Then, multiplying Equation (5.1.22a) by $\sqrt{3}$ and Equation (5.1.22b) by 3, we obtain

$$\begin{aligned} i\hbar\frac{\mathrm{d}\psi_n}{\mathrm{d}t} &= \frac{\chi}{2}\psi_n\left[(S_n + S_{n-1}) + \beta\left(S_n - S_{n-1}\right)\right] \\ &\quad - J_1\left(\psi_{n+1} + \psi_{n-1} - 2\psi_n\right) - eER(n - n_0)\psi_n, \end{aligned} \tag{5.2.5a}$$

$$\begin{aligned} \widetilde{M}\zeta^{-2}\frac{\mathrm{d}^2U_n}{\mathrm{d}t^2} &= \widetilde{M}\zeta^{-2}\Omega^2\left(S_n - S_{n-1}\right) + \frac{\chi}{2}\left(|\psi_{n+1}|^2 - |\psi_{n-1}|^2\right) \\ &\quad - \frac{\chi}{2}\beta\left(|\psi_{n+1}|^2 + |\psi_{n-1}|^2 - 2|\psi_n|^2\right) - \widetilde{\Gamma}\frac{\mathrm{d}U_n}{\mathrm{d}t} + \widetilde{F}_n, \end{aligned} \tag{5.2.5b}$$

for $n = 0, 1, \ldots, N$, where

$$\widetilde{M} = 3M, \quad \widetilde{\Gamma} = 3\Gamma, \quad \widetilde{F}_n = 3F_n. \tag{5.2.6}$$

We see that the A-mode symmetry, together with the gauge transformation (5.1.18), has eliminated the J_2 term that appeared in Equation (5.1.22b). Scaling time and length by

$$t = \Omega^{-1}\tau, \quad U_n = Lu_n, \quad S_n = Ls_n, \tag{5.2.7}$$

where

$$L := \sqrt{\hbar\widetilde{M}^{-1}\Omega^{-1}}, \tag{5.2.8}$$

we obtain the following dimensionless dynamical equations:

$$\begin{aligned} i\dot{\psi}_n &= \kappa\psi_n\left[(s_n + s_{n-1}) + \beta\,(s_n - s_{n-1})\right] - \rho\,(\psi_{n+1} + \psi_{n-1} - 2\psi_n) \\ &\quad - \epsilon(n - n_0)\psi_n, \qquad (5.2.9a) \\ \ddot{u}_n &= (s_n - s_{n-1}) + \kappa\zeta^2\left[\left(|\psi_{n+1}|^2 - |\psi_{n-1}|^2\right) - \beta\left(|\psi_{n+1}|^2 + |\psi_{n-1}|^2 - 2|\psi_n|^2\right)\right] \\ &\quad - \gamma\dot{u}_n + f_n, \qquad (5.2.9b) \end{aligned}$$

for $n = 0, 1, \ldots, N$, where the overdot denotes differentiation with respect to τ, and

$$\psi_{-1} = \psi_{N+1} = 0, \quad \psi_0 = \psi_N = 0, \quad s_{-1} = s_N = 0, \quad u_0 = \dot{u}_0 = 0. \qquad (5.2.10)$$

The dimensionless parameters that appear in Equation (5.2.9) are

$$\kappa = \frac{\chi}{2\sqrt{\hbar\widetilde{M}\Omega^3}}, \quad \rho = \frac{J_1}{\hbar\Omega}, \quad \epsilon = \frac{eER}{\hbar\Omega}, \quad \gamma = \frac{\zeta^2\widetilde{\Gamma}}{\widetilde{M}\Omega}, \quad f_n = \frac{\zeta^2\widetilde{F}_n}{\sqrt{\hbar\widetilde{M}\Omega^3}}, \qquad (5.2.11)$$

where, according to Equation (5.1.17), Equation (5.2.6) and the re-scalings, the stochastic forces f_n have zero mean and are correlated by

$$\begin{aligned} \langle f_m(\tau) f_n(\tau')\rangle &= \frac{18\zeta^4\Gamma k_{\mathrm{B}}\Theta\delta_{m,n}\delta(\tau - \tau')\Omega}{\hbar\widetilde{M}\Omega^3} \\ &= \frac{6\zeta^2\gamma\theta\delta_{m,n}}{\Delta\tau}, \qquad (5.2.12) \end{aligned}$$

with

$$\theta = \frac{k_{\mathrm{B}}\Theta}{\hbar\Omega} \qquad (5.2.13)$$

being thermal energy in units of $\hbar\Omega$, and $\Delta\tau$ being a small time-step which we employ in our numerical experiments. Equation (5.2.9) holds subject the normalisation condition,

$$\sum_{n=0}^{N} |\psi_n|^2 = 1, \qquad (5.2.14)$$

which is a consequence of the fact that $\sum_{j=1}^{3}\sum_{n=0}^{N}|\psi_{n,j}|^2 = 1$ and $\psi_n = \sqrt{3}\psi_{n,j}$ for all j. We see that Equation (5.2.9) differs from Equation (4.2.40) for the single-channel system only in the definitions of some dimensionless parameters and the appearance of ζ in Equation (5.2.9). It is clear that the ζ parameter truly is non-trivial: it represents an imbalance between the effect on the electron and on the lattice of the electron-phonon coupling, and it is impossible to make ζ disappear from the equations by re-scaling.

We take values of the parameters J_1, R, M, Ω and Γ from Chapter 4, specifically Section 4.2.3, where we justified the choices of these values. Here we present J_1, R and Ω again for completeness, as well as $\widetilde{M}, \widetilde{\Gamma}$ which are related to M, Γ by Equation (5.2.6).

$$\begin{aligned} &J_1 = 11 \text{ meV}, \quad R = 4.5 \text{ Å}, \quad \Omega = 8.1 \times 10^{12} \text{ s}^{-1}, \\ &\widetilde{M} = 5.322 \times 10^{-25} \text{ kg}, \quad \widetilde{\Gamma} = 102 \text{ pg} \cdot \text{s}^{-1}. \end{aligned} \tag{5.2.15}$$

In order to calculate ζ from Equation (5.1.5), we need

$$\zeta = \left| \mathbf{e}^0_{n,j} \cdot \mathbf{e}^0_z \right| = \frac{\left| \mathbf{v}^0_{n,j} \cdot \mathbf{e}^0_z \right|}{\left| \mathbf{v}^0_{n,j} \right|}, \tag{5.2.16}$$

where $\mathbf{v}^0_{n,j}$ is the vector from one peptide unit to the next in an α-channel at equilibrium. In cylindrical coordinates, $\mathbf{v}^0_{n,j}$ is the vector from $(R_0, \sigma^0_{n,j}, Z^0_{n,j})$ to $(R_0, \sigma^0_{n+1,j}, Z^0_{n+1,j})$:

$$\begin{aligned} \mathbf{v}^0_{n,j} &= \left(R_0 \left(\cos \sigma^0_{n+1,j} - \cos \sigma^0_{n,j} \right),\ R_0 \left(\sin \sigma^0_{n+1,j} - \sin \sigma^0_{n,j} \right),\ Z^0_{n+1,j} - Z^0_{n,j} \right) \\ &= \Bigg(-2R_0 \sin \left(\frac{\sigma^0_{n+1,j} - \sigma^0_{n,j}}{2} \right) \sin \left(\frac{\sigma^0_{n+1,j} + \sigma^0_{n,j}}{2} \right), \\ &\qquad 2R_0 \sin \left(\frac{\sigma^0_{n+1,j} - \sigma^0_{n,j}}{2} \right) \cos \left(\frac{\sigma^0_{n+1,j} + \sigma^0_{n,j}}{2} \right),\ Z^0_{n+1,j} - Z^0_{n,j} \Bigg), \end{aligned} \tag{5.2.17}$$

where R_0 is the mean radius of the α-helical coil, $\sigma^0_{n+1,j} - \sigma^0_{n,j}$ is the angle of rotation from one peptide unit to the next projected onto the plane perpendicular to the helical axis, and $Z^0_{n+1,j} - Z^0_{n,j}$ is the distance from one peptide unit to the next projected onto the helical axis, all in the equilibrium state. Taking values from [BT88], we have

$$R_0 = 2.3\text{Å}, \quad \sigma^0_{n+1,j} - \sigma^0_{n,j} = \frac{5\pi}{3}, \quad Z^0_{n+1,j} - Z^0_{n,j} = R = 4.5 \text{ Å}. \tag{5.2.18}$$

It therefore follows that

$$\begin{aligned} \zeta &= 4.5 \left| \left(-4.6 \sin \frac{5\pi}{6} \sin \frac{\sigma^0_{n+1,j} + \sigma^0_{n,j}}{2},\ 4.6 \sin \frac{5\pi}{6} \cos \frac{\sigma^0_{n+1,j} + \sigma^0_{n,j}}{2},\ 4.5 \right) \right|^{-1} \\ &= 0.89. \end{aligned} \tag{5.2.19}$$

As a result of $J_1, \Omega, \widetilde{M}, \widetilde{\Gamma}$ and ζ being fixed, the following are also fixed:

$$\rho = 2.1, \quad \gamma = 0.019. \tag{5.2.20}$$

β, κ and θ are left to vary, as is the electric field strength ϵ, and in the subsequent Sections we investigate the effects of varying these parameters on the polarons in our system.

Finally, we note that the characteristic time-scale, length-scale [cf. Equation (5.2.8)] and energy-scale in our system are, respectively,

$$\Omega^{-1} = 0.12 \text{ ps}, \quad L = 0.049 \text{ Å} = 0.011R, \quad \hbar\Omega = 5.3 \text{ meV}. \tag{5.2.21}$$

5.2.2 Energetics

As we did in Chapter 4, we measure the polaron's internal energy E_b with respect to the lowest energy in the electron band, now $J_0 - 2J_1 - 2J_2$, and in units of meV:

$$E_\mathrm{b} := 5.3 \times \frac{\langle\Psi|\widehat{H}_\mathrm{e} + \widehat{H}_\mathrm{p} + \widehat{H}_\mathrm{int}|\Psi\rangle - J_0 + 2J_1 + 2J_2}{\hbar\Omega}. \tag{5.2.22}$$

Defining $\langle\widehat{H}_\mathrm{e}\rangle := \langle\Psi|\widehat{H}_\mathrm{e}|\Psi\rangle$, similarly $\langle\widehat{H}_\mathrm{p}\rangle$ and $\langle\widehat{H}_\mathrm{int}\rangle$, we can compute the three components of E_b separately. For each component, we first derive an expression which is valid even without assuming A-mode symmetry, and then simplify the expression by invoking the A-mode symmetry.

Firstly, using $|\Psi\rangle = \sum_{n=0}^{N} \psi_n \exp\left[-\frac{it}{\hbar}(J_0 - 2J_1 - 2J_2)\right] \widehat{A}_n^\dagger |0\rangle$, we obtain

$$\begin{aligned}
\frac{\langle\widehat{H}_\mathrm{e}\rangle}{\hbar\Omega} &= \sum_{j=1}^{3}\sum_{l=1}^{3}\sum_{m=0}^{N_j}\sum_{q=0}^{N_l}\Bigg[\frac{J_0}{\hbar\Omega}\psi^*_{m,j}\psi_{q,l}\sum_{k=1}^{3}\sum_{n=0}^{N_k}\langle 0|\,\widehat{A}_{m,j}\widehat{A}^\dagger_{n,k}\widehat{A}_{n,k}\widehat{A}^\dagger_{q,l}\,|0\rangle \\
&\quad - \frac{J_1}{\hbar\Omega}\psi^*_{m,j}\psi_{q,l}\sum_{k=1}^{3}\sum_{n=0}^{N_k-1}\langle 0|\,\widehat{A}_{m,j}\widehat{A}^\dagger_{n+1,k}\widehat{A}_{n,k}\widehat{A}^\dagger_{q,l} + \widehat{A}_{m,j}\widehat{A}^\dagger_{n,k}\widehat{A}_{n+1,k}\widehat{A}^\dagger_{q,l}\,|0\rangle \\
&\quad - \frac{J_2}{\hbar\Omega}\psi^*_{m,j}\psi_{q,l}\sum_{k=1}^{3}\sum_{n=0}^{N_k}\langle 0|\,\widehat{A}_{m,j}\widehat{A}^\dagger_{n,k+1}\widehat{A}_{n,k}\widehat{A}^\dagger_{q,l} + \widehat{A}_{m,j}\widehat{A}^\dagger_{n,k}\widehat{A}_{n,k+1}\widehat{A}^\dagger_{q,l}\,|0\rangle \\
&= \frac{J_0}{\hbar\Omega}\sum_{k=1}^{3}\sum_{n=0}^{N_k}|\psi_{n,k}|^2 - \frac{J_1}{\hbar\Omega}\sum_{k=1}^{3}\sum_{n=0}^{N_k-1}\left(\psi^*_{n+1,k}\psi_{n,k} + \psi^*_{n,k}\psi_{n+1,k}\right), \\
&\quad - \frac{J_2}{\hbar\Omega}\sum_{k=1}^{3}\sum_{n=0}^{N_k}\left(\psi^*_{n,k+1}\psi_{n,k} + \psi^*_{n,k}\psi_{n,k+1}\right),
\end{aligned} \tag{5.2.23}$$

where we have utilised the anti-commutation relation (5.1.3). Invoking the A-mode symmetry assumption that $\psi_n := \sqrt{3}\psi_{n,k}$ and $N_k = N$ for all k, we deduce

$$\frac{\langle\widehat{H}_\mathrm{e}\rangle}{\hbar\Omega} = \frac{J_0}{\hbar\Omega}\sum_{n=0}^{N}|\psi_n|^2 - \frac{J_1}{\hbar\Omega}\sum_{n=0}^{N-1}\left(\psi^*_{n+1}\psi_n + \psi^*_n\psi_{n+1}\right) - \frac{J_2}{\hbar\Omega}\sum_{n=0}^{N}2|\psi_n|^2. \tag{5.2.24}$$

Due to the normalisation condition for ψ_n, and the definition of ρ according to Equation (5.2.11), it follows that

$$\frac{\langle\widehat{H}_\mathrm{e}\rangle - J_0 + 2J_1 + 2J_2}{\hbar\Omega} = \rho\left[2 - \sum_{n=0}^{N-1}\left(\psi^*_{n+1}\psi_n + \psi^*_n\psi_{n+1}\right)\right]. \tag{5.2.25}$$

For $\langle \widehat{H}_{\rm p} \rangle$, we make use of $P_{n,k} = M\zeta^{-2}{\rm d}U_{n,k}/{\rm d}t$, and the length scale L defined by Equation (5.2.8), to write

$$\begin{aligned}\frac{\langle \widehat{H}_{\rm p} \rangle}{\hbar\Omega} &= \sum_{k=1}^{3}\sum_{n=0}^{N_k} \frac{\zeta^2 M^2 \zeta^{-4}}{2M\hbar\Omega} L^2\Omega^2 \dot{u}_{n,k}^2 + \sum_{k=1}^{3}\sum_{n=0}^{N_k-1} \frac{M\zeta^{-2}\Omega^2}{2\hbar\Omega} L^2 \Big(u_{n+1,k} - u_{n,k}\Big)^2 \\ &= \frac{1}{2\zeta^2}\left[\sum_{k=1}^{3}\sum_{n=0}^{N_k} \frac{M^2}{M\hbar\Omega}\frac{\hbar}{3M\Omega}\Omega^2\dot{u}_{n,k}^2 + \sum_{k=1}^{3}\sum_{n=0}^{N_k-1} \frac{M\Omega^2}{\hbar\Omega}\frac{\hbar}{3M\Omega}\Big(u_{n+1,k} - u_{n,k}\Big)^2\right] \\ &= \frac{1}{6\zeta^2}\left[\sum_{k=1}^{3}\sum_{n=0}^{N_k} \dot{u}_{n,k}^2 + \sum_{k=1}^{3}\sum_{n=0}^{N_k-1}\Big(u_{n+1,k} - u_{n,k}\Big)^2\right]. \end{aligned} \tag{5.2.26}$$

Now we invoke the A-mode symmetry assumption, that $u_{n,k} = u_n$ and $N = N_k$ for all k, and due to Equation (5.2.10), it follows that

$$\frac{\langle \widehat{H}_{\rm p} \rangle}{\hbar\Omega} = \frac{1}{2\zeta^2}\left[\sum_{n=0}^{N} \dot{u}_n^2 + \sum_{n=0}^{N-1}(u_{n+1} - u_n)^2\right]. \tag{5.2.27}$$

Finally, using Equation (5.1.9) for the definition of $\widehat{H}_{\rm int}$, and the condition that $\psi_0 = \psi_N = 0$, we calculate

$$\frac{\langle \widehat{H}_{\rm int} \rangle}{\hbar\Omega} = \frac{\chi L}{2\hbar\Omega}\sum_{k=1}^{3}\sum_{n=1}^{N_k-1}|\psi_{n,k}|^2\Big[\Big(u_{n+1,k} - u_{n-1,k}\Big) + \beta\Big(u_{n+1,k} + u_{n-1,k} - 2u_{n,k}\Big)\Big], \tag{5.2.28}$$

which, with the A-mode symmetry in place, becomes

$$\frac{\langle \widehat{H}_{\rm int} \rangle}{\hbar\Omega} = \kappa\sum_{n=1}^{N-1}|\psi_n|^2\Big[(u_{n+1} - u_{n-1}) + \beta(u_{n+1} + u_{n-1} - 2u_n)\Big]. \tag{5.2.29}$$

Putting Equations (5.2.25), (5.2.27) and (5.2.29) into Equation (5.2.22), we have

$$\begin{aligned} E_{\rm b} = 5.3\rho&\left[2 - \sum_{n=1}^{N-2}\Big(\psi_{n+1}^*\psi_n + \psi_n^*\psi_{n+1}\Big)\right] + \frac{5.3}{2\zeta^2}\left[\sum_{n=1}^{N}\dot{u}_n^2 + \sum_{n=0}^{N-1}(u_{n+1} - u_n)^2\right] \\ &+ 5.3\kappa\sum_{n=1}^{N-1}|\psi_n|^2\Big[(u_{n+1} - u_{n-1}) + \beta(u_{n+1} + u_{n-1} - 2u_n)\Big]. \end{aligned} \tag{5.2.30}$$

ψ_0, ψ_N and $\dot{u}_0$ do not feature in Equation (5.2.30) due to the boundary conditions.

5.3 Stationary Polarons

In Section 5.3.1, we present stationary solutions to Equation (5.2.9) under $\epsilon = f_n = 0$, and in Section 5.3.2, we present quasi-stationary solutions under non-zero f_n. Where any methodologies were detailed in Chapter 4 in relation to the α-channel model, we do not detail them again here, and focus instead on the results.

5.3.1 Analytical and Numerical Solutions in the Deterministic System

The stationary solution to Equation (5.2.9b), assuming $f_n = 0$, is given in terms of the relative displacement of peptide units, $s_n = u_{n+1} - u_n$, as

$$s_n = \kappa\zeta^2 \left[(\beta - 1)|\psi_{n+1}|^2 - (\beta + 1)|\psi_n|^2 \right]. \tag{5.3.1}$$

Putting Equation (5.3.1) into Equation (5.2.9a) transforms the latter into

$$i\rho^{-1}\dot{\psi}_n + \Delta\psi_n + \lambda|\psi_n|^2\psi_n + \eta\Delta|\psi_n|^2\psi_n = 0, \tag{5.3.2}$$

where we have set $\epsilon = 0$, and defined

$$\lambda := \frac{4\kappa^2\zeta^2}{\rho} \equiv \frac{\chi^2\zeta^2}{\widetilde{M}\Omega^2 J_1}, \tag{5.3.3a}$$

$$\eta := \frac{\kappa^2\zeta^2}{\rho}\left(1 - \beta^2\right) \equiv \frac{\lambda}{4}\left(1 - \beta^2\right). \tag{5.3.3b}$$

Equation (5.3.2) is identical to Equation (4.3.8), but contrasting Equation (5.3.3) with Equation (4.3.7) reveals that the *effective coupling parameter* λ now contains an extra factor of $\zeta^2/3$ as a result of the non-linear structure (twisting) of α-channels within the α-helix. With ρ being fixed, and η being a convenient combination of β and λ, we see that our stationary system of Equations (5.3.1) and (5.3.2) is parametrised entirely by ζ, β and λ. If we assume the stationary-state ansatz [cf. Equation (4.3.9)]

$$\psi_n(\tau) = \exp\left(i\rho H_0\tau + ikx\right)\phi(x)\big|_{x=n-N/2,} \tag{5.3.4}$$

then in the continuum limit ($N \gg 1$), we have that $k = 2l\pi$ (l any integer) are the only wavenumbers that permit a square-normalisable $\phi(x)$, and that $\phi(x)$ satisfies the following differential equation involving the eigenvalue H_0:

$$\begin{aligned} &- H_0\phi(x) + \phi''(x) + \lambda\phi(x)^3 \\ &+ \eta\left[2\phi(x)\phi''(x) + 2\left(\phi'(x)\right)^2\right]\phi(x)\Big|_{x=n-N/2} = 0, \end{aligned} \tag{5.3.5}$$

where $'$ denotes differentiation with respect to x. When x is permitted to take all real values, rather than only $n - N/2$, Equation (5.3.5) becomes a stationary generalised nonlinear Schrödinger equation (GNLSE) for $\phi(x)$ on the continuum domain, $-N/2 \leq x \leq N/2$:

$$-H_0\phi + \phi'' + \lambda\phi^3 + \eta\left(\phi^2\right)''\phi = 0. \tag{5.3.6}$$

As $N \to \infty$, we showed analytically in Section 4.3.3 that a unique, normalisable global solution to Equation (5.3.6) exists, given λ and η. The solution is written implicitly in terms of $\Phi := \phi^2$ as follows:

$$\sqrt{\lambda\eta} = \sqrt{2\eta\Phi_0} + (1 + 2\eta\Phi_0) \arctan \sqrt{2\eta\Phi_0}, \tag{5.3.7a}$$

$$\Phi(0) = \Phi_0 = \frac{2H_0}{\lambda}, \tag{5.3.7b}$$

$$\operatorname{sgn}(x)\sqrt{H_0}\; x = \operatorname{arsinh}\sqrt{\frac{1 - (\Phi/\Phi_0)}{(1+\nu)\,(\Phi/\Phi_0)}} + \sqrt{\nu}\;\arctan\sqrt{\frac{\nu\,(1 - (\Phi/\Phi_0))}{1 + (\nu\Phi/\Phi_0)}}. \tag{5.3.7c}$$

In particular, Equation (5.3.7a) provides a unique solution for the number Φ_0 given parameters (λ, η), then Equation (5.3.7b) gives both the eigenvalue H_0 and the inital value $\Phi(0)$, the latter ensuring the normalisation of $\Phi(x)$ over $-\infty < x < \infty$, and finally Equation (5.3.7c) gives a unique global solution $\Phi(x)$.

Numerically, using a non-standard iterative method which we described in Section 4.3.4, we are able to find stationary solutions to Equation (5.3.2) in the form of

$$\psi_n^0(\tau) = \exp\left(i\rho H_0 \tau\right) \phi_n^0, \tag{5.3.8}$$

by computing H_0 and ϕ_n^0. The analytical solutions, namely Equation (5.3.7), serve not only as approximations to H_0 and $(\phi_n^0)^2$, but also as initial guesses for those quantities, which we utilise in our iterative scheme. In Figure 5.1, we present stationary solutions to our system representing polaron states, obtained either analytically as approximate solutions in the large-lattice limit, or numerically on a lattice of size $N = 200$. We make the following observations. Firstly, solutions corresponding to $\lambda = 1.0$ at various values of β are virtually identical. On the other hand, when $\lambda = 3.6$, we see that at $\beta = 0$, the U_n^0 solution is centred at the location of $\max |\psi_n^0|^2$, in the sense that its graph is rotationally symmetric about $n = 75$, whereas at $\beta = 1$, the centre of rotational symmetry in U_n has shifted towards large n. This phenomenon is caused by the fact that when $\beta = 0$, the electron-phonon interaction is spatially symmetric, so the electron in the stationary state causes equal lattice distortion to its left and right; but as β increases, the electron-phonon coupling becomes stronger to the right of the localisation site, and as a response the centre of U_n^0 shifts to the right. In order for the point-dipole model of lattice units to be valid, the magnitude of lattice distortions must be such that $|U_{n+1}^0 - U_n^0| \ll R$ [Bar07], and indeed we infer from Figure 5.1 that $\max\left(|U_{n+1}^0 - U_n^0|/R\right) \sim \mathcal{O}(10^{-2})$. Moreover, $|U_{n+1}^0 - U_n^0|$ is negligible except at a few sites around the location of $\max |\psi_n^0|^2$, and larger values of

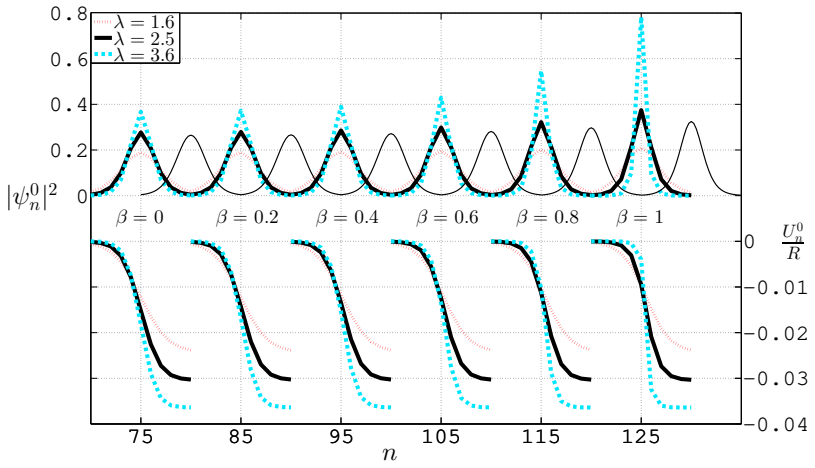

Figure 5.1: Stationary solutions parametrised by β and λ. Thick lines: electron probability distribution $|\psi_n^0|^2$ (left axis) and associated lattice distortions U_n^0 in units of the equilibrium lattice spacing R (right axis), obtained numerically by iterative method. Solutions are shifted along the n-axis to avoid overlap. Thin lines: approximate stationary solutions obtained analytically in the continuum limit, all with $\lambda = 2.5$.

β induce steeper gradients there. Thus, in the stationary state, systems with greater spatial asymmetry store more potential energy in the lattice. Finally, given any fixed λ, for example $\lambda = 2.5$ as Figure 5.1 illustrates, the accuracy of $\Phi(x)$ as an approximantion for $|\psi_n^0|^2$ decays as β increases.

In a stationary state, E_b [cf. Equation (5.2.30)] becomes the polaron's *binding energy*, which we denote by E_b^0. Using Equation (5.3.1), we deduce that in units of meV,

$$E_\mathrm{b}^0 = 5.3\rho\Bigg[2 - \sum_{n=1}^{N-2}\left(\psi_{n+1}^*\psi_n + \psi_n^*\psi_{n+1}\right) + \frac{\lambda}{8}\sum_{n=0}^{N-1}\left[(\beta-1)|\psi_{n+1}|^2 - (\beta+1)|\psi_n|^2\right]^2 - \eta\sum_{n=1}^{N-1}|\psi_n|^2\left(|\psi_{n+1}|^2 + |\psi_{n-1}|^2 - 2|\psi_n|^2\right) - \lambda\sum_{n=1}^{N-1}|\psi_n|^4\Bigg]. \tag{5.3.9}$$

This is identical to Equation (4.3.104) for the linear α-channel model, except now we have different definitions of the parameters λ and η. The electron's maximum localisation probability and polaron binding energy in the stationary state as functions of (β, λ) as shown as surfaces over the parameter space, in Figure 5.2. For every β, $\max|\psi_n^0|^2$ increases with the effective coupling parameter λ, while E_b^0 decreases. Meanwhile, if λ is fixed and small (close to 1) then both $\max|\psi_n^0|^2$ and E_b^0 as functions of β are roughly constant, whereas if λ is large then $\max|\psi_n^0|^2$ becomes an increasing function of β and E_b^0 a decreasing one. Thus, increasing either the model's spatial asymmetry (β) or its coupling strength (λ)

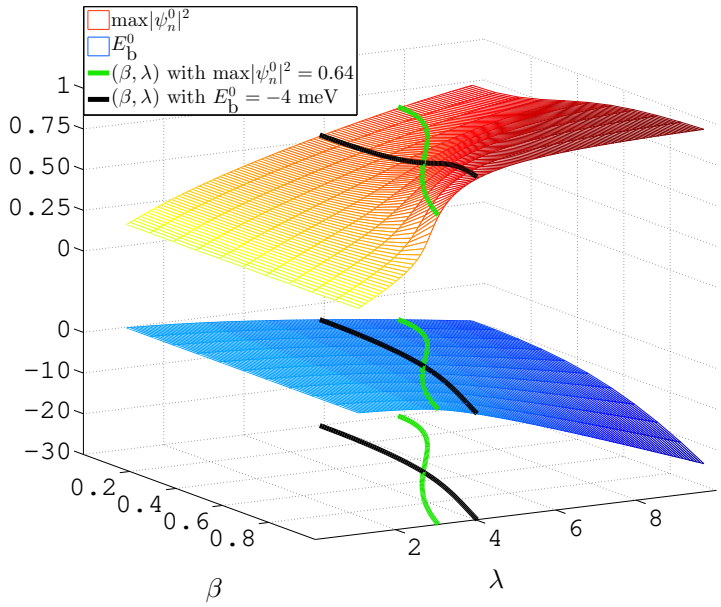

Figure 5.2: The electron's maximum localisation probability, $\max|\psi_n^0|^2$, and stationary polaron binding energy E_b^0 (meV), as functions of (β, λ). Also shown are: the contour line of height 0.64 in the $\max|\psi_n^0|^2$ surface, and the projections of that line on the E_b^0 surface and on the (β, λ) plane; the contour line of height -4 meV in the E_b^0 surface, and the projections of that line on the $\max|\psi_n^0|^2$ surface and on the (β, λ) plane.

makes the stationary polaron more strongly bound. In particular, even though a more asymmetric system stores more energy in the lattice, the asymmetry causes so much decrease in the electronic and interaction components of the binding energy that they offset the growth in lattice energy, making the overall binding energy decrease.

If we draw a contour line of fixed height in the $\max|\psi_n^0|^2$ surface, and another of fixed height in the E_b^0 surface, and project those contour lines onto the (β, λ) plane, then the two lines of projection never have more than one point of intersection. One such set of contour lines and projections are shown in Figure 5.2, and they intersect in the (β, λ) at the point $(0.5, 5.6)$. In Section 5.4, where we study propagating polarons, we will wish to determine the effect of β on the polarons' dynamical properties. To do so, we could study a set of polarons with fixed λ and varying β, but both their $\max|\psi_n^0|^2$ and their E_b^0 would be varying with β. In order to make more meaningful observations about the effect of β, we should vary λ with β along either a $\max|\psi_n^0|^2$ contour line or a E_b^0 contour line, so that all stationary polarons with parameters $(\beta, \lambda(\beta))$ share either the same $\max|\psi_n^0|^2$ or the same E_b^0 (unfortunately, as we see in Figure 5.2, it is not possible to find $\lambda(\beta)$ such that both properties remain constant). We will choose $\lambda(\beta)$ in order to ensure that $\max|\psi_n^0|^2$ remains constant while β varies.

The complete set of stationary polarons in our model is almost identical to that in the linear α-channel model. Indeed, given (β, λ), there is a percentage difference in E_{b}^{0} of $\mathcal{O}(10^{-3})$ compared to the α-channel model. This is not to say that the two models are nearly equivalent *physically*: given an electron-phonon coupling constant χ in physical units, the resulting β is identical in the two models, but λ in the current model is smaller than the λ in the α-channel model by a factor of $3/\zeta^2 = 3.8$ [cf. Equation (5.3.3a)]. We therefore conclude that given identical physical parameters, the resulting stationary polaron in the current model is *less strongly bound* than that in the linear α-channel model. This is due to the electron spreading itself amongst the three channels in the α-helix model. An equivalent way to phrase this difference is that the α-helix model *requires physically stronger electron-phonon coupling*, as χ needs to be $\sqrt{3.8}$ times as large as that in the α-channel model in order to produce an identical polaron.

5.3.2 Quasi-Stationary Solutions under Stochastic Forces

Applying stochastic forces $f_n(\tau)$, characterised by thermal energy θ, to Equation (5.2.9b), and integrating the system forward in time with stationary polarons as initial conditions, we obtain time-evolutions where the polaron's internal energy increases before settling in small oscillations around a mean value. The period of increasing internal energy is the *thermalisation* of the system, and lasts $\mathcal{O}(10^4)$ units of time, or several nanoseconds. Figure 5.3(a) illustrates a typical thermalisation process, in which E_{b} rises from its initial value of -4 meV to about -3 meV is $\mathcal{O}(10^2)$ time-units, and then continues to rise until eventually settling around -2.1 meV. Even though the stochastic forces act directly only on the lattice, it indirectly affects the electron probability distribution due to the electron-phonon coupling. The electron probability distribution, $|\psi_n|^2$, 'spreads out' during thermalisation, decreasing in maximum value and increasing in half-width, before settling in a quasi-stationary state of small fluctuations around a Λ-shaped profile. The lattice itself also settles in small oscillations around some mean configuration. The quasi-stationary states of $|\psi_n|^2$ and u_n constitute the system's *thermal equilibrium*. We write $\psi_n^{(\theta)}(\tau)$ for the fluctuating ψ_n at thermal equilibrium with thermal energy θ. Figure 5.3(b) exhibits a typical $|\psi_n^{(\theta)}|^2$, and it comes from the thermalisation process shown in Figure 5.3(a). We see that at thermal equilibrium, the $\max|\psi_n|^2$ has settled in $\mathcal{O}(10^{-3})$ oscillations around $\max|\psi_n^{(\theta)}|^2 = 0.59$. When we write $\max|\psi_n^{(\theta)}|^2$, we mean the mean value of the maximum of $|\psi_n^{(\theta)}|^2$, taken over a 1000-time-unit period long after thermalisation has completed; and

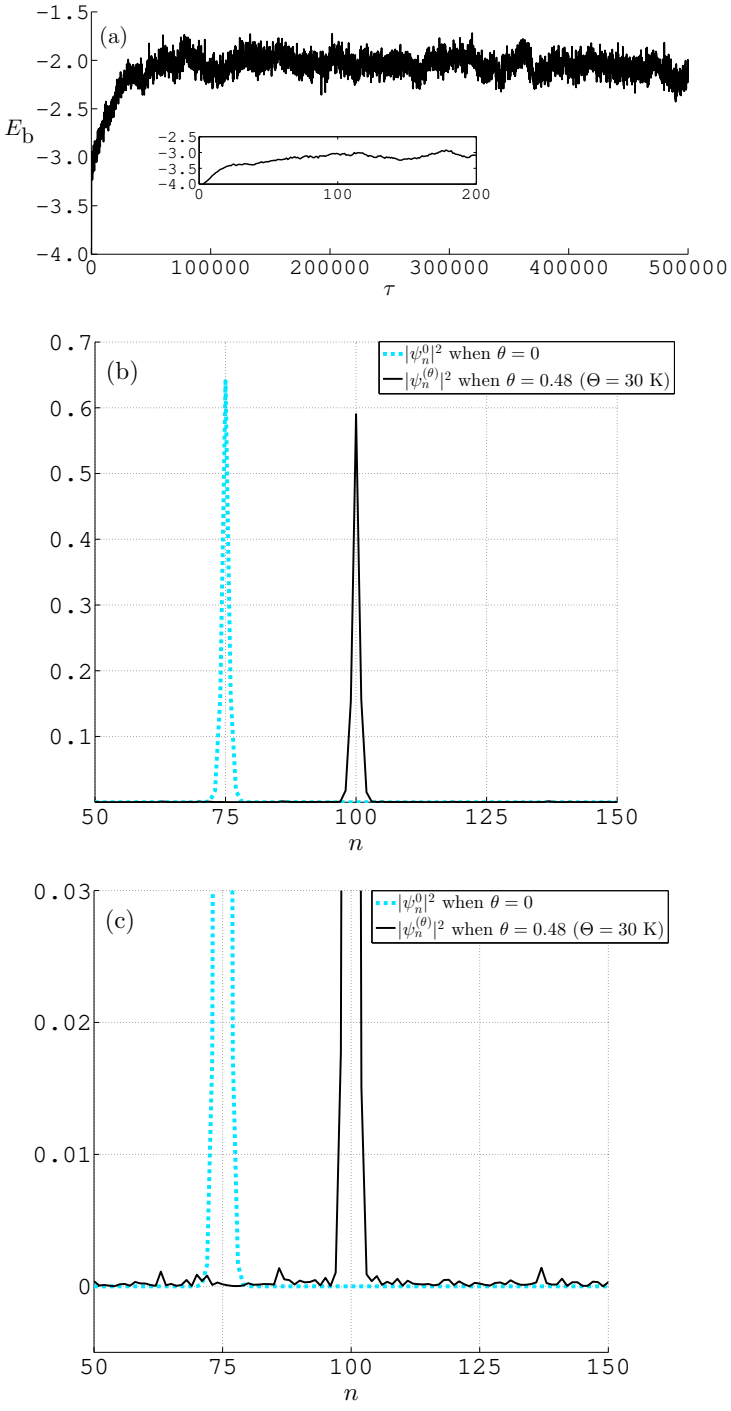

Figure 5.3: (a) Increase in polaron internal energy (meV) during thermalisation; inset: rapid initial rise in internal energy. 10^5 units of τ equals 12 ns. (b) Overview of quasi-stationary polaron at thermal equilibrium, represented by $|\psi_n^{(\theta)}|^2$, taken at some time after the thermalisation of (a) has completed; and the stationary polaron represented by $|\psi_n^0|^2$. (c) Zoomed-in view of (b), showing secondary peaks in $|\psi_n^{(\theta)}|^2$ resulting from thermalisation. Parameters in all subfigures: $\beta = 0.5, \lambda = 5.6$.

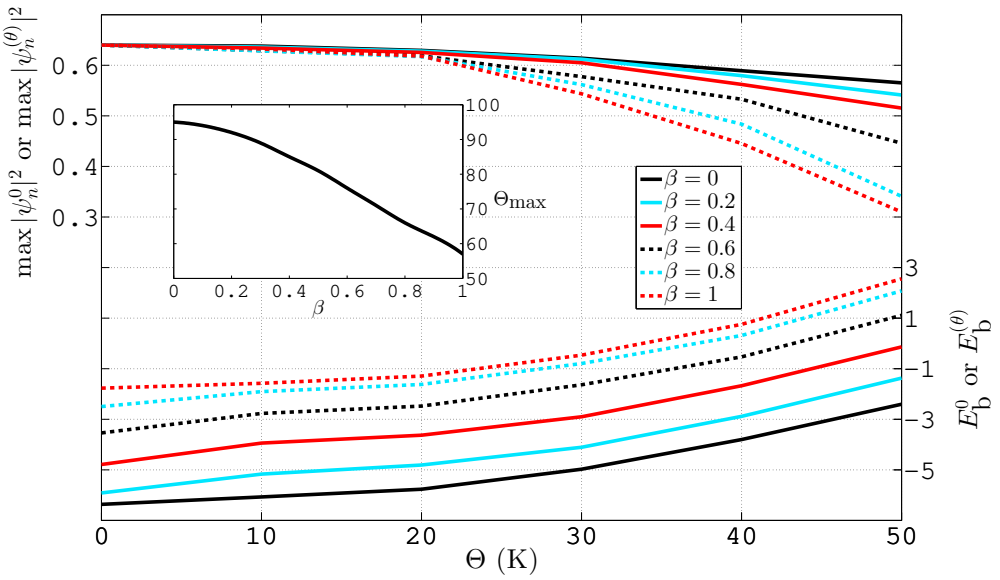

Figure 5.4: The electron's maximum localisation probability (left axis) and polaron internal energy (meV) (right axis), either stationary (when $\Theta = 0$, interpreted as binding energy) or quasi-stationary (when $\Theta > 0$), as functions of temperature Θ, parametrised by β. λ is varied with β in such a way that $\max |\psi_n^0|^2$ remains constant at 0.64. Inset: the maximum temperature at which a quasi-stationary polaron can exist, as a function of β.

similiarly for $E_b^{(\theta)}$. Figure 5.3(c) shows small, secondary peaks in $|\psi_n^{(\theta)}|^2$ at every lattice site away from the location of global maximum, and the relative magnitudes of these secondary peaks compared to $\max |\psi_n^{(\theta)}|^2$ is $\mathcal{O}(10^{-3})$. At thermal equilibrium, the magnitudes and locations of the secondary peaks undergo small fluctuations without affecting the overall shape or size of $|\psi_n^{(\theta)}|^2$, and the magnitudes of the fluctuations are positively correlated with the temperature.

Figure 5.4 shows the ways in which $\max |\psi_n^{(\theta)}|^2$ and $E_b^{(\theta)}$ depend on the temperature Θ (recall that the thermal energy is $\theta = k_B\Theta/(\hbar\Omega)$). We see that $\max |\psi_n^{(\theta)}|^2$ is always a decreasing function of Θ, and $E_b^{(\theta)}$ always an increasing function, meaning that a higher temperature leads to a less localised quasi-stationary polaron state. Larger values of β leads to steeper rates of decrease of $\max |\psi_n^{(\theta)}|^2$, whereas the rate of increase of $E_b^{(\theta)}$ is unaffected by β. That is to say, as the system becomes more spatially asymmetric, the electron becomes more sensitive to temperature, whereas the temperature-sensitivity of overall polaron internal energy is roughly unchanged.

We observe in Figure 5.4 that some quasi-stationary polaron states have positive internal energy. This is because the internal energy is measured from the theoretical lowest

energy in the electron band of an unthermalised system [cf. Equation (5.2.22)]. The key to whether a polaron state exists lies in $\max|\psi_n^{(\theta)}|^2$. For consistency with Chapter 4, we say the system is in a quasi-stationary polaron state if $\max|\psi_n^{(\theta)}|^2 \geq 0.1$, and that the electron has delocalised (thereby destroying the polaron state) if $\max|\psi_n^{(\theta)}|^2 < 0.1$. When $\beta = 1$, we have quasi-stationary polarons at temperatures up to 57 K. Since smaller values of β make the electron less temperature-sensitive, they lead to a larger range of temperatures for which a quasi-stationary polaron can exist. We denote by $\Theta_{\max}$ the maximum temperature at which a quasi-stationary polaron can exist. The inset in Figure 5.4 shows that for $0 \leq \beta \leq 1$, $\Theta_{\max}$ is negatively correlated with β, and at $\beta = 0$ we have $\Theta_{\max} = 95$ K. Comparing these results to the α-channel model of Chapter 4, where we reported that no quasi-stationary polarons existed for $\Theta > 55$ K, we see evidence that polarons in the α-helix model are more thermally stable, as they can exist in quasi-stationary states at higher temperatures. An equivalent view of this comparison is that, in the same way that the α-helix model requires stronger electron-phonon coupling to produce stationary polarons, it also *requires higher temperatures to destroy those polarons.*

5.4 Propagating Polarons

In this Section, we investigate the effects on the polaron of the mean-shifted periodic field (MSPF), which was the optimal type of electromagnetic field for inducing polaron propagation in the linear α-channel model of Chapter 4. We describe in Section 5.4.1 the exact form of the MSPF, expressed as the forcing term $\epsilon(\tau)$ in Equation (5.2.9a), and solve the dynamical equations for the polaron, neglecting stochastic forces. In Section 5.4.2, we examine the interplay between the symmetry parameter β and parameters of the MSPF, and finally in Section 5.4.3, we study the effect on the polaron dynamics of stochastic forces, drawing comparisons with the α-channel model in terms of thermal stability and thermal enhancement of the polaron propagation.

5.4.1 Polaron Motion Under the MSPF

We represent the MSPF by the following forcing term applied to Equation (5.2.9a), with stationary polarons as initial conditions:

$$\epsilon(\tau) = \bar{\epsilon} - A\sin\frac{2\pi\tau}{T} \quad \text{for } \tau \geq 0, \tag{5.4.1}$$

where $\bar{\epsilon}, A$ and T are independent parameters, and we set $f_n(\tau) = 0$ in Equation (5.2.9b). $\bar{\epsilon} \geq 0$ is the constant mean amplitude of ϵ, $A \geq 0$ and $T > 0$ respectively are the amplitude and period of the sinusoidal component of ϵ. As we did in Chapter 4, we have chosen the phase of the electric field, represented by the negative sign before A, to optimise the polaron's stability in the early stages of the MSPF. We define the combined amplitude of the MSPF, which is the maximum value that ϵ can attain, as

$$A^{\text{comb}} := \bar{\epsilon} + A, \tag{5.4.2}$$

Launching a stationary polaron whose parameters are $(\beta, \lambda) = (0.5, 5.6)$, so that the stationary electron's maximum localisation probability is $\max |\psi_n^0|^2 = 0.64$ and the polaron's initial binding energy is $E_{\text{b}}^0 = -4$ meV, we use a variety of $\bar{\epsilon}, A$ and T to achieve directed polaron motion. We present in Figure 5.5 a view of a typical polaron trajectory over two periods of the MSPF, where $|\psi_n|^2$ and U_n/R are plotted against τ. At $\tau \approx 360$, the combined amplitude of the components of ϵ overcomes some critical value for the first time, and the electron accelerates in response. While it accelerates, the electron 'spreads out' as $\max|\psi_n|^2$ decreases. Almost immediately, the electron-phonon interaction, which is a stabilising force, acts to slow down the electron propagation, and a balance of forces causes the electron to move with near-constant speed for about 150 units of τ, during which time the electric field attains its maximum amplitude and begins decaying again. Also during the constant-speed motion, the shape of $|\psi_n|^2$ fluctuates. When ϵ has diminished so much that the electron-phonon interaction regains its role as the dominant force in the system, the electron decelerates once more until it settles in a quasi-stationary position about 30 lattice sites away from its initial position. The lattice distortion field, U_n, always moves and fluctuates in sync with $|\psi_n|^2$, as we clearly see in Figure 5.5. Crucially, both $|\psi_n|^2$ and U_n propagate without substantial changes in shape, so we do indeed have polaron propagation - two parts of the polaron moving solitonically as one. When the polaron has settled after one period of motion, $\max |\psi_n|^2$ has decreased slightly compared to its initial value, though this effect is imperceptible in Figure 5.5. Instead, we can see the accompanying slight increase in polaron internal energy in Figure 5.6.

Corresponding to the polaron trajectory in Figure 5.5, we have the dashed (blue) curves in Figure 5.6: they are the polaron's position and internal energy as functions of time, over the entire lifetime of the polaron. By polaron position, we mean the vertex location of the parabola extrapolated from $(n_0, |\psi_{n_0}|^2), (n_0-1, |\psi_{n_0-1}|^2), (n_0+1, |\psi_{n_0+1}|^2)$, where n_0 is the

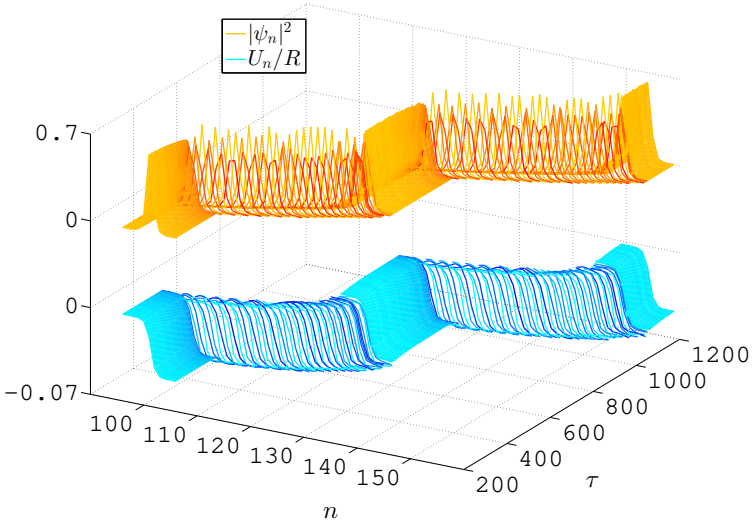

Figure 5.5: An MSPF-induced polaron trajectory, including both the electron probability distribution $|\psi_n|^2$, and the lattice distortions U_n in units of equilibrium lattice spacing R, as functions of time. Each curve represents a $|\psi_n|^2$ or U_n/R at a particular time. The less localised the electron is, the darker the curves are in colour. 100 units of τ equals 12 ps. Parameters: $\beta = 0.5, \lambda = 5.6, \bar{\epsilon} = 0.120, A = 0.051, T = 500$.

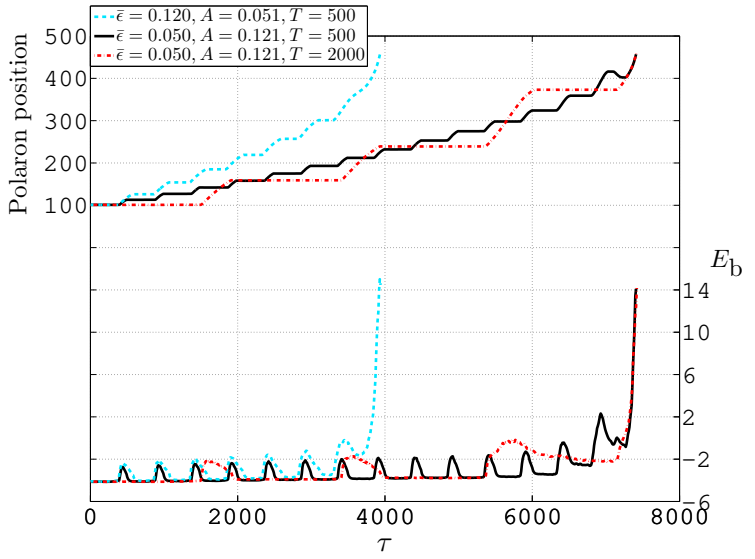

Figure 5.6: Some polaron trajectories (left axis) and corresponding time-evolutions of the polaron's internal energy (meV) (right axis) as functions of time, under the MSPF. 1000 units of τ equals 0.12 ns. Parameters: $\beta = 0.5, \lambda = 5.6$.

n that maximises $|\psi_n|^2$. By polaron lifetime, we mean the amount of time from initialising the electric field to the delocalisation of the electron, which is when $\max |\psi_n|^2$ drops below 0.1 for the first time. We see that the polaron under $\epsilon_1(\tau) = 0.120 - 0.051 \sin(2\pi\tau/500)$

survives for nearly 8 periods of the MSPF. In each period, the internal energy is raised, by an amount which is small for the first period and increasingly larger for later periods. Once the internal energy becomes positive, the polaron does not survive for much longer. Over its lifetime of roughly 4000 time-units (0.48 ns), the polaron travels by nearly 400 sites. The solid (black) lines in Figure 5.6 are the trajectory and internal energy evolution of exactly the same initial polaron under a different MSPF: $\epsilon_2(\tau) = 0.050 - 0.121\sin(2\pi\tau/500)$. Indeed, the difference is that the dominant MSPF component was the constant one in ϵ_1, and is now the sinusoidal one in ϵ_2, but the combined amplitude at $A^{\text{comb}} = 0.171$ has remained the same. We see that by decreasing the constant component $\bar{\epsilon}$ and raising the sinusoidal amplitude A, we decrease the amount by which the polaron moves per MSPF period, but increase its lifetime. Overall, the polaron travels the same distance under ϵ_2 as it does under ϵ_1, but under ϵ_2 it travels at roughly half the speed. This phenomenon is evidence that the polaron's velocity is positively correlated with $\bar{\epsilon}$, whilst its lifetime, hence stability, is negatively correlated with $\bar{\epsilon}$. From an energetics point of view, we may look at the polaron's internal energy *when it arrives at some site* n and ask whether ϵ_1 or ϵ_2 has caused it a larger increase from initial value. The answer is always ϵ_1. For example, we may consider the polaron's internal energy when it arrives at $n = 300$. Under ϵ_1, this occurs at $\tau = 3200$, at which time we have $E_{\text{b}} = -3.6$ meV; but under ϵ_2, this occurs at the later time of $\tau = 5700$, when we have $E_{\text{b}} = -3.9$ meV. Thus, under ϵ_2, which has the smaller $\bar{\epsilon}$, the polaron arrives at $n = 300$ as a more strongly bound compound than it does under ϵ_1. This is true when we look at the polaron's trajectory up to any site n. We say that ϵ_2 is a more energy-efficient MSPF than ϵ_1, or more generally, fixing A^{comb}, an MSPF with a small $\bar{\epsilon}$ is more energy-efficient than one with a large $\bar{\epsilon}$; but we do sacrifice polaron velocity for the better stability. We find that a moderate $\bar{\epsilon}$ around 0.05 provides a good balance between propelling the polaron with reasonable speed and keeping its internal energy stable.

Also in Figure 5.6 we have a polaron trajectory from the same initial state as before but under $\epsilon_3(\tau) = 0.050 - 0.121\sin(2\pi\tau/2000)$. This is identical to ϵ_2 except for the longer period, T. The effect of altering T while keeping all other parameters fixed is not clear from Figure 5.6, because compared to ϵ_2, ϵ_3 leads to the same polaron lifetime and causes the same amount of polaron displacement. The only difference is that a larger T causes more polaron displacement *per period*, due to the electron being exposed to the super-critical electric field for longer. To better understand the significance of T, we look

at Figure 5.7, which also gives us more insight into the dependence of quantities such as the polaron lifetime and velocity on $\bar{\epsilon}$ and A.

At fixed β, the dependencies of the polaron's lifetime τ_{d}, displacement D and velocity V on the MSPF parameters $\bar{\epsilon}, A$ and T are qualitatively the same as those we encountered in Chapter 4 for the α-channel model. We described those dependencies in detail in relation to Figure 4.7. In essence, there exists a *critical combined amplitude*, $A_{\mathrm{c}}^{\mathrm{comb}}$, which is the value such that if $A^{\mathrm{comb}} < A_{\mathrm{c}}^{\mathrm{comb}}$ then no polaron displacement occurs, but if $A^{\mathrm{comb}} \geq A_{\mathrm{c}}^{\mathrm{comb}}$ then the polaron propagates. The value of $A_{\mathrm{c}}^{\mathrm{comb}}$ is independent of $\bar{\epsilon}$ and T, except for one anomaly at $\bar{\epsilon} = 0.12$ in Figure 5.7(d), where $A_{\mathrm{c}}^{\mathrm{comb}}$ at $T = 2000$ is larger than $A_{\mathrm{c}}^{\mathrm{comb}}$ at other values of T. The reason for this is as follows.

When T is as large as 2000, the combined amplitude A^{comb} can be super-critical for a long time during each period of MSPF. Consequently, it can cause a large increase in polaron internal energy even if only one or two periods have passed, leading to short polaron lifetimes. The D and V columns of Figure 5.7 account only for data where the polaron survives for at least two full periods, because otherwise D would have to be measured by the average polaron position over the 1$^{\mathrm{st}}$ full period, and consequently V, first defined by Equation (4.4.4) as an average velocity, would be a highly unreliable indicator of how quickly the polaron really moves. In Figure 5.7(d), when $\bar{\epsilon} = 0.12$ and $T = 2000$, a combined amplitude of $A^{\mathrm{comb}} = 0.160$ (which is the value of $A_{\mathrm{c}}^{\mathrm{comb}}$ given any other combination of $(\bar{\epsilon}, T)$) *does* cause polaron displacement; but it does not register on the figure because the polaron lifetime is too short.

Another type of anomaly sometimes caused by a large T such as 2000 is the following. If A is large enough, then it is possible to have $\epsilon < -A_{\mathrm{c}}^{\mathrm{comb}}$ for some time in each period of MSPF. Due to the minus sign in front of A in the expression for $\epsilon(\tau)$, we would have $\epsilon < -A_{\mathrm{c}}^{\mathrm{comb}}$ in the 1$^{\mathrm{st}}$ period *before* we have $\epsilon > A_{\mathrm{c}}^{\mathrm{comb}}$. This means that the polaron would be propelled in the small-n direction. Whenever we then have $\epsilon > A_{\mathrm{c}}^{\mathrm{comb}}$, the polaron would either stay put or swing back towards the large-n direction, but even in the latter case, we could end up with an overall negative displacement. Indeed we see in Figure 5.7 that some combinations of $(\bar{\epsilon}, A, T = 2000)$ result in overall negative displacements and hence negative velocities.

Fixing $T = 100$ or 500, we make the following observations. The general trend of τ_{d} as a function of A is that if $A^{\mathrm{comb}} < A_{\mathrm{c}}^{\mathrm{comb}}$, then $T \sim \infty$, since the polaron simply remains in its initial state permanently; but as soon as A^{comb} reaches critical, τ_{d} drops

to $\mathcal{O}(10^3)$ time-units, or hundreds of picoseconds, and the value of τ_{d} at critical $A_{\mathrm{c}}^{\mathrm{comb}}$ is negatively correlated with $\bar{\epsilon}$. If $\beta \lessapprox 0.5$ and $\bar{\epsilon}$ is small such as 0.02, then as A increases beyond critical, τ_{d} first decays and then grows before plateauing at some constant value; otherwise, then τ_{d} as a function of A is simply a decreasing one. As for the polaron displacement, we have $D \sim \mathcal{O}(10^2)$ at $A^{\mathrm{comb}} = A_{\mathrm{c}}^{\mathrm{comb}}$, and the general trend of D as a function of super-critical A is always a decreasing one, even though some parameter combinations such as $(\beta = 1, \bar{\epsilon} = 0.12, T = 500)$ lead to an increase in $D(A)$ beyond critical A. Finally, for the polaron velocity, which is roughly the number of lattice sites traversed per unit time, we have $0.01 \lessapprox V \lessapprox 0.4$ at $A^{\mathrm{comb}} = A_{\mathrm{c}}^{\mathrm{comb}}$. For super-critical A, V tends to grow before decaying again, resulting in some value of A at which the polaron attains maximum velocity. This phenomenon occurs because V is roughly the ratio of D to τ_{d}, and even though D is a decreasing function of super-critical A, so is τ_{d} in most cases; if τ_{d} decreases more sharply than D, then we have an increasing V. We call the value of A^{comb} at which the polaron achieves maximum velocity the *optimal combined amplitude*, and denote it by $A_{\mathrm{m}}^{\mathrm{comb}}$; it varies with $\bar{\epsilon}$ and T, unlike the critical $A_{\mathrm{c}}^{\mathrm{comb}}$ which does not depend on either $\bar{\epsilon}$ or T. We discuss these dependencies in more detail in Section 5.4.2.

(a) $\beta = 0$

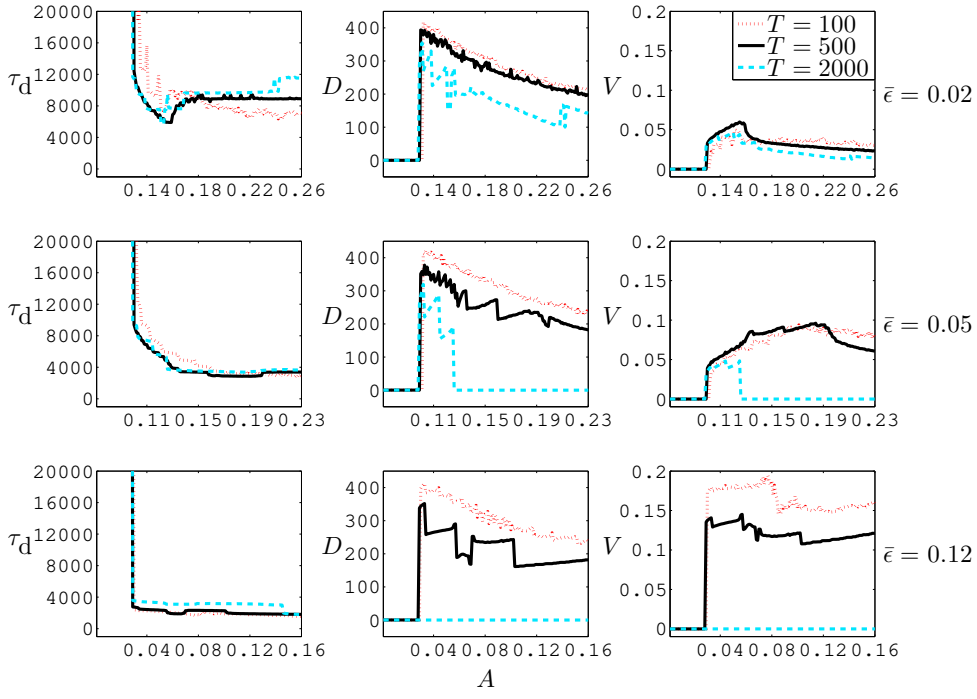

(b) $\beta = 0.1$

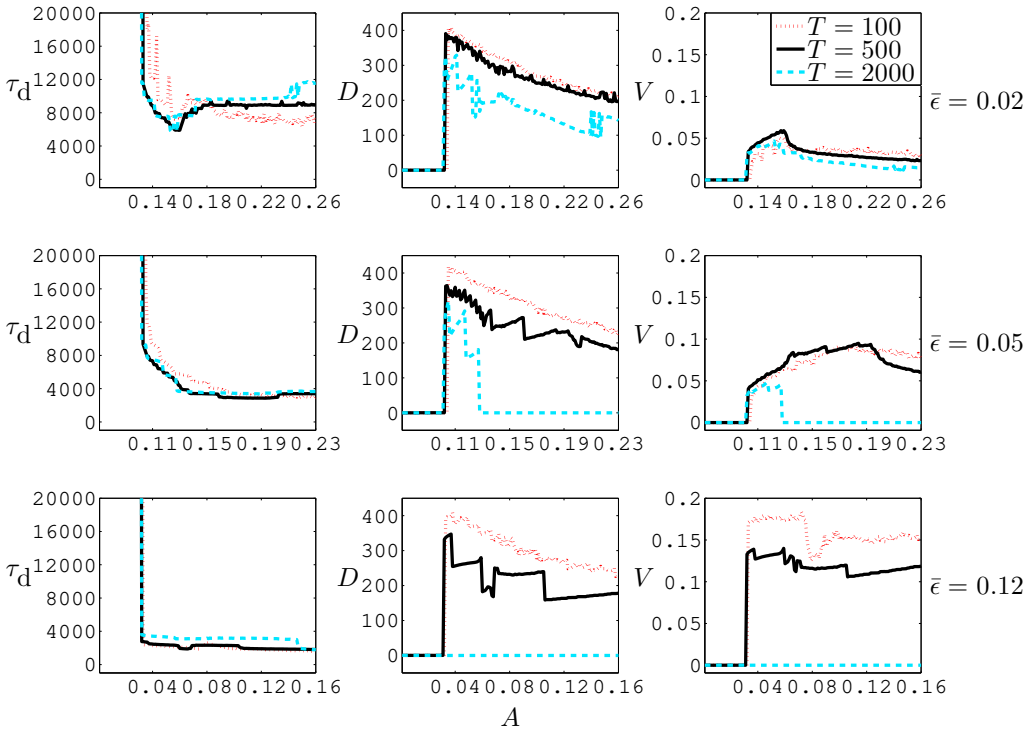

(c) $\beta = 0.2$

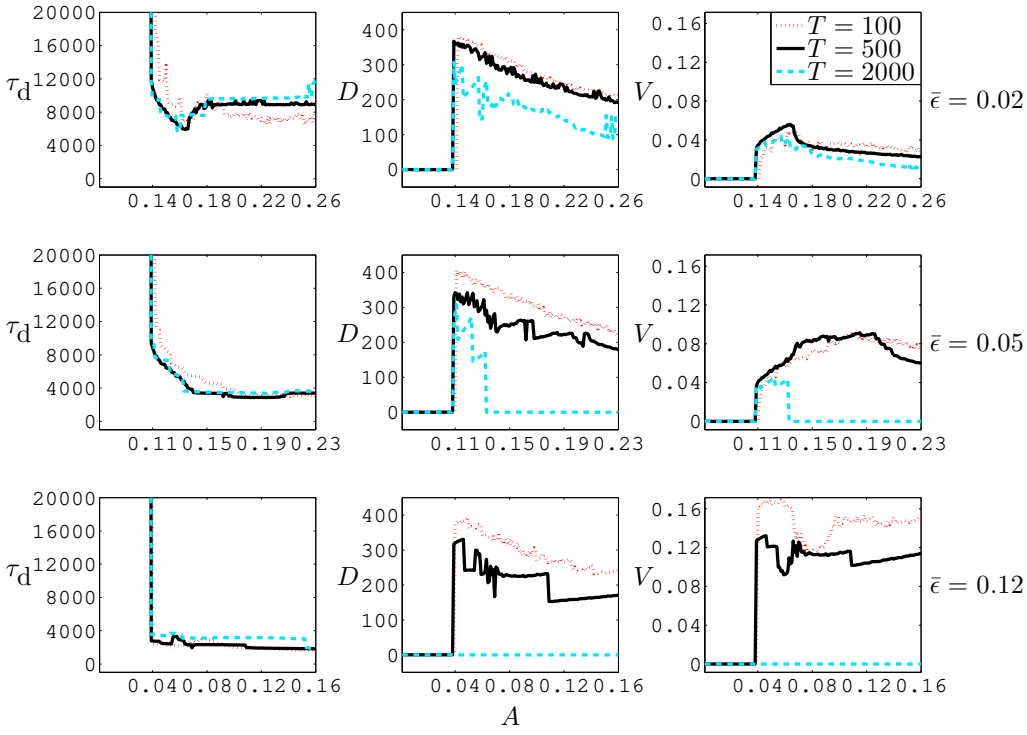

(d) $\beta = 0.3$

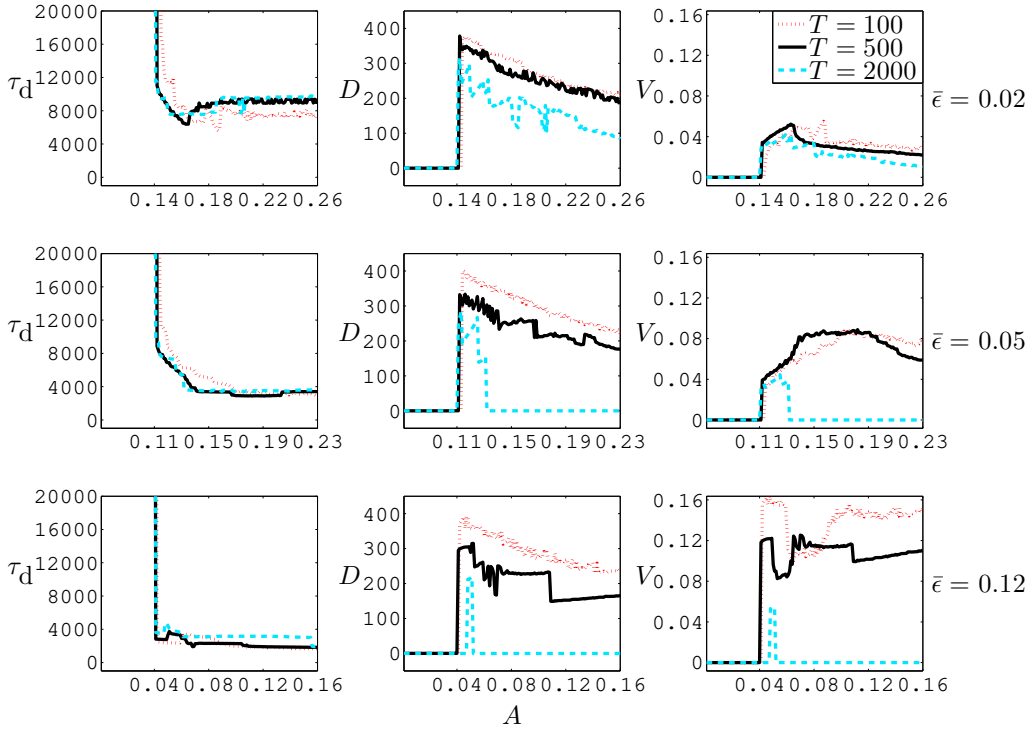

(e) $\beta = 0.4$

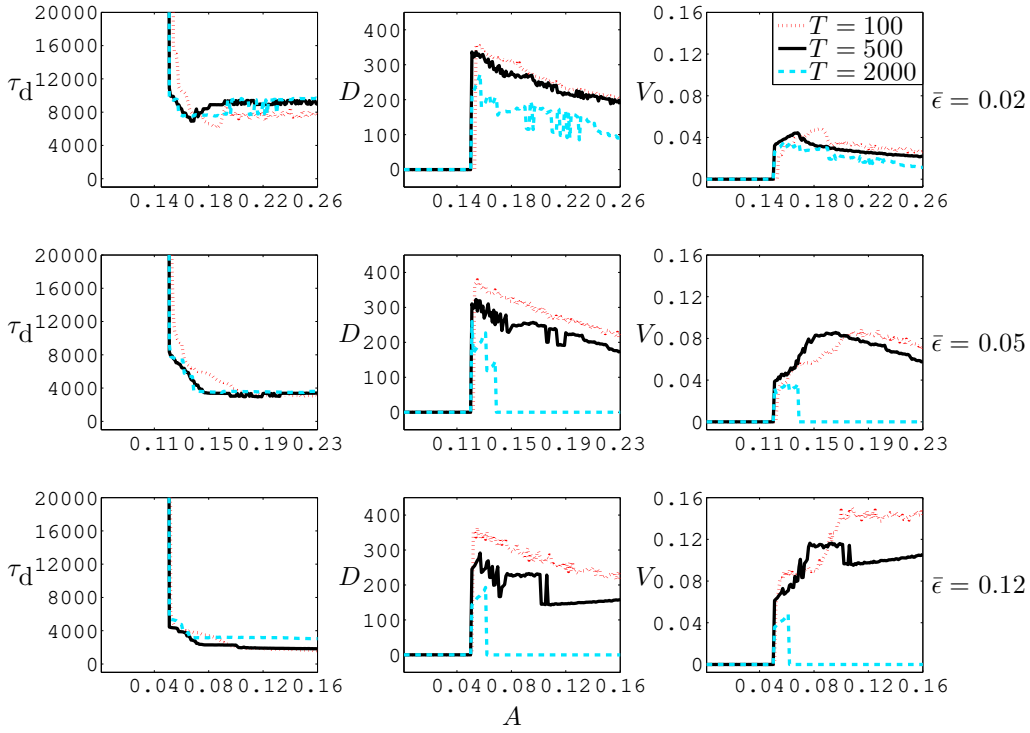

(f) $\beta = 0.5$

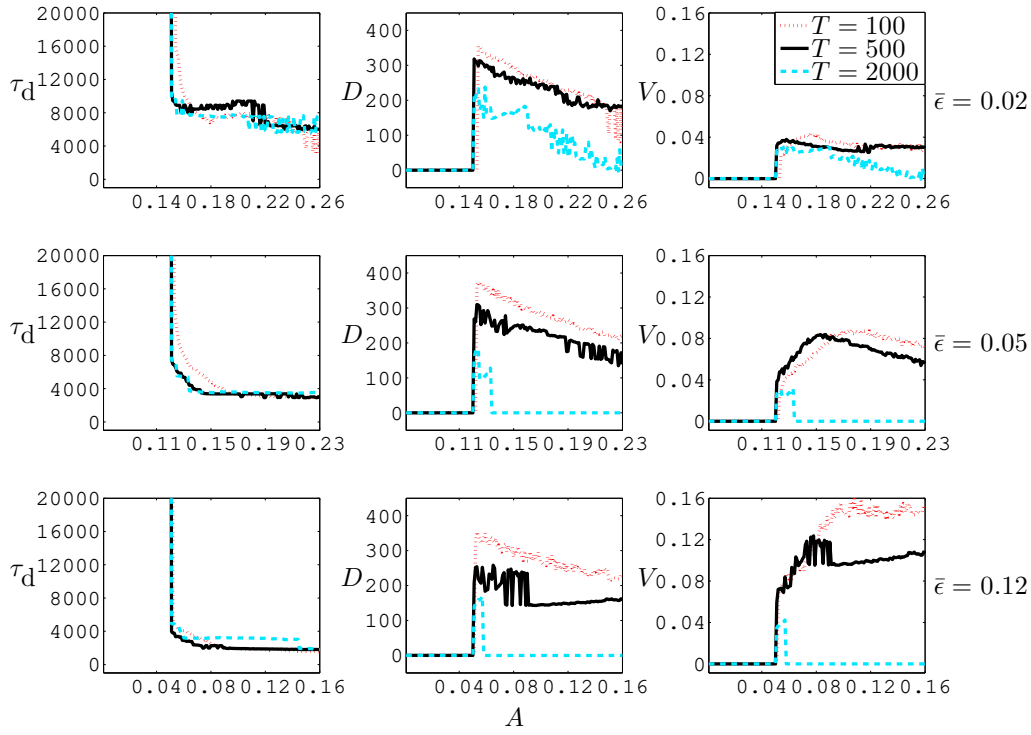

(g) $\beta = 0.6$

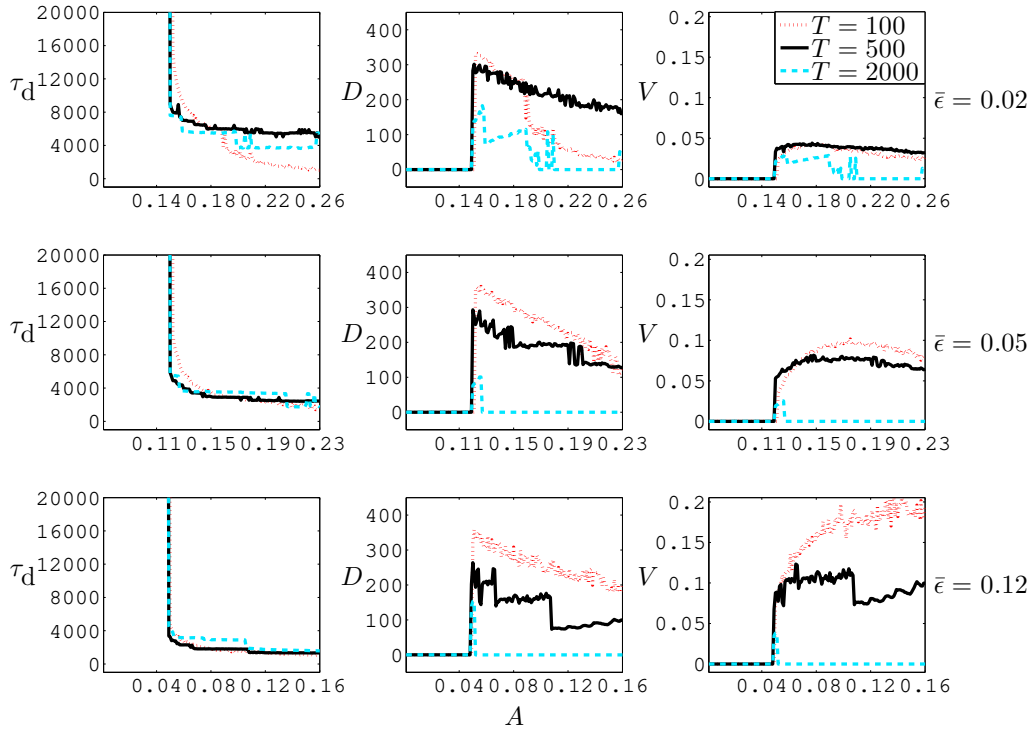

(h) $\beta = 0.7$

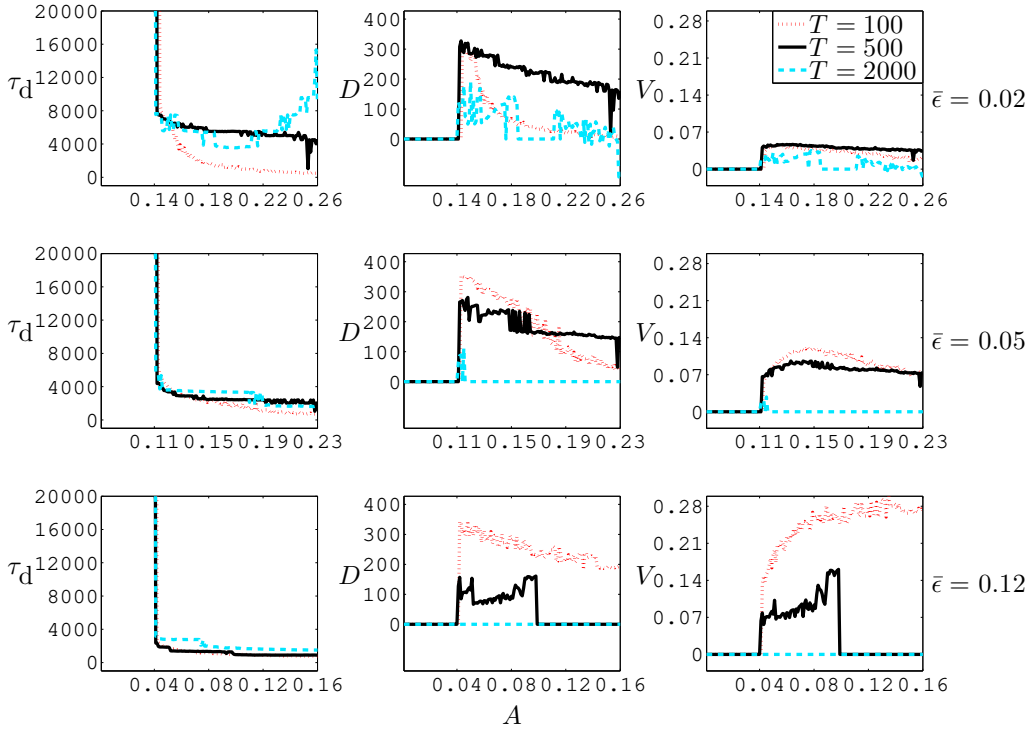

(i) $\beta = 0.8$

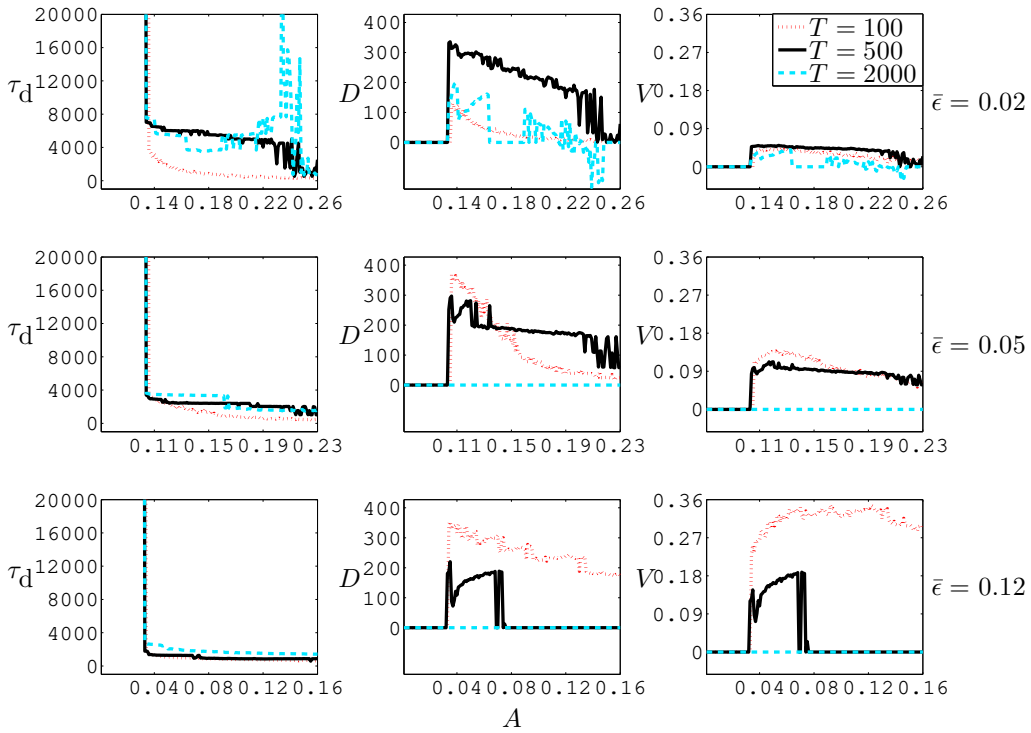

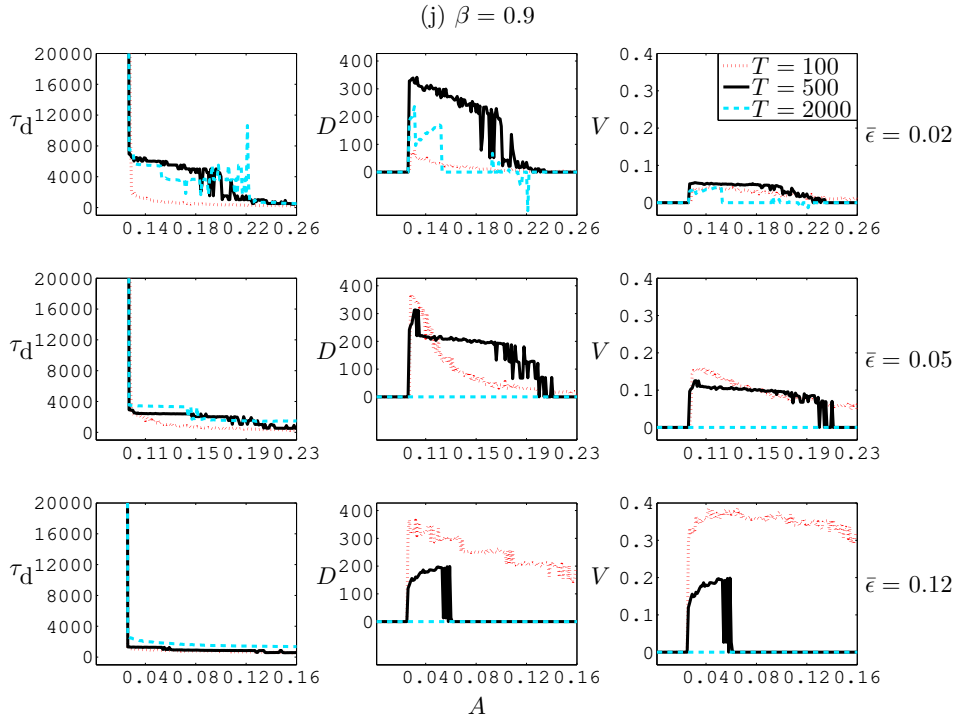

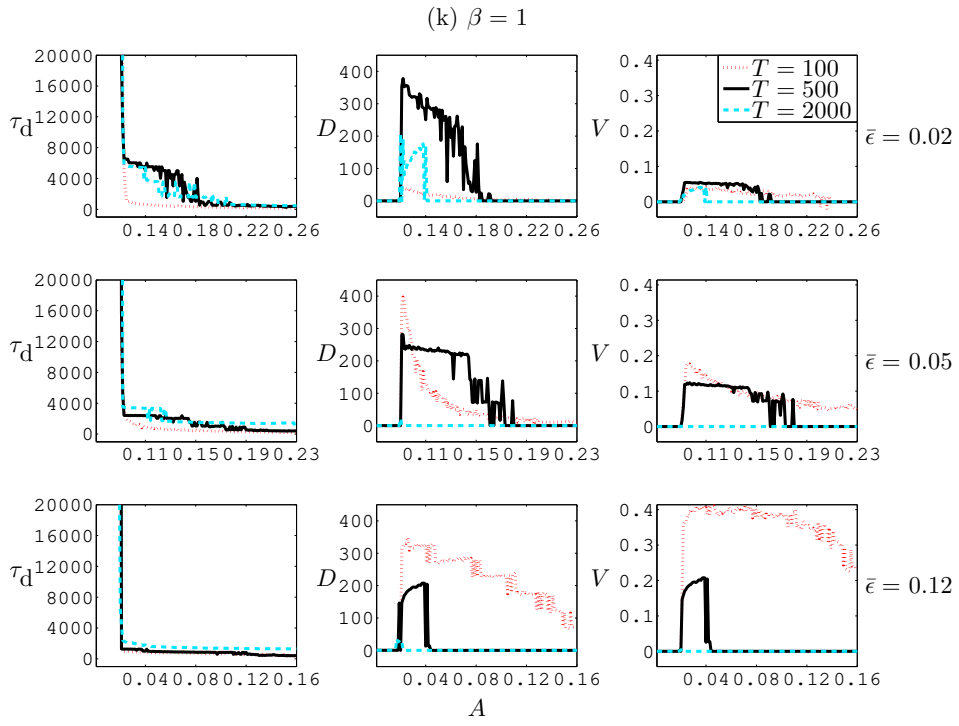

Figure 5.7: Polaron lifetime τ_d, displacement D and velocity V, as functions of the MSPF parameters $\bar{\epsilon}, A$ and T, parametrised by β. For each β, the value of λ is chosen so that $\max |\psi_n^0|^2 = 0.64$ in the stationary state. 1000 units of τ equals 0.12 ns.

5.4.2 Significance of the Symmetry Parameter

Not only does $A_{\mathrm{m}}^{\mathrm{comb}}$ vary with $\bar{\epsilon}$ and T, it varies with β, too. Moreover, $A_{\mathrm{c}}^{\mathrm{comb}}$ also varies with β. We illustrate all of these dependencies in Figure 5.8. Since $T = 2000$ causes anomalies such as those described in Section 5.4.1, we have excluded it from our results.

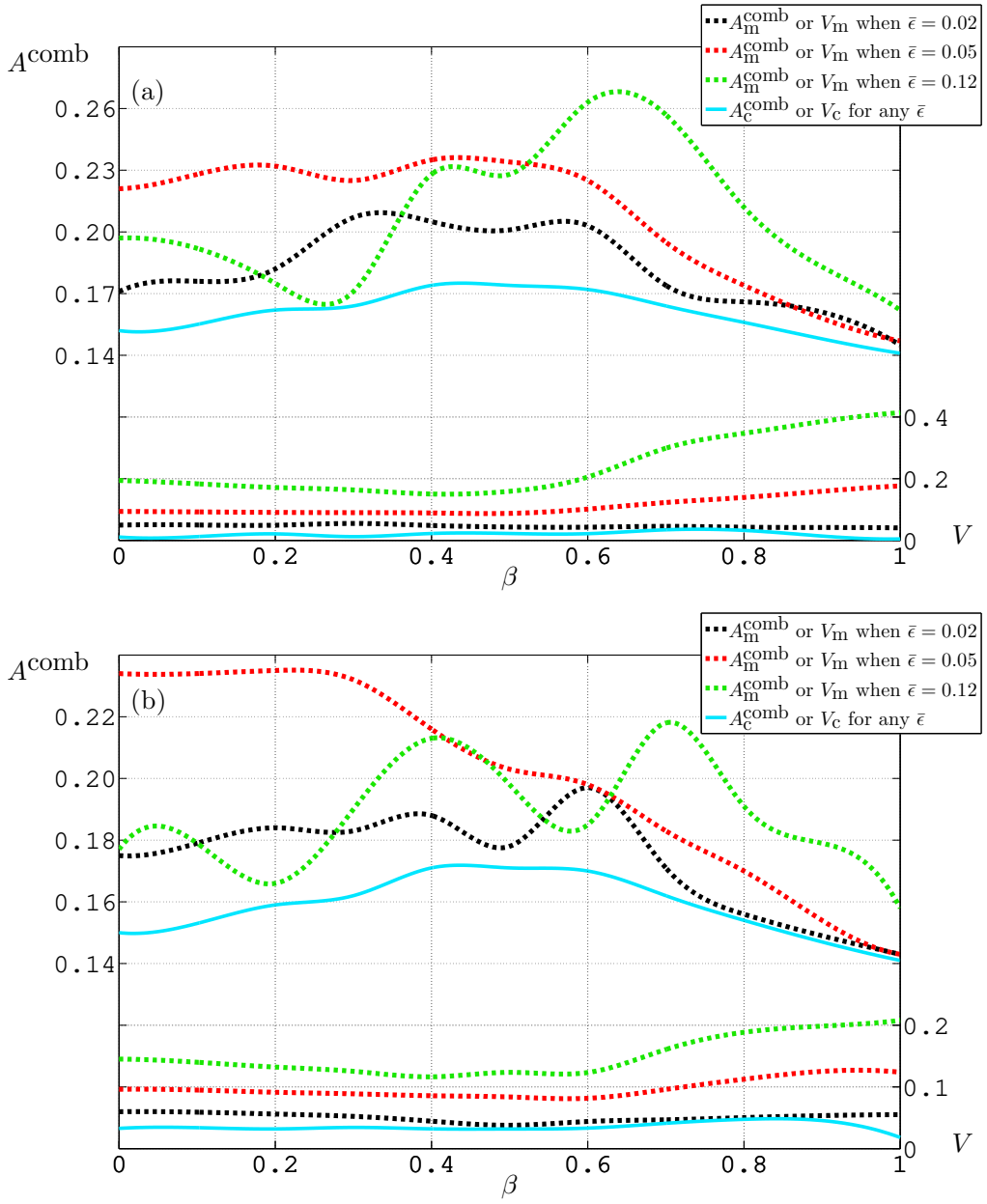

Figure 5.8: Critical combined amplitude $A_{\mathrm{c}}^{\mathrm{comb}}$ and optimal combined amplitude $A_{\mathrm{m}}^{\mathrm{comb}}$ (left axis) as functions of β, the latter being parametrised by $\bar{\epsilon}$. Critical velocity V_{c} and optimal velocity V_{m} (right axis) as functions of β, the latter being parametrised by $\bar{\epsilon}$. $A_{\mathrm{c}}^{\mathrm{comb}}$ and V_{c} are independent of $\bar{\epsilon}$. Parameters: (a) $T = 100$ (12 ps); (b) $T = 500$ (60 ps).

Our first observation is that $A_{\mathrm{c}}^{\mathrm{comb}}$ as a function of β is increasing for $0 \leq \beta \lessapprox 0.45$ and decreasing for $0.45 \lessapprox \beta \leq 1$. This suggests that a moderately spatially asymmetric system ($\beta = 0.45$, at which $A_{\mathrm{c}}^{\mathrm{comb}} = 0.176$) makes the polaron most difficult to displace, compared to a symmetric ($\beta = 0$, at which $A_{\mathrm{c}}^{\mathrm{comb}} = 0.151$) or antisymmetric ($\beta = 1$, at which $A_{\mathrm{c}}^{\mathrm{comb}} = 0.141$) system. These results are similar to those in the α-channel model, where $A_{\mathrm{c}}^{\mathrm{comb}}$ as a function of β was maximised at $\beta \approx 0.6$. Denoting by V_{c} the polaron's velocity at $A^{\mathrm{comb}} = A_{\mathrm{c}}^{\mathrm{comb}}$, or *critical velocity*, we see that whilst $A_{\mathrm{c}}^{\mathrm{comb}}$ is indendependent of T, V_{c} varies slightly with T. This is evidenced by the fact that the two $A_{\mathrm{c}}^{\mathrm{comb}}(\beta)$ curves representing results at $T = 100$ and $T = 500$, respectively in Figure 5.8(a) and (b), are identical, whereas the two $V_{\mathrm{c}}(\beta)$ curves exhibit small differences.

We do not observe any discernible regular pattern of $A_{\mathrm{m}}^{\mathrm{comb}}$ as a function of β, except for the fact that if $\bar{\epsilon}$ is moderate such as 0.05, then $A_{\mathrm{m}}^{\mathrm{comb}}$ exhibits a general decreasing trend as β grows from 0 to 1. Indeed, when $\bar{\epsilon} = 0.05$, we have $A_{\mathrm{m}}^{\mathrm{comb}} \approx 1.5 A_{\mathrm{c}}^{\mathrm{comb}}$ at $\beta = 0$, and at $\beta = 1$ we have $A_{\mathrm{m}}^{\mathrm{comb}}$ and $A_{\mathrm{c}}^{\mathrm{comb}}$ almost coinciding. At larger values of $\bar{\epsilon}$, such as 0.12, $A_{\mathrm{m}}^{\mathrm{comb}}(\beta)$ seems to oscillate in size, between $A_{\mathrm{c}}^{\mathrm{comb}}$ and roughly $1.5 A_{\mathrm{c}}^{\mathrm{comb}}$. It is clear that $A_{\mathrm{m}}^{\mathrm{comb}}$ varies with T, since the corresponding $A_{\mathrm{m}}^{\mathrm{comb}}(\beta)$ curves in Figure 5.8(a) and (b) are significantly different, but our results do not suggest any straightforward positive or negative correlation between $A_{\mathrm{m}}^{\mathrm{comb}}$ and T. Instead, they do suggest a clear relationship between T and the polaron velocity resulting from $A^{\mathrm{comb}} = A_{\mathrm{m}}^{\mathrm{comb}}$, or *optimal velocity*, which we denote by V_{m}. Comparing the corresponding $V_{\mathrm{m}}(\beta)$ curves in Figure 5.8(a) and (b), we see that, fixing all other parameters, the V_{m} at $T = 500$ is roughly half that at $T = 100$. Furthermore, V_{m} is also positively correlated with $\bar{\epsilon}$: fixing all other parameters, we see that V_{m} at $\bar{\epsilon} = 0.12$ is several times as large as that at $\bar{\epsilon} = 0.02$. Indeed, $V_{\mathrm{m}}(\beta)$ at $\bar{\epsilon} = 0.02$ almost coincides with $V_{\mathrm{c}}(\beta)$ for some values of β. Finally, $V_{\mathrm{m}}(\beta)$ is always maximised by $\beta = 1$, regardless of other parameters. We have $V_{\mathrm{m}}(\beta = 1) = 0.42$ if $T = 100$, and $V_{\mathrm{m}}(\beta = 1) = 0.21$ if $T = 500$. In the meantime, $A_{\mathrm{m}}^{\mathrm{comb}}$ is always minimised by $\beta = 1$, similarly to $A_{\mathrm{c}}^{\mathrm{comb}}$ which is also always minimised by $\beta = 1$. These results mean that compared to $\beta < 1$ systems, the spatially antisymmetric system ($\beta = 1$), due to its internal bias of electron-phonon coupling towards one end of the lattice, makes both the *onset* and the *optimisation* of directed polaron propagation achievable with the least amount of EMF forcing.

5.4.3 Effects of Stochastic Forces

The main result that we present in this Section is that stochastic forces arising from temperature in the cell environment *enhances* directed polaron propagation, in the sense that it lowers the critical amplitude of MSPF. The way that we investigate the effects of the stochastic forces is as follows. From a stationary polaron state, we integrate the system of Equation (5.2.9) forward in time under $\epsilon(\tau) = 0$ and a non-zero $f_n(\tau)$ characterised by some thermal energy θ, so that for some amount of τ the system undergoes *thermalisation* [cf. Section 5.3.2] before reaching thermal equilibrium. By $\tau = 2 \times 10^5$, all our polarons have reached thermal equilibrium. At $\tau = 10^6$, long after the polaron has settled in some quasi-stationary state, we set τ to zero and 'switch on' a non-zero MSPF, $\epsilon(\tau)$. We then continue to time-evolve the system and analyse the results. For every initially stationary polaron, and for every set of forcing parameters $\bar{\epsilon}, A, T, \theta$, we run the aforementioned numerical simulation 100 times, and take average values of vital scalar quantities such as the polaron's lifetime τ_{d} , displacement D, and velocity V, from which we deduce system properties such as the critical combined amplitude $A_{\mathrm{c}}^{\mathrm{comb}}$. In the context of thermalised systems, we define $A_{\mathrm{c}}^{\mathrm{comb}}$ to be the smallest combined MSPF amplitude which causes a polaron displacement of at least 10 lattice sites in its lifetime. The reason for this definition is the following. Surveying our results, we observe a large number of $(\bar{\epsilon}, A, T)$ combinations leading to an average (over 100 simulations) polaron displacement of 1 or 2 lattice sites, but they are simply statistical artifacts. Indeed, a polaron fluctuating around its initial position and 'ending up' several sites away at the end of our simulation runtime (10^6 time-units from switching on MSPF) is interpreted as exhibiting an overall displacement; therefore, even if the true mean of polaron displacement under some $(\bar{\epsilon}, A, T)$ combination is zero, the sample mean (over 100 simulations) may easily be 1 or 2. As A^{comb} increases from zero, there is always a jump in the sample mean of D from 1 or 2 to $\mathcal{O}(10^1)$. Thus, saying that A^{comb} reaches critical when it causes a mean D of at least 10 is reasonable.

In Figure 5.9, we present $A_{\mathrm{c}}^{\mathrm{comb}}$ as a function of β, parametrised by $\theta = 0, 0.16$. We have already seen $A_{\mathrm{c}}^{\mathrm{comb}}(\beta)$ at $\theta = 0$ in Figure 5.8. Now we see that compared to $\theta = 0$, a thermal energy of $\theta = 0.16$, which corresponds to a temperature of 10 K, shifts $A_{\mathrm{c}}^{\mathrm{comb}}(\beta)$ by about -0.02 if $\beta \lessapprox 0.8$, and by up to -0.04 if $\beta \to 1$. The overall shape of the $A_{\mathrm{c}}^{\mathrm{comb}}(\beta)$ curve remains roughly unchanged. This is strong evidence for thermal enhancement, meaning the promotion of polaron propagation by the stochastic

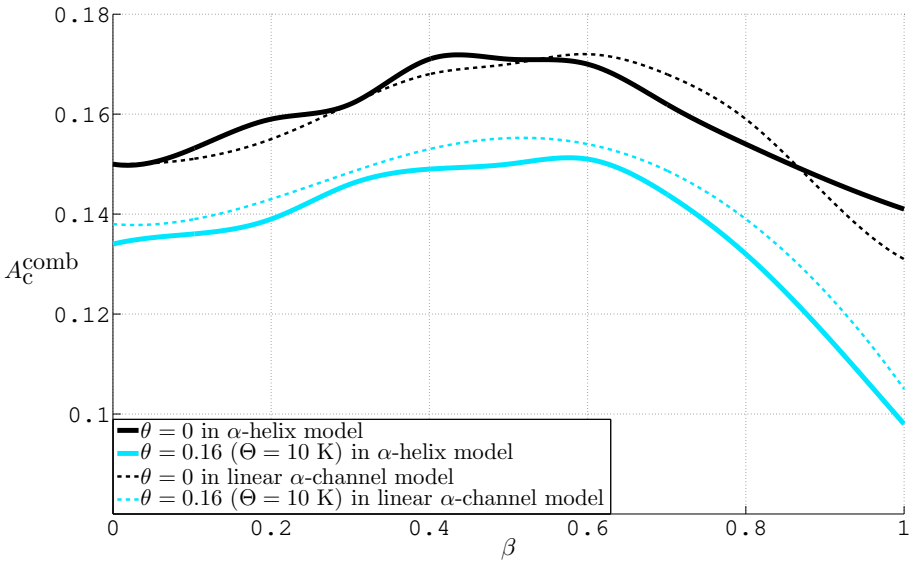

Figure 5.9: The critical combined amplitude of MSPF as a function of β, parametrised by thermal energy θ, in both the α-helix model and the linear α-channel model. Results are unaffected by varying parameters $\bar{\epsilon}$ and T.

forces. Furthermore, the dashed curves in Figure 5.9 represent results from the linear α-channel model of Chapter 4. At $\theta = 0$, results from the α-helix and α-channel models are hardly distinguishable from each other. However at $\theta = 0.16$, corresponding to a temperature of 10 K in both models, we see that the α-helix model produces stronger thermal enhancement than the α-channel model does: $A_c^{comb}(\beta)$ is significantly lower in the α-helix model, across all values of β.

As we discovered in Chapter 4, in the linear α-channel model it was possible at sufficiently high temperatures that the combination of stochastic forces and a constant electric field could displace the polaron in a stable manner, without the need for a sinusoidal component in the MSPF. The same is still true in the α-helix model. Figure 5.10 provides an example of θ being high enough effectively to replace the sinusoidal component of the MSPF. We see that the polaron moves in a characteristically different manner than we have seen in earlier Sections. It still remains a soliton throughout its motion, but it no longer moves in a time-periodic fashion. Instead, it spends almost all of the time oscillating in small amounts, and at random points in time it moves by one or several lattice sites, always in the same direction, contributing to an overall directed motion. All the while, the polaron's internal energy remains highly stable, not deviating far from its thermal equilibrium value of -0.75 meV. As a result of this high stability, the polaron is

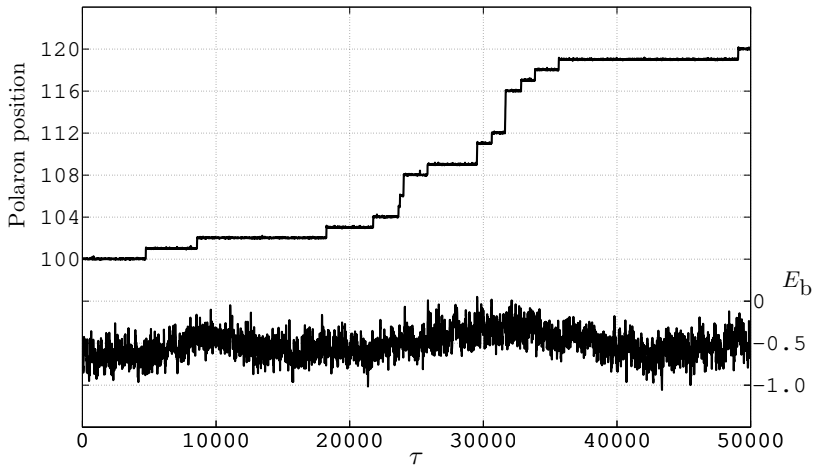

Figure 5.10: A polaron trajectory (left axis) and accompanying time-evolution of polaron internal energy (meV) (right axis). 1000 units of τ equals 0.12 ns. Parameters: $\beta = 0.5, \lambda = 5.6, \bar{\epsilon} = 0.027, A = 0, \theta = 0.64$ ($\Theta = 40$ K).

semi-permanent, with lifetime far exceeding the simulation runtime of 10^6 time-units (120 ns). Thus, the stochastic forces not only promote polaron propagation, they also stabilise it: the issue in the $f_n = 0$ system of rapid delocalisation under constant electric fields is no longer present in the $f_n \neq 0$ system. In the example of Figure 5.10, the polaron takes 50000 time-units (6 ns) to traverse 20 lattice sites, and carries on travelling by about 20 sites per 50000 time-units. This type of semi-permanent, ladder-like trajectory was also characteristic of the α-channel model [cf. Figure 4.13].

We present in Figure 5.11 our final numerical results in this Chapter, and it is the *critical constant amplitude*, $\bar{\epsilon}_c(\beta;\theta)$, defined for every combination of (β,θ) as the smallest $\bar{\epsilon}$ required in order to displace the polaron in a stable manner without the help of a sinusoidal MSPF component. For instance, when $\beta = 0$ and $\theta = 0.64$ ($\Theta = 40$ K), a constant component of $\bar{\epsilon} = 0.04$ is sufficient to facilitate stable polaron propagation (displacing at least 10 lattice sites on average over 100 simulations), without the need for a sinusoidal A component in the MSPF; but if $\bar{\epsilon}$ were any smaller, then we would need to add a non-zero A in order to achieve polaron propagation. Indeed, the polaron trajectory of Figure 4.13 was produced by a critical constant amplitude: $\bar{\epsilon}_c = 0.27$ at $(\beta,\theta) = (0.5, 0.64)$. Our results also show that, if we re-draw Figure 4.13 with a higher electric field amplitude or higher temperature (as long as they are not raised so much that they cause rapid delocalisation), then we would still obtain that ladder-like polaron trajectory, albeit with larger speeds or larger E_b oscillations.

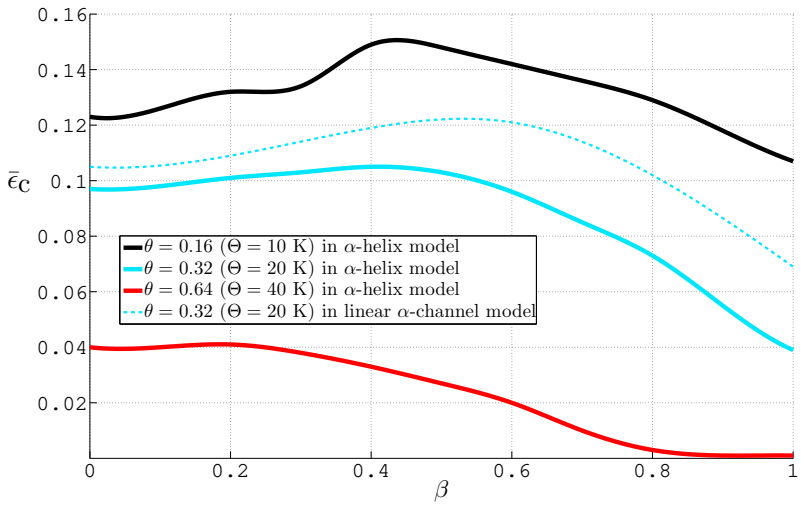

Figure 5.11: The critical constant amplitude as function of β, parametrised by thermal energy θ, in both the α-helix model and the linear α-channel model. Results are unaffected by varying parameters $\bar{\epsilon}$ and T.

Even at temperatures as small as 10 K, the thermal enhancement produced by θ is strong enough that we could use just a constant electric field to produce stable polaon propagation. At larger temperatures, such as $\Theta = 40$ K, and if $\beta \to 1$, then $\bar{\epsilon}_c$ becomes as small as 0.001. However, $\bar{\epsilon} = 0$, in other words stochastic forces on their own without any electric field, is never enough to displace the polaron; they simply cause the polaron to oscillate, or, if θ is large enough, cause delocalisation.

We have included results from the linear α-channel model in Figure 5.11, to enable comparisons with the current α-helix model. Specifically, we may compare the $\bar{\epsilon}_c(\beta)$ curve at $\Theta = 20$ K in the α-helix model to that in the linear α-channel model, and we see that thermal enhancement is stronger in the α-helix model: its $\bar{\epsilon}_c$ curve is lower. We conclude that *the same amount of thermal energy is better at promoting polaron propagation in the α-helix model than in the linear α-channel model.* We may understand this difference by examining the correlation function that defines $f_n(\tau)$ in the α-helix model, Equation (5.2.12), and its counterpart in the α-channel model, Equation (4.2.43). Given the same thermal energy, the correlation $\langle f_m f_n \rangle$ is larger in the α-helix model by a factor of roughly 1.9 (taking into account the different values of γ in the two models). Consequently, we expect whatever effect f_n may have on the system - enhancement in this case - to be magnified in the α-helix model.

5.5 The Model Without A-Mode Symmetry

To make our model even more realistic, we may drop the A-mode symmetry assumption. In this Section, we present analytical results relating to the GDS model for an α-helix without A-mode symmetry.

Our Hamiltonian remains unchanged from Equation (5.1.2), so we still have Equation (5.1.22) as the full dynamical equations of our system. But we no longer assume $\psi_{n,1} = \psi_{n,2} = \psi_{n,3}$ or make any of the assumptions of Equations (5.2.2) and (5.2.3). We re-label our lattice using a single index μ for peptide units along the helical coil, so that the mapping from the (n, j) double index to μ is as follows:

$$\begin{aligned} &(1,1) \mapsto 1, \quad (1,2) \mapsto 2, \quad (1,3) \mapsto 3, \\ &(2,1) \mapsto 4, \quad (2,2) \mapsto 5, \quad (2,3) \mapsto 6, \quad \cdots . \end{aligned} \tag{5.5.1}$$

Or, more generally,

$$(n, j) \mapsto 3(n-1) + j. \tag{5.5.2}$$

Now, μ and $\mu+3$ label neighbouring peptide units along an α-channel, while μ and $\mu+1$ label peptide units in adjacent α-channels which are joined by a peptide bond. We let the total number of peptide units in the α-helix be $N_\alpha + 1$. Then, instead of arriving at Equation (5.2.9) as the dimensionless dynamical equations of our system, we have, for $\mu = 0, 1, \ldots N_\alpha$,

$$\begin{aligned} i\dot{\psi}_\mu = {} & \kappa\psi_\mu \left[(s_\mu + s_{\mu-3}) + \beta\,(s_\mu - s_{\mu-3}) \right] - \rho\,(\psi_{\mu+3} + \psi_{\mu-3} - 2\psi_\mu) \\ & - \rho_\alpha\,(\psi_{\mu+1} + \psi_{\mu-1} - 2\psi_\mu) - \epsilon(\mu - \mu_0)\psi_\mu, \end{aligned} \tag{5.5.3a}$$

$$\begin{aligned} \ddot{u}_\mu = {} & (s_\mu - s_{\mu-3}) + \kappa\zeta^2 \left[\left(|\psi_{\mu+3}|^2 - |\psi_{\mu-3}|^2 \right) - \beta \left(|\psi_{\mu+3}|^2 + |\psi_{\mu-3}|^2 - 2|\psi_n|^2 \right) \right] \\ & - \gamma\dot{u}_\mu + f_\mu, \end{aligned} \tag{5.5.3b}$$

where $|\psi_\mu|^2$ is the electron probability distribution and u_μ the longitudinal lattice site displacement from equilibrium, and

$$s_\mu = u_{\mu+3} - u_\mu \tag{5.5.4}$$

is the amount of distortion of the hydrogen bond between the μ^{th} and $(\mu+3)^{\text{th}}$ peptide units, projected along the helical axis. At the boundaries, we have fictitious points at

$\mu = -3, -2, -1, N_\alpha + 1, N_\alpha + 2, N_\alpha + 3$, such that

$$\psi_{-3} = \psi_{-2} = \psi_{-1} = 0 = \psi_{N_\alpha+1} = \psi_{N_\alpha+2} = \psi_{N_\alpha+3}, \tag{5.5.5a}$$

$$s_{-3} = s_{-2} = s_{-1} = 0 = s_{N_\alpha-2} = s_{N_\alpha-1} = s_{N_\alpha}. \tag{5.5.5b}$$

In particular, Equation (5.5.5b) represents the physical fact that there is no hydrogen bond linking the 0^{th} peptide unit to anything to its left (small-μ direction), similarly for the 1^{st} and 2^{nd} units, and there is no hydrogen bond linking the $(N_\alpha - 2)^{\text{th}}$ unit to anything to its right (large-μ direction), similarly for the $(N_\alpha - 1)^{\text{th}}$ and ${N_\alpha}^{\text{th}}$ units. We also have the boundary conditions

$$\psi_0 = \psi_1 = \psi_2 = \psi_{N_\alpha-2} = \psi_{N_\alpha-1} = \psi_{N_\alpha} = 0, \tag{5.5.6a}$$

$$u_0 = \dot{u}_0 = u_1 = \dot{u}_1 = u_2 = \dot{u}_2 = 0. \tag{5.5.6b}$$

Equation (5.5.6a) is justifiable on a large lattice where the probability distribution is expected to be localised over several sites, and Equation (5.5.6b) is the assumption that all three α-channels in the helix are fixed at one end. Moreover, Equation (5.5.3) holds subject the normalisation condition,

$$\sum_{\mu=0}^{N_\alpha} |\psi_\mu|^2 = 1. \tag{5.5.7}$$

The parameters $\kappa, \rho, \epsilon, \gamma, f_n$ are still defined by Equations (5.2.11) to (5.2.13), and β is still the symmetry parameter, which takes values in $0 \leq \beta \leq 1$ and extrapolates between a spatially symmetric model at $\beta = 0$ and a spatially antisymmetric model at $\beta = 1$. We have a new parameter, ρ_α, which is the electron transfer integral across a peptide bond between adjacent α-channels, measured in units of $\hbar\Omega$:

$$\rho_\alpha := \frac{J_2}{\hbar\Omega}. \tag{5.5.8}$$

Whereas in earlier Sections, ρ_α became nullified under A-mode symmetry, now we cannot make any assumptions except for $\rho_\alpha > 0$. The fixed parameters in our system are still

$$\rho = 2.1, \quad \gamma = 0.019, \quad \zeta = 0.89, \tag{5.5.9}$$

μ_0 in Equation (5.5.3a) is the lattice site at which we set the potential energy due to the EMF, represented by $\epsilon(\tau)$, to zero, and we have dropped the assumption (which we used in earlier Sections) that the electric field has equal influence on the three α-channels. The

internal energy E_{b} of the polaron state is still defined by Equation (5.2.22), but we can no longer simplify the expression using the A-mode symmetry assumption. Instead of Equation (5.2.30), we now have an extra term in the expression for E_{b} (in units of meV) which involves ρ_α:

$$\begin{aligned} E_{\mathrm{b}} = 5.3\rho\Bigg[2 - \sum_{\mu=3}^{N_\alpha-6}\left(\psi^*_{\mu+3}\psi_\mu + \psi^*_\mu\psi_{\mu+3}\right)\Bigg] + 5.3\rho_\alpha\Bigg[2 - \sum_{\mu=3}^{N_\alpha-4}\left(\psi^*_{\mu+1}\psi_\mu + \psi^*_\mu\psi_{\mu+1}\right)\Bigg] \\ + \frac{5.3}{2\zeta^2}\Bigg[\sum_{\mu=3}^{N_\alpha}\dot{u}_n^2 + \sum_{\mu=0}^{N_\alpha-3}\left(u_{\mu+3} - u_\mu\right)^2\Bigg] \\ + 5.3\kappa\sum_{\mu=3}^{N_\alpha-3}|\psi_\mu|^2\Big[\left(u_{\mu+3} - u_{\mu-3}\right) + \beta\left(u_{\mu+3} + u_{\mu-3} - 2u_\mu\right)\Big]. \end{aligned} \tag{5.5.10}$$

In the stationary state, we have $\dot{u}_\mu = \ddot{u}_\mu = 0$, therefore Equation (5.5.3b) is solved by

$$s_\mu = \kappa\zeta^2\left[(\beta-1)\,|\psi_{\mu+3}|^2 - (\beta+1)\,|\psi_\mu|^2\right], \tag{5.5.11}$$

which gives us the following expression for the stationary polaron binding energy:

$$\begin{aligned} E^0_{\mathrm{b}} = 5.3\rho\Bigg[2 - \sum_{\mu=3}^{N_\alpha-6}\left(\psi^*_{\mu+3}\psi_\mu + \psi^*_\mu\psi_{\mu+3}\right)\Bigg] + 5.3\rho_\alpha\Bigg[2 - \sum_{\mu=3}^{N_\alpha-4}\left(\psi^*_{\mu+1}\psi_\mu + \psi^*_\mu\psi_{\mu+1}\right)\Bigg] \\ + \frac{5.3\kappa^2\zeta^2}{2}\sum_{\mu=0}^{N_\alpha-3}\left[(\beta-1)\,|\psi_{\mu+3}|^2 - (\beta+1)\,|\psi_\mu|^2\right]^2 \\ + 5.3\kappa^2\zeta^2\sum_{\mu=3}^{N_\alpha-3}|\psi_\mu|^2\Big[\left(s_\mu + s_{\mu-3}\right) + \beta\left(s_\mu - s_{\mu-3}\right)\Big]. \end{aligned} \tag{5.5.12}$$

By using Equation (5.5.11) to write

$$(s_\mu + s_{\mu-3}) + \beta(s_\mu - s_{\mu-3}) = \kappa\zeta^2\left[-(1-\beta^2)|\psi_{\mu+3}|^2 - (1-\beta^2)|\psi_{\mu-3}|^2 - 2(1+\beta^2)|\psi_\mu|^2\right], \tag{5.5.13}$$

we further deduce

$$\begin{aligned} E^0_{\mathrm{b}} = 5.3\rho\Bigg[2\,(1+r) - \sum_{\mu=3}^{N_\alpha-6}\left(\psi^*_{\mu+3}\psi_\mu + \psi^*_\mu\psi_{\mu+3}\right) - r\sum_{\mu=3}^{N_\alpha-4}\left(\psi^*_{\mu+1}\psi_\mu + \psi^*_\mu\psi_{\mu+1}\right) \\ + \frac{\lambda}{8}\sum_{\mu=0}^{N_\alpha-3}\left[(\beta-1)\,|\psi_{\mu+3}|^2 - (\beta+1)\,|\psi_\mu|^2\right]^2 \\ - \eta\sum_{\mu=3}^{N_\alpha-3}|\psi_\mu|^2\left(|\psi_{\mu+3}|^2 + |\psi_{\mu-3}|^2 - 2|\psi_\mu|^2\right) - \lambda\sum_{\mu=3}^{N_\alpha-3}|\psi_\mu|^4\Bigg], \end{aligned} \tag{5.5.14}$$

where

$$r := \frac{\rho_\alpha}{\rho} > 0, \tag{5.5.15}$$

and λ (the *effective coupling parameter*) and η are as they were defined in Equation (5.3.3), which we present here once more for completeness:

$$\lambda = \frac{4\kappa^2\zeta^2}{\rho}, \tag{5.5.16a}$$

$$\eta = \frac{\kappa^2\zeta^2}{\rho}\left(1-\beta^2\right) \equiv \frac{\lambda}{4}\left(1-\beta^2\right). \tag{5.5.16b}$$

For the remainder of this Section, we focus on stationary solutions to Equation (5.5.3) in the continuum limit. Putting Equation (5.5.13) into Equation (5.5.3a) and setting $\epsilon = 0$, we obtain

$$\begin{aligned} i\dot{\psi}_n = &-\kappa^2\zeta^2\psi_\mu\left[(1-\beta^2)|\psi_{\mu+3}|^2 + (1-\beta^2)|\psi_{\mu-3}|^2 + 2(1+\beta^2)|\psi_\mu|^2\right] \\ &- \rho\left(\psi_{\mu+3} + \psi_{\mu-3} - 2\psi_\mu\right) - \rho_\alpha\left(\psi_{\mu+1} + \psi_{\mu-1} - 2\psi_m\right). \end{aligned} \tag{5.5.17}$$

Defining, for $q = 1, 3$,

$$\Delta_q\psi_\mu := \psi_{\mu+q} + \psi_{\mu-q} - 2\psi_\mu, \quad \Delta_q|\psi_\mu|^2 := |\psi_{\mu+q}|^2 + |\psi_{\mu-q}|^2 - 2|\psi_\mu|^2. \tag{5.5.18}$$

we rewrite Equation (5.5.17) as follows:

$$i\rho^{-1}\dot{\psi}_\mu + \Delta_3\psi_\mu + r\Delta_1\psi_\mu + \lambda|\psi_\mu|^2\psi_\mu + \eta\Delta_3|\psi_\mu|^2\psi_\mu = 0, \tag{5.5.19}$$

In a stationary state, the time-dependence of ψ_μ can be at most a variation of its phase factor. As we did in Section 5.3, we consider the ansatz

$$\psi_\mu(\tau) = \exp\left(i\rho H_0\tau + ikx\right)\phi(x)\big|_{x=\mu-N_\alpha/2,} \tag{5.5.20}$$

where x is a real, continuous variable in the domain $-N_\alpha/2 \leq x \leq N_\alpha/2$, ϕ is a real, smooth function, k is a real, constant wavenumber, and H_0 is a real energy eigenvalue in the sense that

$$i\rho^{-1}\dot{\psi_\mu} = -H_0\psi_\mu. \tag{5.5.21}$$

In the limit $N_\alpha \gg 1$, we write $x = \xi N_\alpha$ for some ξ and $\phi(x) = \widetilde{\phi}(\xi)$ for some $\widetilde{\phi}$, so that

$$\begin{aligned} \psi_{\mu\pm q} &= \exp\left(i\rho H_0\tau + ik\xi N_\alpha\right)\widetilde{\phi}(\xi)\Big|_{\xi=(\mu\pm q)/N_\alpha - 1/2} \\ &= \exp\Big(i\rho H_0\tau + ik\left(\mu \pm q - N_\alpha/2\right)\Big) \\ &\quad\times\left(\widetilde{\phi}(\xi) \pm qN_\alpha^{-1}\widetilde{\phi}'(\xi) + \frac{q^2N_\alpha^{-2}}{2}\widetilde{\phi}''(\xi) + \mathcal{O}\Big(N_\alpha^{-3}\Big)\right)\Bigg|_{\xi=\mu/N_\alpha-1/2.} \end{aligned} \tag{5.5.22}$$

Multiplying Equation (5.5.22) by its complex conjugate yields

$$|\psi_{\mu\pm q}|^2 = \widetilde{\phi}(\xi)^2 \pm 2qN_\alpha^{-1}\widetilde{\phi}(\xi)\widetilde{\phi}'(\xi) + q^2N_\alpha^{-2}\widetilde{\phi}(\xi)\widetilde{\phi}''(\xi) + q^2N_\alpha^{-2}\Big(\widetilde{\phi}'(\xi)\Big)^2 + \mathcal{O}\Big(N_\alpha^{-3}\Big)\Big|_{\xi=\mu/N_\alpha-1/2.} \tag{5.5.23}$$

Putting Equations (5.5.20) to (5.5.23) into Equation (5.5.19), we obtain

$$\begin{aligned} 0 = \exp&\left(i\rho H_0\tau + ik\left(\mu - \frac{N_\alpha}{2}\right)\right) \\ &\times\Bigg[- H_0\widetilde{\phi}(\xi) + \Big(\cos(3k) + i\sin(3k)\Big)\Big(\widetilde{\phi}(\xi) + 3N_\alpha^{-1}\widetilde{\phi}'(\xi) + \frac{9N_\alpha^{-2}}{2}\widetilde{\phi}''(\xi)\Big) \\ &+ \Big(\cos(3k) - i\sin(3k)\Big)\Big(\widetilde{\phi}(\xi) - 3N_\alpha^{-1}\widetilde{\phi}'(\xi) + \frac{9N_\alpha^{-2}}{2}\widetilde{\phi}''(\xi)\Big) - 2\widetilde{\phi}(\xi) \\ &+ r\Big(\cos(k) + i\sin(k)\Big)\Big(\widetilde{\phi}(\xi) + N_\alpha^{-1}\widetilde{\phi}'(\xi) + \frac{N_\alpha^{-2}}{2}\widetilde{\phi}''(\xi)\Big) \\ &+ r\Big(\cos(k) - i\sin(k)\Big)\Big(\widetilde{\phi}(\xi) - N_\alpha^{-1}\widetilde{\phi}'(\xi) + \frac{N_\alpha^{-2}}{2}\widetilde{\phi}''(\xi)\Big) - 2r\widetilde{\phi}(\xi) + \lambda\widetilde{\phi}(\xi)^3 \\ &+ \eta\Big[18N_\alpha^{-2}\widetilde{\phi}(\xi)\widetilde{\phi}''(\xi) + 18N_\alpha^{-2}\Big(\widetilde{\phi}'(\xi)\Big)^2\Big]\widetilde{\phi}(\xi) + \mathcal{O}(N_\alpha^{-3})\Bigg]\Bigg|_{\xi=n/N_\alpha-1/2.} \end{aligned} \tag{5.5.24}$$

Retaining terms up to $\mathcal{O}(N_\alpha^{-2})$, we have

$$\begin{aligned} 0 = &-H_0\widetilde{\phi}(\xi) + \cos(3k)\Big[2\widetilde{\phi}(\xi) + 9N_\alpha^{-2}\widetilde{\phi}''(\xi)\Big] + 6i\sin(3k)N_\alpha^{-1}\widetilde{\phi}'(\xi) \\ &+ r\cos(k)\Big[2\widetilde{\phi}(\xi) + N_\alpha^{-2}\widetilde{\phi}''(\xi)\Big] + 2ri\sin(k)N_\alpha^{-1}\widetilde{\phi}'(\xi) - 2\left(1+r\right)\widetilde{\phi}(\xi) \\ &+ \lambda\widetilde{\phi}(\xi)^3 + 9\eta N_\alpha^{-2}\left[2\widetilde{\phi}(\xi)\widetilde{\phi}''(\xi) + 2\Big(\widetilde{\phi}'(\xi)\Big)^2\right]\widetilde{\phi}(\xi)\Big|_{\xi=n/N_\alpha-1/2.} \end{aligned} \tag{5.5.25}$$

Equating imaginary parts of Equation (5.5.25) gives us

$$3\sin(3k) + r\sin(k) = 0. \tag{5.5.26}$$

We use the identity

$$\sin(3k) \equiv \sin(k)\left(2\cos(2k) + 1\right) \tag{5.5.27}$$

to rewrite Equation (5.5.26) as

$$\sin(k)\Big[2\cos(2k) + \Big(1 + \frac{r}{3}\Big)\Big] = 0. \tag{5.5.28}$$

if $r > 3$, then $\sin(k) = 0$ is the only spectrum of solutions to Equation (5.5.28), and consequently we have $k = l\pi$ where l is any integer, and $\cos(k) = \cos(3k) = \pm 1$. Using

$\widetilde{\phi}'(\xi) = N_\alpha \phi'(x)\Big|_{x=\xi N_\alpha}$ and $\widetilde{\phi}''(\xi) = N^2 \phi''(x)\Big|_{x=\xi N_\alpha}$, where $'$ always denotes differentiation with respect to the argument in parentheses, we write the real part of Equation (5.5.25) as either

$$\begin{aligned} &- H_0\phi(x) + (9+r)\,\phi''(x) + \lambda\phi(x)^3 \\ &\quad + 9\eta\left[2\phi(x)\phi''(x) + 2\left(\phi'(x)\right)^2\right]\phi(x)\Big|_{x=n-N_\alpha/2} = 0, \quad \text{if } \cos(k) = 1, \end{aligned} \tag{5.5.29}$$

or

$$\begin{aligned} &- \widetilde{H_0}\phi(x) - (9+r)\,\phi''(x) + \lambda\phi(x)^3 \\ &\quad + 9\eta\left[2\phi(x)\phi''(x) + 2\left(\phi'(x)\right)^2\right]\phi(x)\Big|_{x=n-N_\alpha/2} = 0, \quad \text{if } \cos(k) = -1, \end{aligned} \tag{5.5.30}$$

where

$$\widetilde{H_0} = H_0 + 4(1+r). \tag{5.5.31}$$

By letting $N_\alpha \to \infty$ and letting x take all real values, we obtain the stationary form of a generalised nonlinear Schrödinger equation (GNLSE), with either a focusing cubic potential ($+\lambda\phi^3$):

$$-H_0\phi(x) + (9+r)\,\phi''(x) + \lambda\phi(x)^3 + 9\eta\Big(\phi(x)^2\Big)''\phi(x) = 0, \quad \text{if } \cos(k) = 1, \tag{5.5.32}$$

or a de-focusing cubic potential ($-\lambda\phi^3$):

$$\widetilde{H_0}\phi(x) + (9+r)\,\phi''(x) - \lambda\phi(x)^3 - 9\eta\Big(\phi(x)^2\Big)''\phi(x) = 0, \quad \text{if } \cos(k) = -1. \tag{5.5.33}$$

In the latter case, the argument that we used at the end of Section 4.3.3 suffices to show that no square-normalisable $\phi(x)$ solution exists. In the case of $\cos(k) = 1$, Equation (5.5.32) differs from Equation (4.3.19) for the α-channel model by only the factors of $(9+r)$ (instead of 1) and 9η (instead of η). Thus, the same phase-space method that we used to solve the GNLSE in the α-channel model still applies now, and the essential steps (which we rigorously validated in Section 4.3.3) are as follows.

We rearrange Equation (5.5.32) and suppress the argument x of ϕ, leading to the autonomous equation,

$$-H_0\phi + \phi''\left(9 + r + 18\eta\phi^2\right) + \lambda\phi^3 + 18\eta(\phi')^2\phi = 0. \tag{5.5.34}$$

In the phase space, where ϕ' is a function of ϕ, we define $h(\phi) := \phi'$, and write $\phi'' \equiv (\mathrm{d}\phi'/\mathrm{d}\phi)\phi' = hh_\phi$, where the subscript ϕ denotes differentiation with respect to ϕ. We then define $y(\phi) := h(\phi)^2 = (\phi')^2$, so that $y_\phi = 2hh_\phi = 2\phi''$. Multiplying Equation (5.5.34) by 2 gives

$$\Big(9 + r + 18\eta\phi^2\Big)y_\phi + 36\eta\phi y = 2H_0\phi - 2\lambda\phi^3, \tag{5.5.35}$$

where the left-hand side is the total derivative of $(9 + r + 18\eta\phi^2)y$ with respect to ϕ. Integrating both sides, we have

$$y \equiv (\phi')^2 = \frac{H_0\phi^2 - \lambda\phi^4/2 + C}{9 + r + 18\eta\phi^2}, \tag{5.5.36}$$

where $C = 0$ due to vanishing boundary conditions at infinity, and $H_0 > 0$, for otherwise the only solution is $\phi \equiv 0$. Multiplying Equation (5.5.36) by $4\phi^2$, we obtain

$$\Big(\Phi'\Big)^2 = \frac{4H_0\Phi^2 - 2\lambda\Phi^3}{9 + r + 18\eta\Phi}, \tag{5.5.37}$$

where we have defined $\Phi := \phi^2$. Being able to solve Equation (5.5.37) relies upon being able to integrate

$$\big[g(\Phi)\big]^{-1} = \left[2\sqrt{H_0}\Phi\sqrt{\frac{1 - \Phi/\Phi_0}{9 + r + 18\eta\Phi}}\right]^{-1} \tag{5.5.38}$$

around the singularity $\Phi = \Phi_0$, where

$$\Phi_0 = \frac{2H_0}{\lambda} \tag{5.5.39}$$

is the only non-zero value of Φ at which Φ' vanishes. We showed in Section 4.3.3 that Φ_0 is the unique global maximum value of Φ, and that we can set $\Phi(x = 0) = \Phi_0$ without loss of generality. Using the method which we described between Equations (4.3.56) and (4.3.66), we express our solution to Equation (5.5.37) as

$$\mathrm{sgn}(x)\frac{\sqrt{H_0}\,x}{\sqrt{9 + r}} = \mathrm{arsinh}\sqrt{\frac{1 - (\Phi/\Phi_0)}{(1 + \nu)\,(\Phi/\Phi_0)}} + \sqrt{\nu}\ \arctan\sqrt{\frac{\nu\,(1 - (\Phi/\Phi_0))}{1 + (\nu\Phi/\Phi_0)}}, \tag{5.5.40}$$

where

$$\nu = \frac{36\eta H_0}{(9 + r)\lambda}. \tag{5.5.41}$$

If H_0 is known, then, as we proved in Section 4.3.3, the combination of Equations (5.5.39) and (5.5.40) *uniquely* provides a globally positive, normalised $\Phi(x)$ which solves Equation (5.5.37); and since $\Phi(x)$ is globally positive, we can use $\phi = \pm\sqrt{\Phi}$ to recover a

solution to the GNLSE, Equation (5.5.32). However, H_0 is not known; it is an energy eigenvalue to be determined. By the same method that we employed in the steps leading up to Equation (4.3.74), we have the similar result that H_0 is given *uniquely* by the algebraic equation,

$$\frac{\lambda}{4\sqrt{H_0(9+r)}} = \sqrt{\nu} + (1+\nu)\arctan\sqrt{\nu}. \tag{5.5.42}$$

The $\Phi(x)$ solution given by Equation (5.5.40) has a highly-localised, bell curve-shaped profile over the real line, characteristic of the stationary polaron states that we have encountered thus far. If we discretise $\Phi(x)$ to obtain an approximation for the electron probability distribution $|\psi_\mu|^2$, then, due to the label μ being along the helical coil, $|\psi_\mu|^2$ represents a polaron which is localised across all three α-channels. If there exist stationary polarons which are localised on a single α-channel, the continuum approximation that we have so far described is unable to capture them. Moreover, without any knowledge of the value of the parameter ρ_α, the use of any numerical experiments we may perform on our system is highly limited, as we expect the system's properties to be sensitively dependent upon the ratio r between ρ_α and ρ.

Now, if we had $r \leq 3$, then Equation (5.5.28) would have more than $\sin(k) = 0$ as its solution. Indeed, we would have an extra spectrum of wavenumbers given by

$$\cos(2k) = -\frac{1}{2} - \frac{r}{6}, \tag{5.5.43}$$

and consequently

$$\cos(k) = \pm\sqrt{\frac{1}{4} - \frac{r}{12}}, \tag{5.5.44a}$$

$$\cos(3k) = \mp\sqrt{\frac{1}{4} - \frac{r}{12}}\left(2 + \frac{r}{3}\right), \tag{5.5.44b}$$

which we can insert into the real part of Equation (5.5.25). This results in a new set of generalised nonlinear Schrödinger equations, but more work is needed in order to make analytical progress on them. Nevertheless, we have shown that $r = 3$ is a bifurcation point in our model, as $r > 3$ and $r \leq 3$ lead to characteristically different systems of equations.

5.6 Summary and Biophysical Interpretations

In all but Section 5.5 of this Chapter, we used a generalised Davydov-Scott model to study polaronic electron transport in the α-helix, under the assumption of A-mode symmetry:

that the electron is equipartitioned amongst the three α-channels. We discovered that the dynamical equations governing the electron-phonon system are similar to those in Chapter 4, which described electron transport along a single α-channel. The fundamental difference between the two sets of equations is that in the α-helix model a parameter ζ appears which encapsulates the twisting of the α-channels around the helical axis. We derived stationary polaron solutions, parametrised by an effective coupling parameter λ, and quasi-stationary solutions under thermal fluctuations, parametrised by λ and thermal energy θ. Given identical values for all physical parameters, we found that the α-helix model admits stationary polarons which are less strongly bound than the α-channel model did. Equivalently, in order to create a stationary polaron with some prescribed binding energy, a larger electron-phonon coupling constant is required in the α-helix model than is required in the α-channel model. This is due to the fact that in the α-helix, the electron tends to disperse amongst the three channels, as dictated by the negative inter-channel electron transfer energy, $-J_2$. We also presented evidence that stationary polarons in the α-helix model are more thermally stable than those in the α-channel model, in the sense that, given equally strong stationary polarons in the two models, in the α-helix model a higher thermalisation temperature is required to destroy the binding.

Using an electromagnetic field (EMF) in the form of a mean-shifted periodic field (MSPF) to displace the stationary polaron, we found results which are directly comparable to those in Chapter 4. The same biophysical conclusions as we reached in Section 4.5 (aided by references therein) still apply. Firstly, the constant component of the MSPF matches in order of magnitude the resting membrane potential in living cells. Secondly, the temporally sinusoidal component matches in frequency those we find in everyday life such as WiFi and satellite communications, but the typical amplitude of the sinusoidal component is several orders larger than the aforementioned artificial electromagnetic waves. Subjecting the system to stochastic forces arising from a thermal environment, we discovered that temperatures up to about 95 K can enhance polaron propagation, in that the stochastic forces effectively remove the need for a sinusoidal component of the MSPF. Under the combination of stochastic forces and a constant electric field, the strength of which matches those resulting from resting membrane potentials, we found that the polaron can remain highly stable while it traverses $\mathcal{O}(1)$ lattice sites per nanosecond, a biologically-relevant time-scale [cf. Figure 5.10]. This is a significant result because it is well-known that a typical transmembrane α-helix comprises 20 to 30 peptide units, or, up to around 10

units per α-channel [Luc08, LWBR10]. Under the A-mode symmetry, 10 peptide units translates precisely into labels $n = 0, 1, \ldots 9$; therefore our model explains how a polaron can propagate from one end of a transmembrane α-helix to the other in several nanoseconds or less, under nothing but inherent forces in the cell environment.

One shortcoming of our model is that it is impossible to raise the thermalisation temperature to beyond roughly $\Theta_{\max} = 95$ K, as doing so destroys the polaron binding. This is already a higher allowance than that under the α-channel model of Chapter 4 (which had $\Theta_{\max} = 55$ K), but the thermal energy resulting from a temperature of 95 K is still roughly 3 times smaller than physiological. We believe that one viable way to address this issue could be to discard the A-mode symmetry assumption, allowing the electron to transfer between the three α-channels rather than be equally distributed among them. We derived the dynamical equations for this general model in Section 5.5 and presented some analytical results, including that in the continuum approximation of the lattice, there exists a stationary electron probability distribution localised on a single α-channel. However we have currently no means to determine whether this system permits higher thermalisation temperatures than it did under A-mode symmetry, due to the lack of empirical data or theoretical estimates concerning the value of the inter-channel electron transfer integral, J_2. It is possible to treat J_2 as a fitting parameter, and to study a family of systems parametrised by its value, but the high computational cost of this endeavour has prohibited us from completing such a task for this thesis. We will work towards completing said task for a future publication.

Chapter 6

Summary and Future Directions

The aim of this thesis was to develop mathematical models capable of explaining the mechanisms by which electrons are transported along an α-helical protein. With the historical context of the problem in mind, we chose to utilise the theoretical framework of polarons, a concept whose roots are deep in the field of condensed matter physics. We set out to generalise two existing polaron models which were best suited to the task: the Holstein-Hennig model of electron-intrapeptide oscillator coupling, and the Davydov-Scott model of exciton-hydrogen bond phonon coupling. In the former case, we represented a single α-channel in the helix as a lattice and quantised its dynamics. We then used an external, pulse-like electromagnetic field to launch stationary polarons that formed on the lattice. We presented our results, adapted from [LP18], in Chapter 3. We found that pulses whose amplitudes and time-spans matched those known naturally to occur in biological complexes were able to facilitate directed polaron motion on the picosecond scale, in a manner which was energetically stable even at physiological temperature. Generalising the Davydov-Scott model, which was originally used to study the transport of vibrational energy, we introduced a parameter to describe the extent to which the electron-phonon interaction in the helix was spatially symmetric. We presented in Chapter 4 results adapted from [LP17], on the application of the generalised Davydov-Scott (GDS) model to a single, linear α-channel; then in Chapter 5, we applied the GDS model to the three-channel structure of the α-helix. In both cases, we found that an electromagnetic field in the form of a mean-shifted periodic field (MSPF), comprising a constant component and a temporally sinusoidal one, could facilitate stable polaron propagation. We also found that stochastic forces arising from the cell's thermal environment promoted polaron propagation, in the sense that they made polarons more susceptible to the influence of the MSPF. Applying

the GDS model to the α-helix under the assumption of A-mode symmetry - that the electron is equipartitioned amongst the three α-channels - we discovered that the twisting of the channels makes polarons more stable against thermal fluctuations than they were in a single, linear channel. In several nanoseconds or less, a polaron can traverse the length of a typical transmembrane α-helix, under nothing but stochastic thermal forces and a constant, resting membrane potential, both of which are intrinsically realisable in the cell environment. However the model also predicts that temperatures higher than 95 K tend to destroy the polaron binding. Overall, our modelling efforts have been fruitful in that we are able to explain α-helical electron transport phenomena within the polaron theory framework, and that both internal and external interactions in the models are realisable in nature. If laboratory tests can help to fit certain internal parameters, such as the electron-lattice coupling constants in the various models, then the models could become useful tools in biotechnology, due to their predictive powers in terms of how a polaron reacts to external forces.

Immediate future work following this thesis shall involve completing the α-helical GDS model under no assumption of A-mode symmetry. We already have some analytical results in that regard, which we presented in Chapter 5, and it remains for us to conduct numerical experiments, parametrising our outputs by the as-yet undetermined inter-channel electron transfer integral. If the numerical study proves successful, then we will look into combining the generalised Holstein-Hennig and GDS models, creating a model which accounts for the electron's coupling to both intrapeptide and interpeptide oscillators. We may need to treat such a model as a multi-scale problem, since there is a large characteristic time-scale separation between typical intrapeptide and interpeptide oscillators in the α-helix.

Bibliography

[AG02] J. F. Atkins and R. Gesteland. The 22nd amino acid. *Science*, 296(5572):1409–1410, 2002.

[AM13] I. Angeli and K. P. Marinova. Table of experimental nuclear ground state charge radii: An update. *Atomic Data and Nuclear Data Tables*, 99(1):69–95, 2013.

[AS06] A. Altland and B. Simons. *Condensed Matter Field Theory,* Ch. 2, pp. 58-60. Cambridge University Press, Cambridge, 2006.

[Bar50] J. Bardeen. Wave functions for superconducting electrons. *Physical Review*, 80(4):567–574, 1950.

[Bar74] R. A. Bari. Small-polaron effects on the DC conductivity and thermoelectric power of the one-dimensional Mott semiconductor. *Physical Review B*, 9(10):4329–4339, 1974.

[Bar07] W. Barford. Exciton transfer integrals between polymer chains. *Journal of Chemical Physics*, 126(13):134905, 2007.

[BBO91] D. N. Beratan, J. N. Betts, and J. N. Onuchic. Protein electron transfer rates set by the bridging secondary and tertiary structure. *Science*, 252(5010):1285–1288, 1991.

[BBO92] D. N. Beratan, J. N. Betts, and J. N. Onuchic. Tunneling pathway and redox-state-dependent electronic couplings at nearly fixed distance in electron-transfer proteins. *Journal of Physical Chemistry*, 96(7):2852–2855, 1992.

[BCHE98] L. S. Brizhik, L. Cruzeiro-Hansson, and A. A. Eremko. Influence of electromagnetic radiation on molecular solitons. *Journal of Biological Physics*, 24(1):19–40, 1998.

[Bec92] A. D. Becke. A new mixing of Hartree-Fock and local density-functional theories. *Journal of Chemical Physics*, 98(2):1372–1377, 1992.

[BELM95] L. S. Brizhik, A. A. Eremko, and A. La Magna. The ground state of an electron or exciton in the Holstein model. *Phyics Letters A*, 200(2):213–218, 1995.

[BELMP95] L. S. Brizhik, A. A. Eremko, A. La Magna, and P. Pucci. The ground state of an extra electron interacting with acoustic phonons in a molecular chain. *Phyics Letters A*, 205(1):90–96, 1995.

[BEPZ04] L. S. Brizhik, A. A. Eremko, B. M. A. G. Piette, and W. J. Zakrzewski. Solitons in α-helical proteins. *Physical Review E*, 70(3):031914, 2004.

[BEPZ06] L. S. Brizhik, A. A. Eremko, B. M. A. G. Piette, and W. J. Zakrzewski. Charge and energy transfer by solitons in low-dimensional nanosystems with helical structure. *Chemical Physics*, 324(1):259–266, 2006.

[BEPZ08] L. S. Brizhik, A. A. Eremko, B. M. A. G. Piette, and W. J. Zakrzewski. Ratchet behaviour of polarons in molecular chains. *Journal of Physics: Condensed Matter*, 20(25):255242, 2008.

[BEPZ10] L. S. Brizhik, A. A. Eremko, B. M. A. G. Piette, and W. J. Zakrzewski. Ratchet dynamics of large polarons in asymmetric diatomic molecular chains. *Journal of Physics: Condensed Matter*, 22(15):155105, 2010.

[BEPZ14] L. S. Brizhik, A. A. Eremko, B. M. A. G. Piette, and W. J. Zakrzewski. Thermal enhancement and stochastic resonance of polaron ratchets. *Physical Review E*, 89(6):062905, 2014.

[BER73] E. J. Baerends, D. E. Ellis, and P. Ros. Self-consistent molecular Hartree-Fock-Slater calculations I. The computational procedure. *Chemical Physics*, 2(1):41–51, 1973.

[BESP72] K. G. Brown, S. C. Erfurth, E. W. Small, and W. L. Peticolas. Conformationally dependent low-frequency motions of proteins by laser Raman spectroscopy. *Proceedings of the National Academy of Sciences of the United States of America*, 69(6):1467–1469, 1972.

[BIST89] J. Bellissard, B. Iochum, E. Scoppola, and D. Testard. Spectral properties of one dimensional quasi-crystals. *Communications in Mathematical Physics*, 125:527–543, 1989.

[BJMBO89] M. Bixon, J. Jortner, M. E. Michel-Beyerle, and A. Ogrodnik. A superexchange mechanism for the primary charge separation in photosynthetic reaction centers. *Biochimica et Biophysica Acta - Bioenergetics*, 977(3):273–286, 1989.

[BKL05] D. W. Boukhvalov, M. I. Katsnelson, and A. I. Lichtenstein. Hydrogen on graphene: Electronic structure, total energy, structural distortions and magnetism from first-principles calculations. *Physical Review B*, 77(3):035427, 2005.

[BLCW69] R. C. Brandt, D. M. Larsen, P. P. Crooker, and G. B. Wright. Polaron Zeeman effect in AgBr. *Physical Review Letters*, 23(5):240–243, 1969.

[Blo28] F. Bloch. Über die Quantenmechanik der Elektronen in Kristallgittern (Quantum mechanics of electrons in crystal lattices). *Zeitschrift für Physik*, 52:555–600, 1928.

[BM72] M. V. Berry and K. E. Mount. Semiclassical approximations in wave mechanics. *Reports on Progress in Physics*, 35(1):315–397, 1972.

[BMS99] A. R. Bausch, W. Möller, and E. Sackmann. Measurement of local viscoelasticity and forces in living cells by magnetic tweezers. *Biophysical Journal*, 76(1):573–579, 1999.

[BO27] M. Born and R. Oppenheimer. Zur Quantentheorie der Molekeln (The quantum theory of molecules). *Annalen der Physik*, 84(20):457–484, 1927.

[BPH+16] K. Bugge, E. Papaleo, G. W. Haxholm, J. T. S. Hopper, C. V. Robinson, J. G. Olsen, K. Lindorff-Larsen, and B. B. Kragelund. A combined computational and structural model of the full-length human prolactin receptor. *Nature Communications*, 7:11578, 2016.

[Bre79] W. Brenig. Theory of inelastic atom-surface scattering: average energy loss and energy distribution. *Zeitschrift für Physik B*, 36:81–87, 1979.

[BT88] D. J. Barlow and J. M. Thornton. Helix geometry in proteins. *Journal of Molecular Biology*, 201:601–619, 1988.

[BTS12] J. M. Berg, J. L. Tymoczko, and L. Stryer. *Biochemistry,* ch. 2, pp. 30-32. W. H. Freeman and Company, Basingstoke, England, 7$^{\text{th}}$ (International) edition, 2012.

[Bur58] K. Burton. Energy of adenosine triphosphate. *Nature*, 181(4623):1594–1595, 1958.

[BWH87] J. L. Brédas, F. Wudl, and A. J. Heeger. Polarons and bipolarons in doped polythiophene: A theoretical investigation. *Solid State Communications*, 63(7):577–580, 1987.

[Cho83] K.-C. Chou. Low-frequency vibrations of helical structures in protein molecules. *Biochemical Journal*, 209:573–580, 1983.

[CHT97] L. Cruzeiro-Hansson and S. Takeno. Davydov model: The quantum, mixed quantum-classical, and full classical systems. *Physical Review E*, 56(1):894–906, 1997.

[CHV$^+$80] K. Cheng, H. C. Haspel, M. L. Vallano, B. Osotimehin, and M. Sonenberg. Measurement of membrane potentials (Ψ) of erythrocytes and white adipocytes by the accumulation of triphenylmethylphosphonium cation. *Journal of Membrane Biology*, 56(3):191–201, 1980.

[CL93] G. N. Chuev and V. D. Lakhno. A polaron model for electron transfer in globular proteins. *Journal of Theoretical Biology*, 163(1):51–60, 1993.

[CLR77] C. Chothia, M. Levitt, and D. Richardson. Structure of proteins: Packing of a-helices and pleated sheets. *Proceedings of the National Academy of Sciences of the United States of America*, 74(10):4130–4134, 1977.

[Con05] E. M. Conwell. Charge transport in DNA in solution: The role of polarons. *Proceedings of the National Academy of Sciences of the United States of America*, 102(25):8795–8799, 2005.

[CR00] E. M. Conwell and S. V. Rakhmanova. Polarons in DNA. *Proceedings of the National Academy of Sciences of the United States of America*, 97(9):4556–4560, 2000.

[Dai08] J. Daintith, editor. *A Dictionary of Chemistry,* pp. 23. Oxford University Press, Oxford, 6^{th} edition, 2008.

[Dav63] R. E. Davies. A molecular theory of muscle contraction: calcium-dependent contractions with hydrogen bond formation plus ATP-dependent extensions of part of the myosin-actin cross-bridges. *Nature*, 199(4898):1068–1074, 1963.

[Dav73] A. S. Davydov. The theory of contraction of proteins under their excitation. *Journal of Theoretical Biology*, 38:559–569, 1973.

[Dav74] A. S. Davydov. Quantum theory of muscular contraction. *Biophysics*, 19:684–691, 1974.

[Dav77] A. S. Davydov. Solitons and energy transfer along protein molecules. *Journal of Theoretical Biology*, 66:379–387, 1977.

[Dav79a] A. S. Davydov. Solitons, bioenergetics and the mechanism of muscle contraction. *International Journal of Quantum Chemistry*, 16:5–17, 1979.

[Dav79b] A. S. Davydov. Solitons in molecular systems. *Physica Scripta*, 20(3/4):387–394, 1979.

[Dav82] A. S. Davydov. Solitons in quasi-one-dimensional molecular structures. *Soviet Physics Uspekhi*, 25(12):898–918, 1982.

[DKM00] P. Dimroth, G. Kaim, and U. Matthey. Crucial role of the membrane potential for ATP synthesis by F(1)F(o) ATP synthases. *Journal of Experimental Biology*, 203(1):51–59, 2000.

[Dov03] M. T. Dove. *Structure and Dynamics: An Atomic View of Materials,* Ch, 5, pp. 108-115. Oxford University Press, Oxford, 2003.

[Dun01] J. D. Dunitz. Pauling's left-handed α-helix. *Angewandte Chemie International Edition*, 40(22):4167–4173, 2001.

[EH02] J. Edler and P. Hamm. Self-trapping of the amide I band in a peptide model crystal. *Journal of Chemical Physics*, 117(5):2415–2424, 2002.

[Eis03] D. Eisenberg. The discovery of the α-helix and β-sheet, the principal structural features of proteins. *Proceedings of the National Academy of Sciences of the United States of America*, 100(20):11207–11210, 2003.

[ELS84] J. C. Eilbeck, P. S. Lomdahl, and A. C. Scott. Soliton structure in crystalline acetanilide. *Physical Review B*, 30(8):4703–4712, 1984.

[Ems80] J. Emsley. Very strong hydrogen bonding. *Chemical Society Reviews*, 9(1):91–124, 1980.

[FAOR89] G. Feher, J. P. Allen, M. Y. Okamura, and D. C. Rees. Structure and function of bacterial photosynthetic reaction centres. *Nature*, 339(6220):111–116, 1989.

[FH63] L. Friedman and T. Holstein. Studies of polaron motion part III. The Hall mobility of the small polaron. *Annals of Physics*, 21(3):494–549, 1963.

[FMD93] R. M. Farid, C. C. Moser, and P. L. Dutton. Electron transfer in proteins. *Current Opinion in Structural Biology*, 3(2):225–233, 1993.

[För93] W. Förner. Quantum and temperature effects on Davydov soliton dynamics: III. Interchain coupling. *Journal of Physics: Condensed Matter*, 5(7):823–840, 1993.

[Frö50] H. Fröhlich. Theory of the superconducting state. I. The ground state at the absolute zero of temperature. *Physical Review*, 79(5):845–856, 1950.

[Frö52] H. Fröhlich. Interaction of electrons with lattice vibrations. *Proceedings of the Royal Society of London A*, 215(1122):291–298, 1952.

[Frö54] H. Fröhlich. On the theory of superconductivity: the one-dimensional case. *Proceedings of the Royal Society of London A*, 223(1154):296–305, 1954.

[FV91] K. Fushimi and A. S. Verkman. Low viscosity in the aqueous domain of cell cytoplasm measured by picosecond polarization microfluorimetry. *Journal of Cell Biology*, 112(4):719–725, 1991.

[FV16] M. V. Fischetti and W. G. Vandenberghe. *Advanced Physics of Electron Transport in Semiconductors and Nanostructures,* Ch. 4, p. 58 ff. and Ch. 5, p. 80 ff. Springer, Basel, 2016.

[FW03] A. L. Fetter and J. D. Walecka. *Theoretical Mechanics of Particles and Continua,* Ch. 4, pp. 108-119. Dover, Mineola, NY, 2003.

[GAK+01] B. Giese, J. Amaudrut, A.-K. Köhler, M. Spormann, and S. Wessely. Direct observation of hole transfer through DNA by hopping between adenine bases and by tunnelling. *Nature*, 412(6844):318–320, 2001.

[GBM+88] Y. Gauduel, S. Berrod, A. Migus, N. Yamada, and A. Antonetti. Femtosecond charge separation in organized assemblies: Free-radical reactions with pyridine nucleotides in micelles. *Biochemistry*, 27:2509–2518, 1988.

[Gil73] M. E. Gilpin. Do hares eat lynx? *American Naturalist*, 107(957):727–730, 1973.

[GK93] J. M. Gruschus and A. Kuki. New Hamiltonian model for long-range electronic superexchange in complex molecular structures. *Journal of Physical Chemistry*, 97(21):5581–5593, 1993.

[Gla63] R. J. Glauber. Coherent and incoherent states of the radiation field. *Physical Review*, 131(6):2766–2788, 1963.

[GW96] H. B. Gray and J. R. Winkler. Electron transfer in proteins. *Annual Review of Biochemistry*, 65:537–561, 1996.

[Hen01] D. Hennig. Mobile polaron solutions and nonlinear electron transfer in helical protein models. *Physical Review E*, 64(4):041908, 2001.

[Hen02] D Hennig. Energy transport in α-helical protein models: One-strand versus three-strand systems. *Physical Review B*, 65(17):174302, 2002.

[HEWM83] R. M. Hochmuth, C. A. Evans, H. C. Wiles, and J. T. McCown. Mechanical measurement of red cell membrane thickness. *Science*, 220(4592):101–102, 1983.

[HH52] A. L. Hodgkin and A. F. Huxley. A quantitative description of membrane current and its application to conduction and excitation in nerve. *Journal of Physiology*, 117:500–544, 1952.

[Hil01] B. Hille. *Ion Channels of Excitable Membranes,* Ch. 2, pp. 45-54. Sinauer, Sunderland, MA, 3rd edition, 2001.

[Hir73] R. Hirota. Exact envelope-soliton solutions of a nonlinear wave equation. *Journal of Mathematical Physics*, 14(7):805–809, 1973.

[HKSS88] A. J. Heeger, S. Kivelson, J. R. Schrieffer, and W.-P. Su. Solitons in conducting polymers. *Reviews of Modern Physics*, 60(3):781–851, 1988.

[Hod71] J. W. Hodby. Cyclotron resonance of the polaron in the alkali and silver halides. III. *Journal of Physics C: Solid State Physics*, 4(1):L8–L11, 1971.

[Hol59a] T. Holstein. Studies of polaron motion part I. The molecular-crystal model. *Annals of Physics*, 8(3):325–342, 1959.

[Hol59b] T. Holstein. Studies of polaron motion part II. The "small" polaron. *Annals of Physics*, 8(3):343–389, 1959.

[Hol64] T. Holstein. Theory of transport phenomena in an electron-phonon gas. *Annals of Physics*, 29(3):410–535, 1964.

[HY70] M. Hatano and M. Yoneyama. Side-chain effect on the helix stability of poly-α-amino acids. *Journal of the American Chemical Society*, 92(5):1392–1395, 1970.

[IEE03] IEEE Std 521-2002 (Revision of IEEE Std 521-1984) IEEE Standard letter designations for radar-frequency bands, 2003. doi: 10.1109/IEEESTD.2003.94224.

[IEE12] IEEE Std 802.11ad-2012 (Amendment to IEEE Std 802.11-2007 (Revision of IEEE Std 802.11-1999)) IEEE Standard for information technology – Telecommunications and information exchange between systems – Local and metropolitan area networks – Specific requirements – Part 11: Wireless LAN Medium Access Control (MAC) and Physical Layer (PHY) Specifications

amendment 3: Enhancements for very high throughput in the 60 GHz band, 2012. doi: 10.1109/IEEESTD.2012.6392842.

[Jac99] J. D. Jackson. *Classical Electrodynamics,* Ch. 4, p. 153 ff. Wiley, New York, 3rd edition, 1999.

[JBVR02] J. Jortner, M. Bixon, A. A. Voityuk, and N. Rösch. Superexchange mediated charge hopping in DNA. *Journal of Physical Chemistry A*, 106(33):7599–7606, 2002.

[JL66] E. J. Johnson and D. M. Larsen. Polaron induced anomalies in the interband magnetoabsorption of InSb. *Physical Review Letters*, 16(15):655–659, 1966.

[JL08] J. Jablonsky and D. Lazar. Evidence for intermediate S-states as initial phase in the process of oxygen-evolving complex oxidation. *Biophysical Journal*, 94(6):2725–2736, 2008.

[Jol03] P. Joliot. Period-four oscillations of the flash-induced oxygen formation in photosynthesis. *Photosynthesis Research*, 76:65–72, 2003.

[Joy74] W. B. Joyce. Classical-particle description of photons and phonons. *Physical Review D*, 9(12):3234, 1974.

[JP88] J. J. Jennings and K. Parslow. Particle size measurement: The equivalent spherical diameter. *Proceedings of the Royal Society of London A*, 419(1856):137–149, 1988.

[KAT98] G. Kalosakas, S. Aubry, and G. P. Tsironis. Polaron solutions and normal-mode analysis in the semiclassical Holstein model. *Physical Review B*, 58(6):3094–3104, 1998.

[Ken61] J. C. Kendrew. The three-dimensional structure of a protein molecule. *Scientific American*, 205(6):96–111, 1961.

[Kit63] C. Kittel. *Quantum Theory of Solids,* Ch. 2-3, p. 12 ff. Wiley, New York, 1963.

[KL87] W. C. Kerr and P. S. Lomdahl. Quantum-mechanical derivation of the equations of motion for Davydov solitons. *Physical Review B*, 35(7):3629–3632, 1987.

[KMB+16] M. Kaucikas, K. Maghlaoui, J. Barber, T. Renger, and J. J. van Thor. Ultrafast infrared observation of exciton equilibration from oriented single crystals of photosystem II. *Nature Communications*, 7:13977, 2016.

[Lak08] V. D. Lakhno. DNA nanobioelectronics. *International Journal of Quantum Chemistry*, 108(11):1970–1981, 2008.

[Lan08] P. Langevin. Sur la théorie du mouvement Brownien (On the theory of Brownian motion). *Comptes Rendus de l'Académie des Sciences*, 146:530–533, 1908.

[Lan33] L. D. Landau. Electron motion in crystal lattices. *Physikalische Zeitschrift der Sowjetunion*, 3:664–665, 1933.

[LDS69] C. W. Litton, R. B. Dennis, and S. D. Smith. Infra-red cyclotron resonance in n-type epitaxial InAs with evidence of polaron coupling. *Journal of Physics C: Solid State Physics*, 2(11):2146–2155, 1969.

[LF03] V. D. Lakhno and N. S. Fialko. Hole mobility in a homogeneous nucleotide chain. *JETP Letters*, 78(5):336–338, 2003.

[LFV+04] S. Lönn, U. Forssén, P. Vecchia, A. Ahlbom, and M. Feychting. Output power levels from mobile phones in different geographical areas; implications for exposure assessment. *Occupational and Environmental Medicine*, 61(9):769–772, 2004.

[LG97] D. S. Lemons and A. Gythiel. Paul Langevin's 1908 paper "On the theory of Brownian motion" ["Sur la théorie du mouvement Brownien," C. R. Acad. Sci. (Paris) 146, 530–533 (1908)]. *American Journal of Physics*, 65(11):1079–1081, 1997.

[Lid04] D. R. Lide, editor. *Handbook of Chemistry and Physics,* Sec. 7-1. CRC Press, Boca Raton, FL, 85nd edition, 2004.

[LLH+07] Z.-D. Li, Q.-Y. Li, X.-H. Hu, Z.-X. Zheng, and Y. Sun. Hirota method for the nonlinear Schrödinger equation with an arbitrary linear time-dependent potential. *Annals of Physics*, 322(11):2545–2553, 2007.

[LLZA13] L. Li, C. Li, Z. Zhang, and E. Alexov. On the dielectric "constant" of proteins: Smooth dielectric function for macromolecular modeling and its implementation in DelPhi. *Journal of Chemical Theory and Computation*, 9(4):2126–2136, 2013.

[Lot20] A. J. Lotka. Analytical note on certain rhythmic relations in organic systems. *Proceedings of the National Academy of Sciences of the United States of America*, 6(7):410–415, 1920.

[LP48] L. D. Landau and S. I. Pekar. Effective mass of a polaron. *Zhurnal Eksperymental'noyi i Teoretychnoyi Fizyky*, 18(5):419–423, 1948.

[LP86] J. M. Luck and D. Petritis. Phonon spectra in one-dimensional quasicrystals. *Journal of Statistical Physics*, 42(3/4):289–310, 1986.

[LP17] J. Luo and B. M. A. G. Piette. A generalised Davydov-Scott model for polarons in linear peptide chains. *European Physical Journal E*, 90:155, 2017.

[LP18] J. Luo and B. M. A. G. Piette. Directed polaron propagation in linear polypeptides induced by intramolecular vibrations and external electric pulses. *Physical Review E*, 98:012401, 2018.

[Luc08] M. Luckey. *Membrane Structrural Biology,* Ch. 9, pp. 230-239. Cambridge University Press, New York, 2008.

[Luo18] J. Luo. A generalised Davydov-Scott model for polarons in the α-helix. *In preparation*, 2018.

[LWBR10] D. N. Langelaan, M. Wieczorek, C. Blouin, and J. K. Rainey. Improved helix and kink characterization in membrane proteins allows evaluation of kink sequence predictors. *Journal of Chemical Information and Modeling*, 50(12):2213–2220, 2010.

[Mah13] G. D. Mahan. *Many-Particle Physics,* Ch. 1, pp. 1-11. Springer Science & Business Media, New York, 3$^{\text{rd}}$ edition, 2013.

[MB61] T. Miyazawa and E. R. Blout. The infrared spectra of polypeptides in various conformations: amide I and II bands. *Journal of the American Chemical Society*, 83(3):712–719, 1961.

[McC61] H. M. McConnell. Intramolecular charge transfer in aromatic free radicals. *Journal of Chemical Physics*, 35(2):508–515, 1961.

[MDC08] D. L. Mobley, K. A. Dill, and J. D. Chodera. Treating entropy and conformational changes in implicit solvent simulations of small molecules. *Journal of Physical Chemistry B*, 112(3):938–946, 2008.

[Mis12] P. K. Misra. *Physics of Condensed Matter,* Ch. 2, pp. 37-47. Academic Press, Burlington, MA, 2012.

[Mit61] P. Mitchell. Coupling of phosphorylation to electron and hydrogen transfer by a chemi-osmotic type of mechanism. *Nature*, 191(4784):144–148, 1961.

[MK80] L. McCaughan and S. Krimm. X-ray and neutron scattering density profiles of the intact human red blood cell membrane. *Science*, 207(4438):1481–1483, 1980.

[MKW$^+$92] C. C. Moser, J. M. Keske, K. Warncke, R. S. Farid, and P. L. Dutton. Nature of biological electron transfer. *Nature*, 355(6363):796–802, 1992.

[MKY$^+$11] C. Margraves, K. Kihm, S. Y. Yoon, C. K. Choi, S.-H. Lee, J. Liggett, and S. J. Baek. Simultaneous measurements of cytoplasmic viscosity and intracellular vesicle sizes for live human brain cancer cells. *Biotechnology and Bioengineering*, 108(10):2504–2508, 2011.

[MM67] P. Mitchell and J. Moyle. Chemiosmotic hypothesis of oxidative phosphorylation. *Nature*, 213(5072):137–139, 1967.

[MYY$^+$04] J. Ma, M. Yoshimura, E. Yamashita, A. Nakagawa, A. Ito, and T. Tsukihara. Structure of rat monoamine oxidase A and its specific recognitions for substrates and inhibitors. *Journal of Molecular Biology*, 338(1):103–114, 2004.

[Nag77] K. Nagasaka. Piezoelectric polaron and polaron pinning in n-CdS. *Physical Review B*, 15(4):2273–2277, 1977.

[NC76] N. A. Nevskaya and Y. N. Chirgadze. Infrared spectra and resonance interactions of amide-I and II vibrations of α-helix. *Biopolymers*, 15(4):637–648, 1976.

[OB04] M. A. O'Neill and J. K. Barton. DNA charge transport: Conformationally gated hopping through stacked domains. *Journal of the American Chemical Society*, 126(37):11471–11483, 2004.

[OH68] D. S. Olander and A. Holtzer. The stability of the polyglutamic acid α helix. *Journal of the American Chemical Society*, 90(17):4549–4560, 1968.

[Oka74] K. Okamoto. Ground-state energy of piezoelectric polaron. *Journal of the Physical Society of Japan*, 36(1):62–68, 1974.

[PBM90] P. C. F. Pau, J. O. Berg, and W. G. McMillan. Application of Stokes' law to ions in aqueous solution. *Journal of Physical Chemistry*, 94(6):2671–2679, 1990.

[PCB51] L. Pauling, R. B. Corey, and H. R. Branson. The structure of proteins: two hydrogen-bonded helical configurations of the polypeptide chain. *Proceedings of the National Academy of Sciences of the United States of America*, 37(4):205–211, 1951.

[Pek46] S. I. Pekar. Autolocalization of the electron in a dielectric inertially polarizing medium. *Zhurnal Eksperymental'noyi i Teoretychnoyi Fizyky*, 16(4):335–340, 1946.

[PY58] J. K. Percus and G. J. Yevick. Analysis of classical statistical mechanics by means of collective coordinates. *Physical Review*, 110(1):1–13, 1958.

[RAT63] J. M. Rowell, P. W. Anderson, and D. E. Thomas. Image of the phonon spectrum in the tunneling characteristic between superconductors. *Physical Review Letters*, 10(8):334–336, 1963.

[Ric03] P. R. Rich. The molecular machinery of Keilin's respiratory chain. *Biochemical Society Transactions*, 31(6):1095–1105, 2003.

[SAH+15] M. Suga, F. Akita, K. Hirata, G. Ueno, H. Murakami, Y. Nakajima, T. Shimizu, K. Yamashita, M. Yamamoto, H. Ago, and J.-R. Shen. Native structure of photosystem II at 1.95 Å resolution viewed by femtosecond X-ray pulses. *Nature*, 517(7532):99–103, 2015.

[SB80] R. Sedlmeir and W. Brenig. Inelastic atom-surface scattering: a comparison of classical and quantum treatments. *Zeitschrift für Physik B*, 36:245–250, 1980.

[Sch10] T. Schlick. *Molecular Modeling and Simulation: An Interdisciplinary Guide,* Ch. 10, pp. 335-338. Springer-Verlag, New York, 2nd edition, 2010.

[Sco81] A. C. Scott. The laser-Raman spectrum of a Davydov soliton. *Physics Letters A*, 86(1):60–62, 1981.

[Sco82a] A. C. Scott. Dynamics of Davydov solitons. *Physical Review A*, 26(1):578–595, 1982.

[Sco82b] A. C. Scott. The vibrational structure of Davydov solitons. *Physica Scripta*, 25(5):651–658, 1982.

[Sco92] A. C. Scott. Davydov's soliton. *Physics Reports*, 217(1):1–67, 1992.

[SDSC10] M. W. Shinwari, M. J. Deen, E. B. Starikov, and G. Cuniberti. Electrical conductance in biological molecules. *Advanced Functional Materials*, 20(12):1865–1883, 2010.

[Ser03] M. N. Sergeenko. Classical solution of the wave equation. *International Journal of Modern Physics A*, 18(17):3041–3055, 2003.

[Sin01] J. Singleton. *Band Theory and Electronic Properties of Solids,* Ch. 4, pp. 32-40. Oxford University Press, Oxford, 2001.

[SK54] J. C. Slater and G. F. Koster. Simplified LCAO method for the periodic potential problem. *Physical Review*, 94(6):1498–1524, 1954.

[SS80] W.-P. Su and J. R. Schrieffer. Soliton dynamics in polyacetylene. *Proceedings of the National Academy of Sciences of the United States of America*, 77(10):5626–5629, 1980.

[SSF98] R. E. Stratmann, G. E. Scuseria, and M. J. Frisch. An efficient implementation of time-dependent density-functional theory for the calculation of excitation energies of large molecules. *Journal of Chemical Physics*, 109(19):8218–8224, 1998.

[SSH79] W.-P. Su, J. R. Schrieffer, and A. J. Heeger. Solitons in polyacetylene. *Physical Review Letters*, 42(25):1698–1701, 1979.

[SSH80] W.-P. Su, J. R. Schrieffer, and A. J. Heeger. Soliton excitations in polyacetylene. *Physical Review B*, 22(4):2099–2111, 1980.

[STS67] H. Susi, S. N. Timasheff, and L. Stevens. Infrared spectra and protein conformations in aqueous solutions I. The amide I band in H_2O and D_2O solutions. *Journal of Biological Chemistry*, 242(23):5460–5466, 1967.

[SY08] V. Z. Spassov and L. Yan. A fast and accurate computational approach to protein ionization. *Protein Science*, 17(11):1955–1970, 2008.

[SZGR78] L. Swierkowski, W. Zawadzki, Y. Guldner, and C. Rigaux. Two-mode resonant polaron in the $Hg_{0.72}Cd_{0.28}Te$ semiconductor. *Solid State Communications*, 27(11):1245–1247, 1978.

[Tam29] I. Y. Tamm. Über die Quantentheorie der molekularen Lichtzerstreuung in festen Körpern (On the quantum theory of molecular light-scattering in solid bodies). *Zeitschrift für Physik*, 60:345–363, 1929.

[TK75] T. Takeda and T. Kasuya. A theory for self-trapped magnetic polaron in ferromagnetic semiconductor with a narrow band. *Journal of the Physical Society of Japan*, 39(6):1443–1453, 1975.

[Tur52] A. M. Turing. The chemical basis of morphogenesis. *Philosophical Transactions of the Royal Society of London B*, 231(641):37–72, 1952.

[TW74] J. Thomchick and G. Whitfield. Structure of the moving piezoelectric polaron. *Physical Review B*, 10(8):3458–3463, 1974.

[UKSK11] Y. Umena, K. Kawakami, J.-R. Shen, and N. Kamiya. Crystal structure of oxygen-evolving photosystem II at a resolution of 1.9 Å. *Nature*, 473(7345):55–60, 2011.

[VBKH05] J. Vondrášek, L. Bendová, V. Klusák, and P. Hobza. Unexpectedly strong energy stabilization inside the hydrophobic core of small protein rubredoxin mediated by aromatic residues: Correlated ab initio quantum chemical calculations. *Journal of the American Chemical Society*, 127(8):2615–2619, 2005.

[VEB+86] Z. Vardeny, E. Ehrenfreud, O. Brafman, M. Nowak, H. Schaffer, A. J. Heeger, and F. Wudl. Photogeneration of confined soliton pairs (bipolarons) in polythiophene. *Physical Review Letters*, 56(6):671–674, 1986.

[Vil73] I. Vilfan. Small polaron model of the electron motion in organic molecular crystals. *Physica Status Solidi B: Basic Solid State Physics*, 59(1):351–360, 1973.

[vMG02] T. van Mourik and R. J. Gdanitz. A critical note on density functional theory studies on rare-gas dimers. *Journal of Chemical Physics*, 116(22):9620–9623, 2002.

[Vol26] V. Volterra. Variazioni e fluttuazioni del numero d'individui in specie animali conviventi (Variations and fluctuations of the number of individuals in animal species living together). *Memoria della Regia Accademia Nazionale dei Lincei 6*, 2:31–113, 1926.

[VRW09] S. Vicatos, M. Roca, and A. Warshel. Effective approach for calculations of absolute stability of proteins using focused dielectric constants. *Proteins: Structure, Function, and Bioinformatics*, 77(3):670–684, 2009.

[Wal56] C. B. Walker. X-ray study of lattice vibrations in aluminum. *Physical Review*, 103(3):547–557, 1956.

[Wen51] G. Wentzel. The interaction of lattice vibrations with electrons in a metal. *Physical Review*, 83(1):168–169, 1951.

[WS03] J. C. Weaver and K. H. Schoenback. Biodielectrics. *IEEE Transactions on Dielectrics and Electrical Insulation*, 10(5):715–716, 2003.

[YC10] P. Y. Yu and M. Cardona. *Fundamentals of Semiconductors: Physics and Materials Properties,* Ch. 2, pp. 71-96. Springer-Verlag, Heidelberg, 4$^{\text{th}}$ edition, 2010.

[Zav87] A. A. Zavitsas. Quantitative relationship between bond dissociation energies, infrared stretching frequencies, and force constants in polyatomic molecules. *Journal of Physical Chemistry*, 91(22):5573–5577, 1987.

[Zim72] J. M. Ziman. *Principles of the Theory of Solids,* Ch. 6, pp. 200-203. Cambridge University Press, Cambridge, 2nd edition, 1972.

[ZR77] T. Ziegler and A. Rauk. On the calculation of bonding energies by the Hartree Fock Slater method. *Theoretica Chimica Acta*, 46(1):1–10, 1977.

[ZS72] V. E. Zakharov and A. B. Shabat. Exact theory of two-dimensional self-focusing and one-dimensional self-modulation of waves in nonlinear media. *Soviet Physics JETP*, 34(1):62–69, 1972.

[ZZ01] D. Zhong and A. H. Zewail. Femtosecond dynamics of flavoproteins: Charge separation and recombination in riboflavine (vitamin B_2)-binding protein and in glucose oxidase enzyme. *Proceedings of the National Academy of Sciences of the United States of America*, 98(21):11867–11872, 2001.